Solidification in metal additive manufacturing: challenges, solutions, and opportunities

Shubham Chandra[1,2], Jayaraj Radhakrishnan[2], Sheng Huang[2], Siyuan Wei[3], Upadrasta Ramamurty[2,3]

[1]Singapore Centre for 3D Printing, School of Mechanical and Aerospace Engineering, Nanyang Technological University, Singapore 639798, Republic of Singapore.

[2]School of Mechanical and Aerospace Engineering, Nanyang Technological University, Singapore 639798, Republic of Singapore.

[3]Institute of Materials Research and Engineering (IMRE), Agency for Science, Technology and Research (A∗STAR), 2 Fusionopolis Way, Innovis #08-03, Singapore 138634, Republic of Singapore.

Abstract: The physics of alloy solidification during additive manufacturing (AM) in methods such as laser powder bed fusion (LPBF), electron beam powder bed fusion (EPBF), and laser directed energy deposition (LDED), is distinct due to the combination of (a) the rapid solidification conditions that often prevail in AM, (b) adjoining scan tracks that result in the overlap of the adjacent melt pools, and (c) layer-wise fabrication that causes the pre-deposited layer to influence the subsequent layer's microstructural evolution. The complex interplay between these and each alloy's distinct solidification characteristics results in a wide spectrum of hierarchical microstructures that span multiple length scales, with diverse grain morphologies and non-equilibrium phases. Consequently, a detailed understanding of the solidification phenomena that occur during LPBF, EPBF, and LDED is necessary for controlling the microstructural evolution, which ensures repeatable and predictable mechanical response of the built part, and hence structural reliability of it in service. Keeping this in view, substantial efforts have been made to develop a detailed understanding of the solidification during AM of alloys, which are summarized in this review. From the local interfacial equilibrium applicable to a range of rapid solidification conditions to non-equilibrium conditions that prevail during ultra-fast solidification are reviewed. Numerical efforts ranging from atomic scale to macro-scale have been reviewed with a central goal of highlighting the phenomenon of dislocation evolution, grain growth, and phase formation during solidification. Specific challenges such as solidification cracking in non-weldable alloys and porosity-cracking dilemmas are discussed. Unique opportunities for tailoring the microstructures such as in-situ alloying are presented.

Table of Contents

List of abbreviations

AM	Additive manufacturing
CM	Conventional manufacturing
PBF	Powder bed fusion
DED	Directed energy deposition
LPBF	Laser powder bed fusion
EPBF	Electron beam powder bed fusion
LDED	Laser directed energy deposition
BJP	Binder jet printing
PFAM	Powder fusion-additive manufacturing
FCC	Face-centred cubic
BCC	Body-centred cubic
HCP	Hexagonal close-packed
CET	Columnar-to-equiaxed transition
SEM	Scanning electron microscopy
EBSD	Electron back-scattered diffraction
BSE	Backscattered Electron
EDS	Energy dispersive spectroscopy
CA	Cellular automata
MD	Molecular dynamics
PF	Phase-field
FEA	Finite element analysis
FEM	Finite element method
CFD	Computational fluid dynamics
FVM	Finite volume method
FDM	Finite different method
DPM	Discrete particle method
MD	Molecular Dynamics
SS	Stainless steel
AA	Aluminium alloy
ML	Machine learning
DFT	Density functional theory
KGT	Kurz-Giovanola-Trivedi
LGK	Lipton–Glicksman–Kurz
HEA	High entropy alloy
MEA	Medium entropy alloy
MPEA	Multi-princinpal element alloy
PDF	Pair distribution function
HIP	Hot-isostatic pressing
GB	Grain boundary
HAGB	High-angle grain boundary
LAGB	Low-angle grain boundary
XRD	X-ray diffraction
CR	Cooling rate
μ-SLM	Micro-selective laser melting
PDAS	Primary dendrite arm spacing
CA	Cellular automata
KMC	Kinetic Monte Carlo
PFM	Phase-field method

LB	Lattice Boltzmann
DEM	Discrete element method
TWIP	Twinning induced plasticity
SLM	Selective laser melting
LE	Longitudinal elliptical
TE	Transverse elliptical
HAZ	Heat affected zone
PDAS	Primary dendrite arm spacing
SDAS	Secondary dendrite arm spacing
SX	Single crystal
RDG	Rappaz-Drezet-Gremaud
AR	Aspect ratio
MPE	Melt pool engineering
LOF	Lack-of-fusion
BD	Build direction
TEM	Transmission electron microscopy
ASLM	Anchorless selective laser melting
EPMA	Electron probe micro analysis
LBM	Lattice boltzmann method
UV	Ultrasonic vibration
SMF	Static magnetic fields
MHD	Magneto hydrodynamic damping
EMD	Electric magnetic damping
MDF	Magnetic damping force
TEMHD	Thermoelectric magnetohydrodynamic
TEMF	Thermoelectric magnetic force
MFD	Magnetic flux density
CP	Commercially pure
DSC	Differential scanning calorimetry
PH	Phase-hardened
IPF	Inverse pole figure
LEGO	Layer-wise engineering of grain orientation

List of symbols

q	Heat flux
A	Surface area
v'	Volume
c	Specific heat capacity
T	Temperature
Δh_f	Latent heat of fusion per unit volume
f_s	Fraction solid
t	Time
dT/dt or $\dot{T}$	Cooling rate (CR)
r_c	Critical radius
σ	Surface energy per unit area
Δg	Gibbs free energy change per unit volume
ψ	Contact angle or solid-solid wetting angle
V	Solidification rate or growth rate
ΔT	Total undercooling
ΔT_t	Thermal undercooling
ΔT_c	Constitutional undercooling
ΔT_r	Curvature undercooling
ΔT_k	Kinetic undercooling
ΔT_0	Solidification interval/Equilibrium freezing range
k	Equilibrium partition coefficient
m	Equilibrium liquidus slope
C_0	Solute concentration in the nominal alloy
C_s	Solute concentration in the solid
C_l	Solute concentration in the liquid
Γ	Gibbs-Thomson coefficient
T_m	Melting temperature
T_{mp}	Meltpool temperature
ΔH	Latent heat
G	Thermal gradient
R	Dendrite tip radius
D	Coefficient for solute diffusion
D_L	Coefficient for solute diffusion in liquid
ΔS	Entropy change
R'	Gas constant
L	Length of the liquid
μ	Kinetic mobility
V	Solidification rate
V_a	Limit for absolute stability
V_{ab}	Solidification rate for absolute stability
Q	Growth restriction factor
V_{cs}	Solidification rate for constitutional supercooling
K^*	Velocity dependent partition coefficient

m^*	Velocity dependent liquidus slope
D^*	Velocity dependent diffusion coefficient
V_{Di}	Diffusion speed of solute in interface region
V_{Db}	Diffusion speed of solute in bulk liquid
I_v	Ivanstov function
P_t	Thermal Péclet number
P_c	Solutal Péclet number
G_c	Concentration gradient
σ^*	Stability constant
E	Energy
γ	Specific grain boundary energy per unit length
$\delta_{(i,j)}$	Kronecker delta function
ΔT_{nuc}	Mean undercooling
ΔT_σ	Standard deviation in undercooling
n_{max}	Maximum nuclei density
P	Probability of heterogeneous nucleation
V_{cell}	Volume of lattice site
Δt	Time step
Γ_{gl}	Solid-liquid interface mobility
φ	Phase field variable
λ	Primary dendrite arm spacing (PDAS)
λ_d	PDAS for a dendrite
λ_c	PDAS for a cell
$\dot{\varepsilon}$	Strain rate
λ_2	Secondary dendrite arm spacing (SDAS)
T_L	Liquidus temperature
T_s	Solidus temperature
C_p	Specific heat at constant pressure
β	Solidification shrinkage
ν	Melt viscosity
V_T	Isotherm velocity
ε_{local}	Local strain
v_z	Liquid feeding velocity
θ	Inclination angle of neighbouring grains
φ	Grain width
N_o	Nucleation density
ΔT_n	Nucleation undercooling
E^*_{min}	Normalized minimum volumetric energy density
p^*	Dimensionless laser power
v^*	Dimensionless scan speed
l^*	Dimensionless layer thickness
h^*	Dimensionless hatch spacing
p	Laser power
v	Scanning speed

l	Layer thickness
h	Hatch spacing
A'	Surface absorptivity
r_b	Beam radius
ρ	Density
P_s	Saturated vapour pressure
T_0	Powder bed temperature

1. Introduction

Additive manufacturing (AM) of engineering alloy components offers many advantages from the fabrication point of view, as compared to the conventional manufacturing (CM) processes, which involve casting that is often followed by thermo-mechanical processing steps such as forging, rolling, and extrusion. As a result, there is a considerable current interest metal AM, both from scientific and technological perspectives. However, not all the well-established engineering alloys are amenable to AM. Developing new alloy compositions that can exploit the intrinsic metallurgical processes associated with AM, especially with techniques such as laser powder bed fusion (LPBF), e-beam powder bed fusion (EPBF), and laser directed energy deposition (LDED), is a major challenge. For this, a detailed understanding of the ultra-fast solidification process associated with the aforementioned AM techniques is the key, not only for improving the printability of the alloy under consideration, but also for imparting superior mechanical, tribological and thermophysical properties to the built part, and, in the process, advance AM to the forefront of industrial and large-scale manufacturing [1,2]. A variety of AM techniques have progressed enough to have suitability in producing functional parts that often outperform their CM counterparts in terms of perfoamnce and are also economical [3–7]. Regardless of their distinctive features, AM techniques follow a generic procedure for part fabrication. Powder or wire feedstock [3–8] is laid out and fused line-wise using an energy source such as a high-power laser or an electron beam (or a binder – in the case of binder jet printing (BJP) [9–14]) for repeated deposition in a layer-wise fashion that results in a part that often requires minimal post-processing.

AM techniques offer a substantial advantage in terms of fabricating a wide range of engineering components with complex geometries [15]. However, producing such parts that are free from any defects (pores and cracks) and have microstructural uniformity across them, or, better yet, a controlled heterogeneity, is harder to accomplish. It requires an understanding of the microstructural evolution not only within one ‘track,’ but through overlapping tracks that result in a ‘layer’ and overlapping layers that result in a 3D part. This implies considering the most fundamental element of the AM process: a rapidly solidifying melt pool and deciphering the microstructural evolution mechanisms involved within. The microstructures of components manufactured using the powder-based binder jet printing (BJP) technique are akin to well-annealed alloys, due to the fact that they undergo high-temperature sintering. In the wire-based DED technique, the feedstock microstructure is retained due to the surface-level melting

[10,13,14,16–21]. Therefore, the microstructural evolution mechanisms in these two processes occur as per the well-understood mechanisms, and, hence, will not be covered in this review. On the other hand, EPBF, LPBF, and LDED involve complete remelting of the original feedstock powders before solidification. Hence, it is crucial to understand the key fundamental building block of the parts fabricated using them: a melt pool and its rapid solidification. Over the years, researchers in AM have allocated substantial efforts in discerning the rapid solidification associated with a melt pool in sub-millimetre scales for a myriad of processing conditions for the aforementioned techniques with the help of numerical modelling [22] and extensive experimental observations such as in-situ X-ray imaging [23–26]. This review exclusively focuses on them.

The three techniques of EPBF, LPBF, and LDED, although follow the central theme of line-wise and layer-wise material deposition, have substantially different inherent thermal histories that govern the fundamental unit of a melt pool, and thus the microstructural evolution within, as illustrated using the schematic shown in Figure 1. For instance, the shallow and wide melt pools that form due to high build temperatures, high vacuum build environment, and high thermal gradients in an EPBF process often assist in the epitaxial grain growth through multiple layers and strengthening of the <001> crystallographic texture in the alloys with the face-centred cubic (FCC) crystal structures [27–32]. Although the melt pool profiles in the LPBF and LDED processes exhibit some similarity, in terms of the convection mode of solidification (caused by the convective heat transfer that occurs through the flowing inert gases), their length scales significantly differ [8]. While the sizes of the melt pools in LPBF range from several tens to hundreds of micrometres, those in LDED are often in the millimetre scale. Moreover, the latter, due to its dependence on the powder flow rate, tends to offer a more flexible deposited bead-to-melt depth ratio, in contrast to the prefixed layer heights in LPBF. Consequently, the <111> oriented grains that nucleate in the central regions of a melt pool in LDED can epitaxially grow to (and through) the proceeding layers, in contrast to the <011> crystallographic texture that prevails in LPBF. Because of the intricacies involving the effect of melt pool geometries, solidification parameters, and track- and layer-overlap ratios on the resultant grain growth, neither of these three crystallographic directions or a combination of them is exclusive to either of the three powder fusion-based AM (PF-AM) processes. Researchers have extensively reported a variety of crystallographic textures and grain morphologies in EPBF [33–43], LPBF [44–49], and LDED [35,50–55] processes. However, as we shall point out in later sections, there is still a substantial research gap for the three

techniques to produce a desired microstructure that is independent of geometry and alloy systems. Keeping this in view, we review in this article the literature on these three techniques with a central theme – understanding the rapid solidification phenomena and its impact on AM microstructures such as columnar-to-equiaxed transition (CET), solidification-cracking, porosity, segregation-induced phase transformations and so on.

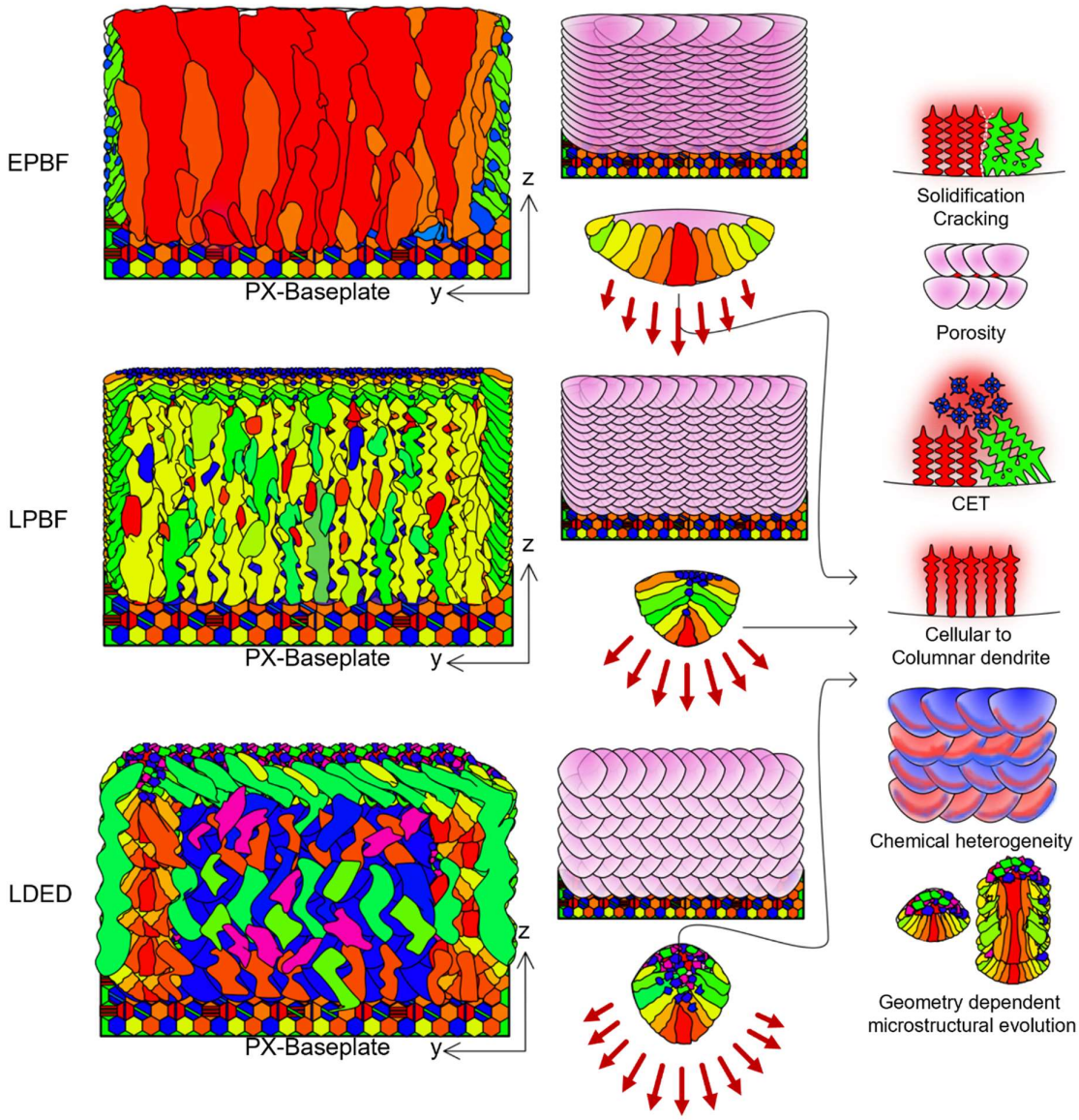

Figure 1. Schematic diagrams showing the typical microstructures obtained in powder fusion AM processes of EPBF, LPBF, and LDED. The hierarchical schematic shows the unique melt pool shapes which translate through their equally distinct solidification parameters to the microstructural features such as solidification cracking, lack of fusion porosity, columnar-to-

equiaxed transition (CET), segregation-induced columnar dendritic structures, chemical heterogeneity-induced phase transformations, geometry-dependent microstructural evolution.

Since microstructural design and control are critical for consistent and reliable mechanical performance, understanding the solidification phenomenon, along with the microstructural features that result from it, in the three AM techniques, namely LPBF, EPBF, and LDED, is crucial in advancing the state-of-the-art. Through this review, we summarize the current understanding, list the outstanding challenges and point to future directions of research. This review is structured in the following manner. In the following section (section 2), the fundamentals of solidification that occur under local interfacial equilibrium as well as the non-equilibrium conditions are summarized first. The deviation from the equilibrium solidification conditions in AM and its impact on the microstructural evolution is discussed next. Theoretical and numerical modelling efforts in nano-, micro-, and macro-scale specific to AM are detailed in section 3. Section 4 summarizes several challenges that are specific to the solidification processes in AM. Section 5 provides opportunities, which the unique solidification phenomena inherent to AM provide, for producing novel micro- and meso-structures that can enhancing the mechanical performance of the 3D printed parts. This review concludes with an outlook on the future directions that the solidification research in AM can (and should) take.

2. Summary of relevant solidification theories

Understanding the fundamentals of metal solidification has been key for making better castings, one of the pillars of manufacturing for centuries. Over the years, they have been revised for rapid conditions and reapplied to techniques such as welding and, in more recent years, AM. However, as the melt pools get smaller in AM, their cooling rates get faster, which leads to ultra-fast solidification conditions. For deciphering the microstructures (with hierarchical structures, phases, and defects) that result from such conditions, it is imperative to familiarize oneself with the kinetic and thermodynamic principles of rapid solidification, such that the impact of this phenomenon can be understood on the microstructural evolution during the AM of complex alloy systems. While doing so, we shall limit the discussion in the following to alloy systems and not pure metals, since AM is mostly used for fabricating alloy components.

2.1. Nucleation and growth

The energy supplied to an alloy system which leads to its transformation from solid to liquid phase needs to be extracted to form the final part or a component. Mathematically, the rise in enthalpy of an alloy as it melts is expressed in terms of the specific heat capacity and the latent heat of fusion. Hence, the heat flux – q, out of the liquid metal to cool it down and drive solidification can be determined by using the relation [56]:

$$q \cdot \left(\frac{A}{v'}\right) = c\left(\frac{dT}{dt}\right) - \Delta h_f \left(\frac{df_s}{dt}\right). \quad (1)$$

Though originally A and v' were specified as the surface area and volume of a cast, respectively; they can also be interpreted as the surface area for the heat transfer and volume of the melt, c is the specific heat capacity per unit volume, T is the temperature, Δh_f is the latent heat of fusion per unit volume, and f_s is the fraction of solid formed in the molten pool at any given time, t. It should be highlighted that this equation is derived from the heat balance for isothermal solidification conditions (low cooling rate) and a constant specific capacity across the solid/liquid interface. For an alloy composition Eq. (1) can be modified to calculate the cooling rate, $\frac{dT}{dt}$ or $\dot{T}$ as:

$$\dot{T} = q \cdot \frac{\left(\frac{A}{v'c}\right)}{1 - \left(\frac{\Delta h_f}{c}\right)\left(\frac{df_s}{dT}\right)}. \quad (2)$$

A key understanding to be gained from the above equation is that with a decrease in temperature, the fraction of solid increases and $\frac{df_s}{dT}$ is always negative. Hence, the solidification process leads to a reduction in the cooling rate.

The critical radius, r_c, of the nuclei, above which they are energetically stable during solidification, is given by the equation:

$$r_c = \frac{2\sigma}{\Delta g}, \quad (3)$$

where σ is the surface energy per unit area of the solid/liquid interface and Δg is the magnitude of the Gibbs free energy change from liquid to solid per unit volume [56]. For a process to be spontaneous, its Δg has to be negative which is also zero at equilibrium conditions. Therefore at liquidus temperature, r_c for a potent nucleation event is infinite. Hence, nucleation can only occur spontaneously at a temperature below the liquidus and this process varies with the alloying composition and is termed nucleation undercooling. The energy barrier for

homogeneous nucleation, which occurs in the absence of impurities or solid surfaces, is the total free energy change at the critical radius and is given as [56]:

$$\Delta G_{homogeneous} = \frac{16\pi\sigma^3}{3\Delta g^2}. \quad (4)$$

In cases where the melt is in contact with a wall or certain impurities are present in the melt, heterogeneous nucleation occurs. The energy barrier necessary for the occurrence of it is written as [56]:

$$\Delta G_{heterogeneous} = \frac{16\pi\sigma^3}{3\Delta g^2} \cdot \frac{[2 + cos\,\psi][1 - cos\,\psi]^2}{4}. \quad (5)$$

Here, φ is the contact angle or the solid-solid wetting angle between the solid nucleus and the existing solid. It should be noted that the variation in ψ from 0° to 180°, $\Delta G_{heterogeneous}$ varies from 0 to $\Delta G_{homogeneous}$. Therefore, in metallic melts such as those obtained during AM, heterogeneous nucleation will always be preferred over homogeneous nucleation leading to epitaxial grain growth. However, in regions farther away from the predeposited metal, homogeneous nucleation can be initiated by solidification undercooling.

Undercooling which is the key to grain nucleation and the driving force during the solidification of metals and alloys can be subdivided into constitutional, thermal, curvature, and kinetic undercooling [57,58]. *Constitutional undercooling* occurs due to the partitioning of alloying elements upon solidification, where the solute enriches the solid/liquid interface. *Thermal undercooling* is related to the release of latent heat during the solid-liquid phase transformation. *Curvature undercooling* can be attributed to the Gibbs-Thomson effect, which predicts that the melting point of a crystal is inversely proportional to the radius of curvature of its surface. *Kinetic undercooling* depends on a number of factors, including the crystallographic orientation of the solidifying material and the atoms' kinetic attachment mechanism, which affects nucleation and crystal growth. For conventional casting of alloys with slow solidification rates (*V < 100 mm/s)*, constitutional supercooling has been considered to be the dominant factor in determining the size and morphology of the grains in the solidified alloy [59]. However, as the deposition speeds get faster in AM [60], the melt pools get smaller and solidify quicker resulting in finer dendritic sub-grain structures, the roles of thermal [61], curvature, and kinetic undercooling will become comparable to or supersede the constitutional undercooling, and hence, should be explored when investigating solidification in AM. *Constitutional undercooling* can be estimated using the equilibrium phase diagram as [62]:

$$\Delta T_c = m(C_0 - C_l), \quad (6)$$

where m is the liquidus slope, C_0 is the nominal composition, and C_l is the composition of the liquid ahead of the solidifying interface.

Curvature undercooling can be written for a solid with radii r_1 and r_2 as [56,62]:

$$\Delta T_r = \Gamma\left(\frac{1}{r_1} + \frac{1}{r_2}\right), \quad (7)$$

where Γ is the Gibbs-Thomson coefficient given by [63]:

$$\Gamma = \frac{\sigma \cdot T_m}{\Delta H}. \quad (8)$$

For pure metals, such as chromium and nickel, Γ has been estimated to be 3.19 x10^{-07} and 1.91×10^{-07} Km, respectively [63]. Kurz and Fisher [64] developed the following correlation between growth rate (V), thermal gradient at the interface (G), and radius of a dendrite tip (R) on the basis of the Mullins and Sekerka's stability criterion [65]:

$$V = \frac{2D(G \cdot R^2 + 4\pi^2 \cdot \Gamma)}{R^3 \cdot p \cdot G - 2R^2 \cdot p \cdot C_0 \cdot m + 4\pi^2 \cdot \Gamma \cdot R \cdot p}. \quad (9)$$

Here, D is the diffusion coefficient of solute in the liquid and $p = (1 - k)$ where k is the partition coefficient. For high V values, the Eq. (9) can be revised to give:

$$R = 2\pi\left(\frac{D\Gamma}{Vk\Delta T_0}\right)^{1/2}. \quad (10)$$

For the AM processes, diffusion rates are of the order of 10^{-9} m^2/s [66,67], Γ is in the order 10^{-08} Km [67], a typical partition coefficient is between 0 to 1, and V is on the order of ~ 0.05 – 0.4 m/s [67]. The dendrite tip radius, calculated using Eq. (10), is in the range of 10^{-8} – 10^{-9} m – smaller for faster solidification. Hence, ΔT_r is in order of 10 K, which can not be considered negligible.

Kinetic undercooling, ΔT_k*,* is also correlated to the interface velocity (or solidification rate) V through the following equation [68,69]:

$$V = V_0\left(1 - exp\left(-\frac{\Delta S \Delta T_k}{R'T}\right)\right). \quad (11)$$

Here, V_0 is in the order of the velocity of sound for pure metals, ΔS is the entropy change, and R' is the gas constant. For $V \ll V_0$, this equation can be simplified as:

$$V = \mu \Delta T_k, \quad (12)$$

where, μ is the kinetic mobility that referes to the ease with which atoms can move within the liquid phase. With an increasing kinetic mobility, at a fixed interface velocity, undercooling decreases.

Post nucleation, the conditions for growth are governed by the thermodynamic factors imposed by the solidification kinetics at the interface. With an increasing V or the growth rate, the thermodynamic conditions that govern the solidification transit from a complete diffusional equilibrium state to a state with local interfacial equilibrium, followed by the metastable local interfacial equilibrium, and finally, to local interfacial non-equilibrium. Full diffusional equilibrium exists only for very slowly cooled melts of pure metals – a condition that is highly unlikely in the AM processes. On the other hand, the local interfacial non-equilibrium prevails when the growth rate of the interface supersedes the local solutal diffusion over an interatomic distance. In the following sub-sections, we shall briefly discuss the conditions that prevail primarily in the AM processes.

2.2. Local interfacial equilibrium

Local interfacial equilibrium solidification condition implies that the solute concentrations in the regions at or near the advancing interface can be predicted with the aid of the equilibrium phase diagram [70], which provides information on the equilibrium partition coefficient, k, and liquidus slope, m. Based on the extent of diffusion in the liquid and assuming that no diffusion occurs in the solid, three primary subcategories of this solidification mode can be identified, as illustrated in Figure 2. The extent of solute diffusion in the liquid is determined by comparing $D_L t$ to L^2, where D_L is the solutal diffusivity in liquid, t is the time available for diffusion, and L is the length of the melt column before the initiation of solidification. Figure 2 (a) shows the concentration profiles in cases where $D_L t \gg L^2$, i.e., no diffusion in solid and complete diffusion in liquid. This is the most frequently employed assumption for modelling the solidification during AM of alloys. Within this assumption also one finds the Scheil equation (also known as the Scheil-Gulliver model) [70]:

$$C_s \leq kC_0(1 - f_s)^{k-1} \tag{13}$$

being employed for estimating the solute segregation. Here, C_s and C_0 are solute concentrations in the solid and nominal alloy, respectively, and f_s is the fraction of the solid.

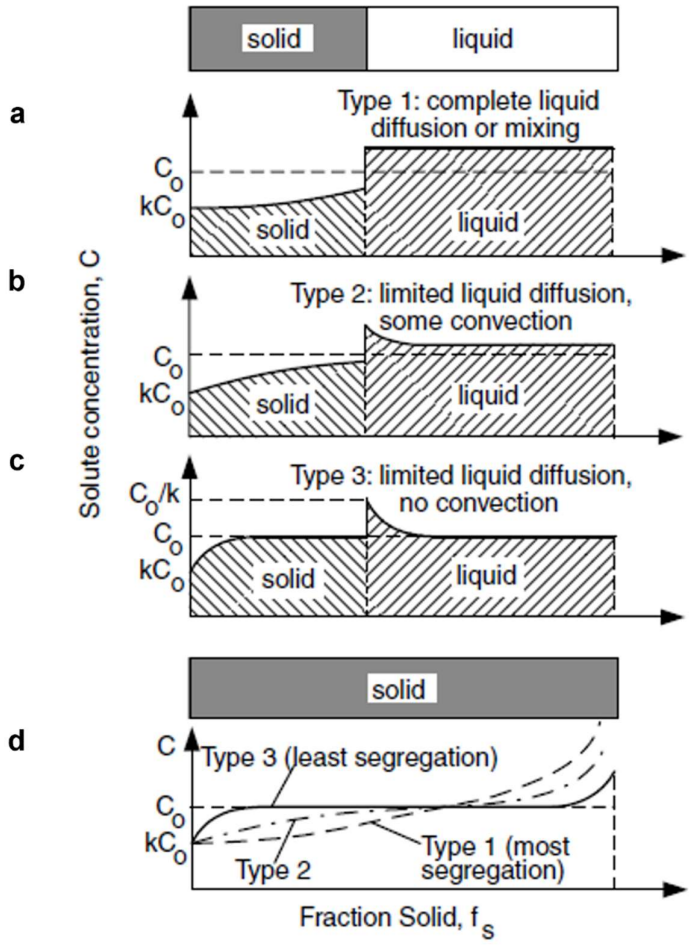

Figure 2. Modes of solidification within the umbrella of local interfacial equilibrium and no solid diffusion [70]. (a) – (c) Diffusion in a liquid varies with increasing solidification rate or decreasing solidification time. (d) Segregation profiles corresponding to (a) – (c).

The Scheil solidification condition has been employed consistently across the LPBF [71–76], EPBF [31,77,78], and LDED [79–81] techniques. However, it should be employed judiciously, making sure that the solidification velocity obtained at the melt pool interface is within the limit of absolute stability given by Eq. (17) which shall be detailed later. While the Scheil solidification model is widely used to simulate non-equilibrium solidification in AM, it is important to note that it assumes local equilibrium at the solid-liquid interface. Therefore, it would technically be incorrect to refer to solidification conditions simulated using this model as non-equilibrium ones.

The breakdown of the planar interface during the solidification of alloys was correlated to the constitutional undercooling by Rutter and Chalmers [82] and Tiller et al. [83]. According to them, the planar interface of a solidification front will break if the following condition is met:

$$\frac{G}{V} \leq \frac{\Delta T}{D_L}. \quad (14)$$

The microstructural evolution during molten metal solidification depends, primarily, on the following three solidification parameters – thermal gradient (G), solidification rate (V), and cooling rate (CR) [84,85]. This equation can be further simplified, with an assumption of local interfacial equilibrium, as following:

$$\frac{G}{V} \leq m\frac{C_0}{D_L}\left(\frac{k-1}{k}\right). \quad (15)$$

The parameters on the right-hand side, m (slope of the liquidus), C_0 (content of the solute in the nominal composition), D_L (diffusion coefficient), and k (equilibrium partitioning coefficient), are related to the intrinsic properties of the alloy composition and are generally determined through the relevant phase diagram. The G/V ratio plays a significant role in affecting the level of constitutional undercooling and, consequently, the solidified microstructure, as illustrated in **Figure 3** (a) [70]. As seen from it, the equilibrium curve in the temperature-distance plots remains invariant in all the scenarios. However, varying slopes of actual temperature-distance plots result in distinct intersect areas (shadowed areas) and thus, different levels of constitutional undercooling. With increasing constitutional undercooling, the solidified microstructures vary from planar to cellular, columnar dendritic, and eventually equiaxed dendritic.

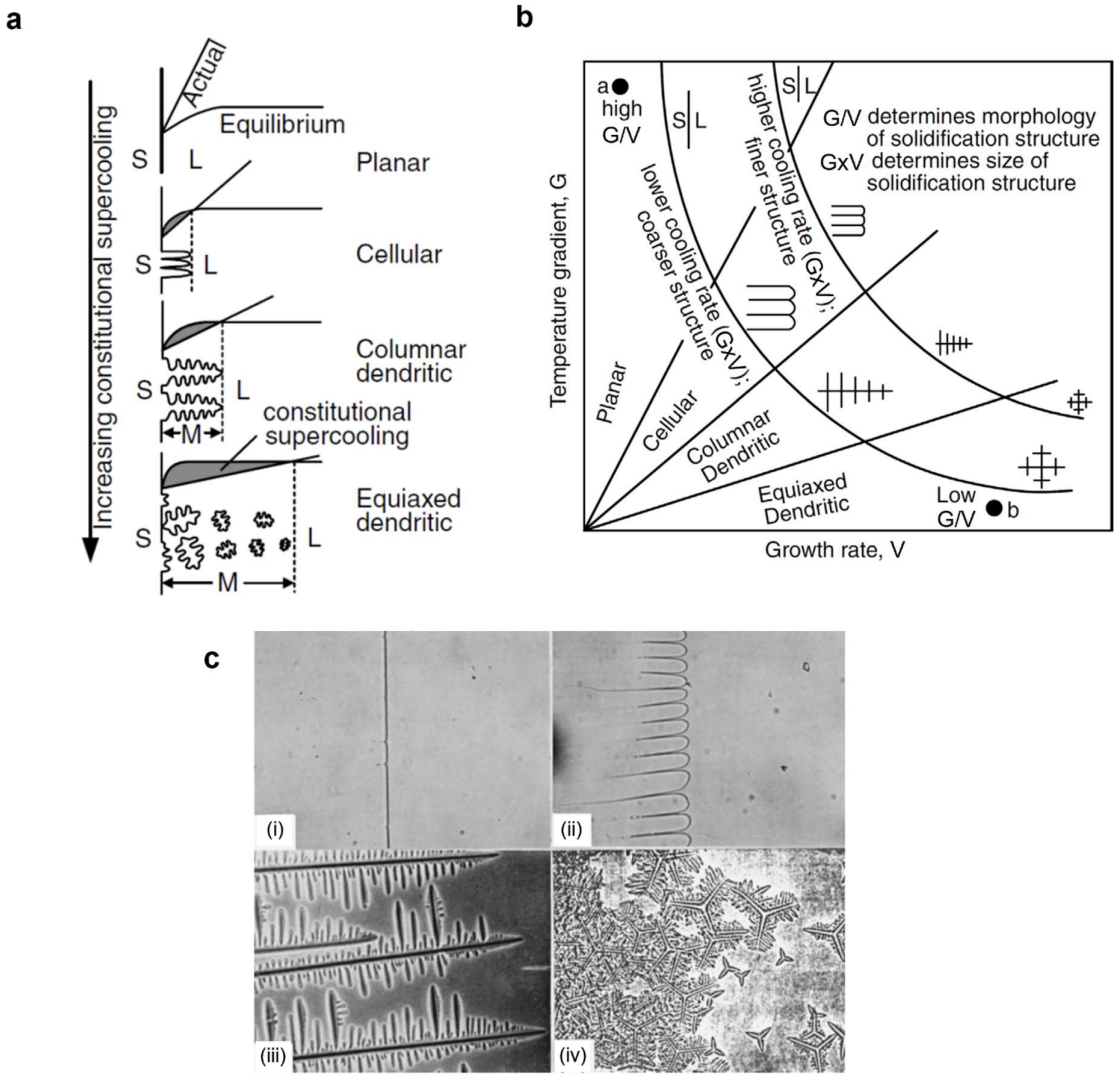

Figure 3. Solidification modes in conventional solidification processes (Adapted from [70]). (a) Varying level of constitutional undercooling and the corresponding effect of the solidification structure. S and L indicate solid and liquid, respectively. (b) Solidification map showing the effect of G/V and $G \cdot V$ on the solidification structures. (c) In clockwise direction (i) Planar, (ii) Cellular, (iii) Columnar dendritic, and (iv) Equiaxed dendritic modes of solidification.

A solidification map can be constructed using the G and V parameters, in their combined forms of $G \cdot V$ and G/V, where the G/V ratio determines the morphologies of the solidification structure, and the product $G \cdot V$ governs the scale. **Figure 3**(b) and (c) illustrate the effect of G/V and $G \cdot V$ on the solidification microstructure. The solidified microstructure successively changes from being planar, to cellular, to columnar dendritic, and finally to equiaxed dendritic

with a decreasing G/V, while their dimension decreases with increasing cooling rate $G \cdot V$. A more specific example is given in **Figure 4** for the laser welded AA6061 [86], where the effects of G/V and $G \cdot V$ are illustrated.

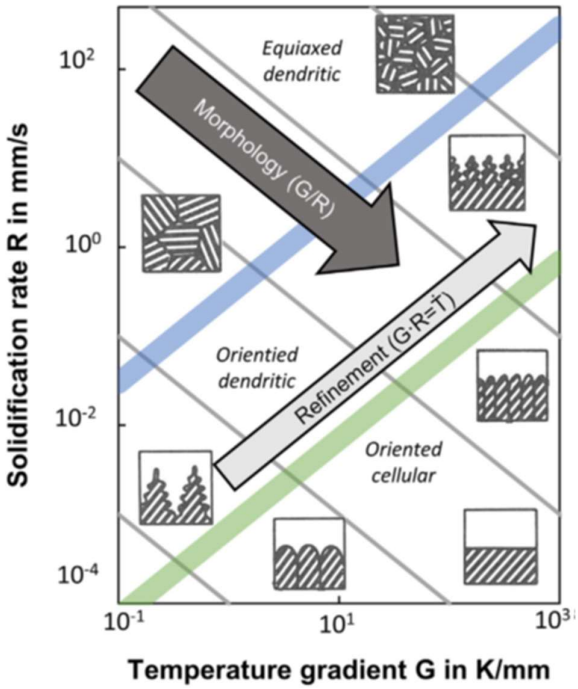

Figure 4. Solidification map of AA6061 Al alloy [86].

However, as it is highly challenging to quantify and manipulate the values of G and V in the AM processes of interest for the current review, such an approach is not as applicable. Therefore, recent studies have been focusing on the right-hand side of Eq. (15) which is associated with intrinsic material properties. Moreover, it has been proposed that the growth restriction factor, Q, is effective to describe the level of constitutional undercooling in AM:

$$Q = mC_0(k-1). \quad (16)$$

For example, in a recent study on LDED Ti-based alloys (**Figure 5**), Zhang et al. [87] revealed that, compared to Ti-6Al-4V and Ti-Si, Ti-8.5Cu can generate sufficient constitutional undercooling to induce the formation of equiaxed grains. This effect is also observed in EPBF Ti-7Cu (50 K of Q) [88]. Recently, Wei et al. [89] varied the Al composition along the build direction in LPBF Fe-Al_x binary alloy and achieved a gradation in the crystallographic texture (**Figure 5** (c) and (d)). They found that the fraction of equiaxed grains or the tendency of CET was proportional to the Al content which could be explained by a gradual increase in growth restriction factor from ~0 ºC (Al at. % of 6.2 ± 0.5) to ~28.7 ºC (Al at. % of 39.1±2.1).

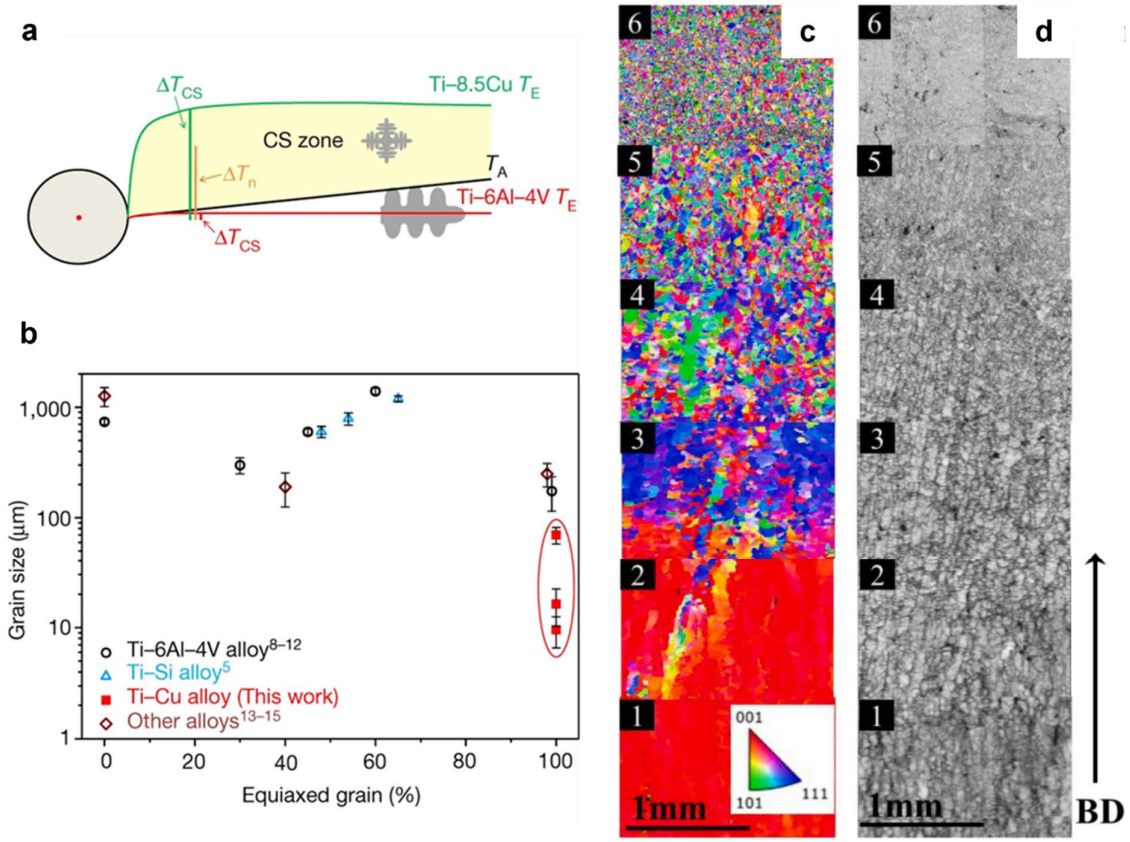

Figure 5. (a) Schematic of the grain growth mechanism of Ti–8.5Cu and Ti–6Al–4V alloys. T_A is the profile of the temperature of the melt and T_E is the profile of the equilibrium liquidus temperature. (b) Summary of the area percentage of equiaxed grains versus grain size for the as-printed titanium alloys [87]. CET with increasing Al content along the build direction in Fe-Al alloy printed using LPBF shown through (c) electron backscatter diffraction (EBSD) and (d) backscattered electron (BSE) maps [89].

It is worth noting here that the heat sources used in AM are similar to those used in most traditional welding processes, including arcs, lasers, and electron beams. Moreover, individual line scans of the energy sources during AM are akin to those during welding processes. As a result, they result in similar microstructures, at least at the single-track level. Therefore, process-structure-property relationships established for the welding of various alloys can provide useful knowledge for understanding the microstructural development during AM.

2.3. Metastable local interfacial equilibrium

With varying growth kinetics in AM (such as increasing growth rate), the nucleation of thermodynamically stable phases from the melt may become difficult and prevalence of the metastable phases in the AM alloys is often noted. Several examples of the metastable phase formation during the rapid solidification include the α' martensitic phase microstructure observed in EPBF Ti-6Al-4V [90], δ-ferrite phase in the otherwise purely austenite LPBF 316L stainless steel (referred to as 316L from here on) [91], and irregular Laves-based phases in EPBF Re-free Ni-based superalloy [27]. A detailed review of metastable phase formation during AM of significant alloy compositions can be found in **Section 4**.

2.3. Non-equilibrium solidification

As the solidification process becomes more rapid, a departure from chemical equilibrium at the local interface occurs. Under such a condition, the aforementioned equations which have been derived with the condition of local interfacial equilibrium at the solid/liquid interface cease to be valid [85]. Hence, a phase diagram cannot predict the liquid and solid compositions. For an alloy, this situation occurs when the solidification growth rate exceeds the rate of diffusion over an interatomic distance. The equation for the velocity at the limit of absolute stability, beyond which non-equilibrium solidification persists can be written as [85,92]:

$$V_{ab} = \frac{\Delta T_0 D_L}{k\Gamma}, \tag{17}$$

where, Γ is the Gibbs-Thomson coefficient, ΔT_0 is the equilibrium freezing range for an alloy composition and D_L is the coefficient for solute diffusion in the liquid. Sobolev [93] developed the analytical frameworks for predicting the solute concentration in solidification conditions involving departure from local interfacial equilibrium conditions. In their work, the generalized partition coefficient, K^*, is given as:

$$K^*(V) = \begin{cases} \dfrac{k\left(1 - \dfrac{V^2}{V_{Db}^2}\right) + \dfrac{V}{V_{Di}}}{\left(1 - \dfrac{V^2}{V_{Db}^2}\right) + \dfrac{V}{V_{Di}}}; & V < V_{Db}, \\ 1; & V > V_{Db}. \end{cases} \tag{18}$$

Here, k is the equilibrium partition coefficient, V_{Di} is the average diffusion speed of solute in the interface region calculated as D_i/δ_i (D_i is the diffusion coefficient of solute within the interface thickness δ_i [56]), and V_{Db} is the diffusion speed of solute in the bulk liquid. This model not only works for local non-equilibrium conditions, when the partition coefficient is 1

and complete solute trapping occurs, but also in the solidification velocity regimes leading to the solute diffusion speed in the bulk.

Similarly, the velocity dependent diffusion coefficient is given by

$$D^*(V/V_{Db}) = \begin{cases} D\left(1 - \dfrac{V^2}{V_{Db}^2}\right); & V < V_{Db}, \\ 0; & V > V_{Db}. \end{cases} \quad (19)$$

Sobolev [93] also provided a limit of absolute stability with the allowance for the local interfacial non-equilibrium effect as:

$$V_a = V_{ab}\left(1 - \frac{V_{ab}^2}{4V_{Db}^2}\right), \quad (20)$$

where, V_{ab} is determined from Eq. (17). Together with the constitutional supercooling criterion given in Eq. (15) expressed as $V_{cs} = \frac{GD_L}{\Delta T}$, the absolute stability criterion given by Eq. (17) and Eq. (20) provides a solidification rate regime in which the cellular or cellular dendritic microstructure is stable. Beyond, V_a the dendritic microstructure transforms into cellular and back to a planar S/L interface [68,94].

Though there are established frameworks for predicting the solidification conditions during interfacial non-equilibrium solidification processes, solidification modeling in AM often has been constrained to the assumptions of local interfacial equilibrium conditions, despite the observed growth rates of the melt pool being in the scale of m/s and cellular structures with primary dendrite arm spacings (PDAS) ranging in the sub-micron to micron scale. Hence, there is a critical need for embracing the interfacial non-equilibrium solidification conditions to mimic the conditions that prevail in reality, and hence, for better understanding of the microstructural evolution that occurs during AM. Since analytical modelling of the solidification process(es) that occur during AM is difficult because of the complexity involved, computational modelling is resorted to. These efforts are summarized next.

3. Modelling of solidification

The modelling efforts associated with the solidification phenomena in AM processes cover a broad range of length scales and are classified, on the basis of the simulated length scales, into several categories. Macro-scale simulations confine themselves to a length scale ranging over several millimetres. They are primarily continuum based and are solved using finite element

analysis (FEA) with the finite element method (FEM), computational fluid dynamics (CFD) simulation that employs either finite volume method (FVM) or finite difference method (FDM), and, in a few instances, discrete particle methods (DPM). Their primary focus is to decipher the solidification parameters and investigate the formation of macro-scale phenomena that occur during AM, such as keyhole formation, lack-of-fusion porosity formation, and residual stress evolution. Micro-scale simulations are performed at the scale of a few to tens of microns with a focus on simulating the physics associated with the grain growth and microstructural evolution, with emphasis on the solute segregations that take place as a consequence of the cellular/dendritic solidification in the AM processes. A recent addition to the simulations in deciphering the far-from-equilibrium solidification conditions associated with the AM processes is the atomic-scale simulations, primarily consisting of molecular dynamics (MD) and density functional theory (DFT) simulations. The numerical modelling at this scale has the promise of allowing insights into the nucleation physics associated with the molten-metal solidification [95]. However, they suffer from the limitation of being more idealistic and detached from the macro-scale solidification conditions.

The confines of the length-scale-based classifications are quite diffuse as simulation methods most often used at a particular length scale at a time can be used with more resources to simulate physics at slightly higher length scales. As such, atomic scale models can be applied to nano- to sub-micron scales by increasing the number of atoms in the simulated material volume. Similarly, and quite often, the macro-scale models are developed to investigate the features in a scale just above that of the micro-scale, termed as meso-scale. In this section, we shall follow a bottom-up approach—akin to the AM process itself and identify the extent to which a variety of modelling techniques have been applied for understanding solidification from different standpoints—atomic scale to a system scale. In doing so, we steer clear of judging the merits or demerits of one technique over the other, but merely put forth the scale of phenomena that can be incorporated in performing the task at hand, i.e., understanding the complex solidification phenomena associated with a multi-layer, multi-scale melt pool solidification process. We also avoid detailing the mathematical equations particular of the application algorithm of any modelling technique and instead, focus on the solidification-related fundamentals which form the common ground for these wide range of numerical modelling techniques.

3.1. Molecular Dynamics (MD) simulations

As mentioned in **Section 2**, considerable commonality exists between several AM techniques and conventional fabrication techniques such as welding that involve rapid melting and solidification. As a result, the former derives significant benefit from the latter, in terms of well-established theoretical foundations of solidification. This is also true in the case of numerical modelling of the associated rapid solidification phenomena on the atomic scale. Given this, we first discuss the status of the MD simulations that are applied to general rapid solidification techniques, before moving to its applications to AM.

The primary objective of early studies that used MD on rapid solidification is the determination of the final microstructures obtained with distinct cooling rates [96–101] in pure Al [96,102], Ti_3Al [97,103], Ag [98], Cu-Ag [99], Pd-Ni [100,104], Au [101], Cu [105,106], Cu_3Au [107], Ni [108], Cu-Ni [109] melts or for distinct pressures in Al [110], Cu-Ni [111], Cu [112–114] or for the number constituent elements in a Ni-Al-Cu-Co-Ti-V-Zn-Zr high entropy alloy (HEA) [115]. These works employed the pair distribution function (PDF) as an indicator of the amorphous, liquid, and crystal structure for the quenched or quenched + annealed set of atomic arrangements. Even the state-of-the-art MD simulations associated with AM or rapid solidification suffer with the following limitations (in terms of the solidification parameters). In general, the cooling rates applied in the simulations are around five orders of magnitude higher than those reported for the AM processes—determined either through measurements from external devices or by the estimations from the observed microstructural features such as primary dendrite arm spacing (PDAS) [44]. Same is true for the thermal gradients applied in the MD simulations. Though these limitations come with the scale of the simulations, as we shall detail later, a few observations made using them aid in improving the understanding of the microstructural development during the rapid solidification conditions that generally prevail during AM.

MD simulations for nano-scale LPBF by Chen et al. [116] dealt with the in-process melting and solidification of the FeCrNi medium entropy alloy (MEA) powders arranged on a pure Fe substrate. Effects of laser power density and scanning speed were explored on the surface morphology of the melt track, segregation of the alloying elements, and the formation of stacking faults. Their simulations show that a higher energy density results in an increase in the stacking fault densities, which are primarily located at the melt pool boundaries, in comparison

to a few in the melt pool centre. Among the three constituent alloying elements, the segregation of Cr to form interconnected clusters is most severe and is shown to proportionally vary with the laser energy density.

Singh et al. [117] employed MD simulations to provide the effect of inclusions on solidified structure of Cu in an idealized multi-layer nano-scale AM process akin to LPBF, besides layer thickness, cooling time, and target cooling temperature. While the SiC inclusions are shown to slow down the solidification front, which results in a higher content of defect structures, SiS_2 does not seem to influence the solidification front and reduces the defect content in the solidified Al (**Figure 6**).

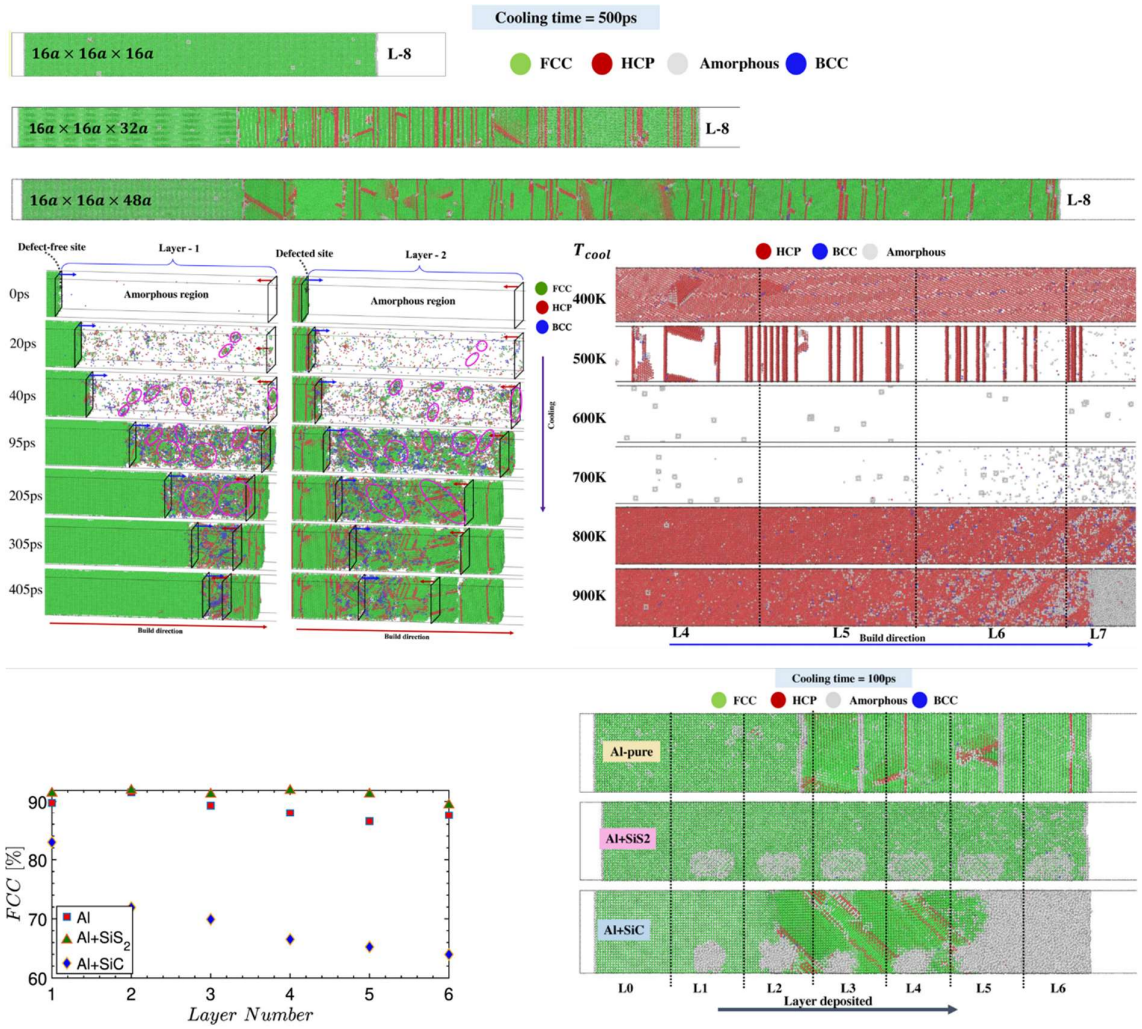

(a) *FCC %* (b) CNA snapshots

Figure 6. Understanding defect structures in nanoscale metal additive manufacturing via molecular dynamics [117].

Kurian et al. [118] employed MD to simulate micro-LPBF of Al nanopowders, with the sequential simulation of solidifying melt pools, and report epitaxial grain growth from the un-melted powders, competition among different grain orientations, homogeneous nucleation in the top central regions of the melt pool, formation of twins, stacking faults, and vacancies in the melt pool (**Figure 7**(a)). Jamil et al. [119] present an example of the strengths of MD and its application to metal AM processes on the LPBF of nano-scale powders of the FeNiCoCrCu HEA (**Figure 7**(b)). They simulated the fusion of HEA powders under the influence of a micro-Watt laser, with the objective of investigating the effect of simulated laser scan speed and number of laser passes on the microstructure formation. They report that for a single-pass deposition, the laser scan speed of 0.2 Å/ps (angstrom/picoseconds), among the four explored values of 0.1 – 0.4 Å/ps in the intervals of 0.1 Å/ps, minimized the dislocations and hexagonal close-packed (HCP) stacking faults in the solidified microstructure.

Recently, Bahramyan et al. [120] reported the formation of twins and asignificant density of dislocations, through the MD simulation of rapid solidification in a Fe-Ni-Cr system that mimics the LPBF of austenitic stainless steels (316L grade), as shown in **Figure 8**(a). The CR and G values applied by them are in the order of 10^{11} K/s and 10^{9} K/m (300 K temperature difference for a distance of 58 nm), respectively. Recent application of MD to the AM process by Bizot et al. [121] investigates the solidification of Ni melt under conditions resembling those observed in a melt pool obtained in typical AM processes. The implemented solidification conditions to the molten pool have been categorized into two types: fixed thermal gradient without and with additional cooling. For fixed thermal gradient without assisted cooling, a mostly planar solidification front is obtained with columnar grains whereas CET is observed for conditions of high thermal gradient and fast cooling rates, as shown in **Figure 8**(b). The tendency of CET reduces with the combined reduction of CR and G. The authors also provided a scaling factor for heat conduction, which is taken as the square root of the ratio of experimental and numerical diffusivities and equal to 4.2. This can enable analysis of thermal effects at the atomic scale in terms relatable to the macro-scale.

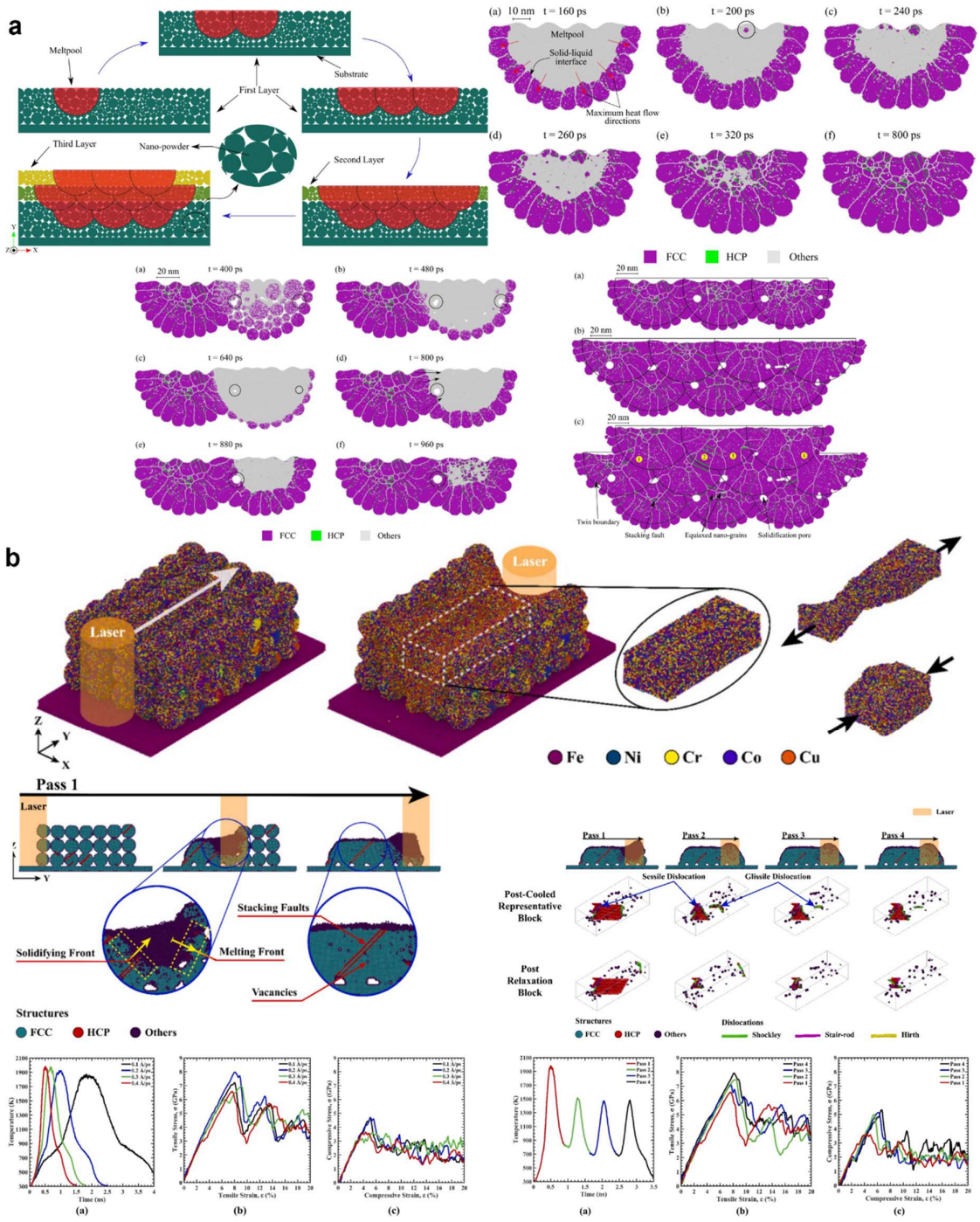

Figure 7. (a) Selective laser melting of aluminum nano-powder particles, a molecular dynamics study [118] (b) Molecular dynamics perspective of the effects of laser thermal configurations on the dislocation and mechanical characteristics of FeNiCrCoCu HEA through the powder bed fusion process [119].

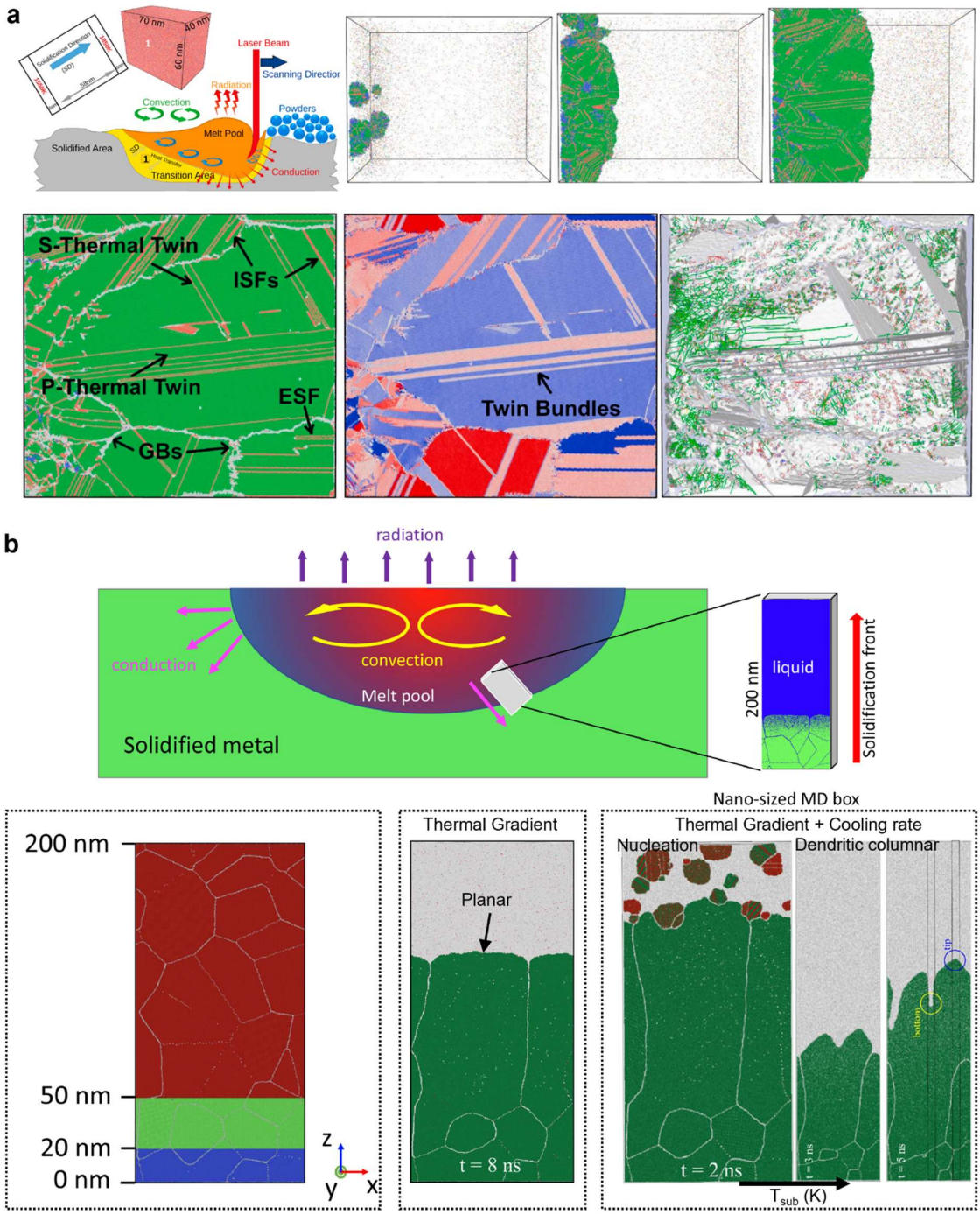

Figure 8. (a) Nano-scale simulation of directional solidification in TWIP stainless steels: A focus on plastic deformation mechanisms [120] (b) MD simulations of nanoscale solidification in the context of Ni additive manufacturing [121].

As the above examples illustrate, there are two main advantages of the MD simulations applied to AM. They allow for the studying of the (1) dislocation evolution during solidification of melt

tracks and (2) atomic-level insights into the formation of crystal nuclei, twins, and stacking faults.

In its current state, MD simulations of the melting/solidification of nano-scale powders can be successfully applied to micro-LPBF (μ-LPBF) – a technique which is still far from mainstream applications. Treating a smaller region out of the physical melt pool with the MD simulations, however, should provide more realistic domains, simulation of multiple layers a few nanometres thick needs accurate scaling of physical parameters to be correlated with the actual AM process.

On the micrometre scale, three methods have been applied widely to the solidification process in AM. Two of these – cellular automata (CA) and kinetic Monte Carlo (KMC), are probabilistic in their very nature, whereas the third, phase-field modelling (PFM), is derived from irreversible thermodynamics. These are discussed next.

3.2. Cellular Automata based simulations

The new 3D CA algorithm for the dendritic grain growth, developed by Gandin and Rappaz [122], has been applied to microstructural evolution in a broad range of alloy systems subjected to conventional casting. It, being simple and computationally efficient in comparison to the alternatives such as KMC and PF, has found extensive application in nearly all of the fields of PF-AM, be it LDED [51,92,123–141], LPBF [139,142–161], or EPBF [139,162–169] or for a range of rapid solidification parameters that can be associated with the AM processes in general [61,170–176]. Some novel works have also successfully coupled CA to PF models and applied them to laser-based rapid solidification processes [177,178]. Primarily, CA is coupled to a macro-scale model developed either through CFD, FEA, lattice-Boltzmann (LB) model, or DPM and uses the thermal history as an input to predict CET, macro-segregation, and epitaxial grain growth through multiple layers.

Figure 9 presents a summary of the state-of-the-art application of CA to the solidification and microstructural evolution phenomena that occur during LDED. Rolchigo and LeSar [92] showcased the use of a standalone CA model at grain scale for investigating the impact of processing parameters, solute concentrations, and alloying elements on the tendency of CET during the microstructural evolution in multiple binary β-Ti alloy systems. For this, they employed the simplified version of the Kurz-Giovanola-Trivedi (KGT) model [85] given by

Eq. (26). The probability of the heterogeneous nucleation occurring over each time step was similar to that given in Eq. (29). They chart a pixelated matrix of the microstructural evolution response to solidification velocity and thermal gradient, as shown in **Figure 9**(a). The addition of solute to the alloy shows an increasing tendency for CET due to the change in the interfacial response function that relates the undercooling to the solidification velocity. Lian et al. [179] implemented a 3D multi-scale numerical model where heat transfer and fluid flow during laser beam motion (and consequently, the melt pool solidification) were simulated at the macro-scale using the finite volume method (FVM) and implemented the Lipton–Glicksman–Kurz (LGK) model for estimation of solidification velocity with undercooling (**Figure 9**(b)). They report that finer grain microstructure is obtained for faster laser scan speeds or decreasing laser power, which is a direct consequence of those parameters' effect on the cooling rate. They also found that the cooling rate, and resulting microstructure, are more sensitive to variations in the laser scanning speed as opposed to laser power.

Rolchigo and LeSar [141] applied solute transport and solidification equations to standalone 2D CA models for simulating the dendritic structure transformation during LDED of Ti-W, Ti-Cu, and Ti-Ni binary alloys. A special feature of this work is that it simulated non-equilibrium nature of solidification. As a result, they showcase the transitioning of the dendritic solidification front to a planar one with increasing solidification speed, as shown in **Figure 9**(c). They could also simulate the banded structure that forms as the solidification conditions approach those of the interfacial non-equilibrium. They employed velocity-dependent solute partition coefficient, given in Eq. (18) in **Section 2,** and liquidus slope for velocities beyond the absolute stability given by [93]:

$$m^*(V) = m \cdot \left(\frac{1 - K^* + K^* \, ln\left[\frac{K^*}{k}\right]}{1 - k} \right). \tag{21}$$

Aggarwal et al. [125] implemented a 2D CA model in conjunction with a 3D discrete element method (DEM) – CFD model to simulate the microstructural evolution in the spot melt during the LDED of IN625 (**Figure 9**(d)). They employed the KGT model with the thermal undercooling information obtained from the macro-scale simulations. They could predict the distinct grain growth behaviour in the melt pools obtained during single-track deposition with laser powers of 200 and 400 W. For the parameters employed, the simulated microstructures were devoid of equiaxed grains and consisted primarily of elongated grains directed towards

the melt pool centre lines. Li and Tan [140] implemented a multi-scale model combining a macro-scale thermal model and meso-scale CA model with nucleation physics and KGT model to simulate the grain growth through multiple layers during LDED of SS304 with reasonable accuracy, as illustrated by (**Figure 9**(e)). Their multi-layer simulations could replicate the zig-zag grain growth (ii) with build height as observed in the crystallographic orientation map (i). Recently, Meng et al. [131] implemented a multi-scale CA-FE model to simulate the microstructural variations with the LDED process parameters for IN718 with a binary alloy approximation of Ni-5 wt.% Nb. As seen in (**Figure 9**(f)), substantial similarities are observed in the simulated and experimental microstructures, both in terms of grain morphologies and sizes.

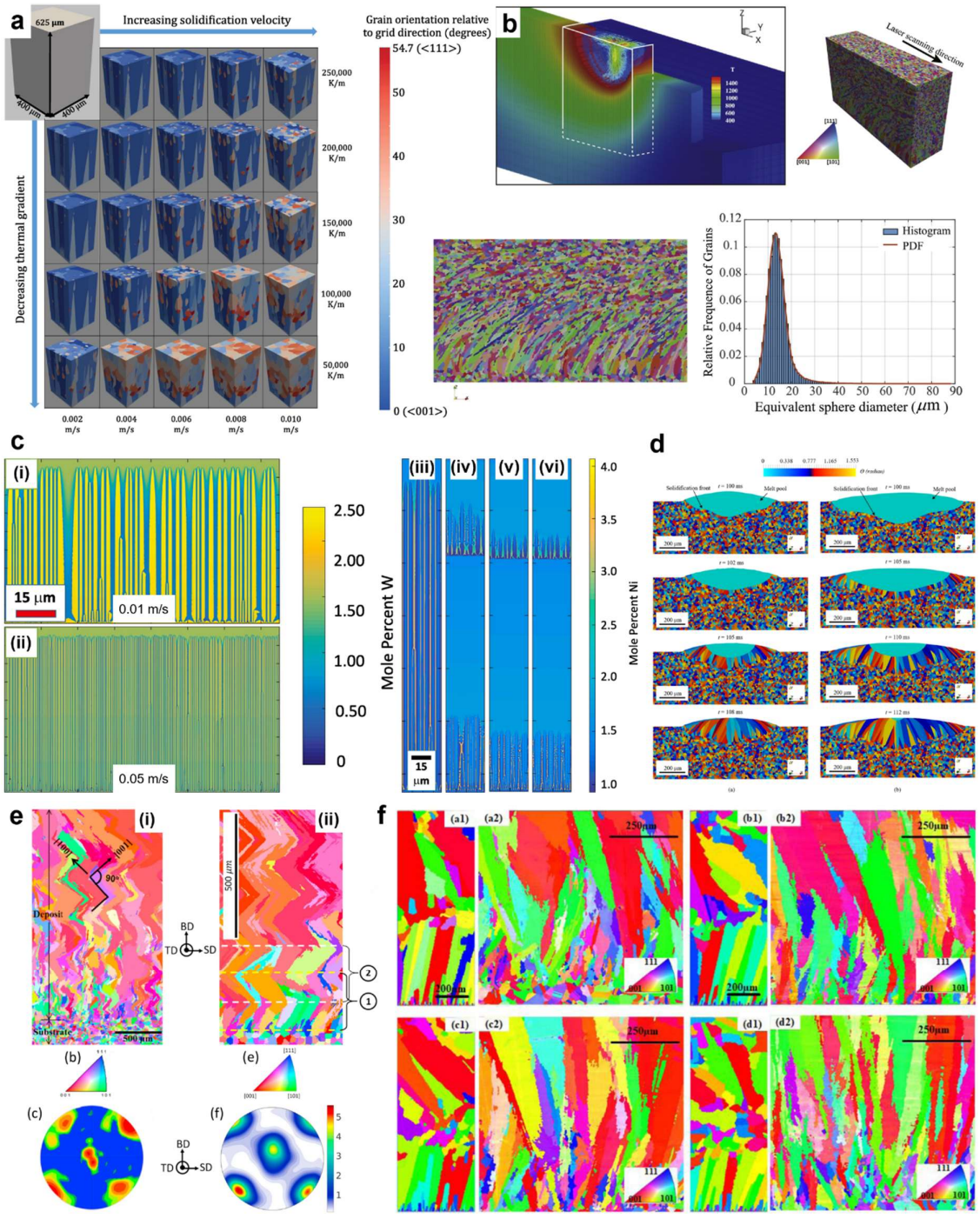

Figure 9. Application of cellular automata to LDED processing of a variety of materials. (a) Modelled microstructures obtained for LDED deposition conditions with varying solidification velocity and thermal gradient for Ti-5 wt.% Cu binary alloy system [92] (b) CA-FV coupling for prediction of multilayer microstructural evolution in LDED IN718 alloy [123]. (c) CA-based microstructure predictions for non-equilibrium solidification conditions obtained at high

growth rates—transition from dendritic to planar solidification front and the formation of banded structures obtained consequently in a layering process [141]. (d) CA prediction of grain growth using a coupled DEM-CFD-CA model [125]. (e) 3D CA simulation of microstructural evolution in SS304 (i) orientation map obtained from EBSD (ii) simulated orientation map using 3D CA [140]. (f) Multi-scale CA-FE model denoting the impact of laser power on the microstructural evolution in IN718 (with binary alloy approximation at the CA-scale [131].

Figure 10 summarizes the key results of some of the recent studies, in which CA was applied for simulating the grain growth during LPBF. Mohebbi and Ploshikhin [160] implemented a multi-layer, multi-scale CA-FD numerical model for the deposition of the AlSi10Mg alloy with an additional nucleation model for the fusion boundary, aside from the bulk nucleation mechanism implemented in the traditional CA model (**Figure 10**(a)). Consequently, a widely observed feature of fine-equiaxed grains at the fusion boundary observed in LPBF AlSi10Mg was successfully simulated. Zhang and Zhang [159] implemented a multi-scale DEM-CA model that involved Marangoni convection and the recoil pressure for 316L deposition. The CA model also employed an air-metal interface, where the microstructural variations on the free surface of a track are also simulated with substantial accuracy, as shown in **Figure 10**(b). Shi et al. [161] implemented a 3D FE-CA coupled numerical model to investigate the effect of laser beam shape on the single-track LPBF 316L. The simulation models also implement the Marangoni convection and recoil pressure effect on the melt surface. They observed that contrary to a longitudinal elliptical (LE) beam, a transverse elliptical (TE) beam results in a wider and shallower melt pool as shown in **Figure 10**(c). They also report higher nucleation events in the TE melt pool over LE during beam propagation. This could be correlated to the larger undercooled low G/V region in the trailing edge of the melt pool obtained for the former. However, the behaviour is reversed once the beam was turned off. Wang et al. [151] developed a multi-scale 3D FVM-2D CA framework for simulating the microstructural evolution in LPBF Mg-3.4Y-3.6Sm-2.6Zn-0.8Zr alloy, which was approximated to a binary alloy of Mg-3.4Y. Through their macro-scale model, which includes the recoil pressure effect and Marangoni convection, a gradual decrease in thermal gradient (from 1.11×10^7 to 2.6×10^6 K/m) and an increase in solidification rate (from 0.06 to 0.37 m/s) along the build direction in keyhole mode melt pool was found. As shown in **Figure 10**(d), for the alloy under consideration, the columnar dendrites formed epitaxially from the base region coarsen along the growth direction before the CET occurs. Further investigations on the solubility of Zr to α-Mg by the authors also reveal an increased tendency for CET with Zr. Teferra and Rowenhorst [148] implemented a multi-

scale 3D CAFE model to simulate the multi-layer microstructural evolution in LPBF 316L. They employed an analytical approximation to the LGK model for correlating the solidification velocity to total undercooling (ΔT), given by

$$V(\Delta T) = \frac{D_L}{5.51\pi^2\left(-m(1-k)\right)^{1.5}\Gamma}\left(\frac{\Delta T^{2.5}}{C_0^{1.5}}\right). \quad (22)$$

As shown in **Figure 10**(e), an impressive 3D multi-layer microstructure could be simulated that shows significant similarities, both in terms of crystallographic textures and grain morphology, to experimental results [180]. Baumard et al. [147] implemented a 3D CA-FE numerical model also for a powder-free LPBF test of 316L. As shown in **Figure 10**(f), their macro-scale simulation results present a gradual decrease in the thermal gradient at the moving S/L interface. Moreover, the microstructural evolution simulations show that decreasing the laser power at constant travel speed or increasing the travel speed at constant power can lead to a decrease in grain size and aspect ratio. In a relatively recent effort, Ren et al. [181] presented a two-way fully coupled CA-FV model to understand the solute segregation during the non-equilibrium solidification in the LPBF IN718 superalloy. A key observation here is that the solute transport from the melt convection tends to dilute the solute partitioning at the solidification front. Consequetly, solute trapping is promoted over segregation which could be beneficial for crack-free AM non-weldable superalloys.

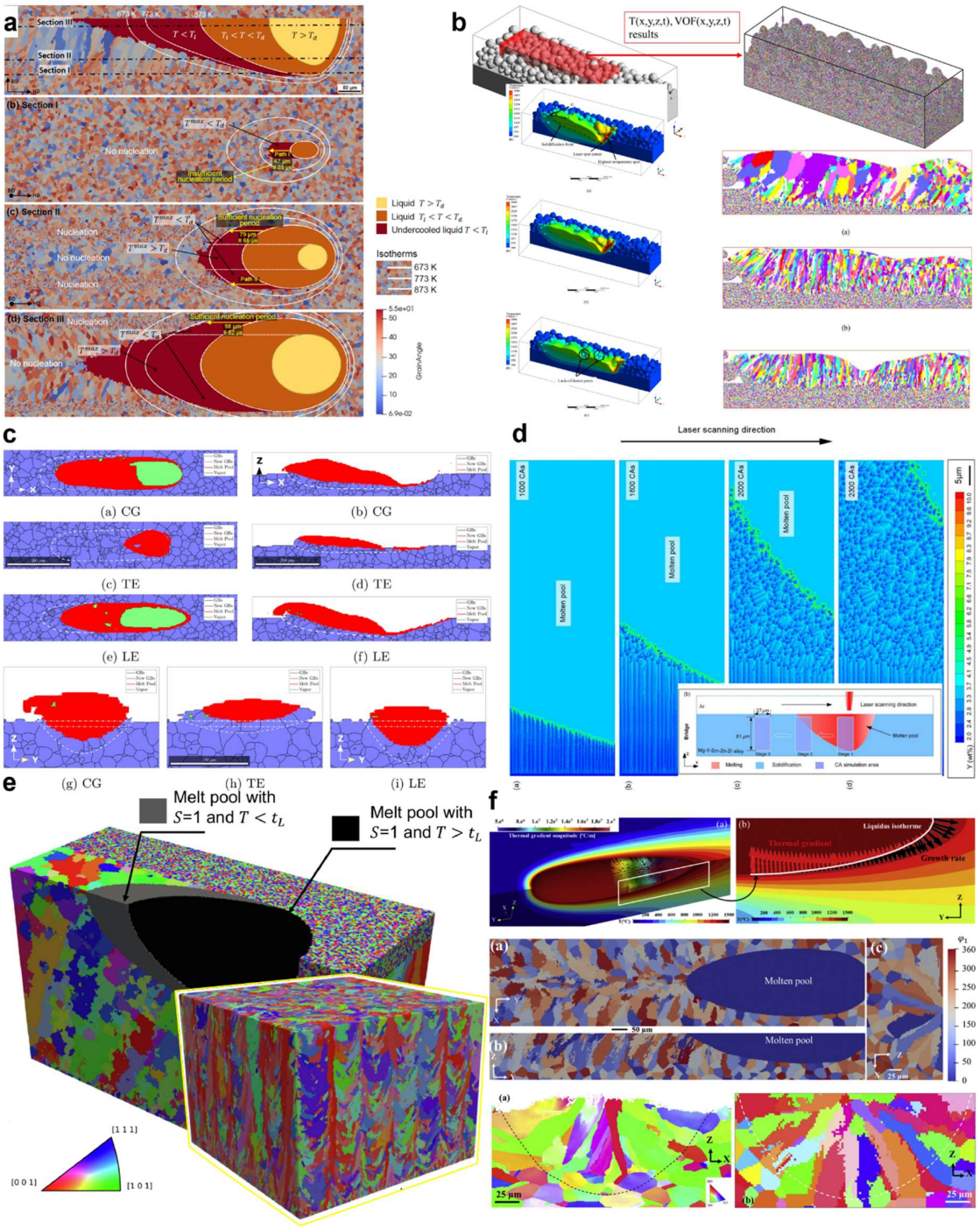

Figure 10. Application of cellular automata to LPBF processing of a variety of materials (a) Nucleation and grain growth with CA simulation of AlSi10Mg. (Continuum media approximation for the powder bed with reduced thermal conductivity) [160] (b) CFD-CA coupling for prediction of microstructural evolution considering the Marangoni convection and recoil pressure [159] (c) CA-based microstructure predictions for varying beam shapes for deposition of SS316L [161] (d) CA-FVM coupled numerical model showing microstructural

evolution with the movement of the melt pool. (Binary alloy approximation for the solution of solute diffusion during CA) [151] (e) Mesoscale CAFE modelling of multi-layer microstructural evolution in 316L (LGK model) [148] (f) Multi-scale CA-FE model for investigating the single-track microstructural evolution in 316L (KGT model) [147].

Figure 11 summarizes the key results of some of the approaches in recent years where CA was applied for the grain growth simulations in EPBF processes. Rai et al. [162] implemented a coupled CA-LB method in 2D to simulate the effects of multi-layer hatching of powder particles on the microstructural evolution for IN718 alloy, as shown in **Figure 11**(a). The numerical model presents computationally efficient 2D modelling for predicting the 3D microstructures, inclusive of powder consolidation and epitaxial grain growth from powder particles and through multiple layers. Koepf et al. [164] coupled a macro-scale analytical heat-transfer model to a microscale CA-based algorithm to simulate the multi-layer crystal growth associated with the EPBF IN718 superalloy. As shown in **Figure 11**(b), the simulated microstructures are similar to the experimentally observed one (rightmost) in terms of overall crystallographic texture and grain morphology, except for heterogeneous nucleation-driven stray grain formation in the latter whose effects were not included in the numerical models. Later Koepf et al. [182] implemented a CA-FE-based numerical model for a 3D microstructural simulation of EPBF CMSX-4 superalloy in cylindrical specimens. As shown in **Figure 11**(c), the simulated grain-envelop growth can successfully predict both – the grain growth from the loose powder at the part periphery and strong epitaxial growth in the core of the cylinder, resulting in large columnar grains as obtained in the experimental blocks. Chandra et al. [166] implemented a multi-scale numerical model in 2D to simulate the microstructural evolution during EPBF of Ni-based superalloy having single crystal compositions. In a first, they implemented the solute diffusion-driven CA-FD method in conjunction with a pseudo-binary alloy approximation for multi-component Ni-based superalloys [183]. Consequently, they could deconvolute the segregation behaviours of each of the alloying elements in the EPBF rapid solidification conditions as shown in **Figure 11**(d). Xiong et al. [167] implemented a multi-scale numerical DEM-FVM-CA model to simulate the multi-track multi-layer microstructural evolution for EPBF Ti-6Al-4V alloy. As shown in **Figure 11**(e), prior-β grain growth simulations could be performed with complex multi-track and multi-layer hatching which could link the process details on the powder scale to the microstructural evolution at the grain scale. From the simulations, they also confirm that by changing the alignment of the melt tracks, it is possible to break up the vertical columnar grains that are typically formed.

Additionally, disrupting the thermal profile along the build can randomize the crystal orientation. Yu et al. [168] implemented a multi-grid CA model for simulating the 3D dendritic growth and its application to EPBF IN718 superalloy with binary alloy approximation to Ni-Nb. As shown in **Figure 11**(f), their multi-grid model with improved accuracy at the S/L interface simulates the dendrite coarsening in a single-track melt pool along the build direction.

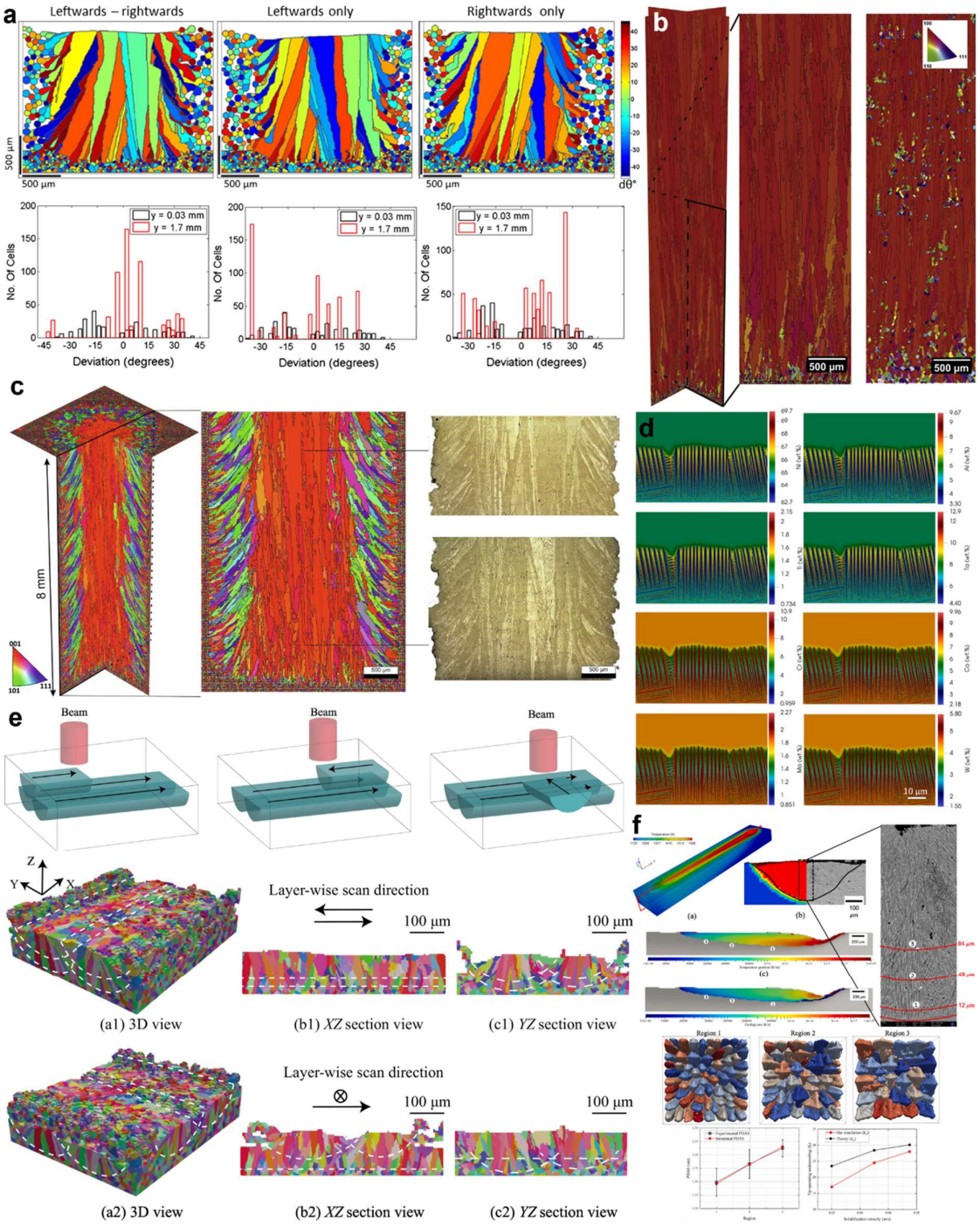

Figure 11. Application of CA-based numerical modelling to EPBF processing. (a) 2D CA-LB simulations highlighting the effect of scanning directions on the crystallographic texture evolution for IN718 [162] (b) 3D FE-CA simulated (left) and experimental (right) microstructure for EPBF IN718 [184]. (c) CA predicted large-scale 3D microstructure for CMSX-4 superalloy [165] (d) 2D CA-FD model predicting the melt pool solute redistribution of Ni-based superalloy [166] (e) 3D CA-LB model for multi-layer microstructural evolution simulations of Ti-6Al-4V [167] (f) Dendrite growth within a melt pool simulated with a multi-grid CA modelling [168].

The models for estimating grain growth with local undercooling have been given by the LGK [185], KGT (binary alloy systems), and extended KGT (multi-component alloy systems) models [186]. Total undercooling in the LGK model is written as a summation of the thermal, constitutional, and curvature-driven undercooling, as given below:

$$\Delta T = \Delta T_t + \Delta T_c + \Delta T_r. \tag{23}$$

The growth rate and dendrite tip curvature relating the fixed undercooling given in the LGK model can be summarised as following:

$$\Delta T = \frac{\Delta H}{C_p} Iv(P_t) + mC_0 \left(1 - \frac{1}{1-(1-k)Iv(P_c)}\right) + \frac{2\Gamma}{R}, \tag{24}$$

and,

$$R = \left\{\frac{\Gamma}{\sigma^*(mG_c - G)}\right\}^{1/2}, \tag{25}$$

where, R is dendrite tip radius, ΔH is the latent heat, C_p is the specific heat capacity at constant pressure, Iv is the Ivantsov function, P_t and P_c are the Péclet numbers for the thermal and solutal fields, respectively – expressed as $VR/2\alpha$ with α being the respective diffusion coefficients, m is the equilibrium liquidus slope, C_0 is the nominal alloy composition, k is the equilibrium partition coefficient, Γ is the Gibbs-Thomson parameter (ratio of solid/liquid interface energy and melting entropy), σ^* is a stability constant, G_c and G are the concentration and thermal gradients, respectively, evaluated at the solid/liquid interface.

The simplified KGT model assumes a hemispherical shape of the dendrite tip and interfacial equilibrium can be employed for solidification velocities not exceeding 0.01 m/s [92] given as:

$$\Delta T = mC_0\left(1 - \frac{1}{1-(1-k)\pi\sqrt{\frac{RT}{D\Delta T_0 k}}}\right). \quad (26)$$

Eq. (26) is also termed as an interfacial response function which can be solved with the solidification velocity, V as a function of undercooling primarily approximated with a cubic polynomial, $V = A(\Delta T)^3 + B(\Delta T)^2 + C(\Delta T) + D$, where A, B, C, and D are material specific parameters often determined through empirical relations or phase-field methods.

Table 1 summarizes the values of these parameters utilized by literature employed primarily in CA-based numerical simulations specific to AM solidification.

Table 1. Material dependent constants for the solution to interfacial response function.

Alloy	A (m/(s·K^3)) (×10^{-07})	B (m/(s·K^2)) (×10^{-05})	C (m/(s·K)) (×10^{-05})	D (m/s) (×10^{-05})	Ref.	Model
Ti-5wt% Mo	121.5	−1.1	35.4	−27.6	[92]	KGT
Ti-3wt% Cu	−16.8	6.4	6.6	−7.6	”	KGT
Ti-2 wt% Fe	−75.4	22.2	4.8	−1.8	”	KGT
Ti-4 wt% Ta	355.6	25.1	66.6	−33.2	”	KGT
IN718	22.9	1.6	1.8	-	[179]	LGK
Pure-Ni	−10.3	105.3	2219.6	-	[187]	KGT
IN718	−1.0	10.5	222.0	-	[162]	KGT
IN625	−1.0	10.5	222.0	-	[125]	KGT
SS304	109.1	−20.3	274.0	11.5	[140]	-N.A.
SS316L	-	0.02	-	-	[159]	KGT
IN718	4.1	0.02	-	-	[164]	KGT
Ti-6Al-4V	-	203.0	54.4	-	[167]	-N.A.

From the above summary, it is evident that the CA numerical modelling technique is most effective in simulating a range of microstructural evolutions during the EPBF, LPBF, and LDED processes. It is also interesting to note that CA codes can be applied with the solute diffusion governing equations (to accurately predict the sub-grain morphologies), which is a computationally intensive process. A result here is the simulations of dendritic to planar solidification with increasing flow rate for a binary alloy, as shown in **Figure 9**(c). An alternative to this is to employ analytical formulations that correlate the tip velocity to undercooling and simulate large-scale microstructures, as showcased by the multi-layer microstructures. However, a significant drawback in this case is the absence of the segregation

behaviour of the constituent elements during solidification. A couple of the limitations of CA-based modelling are the following. (a) So far, the AM literature employing CA with solutal governing equations are limited to binary or pseudo-binary alloy approximations, due to the lack of phase diagrams and the need for an additional non-equilibrium solidification framework for the same. (b) Lack of solid-solid phase transformation research, primarily to investigate the formation of detrimental precipitates of segregation-driven phase transformations.

3.3. Monte Carlo Method

The major application of the CA modelling to metal AM is for predicting and/or understanding the solidification microstructures. In comparison, the MC method has slightly broader applicability as it can predict the grain transition through the solidification and to the lower temperature phase transformations such as recrystallization and martensitic phase transformations. However, the MC methods are computationally more intensive than the CA models (typically the ones employing the analytical models for the prediction of solidification rates with the undercooling). Moreover, the KMC model lacks direct application of the thermal conditions to simulate the microstructural evolution, which is a major reason for it not being employed widely for simulating metal AM.

During a typical MC simulation, the computational domain is discretized into lattice points. Each of the lattice points is assigned a number that would represent a microstructural state. This way different integers could be employed to represent the liquid and solidified states as well crystallographic orientations [124].

A pioneering work on the application of the KMC method by Rodgers et al. [188] implemented the melt pool and heat-affected zone (HAZ) dimensions as parametric values of a double ellipsoidal heat source (**Figure 12**(a)). As a result, a framework is shown to work successfully where the melt pool information taken from the experimental observations of the overlapping tracks and layers could be used directly for simulating the microstructural evolution, without the computationally intensive step of determining temporal fields using the macro-scale numerical simulations. The resultant KMC model shows substantial accuracy in predicting microstructural evolution in the LDED and EPBF processing conditions. Aside from its application to LDED [189–191] (**Figure 12**(b) [190] and **Figure 12**(d) [191]), the KMC method has found several applications in the LPBF [44,192] processes as well (**Figure 12**(c) [44]).

The eventual task of a KMC Potts method is to perform the minimization of the aggregate energy of the microstructure, which, for simulations of microstructural evolution in the metal AM process, is given by [22]:

$$E = \sum_{i=1}^{\alpha} \sum_{j=1}^{\beta} \frac{\gamma}{2} [1 - \delta_{i,j}]. \quad (27)$$

Here, i and j are the site of evaluation and its neighbour, respectively. α is the total number of sites, β is the maximum number of neighbours (26 in 3D and 8 in 2D, respectively), γ is the specific grain boundary energy per unit length and $\delta_{i,j}$ is the Kronecker delta function which is 1 when $i = j$ and 0 when $i \neq j$.

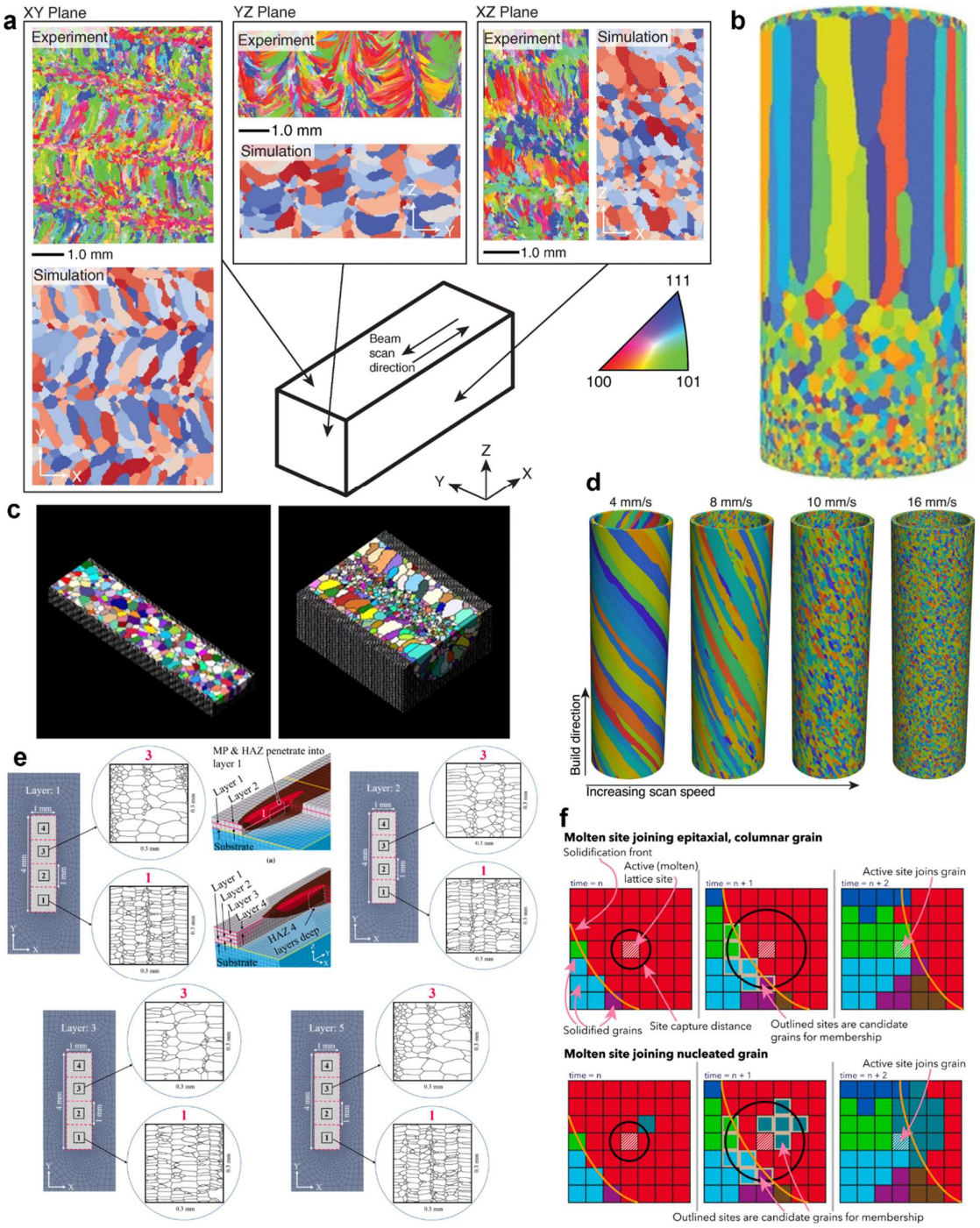

Figure 12. (a) KMC simulations of LDED microstructures obtained for IN718 alloy [188]. (b) Equiaxed to columnar transition in an LDED 304L tube simulated using the KMC method [190]. (c) Microstructural evolution in conduction and a convection type melt pool in an LPBF process [44]. (d) Microstructural variations with increasing scanning speed were simulated using KMC for the LDED process [191]. (e) Layer-wise distinct microstructural evolution is

obtained by the dynamic KMC method [192]. (f) Epitaxial vs equiaxed grain growth scheme implementation to KMC-based simulation model [193].

Two major advancements in the application of the KMC method to simulate AM have been showcased in **Figure 12**(e) [191] and (f) [193]. In the former, Rodgers et al. [191] implemented both macro-scale finite element methods or 3D thermal imaging techniques to determine the temporal evolution of the melt pool and HAZ information, which is then integrated into the KMC model for every timestep of the build. This results in a more accurate prediction of microstructural evolution in the distinct layers of the build, which are likely to differ due to the continuous thermal build-up due to the continuous deposition process. Rodgers et al. [193] implemented the finite difference Monte Carlo (FD-MC) method to employ a diffusion-based model, akin to the FD-CA models. They implemented a nucleation framework to simulate the equiaxed grain nucleation and even provide CET predictions using Hunt's solidification map [194].

3.4. Phase-field simulations

Among the microscale simulation of nucleation and solidification physics associated with the AM processes, phase field simulations have been quite promising [195]. In the PF method applied to solidification simulations, a diffuse solid/liquid interface can be simulated contrary to the sharp interface as seen in the majority of CA and MC methods. An order parameter or a phase-field variable, ϕ, whose value transitions smoothly from solid to liquid is introduced, which removes the need for explicit tracking of the interface [196]. The PF method is relatively more accurate than the CA and MC methods for determining solidification phenomena, because it is derived from irreversible thermodynamics. However, it is also the most computationally intensive as it requires solving a simultaneous system of equations that includes the phase-field variable and the free energy minimization equation.

Since the governing equations of the PF method are thermodynamic, the method can simulate the microstructural evolution for a myriad of solidification conditions. This is the reason for the PF method being continually applied for simulating the microstructural evolution in AM, despite the heavy computational costs associated with it. Akin to CA, albeit not as extensively, the PF method has been applied equally to LDED [197–199], LPBF [94,200–212], and EPBF [195,204,213,214].

The application of PF to LDED processes is shown in **Figure 13**. **Figure 13** (a) – top illustrates the evolution of a dendritic microstructure from the predominantly planar solid/liquid interface during the solidification of a melt pool of a binary alloy approximation of IN718 with Ni-Nb. [197]. With the progression of the grain growth, the planar interface breaks down, as predicted by the Mullins-Sekerka instability criterion [65], followed by the coarsening and elimination of dendrites due to the coarsening instability, a transition state, where an increase in PDAS occurs, followed by a steady-state growth. The simulation results also present the heightened sensitivity of PDAS to solidification velocity, as opposed to the thermal gradient. Hence, as seen in the long section of the single-track, **Figure 13**(a) – bottom, where the observations can infer as a result of unidirectional thermal gradient and solidification rate, the cooling rate at the solid/liquid interface (dashed line) decreases from top to the bottom of the melt pool in a trend similar to the solidification rate. Consequently, PDAS decreases substantially from the melt pool bottom to the surface. This work also rationalizes the deviation of experimental observations from predictions by the models of Hunt [215] and Kurz-Fisher [64].

Figure 13(b) presents the results of another work [198] with a CFD-PF coupling to model the microstructural evolution in laser-deposited T15 high speed steel premixed with CeO_2 powders. The 2D PF model was developed with a binary alloy approximation and an additional heterogeneous nucleation model [216] correlating the rate of nucleation to thermal undercooling in the melt pool given by:

$$\frac{d(n)}{d(\Delta T)} = \frac{n_{i,max}}{\sqrt{2\pi}\Delta T_{i,\sigma}} exp\left[-\frac{1}{2}\left(\frac{\Delta T - \Delta T_{i,nuc}}{\Delta T_{i,\sigma}}\right)^2\right]. \quad (28)$$

Here, ΔT_{nuc} is the mean undercooling, ΔT_{σ} is the standard deviation, and n_{max} is the maximum nuclei density. Quantitative and qualitative comparisons of the simulated microstructure with the SEM/EPMA observations shows a similar trend in grain area variation at different locations in the melt pool and segregation behaviour of alloying elements, respectively.

Recent work on the simulation of 3D microstructural evolution in a multi-layer LDED deposition of Ti-6Al-4V alloy is an apt example of the advancement of the PF method in application to AM processes [199]. They employed the following equation for the probability of heterogeneous nucleation [217]:

$$P = \int_{\Delta T(t-\Delta t)}^{\Delta T(t)} \frac{V_{cell} n_{max}}{\sqrt{2\pi}\Delta T_\sigma} exp\left[-\frac{1}{2}\left(\frac{\Delta T - \Delta T_{nuc}}{\Delta T_\sigma}\right)^2\right] d(\Delta T). \quad (29)$$

Here, V_{cell} is the volume of each lattice site. It should be evident here that Eq. (29) is the integration of Eq. (28) for a time step of Δt. The multi-scale multi-layer numerical simulation process detailed in the research shown in **Figure 13**(c) confirms that thermal undercooling is the most dominant during the LDED of Ti-6Al-4V alloy which also increases from melt pool base to the surface along the S/L interface. With the build height, thermal undercooling in the top regions of the melt pool increases favouring heterogeneous nucleation over epitaxial growth. Solidification velocity decrease induces grain coarsening – an effect similar to that on dendrites reported earlier by [197].

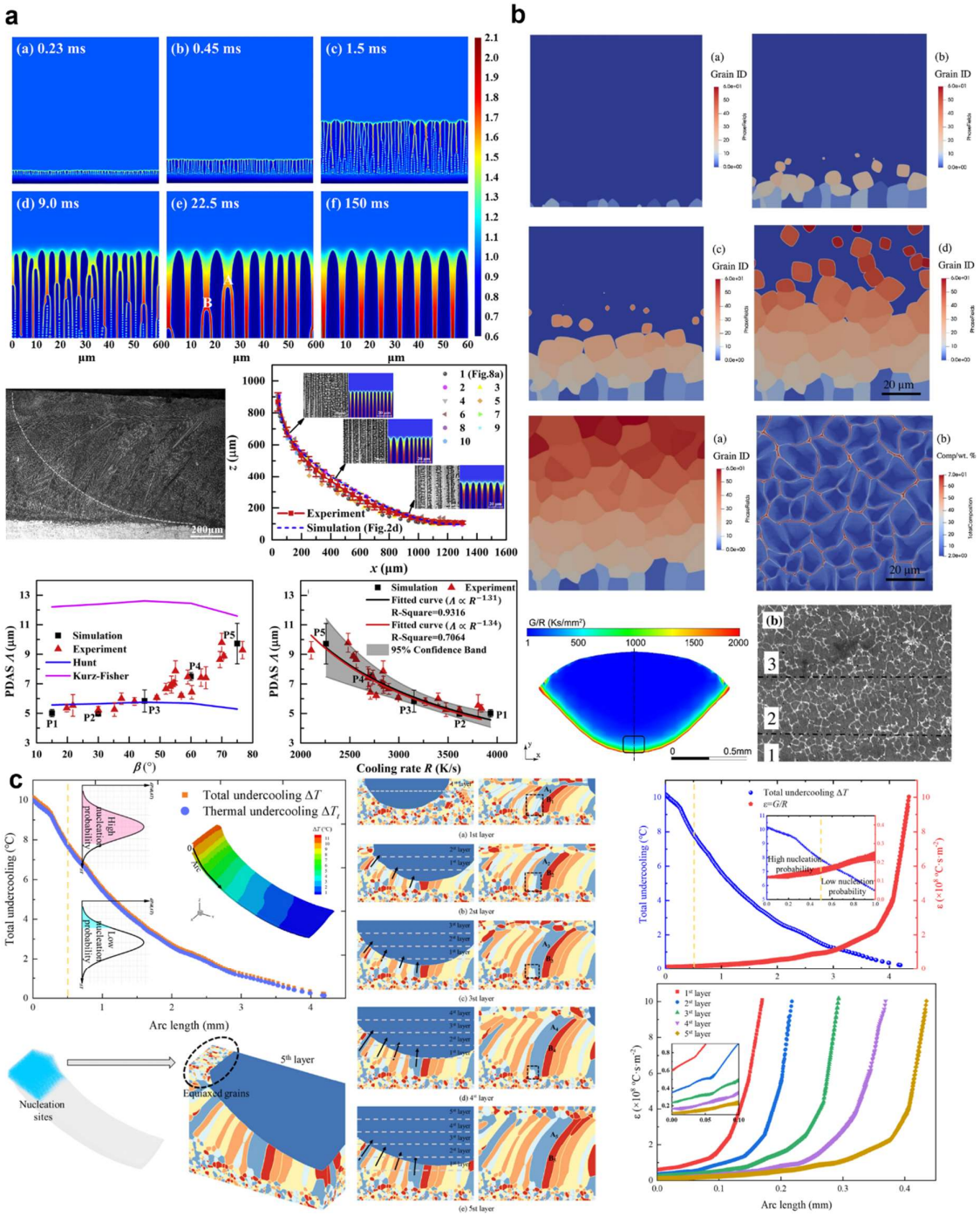

Figure 13. Application of PF modelling to LDED processes. (a) Top – Evolution of columnar dendritic microstructure for varying solidification parameters. Bottom – Dendritic microstructural evolution (numerical and experimental) along the melt pool boundary observed in the long-section of a single-track deposited bead of IN718 alloy. Bottom-most – Inability of conventional models in predicting the PDAS variations in a melt pool [197]. (b) Columnar to equiaxed transition simulated with the implementation of a heterogeneous nucleation model to

the PF simulations for deposition of T15 high-speed steel [198]. (c) The tendency for CET in different layer heights simulated for the Ti-6Al-4V process [199].

The PF method's application to LPBF processes has significnatly advanced the understanding of the rapid solidification phenomena associated with the range of solidification parameters that are typically experimentally measured or simulated during LPBF. **Figure 14** summarizes a few of the recent efforts. Karayagiz et al. [94] coupled a finite element-based macro-scale model to a finite-interface dissipation PF model [218] for simulating the non-equilibrium rapid solidification of Ni-3.2 at.% Nb. They showed through experimental and numerical simulation observations of single-tracks that for the solidification parameters typically obtained during the LPBF of the Ni-Nb binary alloy, the S/L interface evolves from planar to cellular and then to a planar one with increasing growth rate (V_{ab}), as shown in **Figure 14**(a). Chadwick and Voorhees [207] simulated the microstructural evolution during single-track LPBF deposition of SS316L with a Fe-Cr binary alloy approximation for the PF model and employed Rosenthal's solution for a steady-state temperature profile with a moving point source [219], as shown in **Figure 14**(b). An absolute stability limit was assumed and for the solidification of SS316L, neutral stability curves were calculated.

Yang et al. [208] developed a 3D LB-PF model for simulating the phenomenon of grain nucleation, growth, and coarsening during the multi-track multi-layer deposition of SS316L (**Figure 14**(c)). They modelled the effect of grain coarsening along with heterogeneous nucleation, and epitaxial grain growth from the previously deposited layers and powder particles. The PF model can also simulate the TiB_2-driven grain refinement in the SS316L. Okugawa et al. [211] developed a standalone 2D PF model for the laser remelting of Al-10 wt.% Si with constant solidification parameters (**Figure 14**(d)). They determined that the formation of fine equiaxed grains at the melt pool fusion boundaries observed in the LPBF microstructure of Al-Si alloys is driven by the intrinsic heterogeneous nucleation due to the high melting point of the Si-phase. Moreover, they also determined that under a rapid-heating condition such as that encountered in a PBF-type additive manufacturing process, only a short period of several tens of microseconds is allowed for atomic diffusion between the α-Al and solid Si-phases in eutectic regions.

Laskowski et al. [212] coupled a powder scale LB model with a microstructure scale PF model to simulate the microstructural evolution and porosity generation concurrently (**Figure 14**(e)).

They accounted for the grain growth anisotropy by orientation-dependent solid-liquid interface mobility, Γ_{gl} – lower values of which result in a larger thermal undercooling and stronger tendency for equiaxed grains formation. Elahi et al. [210] developed a 3D macro-scale finite element model coupled with a 2D micro-scale phase field model with pseudo-binary alloy approximations for IN718 alloy as Ni-5 wt.% Nb. Digital microstructural characterization of the simulated microstructure indicates varying Nb segregation in different grains of the melt pool in different locations which increases the predictability for the determination of regions where the Ni_3Nb phase could form (**Figure 14**(f)). In a first, Shinjo et al. [203] employed a multi-scale PF-based numerical model to simulate the in-situ alloying of Ni and Ti powders to form the Ni-Ti alloy that too in a keyhole mode of melt pool solidification. As shown in **Figure 14**(g), due to the macro-scale heterogeneity of the Ni concentration in the melt pool, temporal inconsistency occurs in the solidification.

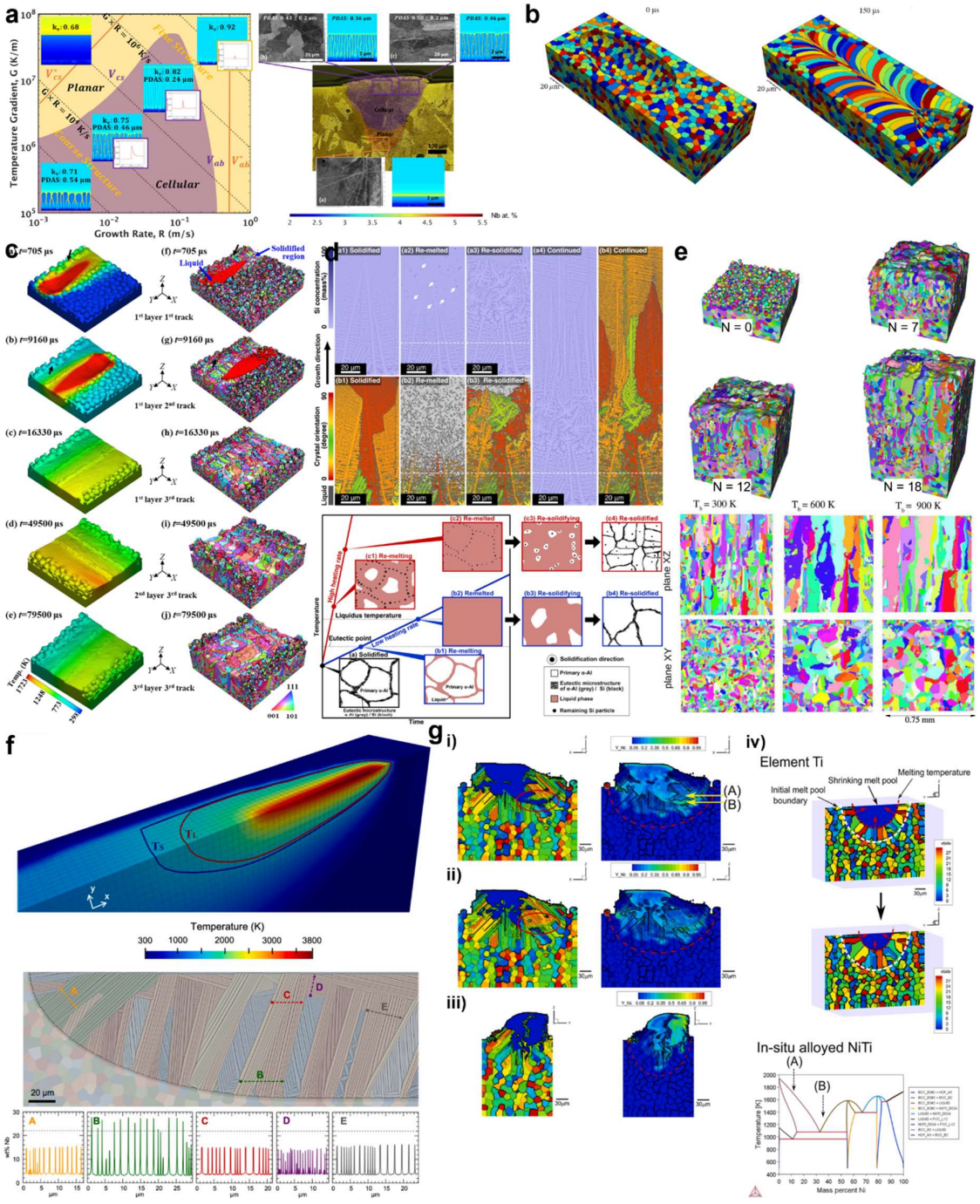

Figure 14. Application of PF method to LPBF process. (a) Finite-interface dissipation PF model for the rapid solidification of Ni-3.2 at.% Nb [94]. (b) Phase-field simulation of a single-track deposition of stainless steel 316L [207]. (c) 3D phase field modelling of microstructural evolution in 316L SS [208]. (d) PF method enlightened Si-driven intrinsic heterogeneous nucleation mechanism driven by laser reheating in Al-Si alloys [211]. (e) Lattice-Boltzmann phase-field coupled multilayer multiscale simulations for IN718 alloy for microstructural and porosity evolution [212]. (f) Multi-scale simulation of single-track deposition of IN718 alloy

(g) Phase-field driven multi-scale modelling of in-situ alloying of Ni and Ti powders for fabrication of Ni-Ti shape memory alloy [203].

Figure 15 presents the recent research on the application of the PF method to EPBF processes, which, as such, is sparse. Liu et al. [204] applied a 3D multi-scale PF model to investigate the columnar-to-equiaxed transition (CET) in spot melting of IN718. As shown in Figure 15(a), the high total undercooling obtained at the arc length of the melt pool cross-section with a minimum value of 40.5 K, which is higher than the mean undercooling of 33.6 K for IN718, is the reason behind heterogeneous nucleation-driven fine equiaxed grains formed from the spot melting strategy reported in earlier works [37]. In a later effort, Liu et al. [214] implemented a transformation mechanism of the alpha phase, based on the Burgers orientation relation, from the simulated beta microstructure of the Ti-6Al-4V melt pool which was further employed for simulated tensile testing. As shown in **Figure 15**(b) CET occurs for a process parameter set which fast beam scanning speed. The higher scanning speed was observed to increase the constitutional undercooling. Uddagiri et al. [195] investigated the effect of partial remelting with an electron beam on nucleation for a model binary alloy system of Ni-20.5 mol % Al. They employed a 2D PF model and as shown in **Figure 15**(c) they decipher not only the complexity of the Al segregation during the remelting process but also the melting and renucleation of the Al-rich γ’ phase.

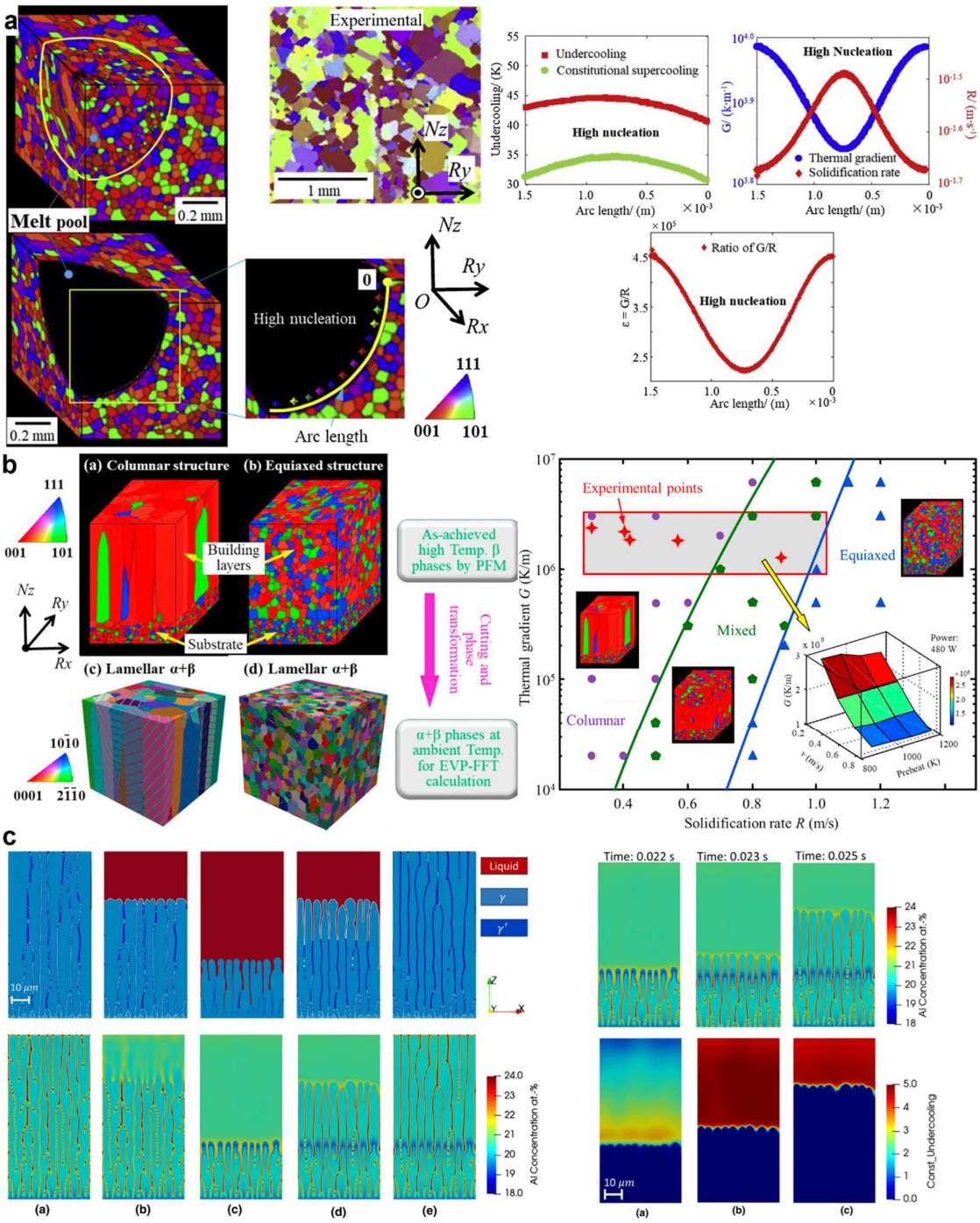

Figure 15. Implementation of PF based modelling frameworks to the microstructural evolutions in EPBF processes. (a) FE-PF multi-scale numerical model for spot-melting strategy implemented for IN718 [204] (b) Effect of beam power and scanning speed on as-built microstructure illustrated by FE-PF coupled model [214] (c) Effect of remelting on undercooling and nucleation in Ni-based superalloys [195].

3.5. Macro-scale modelling

Most microscale simulations of metal AM require coupling with a macroscale numerical model to determine the thermal history. This macroscale corresponds to the millimetre scale or system scale. The most general process of numerical modelling of AM at this scale involves solving the energy conservation and the Navier-Stokes equations using FEM [28,90,166,220–230], FVM or FDM [37,231–235]. The LBM is a new technique for modelling AM. LBM considers the powder bed as discrete particles, which makes it more accurate than other methods for visualizing the effects of relative powder density, balling, capillary, and wetting phenomena [38,236–239]. However, LBM is more computationally intensive than the other methods, especially when simulating large domains and determining the melt pool solidification parameters such as thermal gradient and cooling rate. In this review, we did not provide detailed accounts of macro-scale modelling applied to AM process as reviews on the same are available; interested readers should consult the works of Bayat et al. [240,241].

3.6. Analytical modelling

In addition to numerical modelling of metal AM at the system scale, analytical models derived from Rosenthal's equation [219] have been used to understand the resulting microstructure in manufacturing processes that involve a moving heat source [242–245]. These analytical models can be used to predict the thermal gradient and solidification rate in the melt pool, which can then be used to develop processing microstructure selection maps [242,243]. One such analytical model is a modified form of the Hunt's equation [194], which predicts the CET ahead of an advancing solid/liquid interface concerning the thermal gradient in the melt pool and the solidification rate of the interface.

The estimation of solidification parameters from the solidified microstructure is a critical aspect in the field of AM so far. In processes such as AM, computationally extensive numerical simulations needed to be performed to determine the solidification parameters of the molten pool, which not only vary spatially within a melt pool, but also vary with the consecutive melt pool overlaps due to heat accumulation. Hence, it becomes quite important to have the analytical tools that can determine the solidification parameters from microstructural features such as PDAS. The practice of solidification parameter determination from PDAS is not new to AM and has proven beneficial in providing approximate information to the microstructural growth models such as those employed by Sun et al. specific to LPBF 316L [44]. A general

model to predict the PDAS for dendritic and cellular grain growth was given by Ma and Sahm [246] and can be summarized as following.

For dendritic grain growth:

$$\lambda_d = 2\pi(kD\Gamma\Delta T_0)^{0.25}\left(1-\frac{V_{cs}}{V}\right)^{0.75} G^{-0.5}V^{-0.25}. \quad (30)$$

For cellular grain growth:

$$\lambda_c = 4\pi\left(\frac{D\Gamma}{k\Delta T_0}\right)^{0.25}\left(1-\frac{V_{cs}}{V}\right)^{-0.5} V^{-0.5}. \quad (31)$$

Here, λ_d and λ_c are the PDAS for dendritic and cellular grain growths, respectively. D is the solutal diffusivity, Γ is Gibb's Thomson coefficient, ΔT_0 is the solidification interval, k is the distribution coefficient, G is the thermal gradient along the direction of grain growth, and V is the velocity of the solidification interface. For predicting PDAS, the Kurz-Fisher model [64] is given as following:

$$\lambda = C_0\left(\frac{\Gamma\Delta T_0 D}{k}\right)^{0.25} G^{-0.5}V^{-0.25}. \quad (32)$$

Hunt's model for the PDAS prediction [247] has been provided in a rather simplified form by Wang et al. [248] as:

$$\lambda = 2.83\left(\frac{\Gamma\Delta T_0 D}{k}\right)^{0.25} G^{-0.5}V^{-0.25}. \quad (33)$$

Trivedi's model for PDAS [249]:

$$\frac{\lambda^2 G}{Rk\Delta T_0} = \frac{4\sqrt{2}L\gamma V}{2\Delta S D k\Delta T_0 P_c^2}. \quad (34)$$

Due to the abundance of analytical models, predictions of solidification parameters of G and V should be done judiciously. However, we recommend the model by Ma and Sahm [246] given in the form of equations (30) and (31), as it can be employed to estimate the variation of parameters throughout the melt pool considering cellular-to-dendritic and dendritic-to-cellular transformations, as the interface velocities approach the limit of absolute stability.

4. Challenges and solution/mitigation strategies

4.1. Solidification cracking

Solidification cracking typically takes place in the terminal stages of solidification, wherein the solid fraction ranges between 0.9 and 0.94 [250]. In this regime, incomplete coalescence of the dendritic arms leads to the presence of thin liquid film between them, which could rupture under thermal strains, especially when the fluid supply from the melt is insufficient [251]. This

type of cracking, which is often accompanied by smooth cellular/dendritic fractographic features, can be differentiated from the others, such as liquation and ductility dip cracking, by the absence of secondary phase precipitates at the cracked boundaries [252–256], as shown in **Figure 16**. Strains associated with the solidification shrinkage and thermal contraction of the solid behind the mushy zone are the primary reasons for it. Hence, the grain boundary separation caused by these two strains during solidification must be compensated by the dendritic coalescence and a supply of liquid metal from the molten region to the mushy zone, to suppress solidification cracking [166].

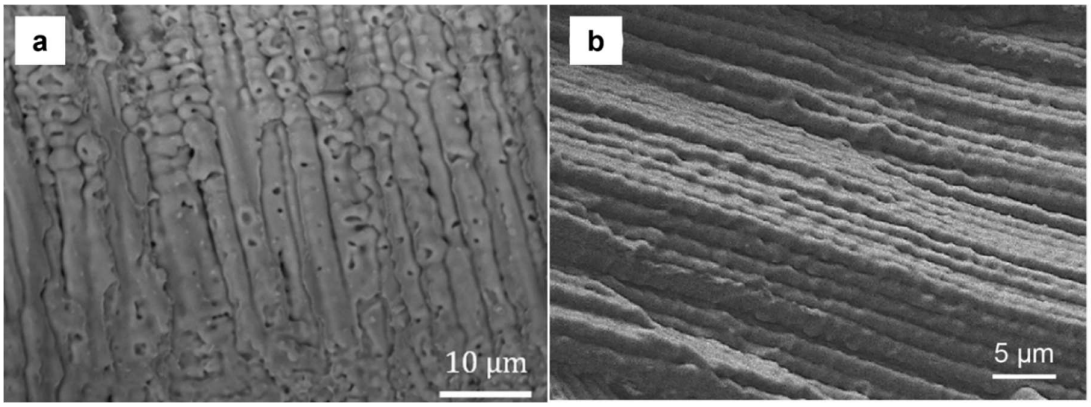

Figure 16. Fractographs obtained from the AM samples that underwent solidification cracking during fabrication. (a) Dendritic fracture surface of the intergranular cracked samples of Ni-based superalloy with single-crystal (SX) compositions printed using EPBF [166]. (b) Cellular fracture surface of the cracked samples of CoCrFeNi HEA manufactured using LPBF process [256].

Earlier works on the non-weldable alloys' AM, especially LPBF and EPBF of Ni-based superalloys, reported the formation of cracks in the as-built samples that could be alleviated through post-processing heat treatments such as hot isostatic pressing (HIP) [257–259]. Though the cracks were shown to be confined to the high-angle GBs [258], no significant correlations could be obtained for rationalising the formation of these cracks in the as-built samples.

Few physics-based models have been applied to investigate the solidification cracking in weld/AM solidification conditions. The Rappaz-Drezet-Gremaud (RDG) model (**Figure 17** (a)) [260] investigated the sensitivity to crack nucleation by considering the liquid feeding into

the mushy zone and uniaxial tensile load applied perpendicular to the growth of columnar dendrites due to solidification shrinkage. Mathematically, it is given as:

$$F\left(\dot{\varepsilon}_{p,\max}\right) = \frac{\lambda_2^2}{180} \cdot \frac{G}{(1+\beta)\nu} \cdot \Delta p_c - V_T \cdot \frac{\beta}{1+\beta} \cdot H', \tag{35}$$

where $\dot{\varepsilon}_{p,\max}$ is the maximum deformation rate sustained by the mushy zone before the nucleation of a void (hot tear), λ_2 is the secondary dendrite arm spacing (SDAS), G is the thermal gradient, β is the solidification shrinkage (ratio of density difference in the solid and liquid states to the density of the liquid state), ν is the melt viscosity, Δp_c is cavitation depression (difference of metallostatic pressure at the dendrite tips and the cavitation pressure), and V_T is the velocity of the isotherms. The functions F and H' are determined by the following equations:

$$F\left(\dot{\varepsilon_p}\right) = \int_{T_S}^{T_L} \frac{E(T) \cdot \left(f_s(T)\right)^2}{\left(1 - f_s(T)\right)^3} dT \tag{36}$$

with

$$E(T) = \frac{1}{G} \int f_s(T) \cdot \dot{\varepsilon_p}(T)\, dT \tag{37}$$

and

$$H' = \int_{T_S}^{T_L} \frac{\left(f_s(T)\right)^2}{\left(1 - f_s(T)\right)^2} dT. \tag{38}$$

Despite its development for the steady state conditions, with an unidirectional orientation of the dendrite arms, and the assumption of the invariable fraction of solid (f_s) in the direction perpendicular to liquid feeding, the RDG model has been applied with significant success in AM for deciphering and alleviation of solidification cracking. Some examples are LPBF CoCrFeNi HEA [256], CoCrFeNiAl HEAs [261,262], Zr-modified Al–Cu–Mg [263], Al–Li [264], CM247LC [265,266], Al6061 [267], AA7075 [268], Ti-modified Al-Cu [269], IN738LC [270,271], Al2024 [272] and LDED René 80 [273].

While the RDG model considered a steady state control volume for the entire mushy zone, a later criterion for solidification cracking proposed by Kou [274] (**Figure 17** (b)) focussed on the grain boundary between parallel columnar grains with an additional effect of grain growth toward each other during solidification. Mathematically, the Kou's criterion for cracking is expressed as:

$$\frac{d\varepsilon_{local}}{dT} > \left\{\sqrt{1-\beta}\cdot\frac{d\sqrt{f_s}}{dT} + \frac{1}{(dT/dt)}\frac{d}{dz}\left[\left(1-\sqrt{1-\beta}\cdot\sqrt{f_s}\right)\cdot v_z\right]\right\}_{\sqrt{f_s}\to 1}. \quad (39)$$

Here, ε_{local} is the local strain and its derivative with T (the term on the left hand side (LHS)) is the local separation term that accounts for the tensile deformation normal to the columnar dendritic grains. The first term on the right hand side (RHS) accounts for the growth of dendritic arms to coalesce while the second term accounts for the liquid feeding with a velocity v_z to resist the crack growth.

Given the above model's application to rapid solidification parameters associated with a weld, it has been widely accepted and applied to problems in metal AM as well [275]. A key limitation of Kou's model is that it considers only parallel columnar grains and ignores the effect of attractive or repulsive GBs. Keeping this in view, Chandra et. al [166] (**Figure 17** (c)) proposed a generalized criterion for solidification cracking by adding the mutual inclination of grains to Kou's existing criterion. Moreover, they extended the attractive and repulsive notation to classify GBs into convergent and divergent ones (on the basis of inclination of subgrains towards or away from each other at a GB, respectively), which, in turn, affect the liquid flow to the mushy zone and the grain boundary separation. Their criterion can be expressed mathematically as follows:

$$\begin{aligned}\frac{d\varepsilon_{local}}{dt} > &\left[\sqrt{1-\beta}\cdot\frac{d\sqrt{f_s}}{dT}\cdot\left(1+\frac{1}{cos\theta}\right)\cdot|CR| - \frac{tan\theta}{\varphi}\cdot\frac{|CR|}{G}\right] \\ &+ \frac{d}{dz}\left[\frac{1}{2}\left(1-\sqrt{1-\beta}\cdot\sqrt{f_s}\right)\cdot\left(1+\frac{1}{cos\theta}\right)\cdot v_z\right]_z.\end{aligned} \quad (40)$$

Here CR is the cooling rate, θ is the inclination angle of the neighbouring grains, φ is the grain width that is assumed to be equal for the neighbouring grains, and G is the thermal gradient. Along with the criterion, they also demonstrated, with the help of diffusion based CA simulations that the divergent grain boundaries ($\theta > 0^o$) are prone to the segregation of heavy elements and a decrease in the permeability of molten metal to resist the crack. This criterion can be particularly beneficial when applied to the general case of metal AM, where the grains are not necessarily unidirectional and severe segregation of the solute elelements at grain boundaries is a norm [276].

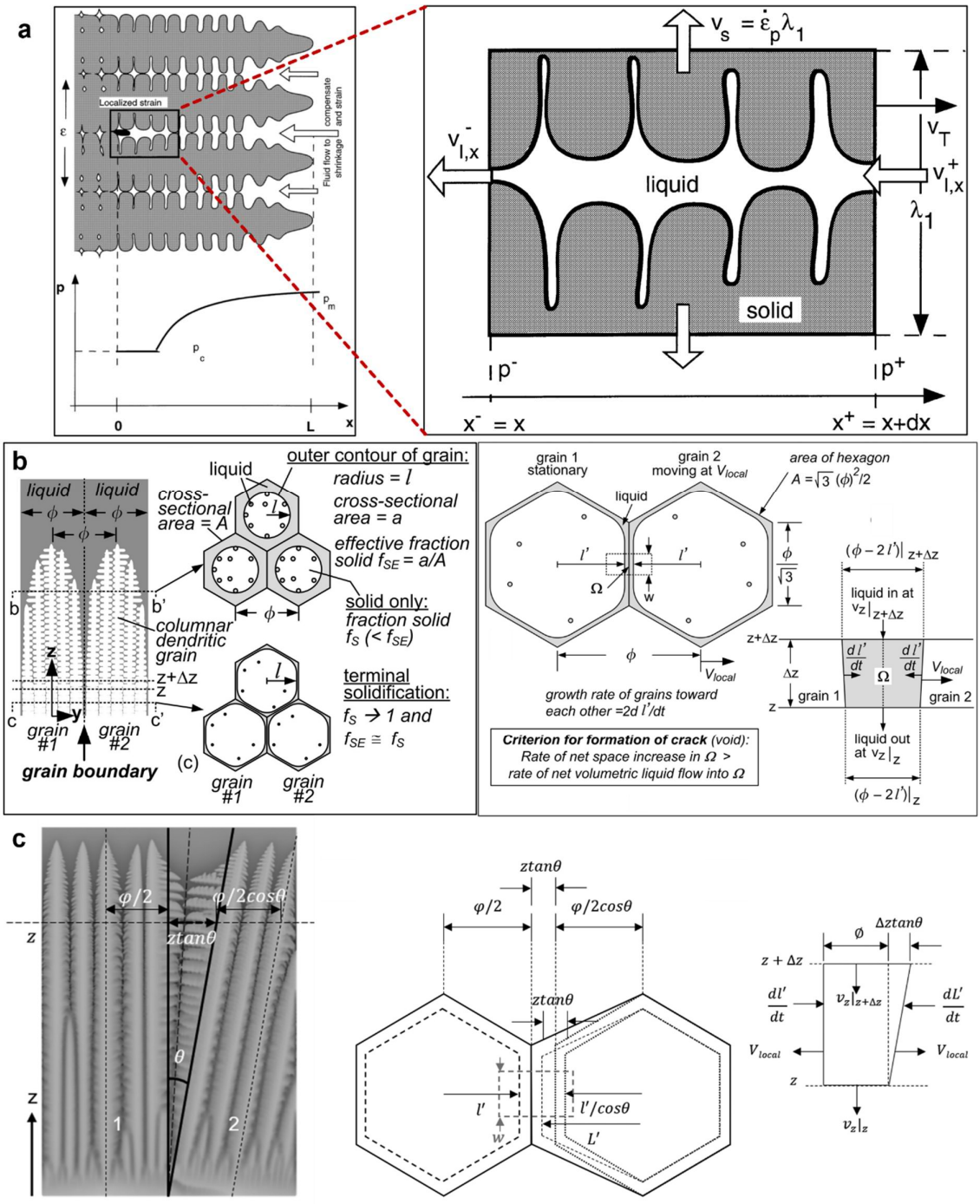

Figure 17. Criterion for solidification cracking. (a) RDG criterion [260] showing a steady state control volume consisting of parallel dendrites that is assumed to move along the dendrite growth direction with the isotherm velocity. (b) Kou's criterion [274] with its fixed control volume primarily focussed at the grain boundary between parallel columnar grains. (c) Generalised criterion by Chandra et al. [166] accounting for the grain tilt angle to the Kou's hot cracking criterion.

Solidification cracking in AM has been tackled through various means – affecting the CET during solidification being the primary one. The idea behind this is to prevent the epitaxial growth of the columnar grains that are prone to solidification cracks, and, instead, promote equiaxed grains that tend to be isotropic. While CET in AM is detailed in the next sub-section, it is worthwhile here to introduce the pioneering work of Martin et al. [277] on inoculation-induced heterogeneous nucleation, as shown in **Figure 18**. They employed nano-scale hydrogen-stabilized zirconium particles as nucleants to print crack-free equiaxed aluminum alloys using LPBF process. Additionally, it is probable that the addition of Zr affected the solidification temperature range of the Al alloy and resulted in increased resistance to cracking.

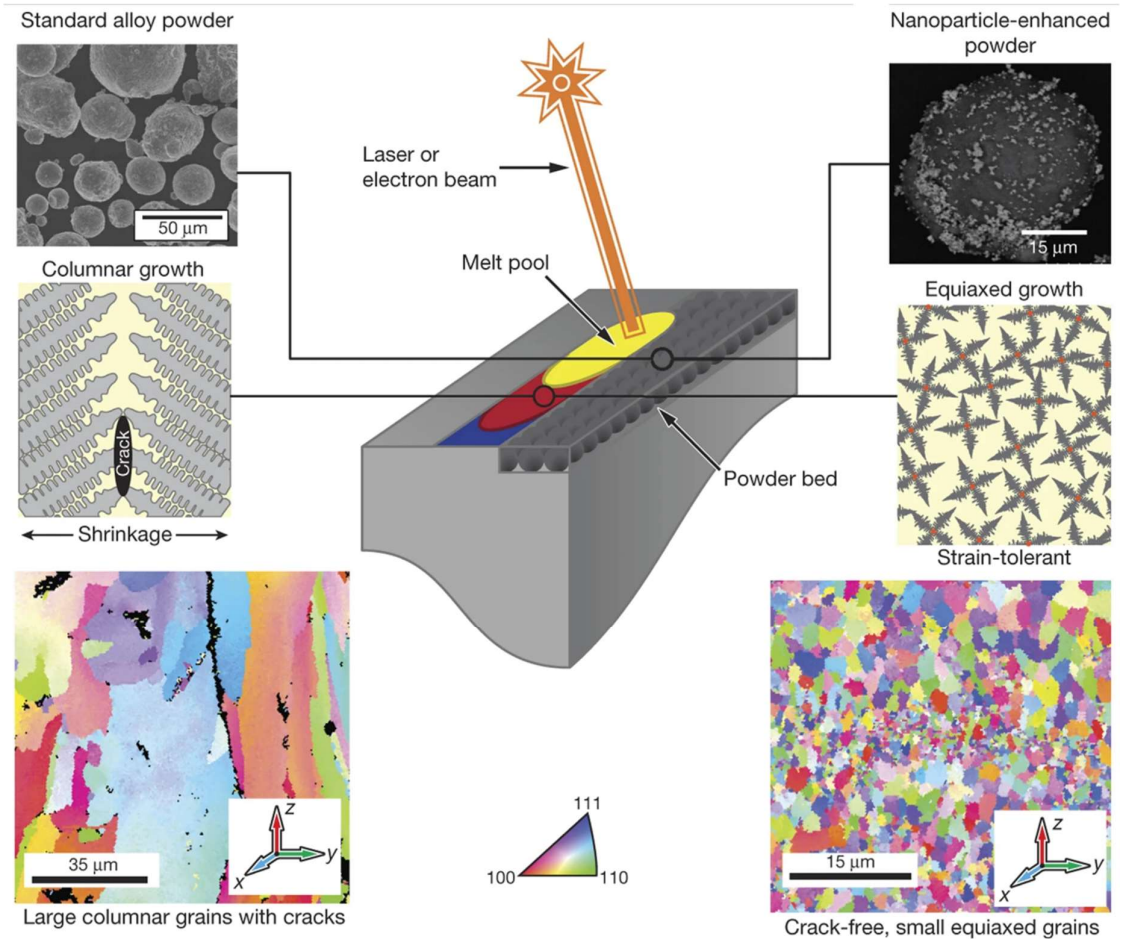

Figure 18. Inoculant-induced heterogeneous nucleation for achieving crack-free equiaxed microstructure via LPBF – addition of nano-scale Zr particles to Al7075 powder [277].

In cases where columnar grain growth is a necessity, so as to form a highly directional or single crystal microstructure for creep-resistant applications, CET cannot be pursued. Hence, it is

important to produce largely columnar microstructure that is free from solidification cracking. Adapting the alloy design principles shows potential in alleviating solidification cracking without much variation to the microstructural evolution. For example, addition of 1 to 5 wt.% Ti to IN625 process was demonstrated to reduce its cracking susceptibility during the LDED process [278]. The following two reasons were attributed to it. (a) Decrease in the solidification temperature range from 210 to 149 °C, and (b) potential healing of cracks from backfilling during the terminal stages of solidification, due to the increase in the low melting point Laves phases + γ eutectic at the grain boundaries and the interdendritic regions.

In their recent work on LPBF Al-alloy, Zhou et al. [279] employed a hybrid approach where TiB_2 particles were added, such that they act as nucleants for equiaxed grain formation, and Si was added to reduce the solidification shrinkage strains. Similarly, the addition of TiC to the LPBF IN738LC superalloy has been shown by Zhou et al. [280] to reduce the aspect ratios of columnar grains. This causes an increase in the high-angle grain boundaries (HAGBs) that leads to a reduced solute enrichment and strain concentration at GBs, resulting in significant inhibition of solidification cracks in the as-printed samples. Recently, Dang et al. [281] investigated the cracking tendency of IN738 superalloy manufactured using LDED and EPBF processes. They highlighted that the shallow and wide melt pools along with the solidification parameters obtained in the latter favour the growth of textured columnar grains. This pair with large cooling rate at the solid/liquid interface that deters solute segregation, results in crack suppression in the EPBF IN738 samples.

It is well established that alloys with increasing solidification range exhibit higher susceptibility to cracking. However, in their recent study with LPBF, Zhao et al. [282] reported an opposite behaviour wherein the addition of Zr to Haynes-230 alloy was shown to inhibit solidification cracking substantially, while the Schiel model shows a large increase in the solidification temperature range. Similarly, in their LPBF $CoCrFeNiAl_x$ HEA Sun et al. [261] observed cracking in Al-rich (1.0 molar ratio) samples which was driven by the formation of network of brittle B2 phases at the GBs despite a decrease in solidification range that was predicted by the Schiel model. These results highlight that the solidification temperature range determined through computational thermodynamics might not be good enough to predict solidification cracking in AM alloys.

4.2. Columnar grains due to epitaxial growth and CET

Epitaxial grain growth during AM implies that the grains in a melt pool grow on the previously deposited layer. As detailed in **Section 2**, the energy barrier for heterogeneous nucleation is much lower than that of the homogeneous one [56,70]. Hence, the former is preferred on the existing grains in an AM melt and, under favourable solidification conditions, the growth of these grains, which have the same crystallographic orientation as their seeds, occurs. Such growth can transcend through several layers and is termed as epitaxial grain growth. In the high width-to-depth aspect ratio (AR) melt pools, termed 'conduction-type' in the AM literature, such an epitaxial grain growth can result in the strong <001> crystallographic textures in alloys that have cubic crystal structures (body centred cubic (BCC) and face centred cubic (FCC)). Fulfilment of the following two conditions is essential for this to take place: (a) a large thermal gradient across the molten region and (b) minimum deviations of the solidification growth front from the build direction [235]. Shallow melt pools satisfy these conditions, as the grain growth front has to traverse relatively shorter distances with a fixed orientation, before being remelted and transferring their orientation information to the grains in the melt pool of the next layers.

Since directionally solidified, large columnar grains are desirous in the Ni-based superalloys, whose primary functionality demands excellent creep resistance, several methodologies that favour the elimination of misoriented grains to form nearly monocrystalline microstructures have been developed [28–30,32,283,284], as evident from a few examples shown in **Figure 19**. The EPBF technique is often associated with the conduction-type melt pool formation due to the high thermal gradient aligned with the build direction in it and hence has resulted in textured columnar microstructures in Ti-6Al-4V [90,245,285], Ni-based superalloys [30,32,164,283,286–288], and stainless steels [28,35,289–291]. Additionally, Gotterbarm et al. [32] implemented a μ-Helix beam scanning technique to strengthen the <001> crystallographic texture in EPBF IN718. Chandra et al. [28] introduced an X-shaped part geometry that could strengthen the epitaxial growth of <001> aligned grains through its neck and the V-shaped section. They also report an optimum prism angle of 90° over 60° and 120° that could result in a near-monocrystalline microstructure for EPBF 316L.

CET in the melt pool will occur, however, when the nucleation of new grains is favoured, either for thermodynamic or kinetic reasons, over the epitaxial growth of columnar grains. In AM, triggering CET has been achieved through various means such as heterogeneous nucleation

[277,292–295] (**Figure 20** (a1), (a2), and (a3)), process parameter variations [29,36,38,39,42,44,296] (**Figure 20** (b1) and (b2)), powder-size driven melt pool engineering (MPE) [35] (**Figure 20** (c)), accessories for in-situ microstructural variations – often limited to LDED processes [297,298], and post-processing heat treatments [293,299,300].

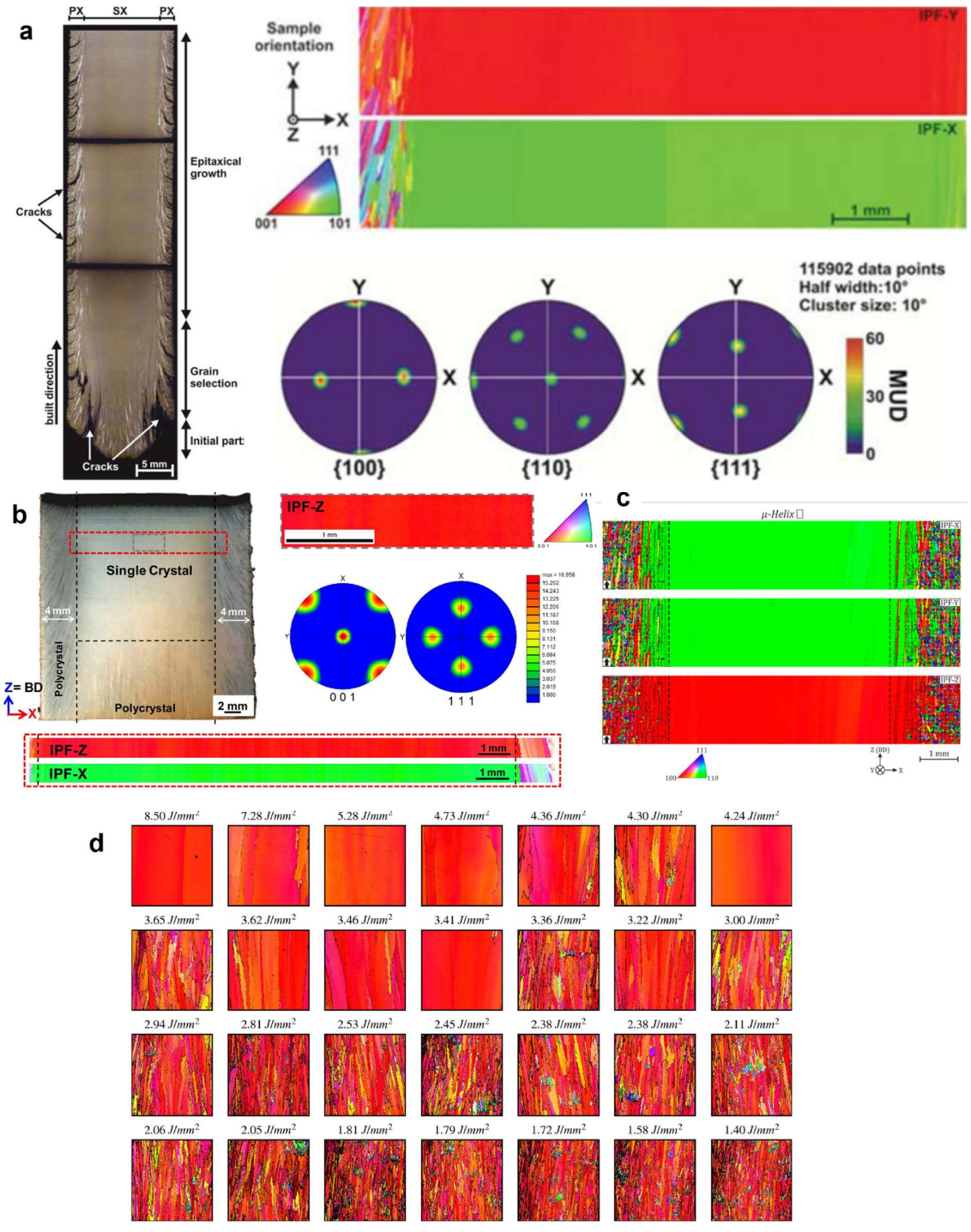

Figure 19 Single crystalline microstructure from EPBF AM processes. (a) EPBF CMSX-4 part and the corresponding IPFx and IPFy maps [30] (b) EPBF Ni-Co-Cr-Mo-Al-Ti-B Ni-based superalloy [283] (c) EBSD IPF maps of SX EPBF IN718 samples [32] (d) IPFz maps for varying energy density obtained in EPBF Nimonic 105 alloy [288].

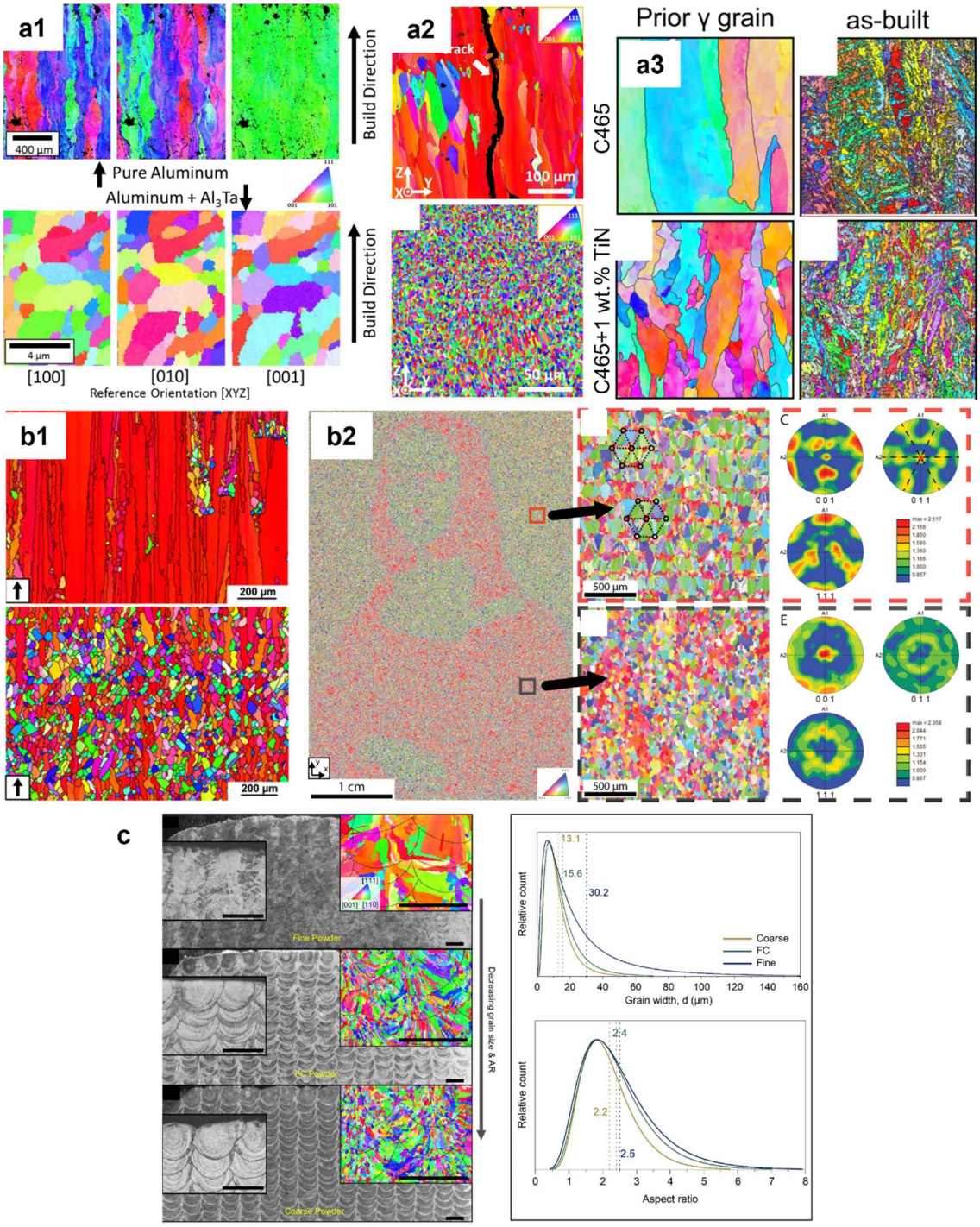

Figure 20 CET in AM as-built samples. Inoculation driven CET in (a1) LPBF Al [292], (a2) LPBF 2024-Al alloy [294], (a3) LPBF C465 maraging steel [295]. Process parameter variation driven CET in (b1) EPBF IN718 [38], (b2) EPBF IN718 [42]. (c) Powder-size driven CET in LDED 316L [35].

The addition of inoculants, as discussed before, can lower the energy barrier by providing heterogeneous nucleation sites. On the other hand, CET can occur if the processing conditions are such that the conditions for homogeneous nucleation ahead of the solidification front are met or strong melt convection occurs leading to flow of the dendrite fragments that could act as heterogeneous nucleation sites (the latter being more likely). Microstructures with equiaxed grains in the AM parts are often desired since columnar grains are prone to hot cracking, introduce obvious anisotropy in mechanical response, and have substantially lower dislocation densities (as compared to their equiaxed counterparts) that result in relatively lower strength (compared to the equiaxed ones).

The following two relations, proposed by Gaumann et al. [242] for rapidly solidified melt pools on the basis of Hunt's criterion [194], can be utilized to generate microstructure selection maps based on the solidification parameters:

$$G \geq G_{columnar} = 0.617 \cdot (100N_0)^{\frac{1}{3}} \cdot \left(1 - \frac{\Delta T_n^3}{\Delta T_c^3}\right) \cdot \Delta T_c \tag{41}$$

$$and, G \leq G_{equiaxed} = 0.617 \cdot (N_0)^{\frac{1}{3}} \cdot \left(1 - \frac{\Delta T_n^3}{\Delta T_c^3}\right) \cdot \Delta T_c. \tag{42}$$

Here N_0 is the nucleation density, ΔT_n is the undercooling of the melt given by the difference between the liquidus and the nucleation temperatures (that can be obtained through the DSC measurements [52]), and ΔT_c is the constitutional undercooling at the dendrite tip that can be estimated using the empirical relation given in [242]:

$$\Delta T_c = (a \cdot V)^{\frac{1}{n}}, \tag{43}$$

where, a and n are material properties, and V is the growth rate. Values for a and n can be determined using the *KGT* model for columnar grain growth front [301] in binary alloys following the steps outlined in Wang et al. [302] or by using Lin's model for multi-component alloy systems [303]. **Table 2** summarizes the values of a and n determined through analytical or empirical basis, for a range of alloy systems available in the literature. Typical assumed

values of 1.25×10^{06} $K^{3.4}.s.m^{-1}$ and 3.4, respectively, for a and n irrespective of the alloy system [52,53,304,305] are not listed here.

Table 2. Material-dependent parameters needed to correlate constitutional undercooling to the growth rate.

Alloy system	Alloy	a ($K^n \cdot s/m$)	n	Reference
Ni-based	CMSX-4	1.25E06	3.4	[242]
Mg-based	Mg-3.64 wt% Al	6.973E05	3.517	[302]
Al-based	Al-0.5Sc-0.5Si	7.1E03	2.96	[306]
	Al-4 wt% Cu	1.042E03	3.1	[55]
	Al-4 wt% Cu	5.6E04	3	[307]
	Al-Cu	2.01E06	4.14	[308]
Ti-based	Ti60	131347.3	4.97	[54]
Fe-based	316L	5.87E04	2.94	[35,303]

Though most of the CET-related research on AM alloys have employed the criteria prescribed in Eqns. (41) and (42) for predicting CET, it should be noted that these are criteria that were originally derived for the steady-state conditions with time-invariant solidification parameters – constant conditions of thermal gradient and growth rate, generally observed in castings that experience the directional solidification conditions. In view of this, Lei et al. [78] recently made an effort to estimate CET under the unsteady state conditions, which often prevail during EPBF, with the multi-track single-layer deposition experiments and simulations. They determined that for EPBF, parameter sets that resulted in shallow and wide melt pools can be manipulated with varying hatch spacing to achieve bulk CET and a 'zig-zag' microstructure. Hence, it is important to consider unsteady state solidification conditions for a more accurate prediction of microstructural evolution during AM.

4.3. Solidification-induced porosity

Porosity is a solidification-related defect that is commonly seen in AM processes, which is detrimental to various mechanical as well as functional properties of an alloy, such as ductility, corrosion resistance, and thermal/electrical conductivity. In particular, the presence of any level of porosity in a structural component that is subjected to fluctuating loads in service can lead to a marked reduction in the unnotched fatigue strength and hence, can compromise the structural integrity and reliability markedly. Therefore, it is necessary to understand the

evolution of these solidification-driven defects so that they can be minimized (if not eliminated entirely) during fabrication.

Based on the formation mechanism, porosity is generally categorized into the following three types: keyhole, gas, and lack-of-fusion (LOF). Their representative morphologies are shown in **Figure 21**. The keyhole mode of laser melting is typically an alternative to the conduction mode – a namesake for the associated heat transfer. In the former, the energy density of the laser power is sufficient to vaporize the feedstock leading to the formation of plasma and vapour cavity [309], that would result in a melt pool far deeper than that from the latter. The vapour cavity, upon solidification, results in a pore with a distinct morphology. As shown in **Figure 21**(a), the keyhole pores typically show characteristic irregular shapes and well-defined rims [310,311]. The critical condition for their formation is collectively determined by the laser power, scan speed, and spot size.

The second type is the gas porosity, which originates from the trapped gases in the powders during the gas atomization process or mixing of the shielding atmosphere/vaporized gas into the melt pool. These types of pores are typically spherical in shape and microscopic in nature, as shown in **Figure 21**(b) [312].

The third type of pores are LOF pores which are caused, as their name suggests, by the insufficient melting of the powder particles and then limited penetration depth of the melt pool into the preceding layers. Therefore, LOF defects commonly appear crack-like and are often located at or near the inter-layer regions (**Figure 21**(c) [313]). Amongst the three types of pores, LOF pores are the most detrimental ones due to their relatively larger sizes and sharp corners/edges that act as stress concentrators, while the gas pores are the least harmful (as they are spherical in shape and often smaller in size).

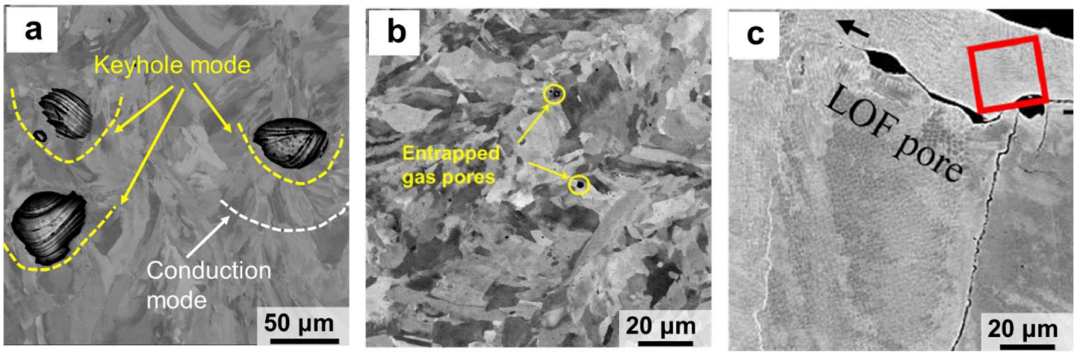

Figure 21. Representative morphologies of (a) keyhole-induced porosity [310], (b) gas-entrapped pores [312], and (c) lack-of-fusion (LOF) defects [313].

The causes of processing induced porosity can be several, which are summarized below.

(i) AM system imperfections induced porosity: Energy source is the key to the functioning of the AM systems. For example, in the laser-based processes, i.e., LPBF and LDED, the quality of optical system, calibration of the laser beam, and beam deflection could all possibly lead to formation of fabrication defects. If the laser source is not well-calibrated, the resulting uneven distribution of the energy can cause distortion of the laser spot and, therefore, result in porosity (typically lack of fusion type) in the built part [314]. When the laser reaches the edges of the substrate, the high deflection angles could lead to an elliptical distortion of the spot, thus resulting in undesired energy distribution and eventually porosity [315]. Insufficient flow of protective gas could also lead to formation of pores. If the splattering and the resolidified evaporations from the feedstock are not promptly removed, they could interact with the laser and lead to unpredictable disturbance of the scanning path [316]. Another case is that when the inert atmosphere carries the impurities passing the top of the printed parts, the impurities can simply fall into the build, causing porosity. Despite the usage of protective atmosphere, oxygen intake in still inevitable during AM process, which could react with the feedstock and lead to porosity. To minimize the AM system-related pores, it is of great importance to meticulously maintain the equipment and carefully handle each step.

(ii) Feedstock defects induced porosity**:** First, the flowability of the powders plays a significant role. More specifically, if the powders are not evenly distributed and packed, the powder packing density can vary from location to location of the powder bed in a significant manner. In regions where it is low, an excess air/gas present can be trapped during

solidification, leading to gas porosity. For this reason, using spherical powders with uniform particle sizes is generally recommended. Moreover, during the atomization process (the most commonly used approach for producing metal powders), the protective atmosphere can be trapped into the powders. These pores are particularly challenging and detrimental, as they are difficult to be eliminated and could grow into larger pores during fabrication [317]. Last but not the least, contamination of the powders (oxidation and surface-absorbed moisture) significantly affects the thermal history of the AM process and can lead to formation of pores. Oxidization of the powder surface (during storage, transportation, and printing) can affect the laser absorbability and surface tension of the melt, leading to instability of the melt pool and thus formation of pores [318]. Surface absorption of moisture could result in powder agglomeration and thus poor flowability. Measures can be taken prior to and during fabrication to minimize the moisture content, e.g., storing the powders in vacuum condition, conducting heat-treatment before fabrication, and substrate heating during the AM process.

(iii) Process-related porosity: In general, formation of pores is closely related to the energy input, where excessive and insufficient energy inputs can lead to keyhole and LOF pores, respectively. Each of the key fabrication parameters, i.e., laser power, scanning speed, hatch spacing, and layer thickness, affects the formation of pores in different ways. Specifically, laser power and scanning speed affect the overall energy density and thus, the formation of LOF and keyhole pores; hatch spacing affects the overlapping between scanning tracks, where excessive hatch spacing could result in pores well-aligned between neighbouring scanning tracks [319]. Layer thickness plays a significant role in affecting the remelting depth. If it is too high or too low, it can lead to overheating or poor interlayer bonding. As discussed above, it is of great significance to understand the relationship between the AM process parameters, microstructures, and, eventually, the mechanical properties. One broadly accepted approach is to plot a normalized processing diagram to categorize the corelation between parameters and porosity, using both printing parameters and intrinsic materials properties.

One example of investigating the process-related porosity is given here for an $AlCoCrFeNi_{2.1}$ eutectic high entropy alloy (**Figure 22** [320]). The key parameters considered are E^*_{min} and h^*, which are defined as below:

$$E^*_{min} = \frac{p^*}{l^* V^*} = \frac{A' p}{2vl\rho r_b C_p (T_m - T_0)} \; and \; h^* = \frac{h}{r_b}, \tag{44}$$

where E^*_{min} is the normalized minimum volumetric energy density; p^*, v^*, l^* and h^* are laser power, scan speed, layer thickness and hatch spacing, respectively, expressed in respective dimensionless forms; A' is the surface absorptivity, p is the laser power, v is the scan speed, l is the layer thickness, h is the hatch spacing, r_b is the laser beam radius, ρ is the density, C_p is the specific heat capacity, T_m is the melting temperature, and T_0 is the powder bed temperature.

Using the normalized equivalent energy density, E^*_0, the researchers identified that $1.5 \leqslant E^*_0 \leqslant 4$ would lead to the HEA samples with near-full density (>99.5%), while $E^*_0 < 1.5$ leads to LOF and $E^*_0 > 4$ triggers the keyhole mode of solidification, as shown in **Figure 22**. Such a diagram could contribute to the understanding of the relationship between processing parameters and pore formation, which, in turn, can be utilized for the successful fabrication of AM components with minimum porosity.

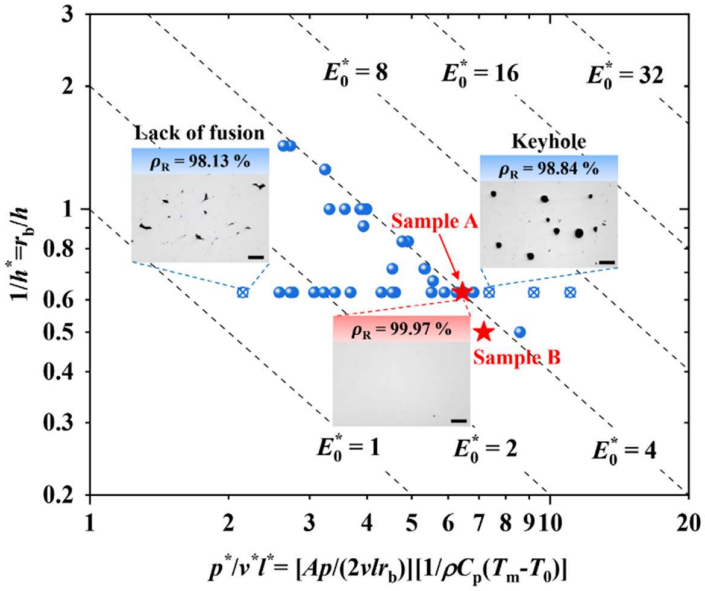

Figure 22. Normalized processing diagram for LPBF of AlCoCrFeNi2.1 [320].

4.4. Cellular structures

A characteristic microstructural feature of many AM alloys is the cellular structure, whose sizes (equivalent diameters) can range from sub-microns to several microns. The size of the cellular structures is closely related to the thermal history and cooling rate. For example, increasing the scanning speed leads to decreasing energy density and thus, smaller cell size [321]. Compared to LPBF, the LDED process is typically associated with higher energy input and therefore,

larger cell sizes [322,323]. In the AlSi10Mg alloy, the cells near the melt pool boundaries are coarser than those in the matrix [324].

The cell boundaries are often decorated with alloying elements – segregated during solidification, nano-sized precipitates, and high density of dislocations (depending on the alloy system) [323,325]. The mechanical behaviour of the AM alloys could be significantly influenced by the cellular structures, if present. Therefore, it is important to understand the origin and different types of cellular structures that have beem reported. In the following, the formation mechanism and typical morphology of the solidification cellular structures, based on the current understanding of the LPBF alloys with the FCC crystal structures, are summarized first [326].

The cellular structures are essentially primary dendrites without secondary arms [301], which are induced by the epitaxial growth during the rapid cooling conditions that prevail during the AM process. Growth of the cellular structures typically initiates at the liquid/solid interface and proceeds along the direction that is parallel to the maximum heat flow [327]. Conduction mode melt pools with large width-to-depth aspect ratio favour dendritic growth that is well-aligned with the build direction (BD). Hence, when observed in a plane perpendicular to BD, cellular structures typically appear to be equiaxed in shape, while a predominantly elongated morphology is observed when the viewing direction is perpendicular to BD, as shown in **Figure 23** (a) and (b), respectively.

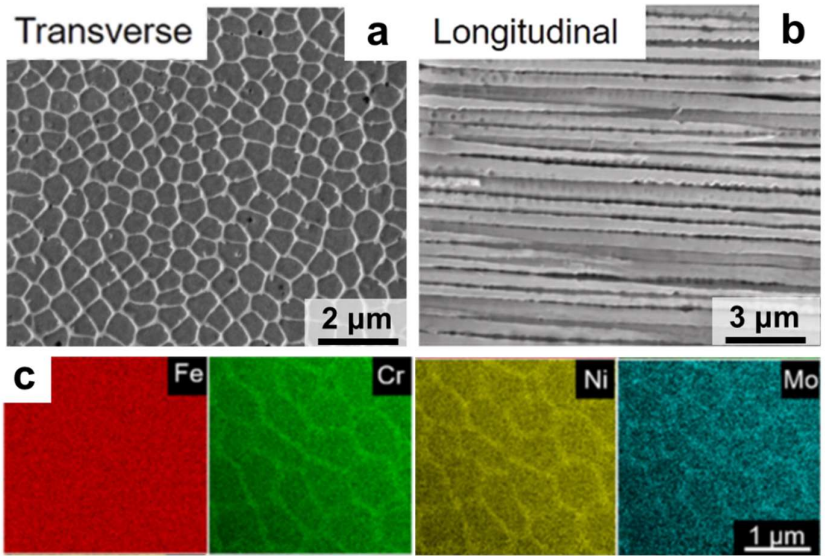

Figure 23. Morphology of cellular structures along (a) transverse and (b) longitudinal directions, showing orientation-relevant morphology [328]. (c) Chemical segregations along the boundaries of cellular structures, observed in LPBF 316L [323].

During the dendritic growth, the solvent ejects the solutes to the solid/liquid interface (for equilibrium partition coefficient, $k < 1$), resulting in chemical segregation at the dendritic interfaces [326]. The differences in the chemical compositions of the dendrite boundaries and their interiors, due to the chemical segregation of the former, provide them the contrast that is often observed during microstructural imaging. Moreover, chemical segregation is closely related to dislocation arrangement/substructures, especially in LPBF fabricated ones [8,323,325,329]. One example of LPBF 316L is shown in **Figure 23** (c), where the chemical segregation to the cell boundaries is illustrated using the energy dispersive spectroscopy (EDS) maps [323]. In the conventionally cast samples, the dendritic microstructures – often undesirable due to the microstructural inhomogeneity they impart, are typically eliminated through suitable thermomechanical processing steps. Since the unique advantage of AM is that it allows for near-net-shaped parts in one processing step, eliminating the cellular structures inherent to some of the AM alloys through the thermomechanical route is not a viable option. Keeping this in view, the cellular structures with all their associated characteristics (such as high density of 'networked' dislocations at their boundaries and segregated elements) are exploited for further modulating the microstructures in some cases, and, in turn, the mechanical performance of the alloy.

The chemical heterogeneity along the cell boundaries can be associated with precipitation, depending on the chemical composition of the materials. For example, fine Si particles are observed along the cell boundaries of AlSi10Mg alloy, since Si's solid solubility in Al at room temperature is nearly-zero [330]. Such phenomenon can be used as a design principle to introduce fine and dispersive precipitates in the AM alloys. For example, a Fe-25Cr-20Ni-Nb-C steel is designed to have various strengthening phases precipitated along the cell boundaries and thus show great promise to be applied under high temperatures [331]. In this alloy, precipitates form *in situ* during the AM process and can also be further modulated by recourse to heat treatment. The typical morphology and EDS maps of the cellular structures in this steel (annealed condition) are shown in **Figure 24** (a) and (b), respectively.

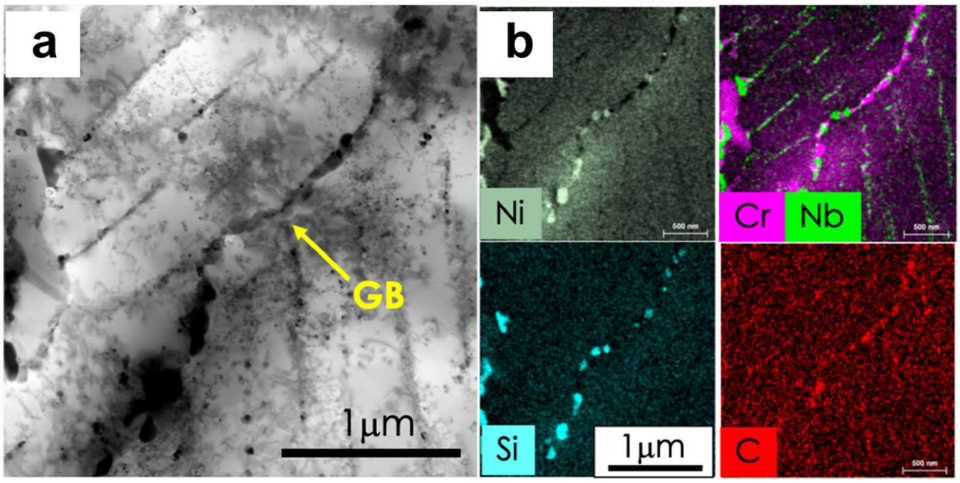

Figure 24 (a) Scanning transmission electron microscopy images and (b) EDS maps on the precipitates along cell boundaries in a LPBF Fe-25Cr-20Ni-Nb-C steel [331].

Recently, the origin of the dislocation substructure was deciphered [325], by investigating 316 L SS in the form of a '1D' rod, '2D' wall, and '3D' block, fabricated using both LPBF and LDED processes. It is revealed that the constraints around the melt pools (mediated by sample design), as well as the fabrication methods (LDED or LPBF), play significant roles in affecting the dislocation density/substructure. In both the LDED and LPBF fabricated samples, increasing constraints (part dimensions) lead to a higher density of dislocations, due to the expansion/shrinkage in a constrained medium. Dendrites (with micro-segregations on the boundaries) exist in all the specimens, but show varying dislocation arrangements. Specifically, dendrites existed without overlapping dislocation structures in LDED fabricated 1D and 2D parts. In the LDED 3D parts, dendrites overlapped with some dislocation cell walls, but many dislocation cell walls with uniform composition existed between the dendrites. In the LPBF parts, dislocation cell structures exhibited the same spacing and orientation as dendrites, and spacing increased with increasing part dimensionality. The schematics and transmission electron microscopy (TEM) images of the samples are shown in **Figure 25** [325]. It is further argued that segregation-induced constitutional stresses, coherency strains due to precipitation networks, and misorientations between dendrites are not the sources of dislocation structures in LPBF 316L.

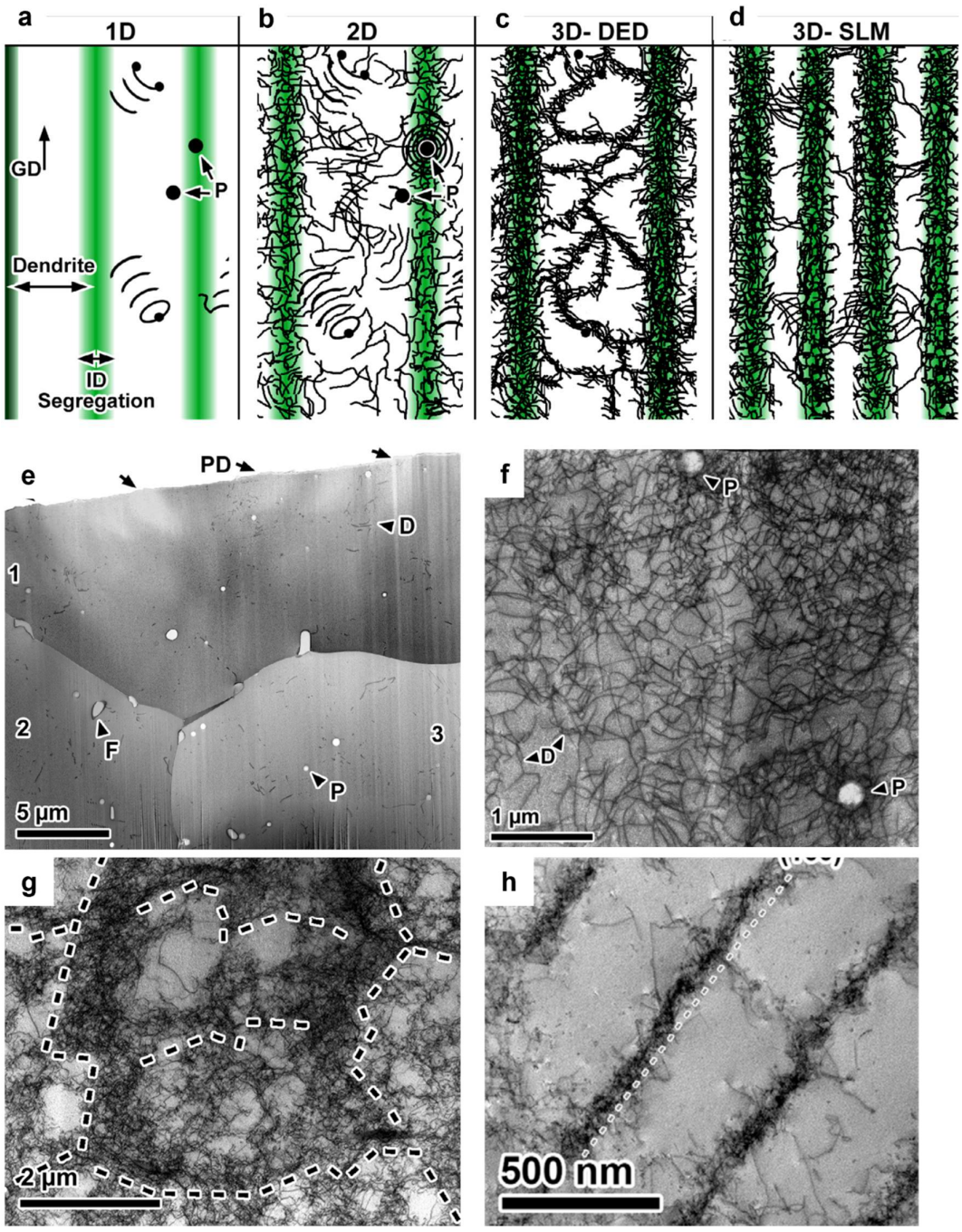

Figure 25. (a-d) Schematics of dislocation structures in 1D-, 2D-, 3D-LDED, and 3D-LPBF samples. (e-h) the corresponding TEM images [325].

The high dislocation density in the AM alloys can significantly enhance their yield strength, which was sometimes rationalized as due to the cell size being the microstructural length scale that determines the yield strength (as the cells are closely related to dislocation substructures/arrangements). However, the cell boundaries in the AM alloys, when present,

cannot be treated as equivalent to HAGBs for causing the Hall-Petch type of yield strength enhancement, as the cell boundaries may only offer resistance to dislocation motion during plastic deformation, but not arrest them altogether (like the HAGBs do). Moreover, as the relationship between cells and dislocations varies in LDED and LPBF, further understanding of the strengthening mechanism is worth studying, especially from the aspects of chemical heterogeneity (dendritic cells) and dislocation arrangement (dislocations networks). It is pointed out in a recent study [323] that the dislocation arrangement/density plays a predominant role in determining the mechanical performance of both LPBF and LDED components. The cell boundaries with only elemental segregation (LDED) have marginal effects on the mechanical behaviour of AM 316L, while dislocation networks (LPBF) are responsible for enhancing the strength and reducing ductility via the reduced work hardening ability. Such difference can be exemplified by **Figure 26** [323]. After 5% pre-straining the LPBF and LDED samples, it is shown that in the LPBF sample, the slip bands are sparse and relatively wavy, whereas sharp and uniform slip bands were observed in LDED sample. Furthermore, slip bands terminating at grain interior is only observed in the LPBF sample. These phenomena suggest that the cell boundaries in the LDED sample are relatively weak obstacles to dislocation motion, allowing them to be easily cut through.

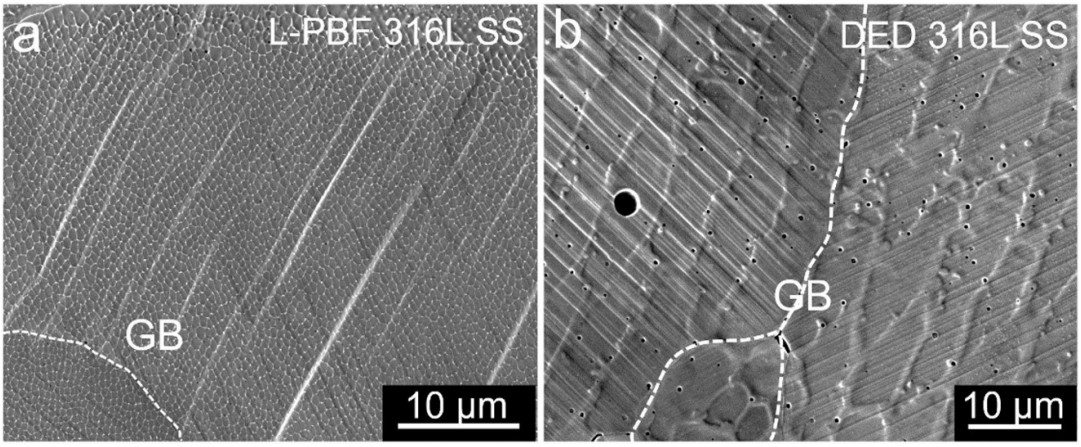

Figure 26 The interactions between cellular structures and dislocations in (a) LPBF and (b) LDED 316L [323].

Due to the high dislocation density, AM samples generally show lower tensile elongation compared to the conventionally fabricated ones. One could consider the AM metals and alloys to be analogous to pre-strained ones, where dislocations multiply and accumulate, leading to higher strength but lower tensile elongation. Interestingly, a recent study has shown that the

dislocation networks in LPBF Ni are similar in size and morphology to those in the pre-strained conventionally manufactured Ni [323]. Such an intrinsically high density of dislocations could lead to challenges during fabrication and post-processing of the AM parts, e.g., residual stress/strain and poor machinability. As AM's unique advantage lies in direct fabrication of complex shapes without the need for complex post thermomechanical process, it would be desired to pursue other critical properties, e.g., fracture toughness, instead of focusing excessively on elongation/ductility.

4.5. Chemical heterogeneity

The AM techniques such as LPBF and LDED often lead to heterogeneous and hierarchical microstructures in the fabricated alloys [4,6,332,333], which are typically accompanied with chemical heterogeneity. Inadequate mixing of powders, size variations between the powder particles, elemental ejection at the solid/liquid interface during the solidification, and differences in the melting temperatures of constituent elements can all induce chemical inhomogeneities [334–336]. Consequently, additional post-fabrication processes or specific processing conditions are often necessary to achieve a 'homogeneous' structure, if homogeneity is expressly desired.

In the case of alloys with good solid solubility and similar melting points, the length scale and degree of segregation of the chemical heterogeneities in the LPBF-manufactured parts depend on the form of powder feedstock used. When pre-alloyed powders are used, chemical segregation occurs due to elemental partitioning at the liquid/solid interface upon solidification, and the resulting heterogeneities are typically confined to the boundaries of the dendrite/cellular structures with limited chemical concentration amplitude (~1–5% [325]). In such cases, the chemical heterogeneities are at the submicron scale and depend on the size and distribution of the cellular structures.

Even when the powders are well mixed and the elements are miscible in each other, macroscale chemical homogeneity can result when the in-situ alloying approach is used for fabricating the parts with a desired final composition, but with mixed powders as the feedstock materials, as chemical segregation can occur between adjacent melt pools. In such cases, the scale of the heterogeneity is often confined to the inter-melt pool level. Under such a scenario, each melt pool is considered homogeneous, and the length scale of chemical heterogeneity is controlled by the melt pool size and the level of overlap between adjacent melt pools. The amplitude of

the chemical segregation is typically limited, with values less than 5% of the mean composition. One example is illustrated in **Figure 27** (a), In an LPBF build using a mixture of 22Cr duplex stainless steel and 6% pure Ni [337], each melt pool captures varying numbers of Ni particles, leading to a duplex microstructure with both FCC and BCC phases, with a mesoscale phase contrast upon solidification.

When the mixed powders are distinct in terms of their physical properties (such as the melting point), chemical heterogeneity occurs due to insufficient chemical mixing/diffusion, even though the powders are physically well-mixed. One example is given in **Figure 27** (b) [338] for the in-situ alloyed Ti-6Al-4V and 4.5 wt.% 316L.The presence of both β and α′ phases within a single melt pool can be seen, due to the chemical heterogeneity. The shapes of these chemical heterogeneities result from the combined effects of various factors that control the melt pool dynamics such as the recoil pressure, Marangoni force, surface tension, melt pool shape, and diffusion. A refractory component in the mixed powders, if present, can lead to the formation of chemical heterogeneities. For example, the un-melted Nb particles, as seen in **Figure 27** (c) of an in situ alloyed Ti-Nb [336], exhibit mesoscale arrangement along the melt pool boundaries with alternating Nb-deficit regions.

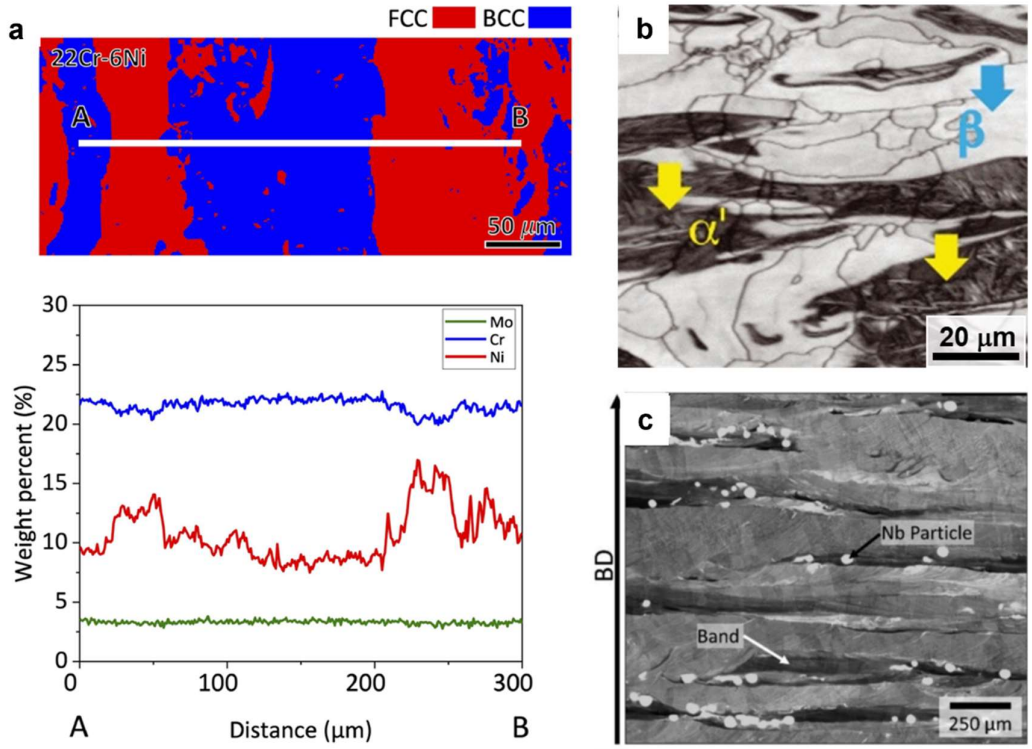

Figure 27. Representative mechanisms of chemical heterogeneity during in situ alloying. (a) Varying minor powders in melt pools [337]. (b) Insufficient chemical mixing/diffusion [338]. (c) Unmelted particles of Nb arranged at the melt pool boundaries as seen in in-situ alloy Ti-Nb printed using LPBF [336].

Recent research has highlighted that the mesoscopic chemical heterogeneities resulting from the LPBF coupons fabricated using mixed powders can have a positive effect on the mechanical properties of the final product. Particullarly, the mesostructure resulting from LPBF 22Cr-6Ni SS mixed with 6% pure Ni exhibits a distinct mesoscale phase distribution, which leads to improved tensile response compared to conventional wrought duplex stainless steel and LPBF 22Cr without any Ni addition [337] as shown in **Figure 28**.

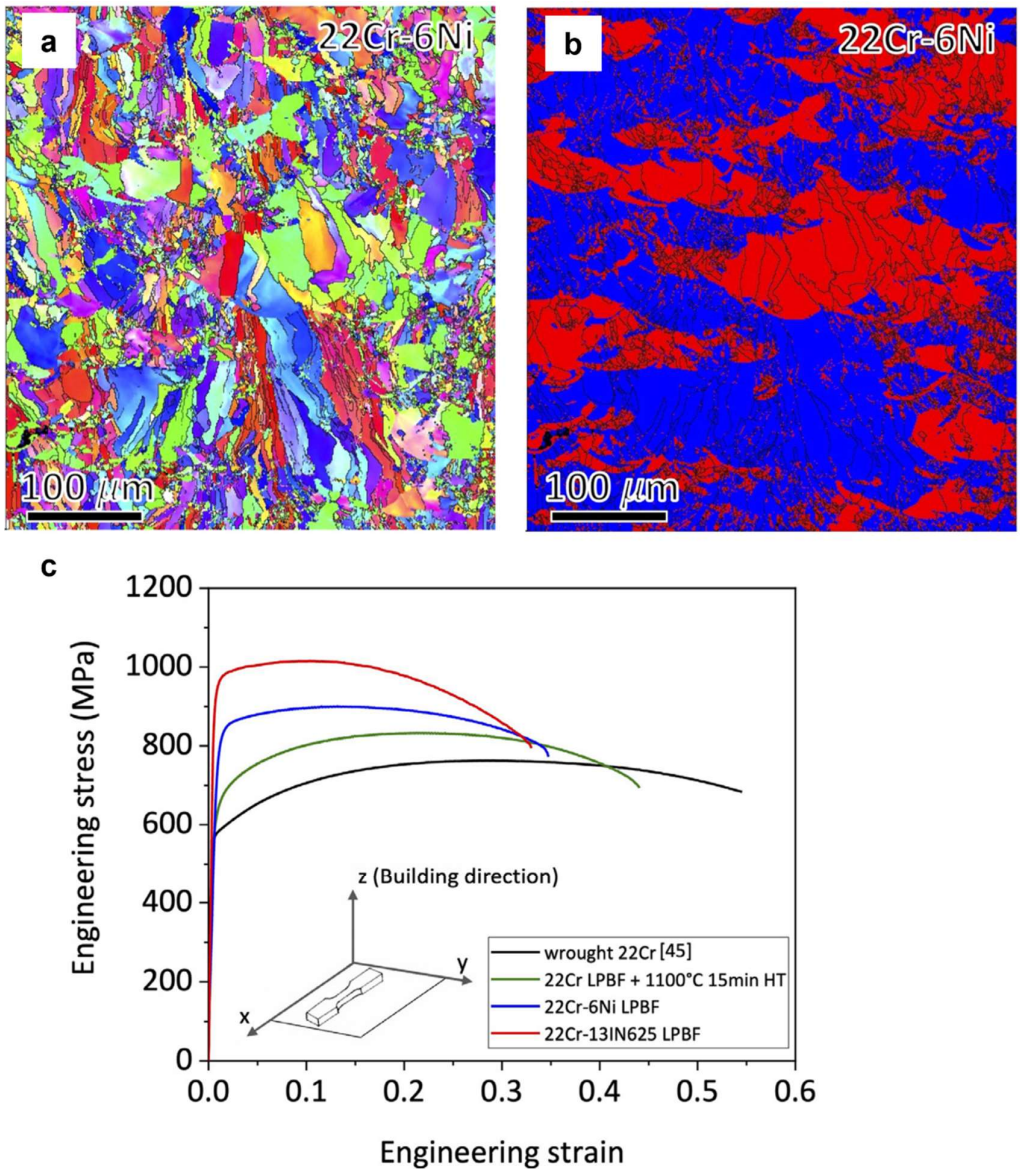

Figure 28. (a) Crystallographic orientation and (b) phase mapping of duplex steel fabricated using mixed 22Cr and 6 wt.% Ni. (c) Tensile properties in varying conditions [337].

The addition of 316L to Ti-6Al-4V also affects the phase variation and meso-/micro-structures of the alloy, with the morphology and proportion of β-phase closely linked to the amount of 316L added to the system [338]. The tensile response of the Ti-6Al-4V alloy is strongly influenced by the 316L addition, with an optimal amount able to enhance both strength and ductility [338] as shown in Figure 29. These findings suggest that mesoscopic chemical heterogeneities resulting from mixed powder prints can be a useful tool for tailoring the mechanical properties of AM alloys.

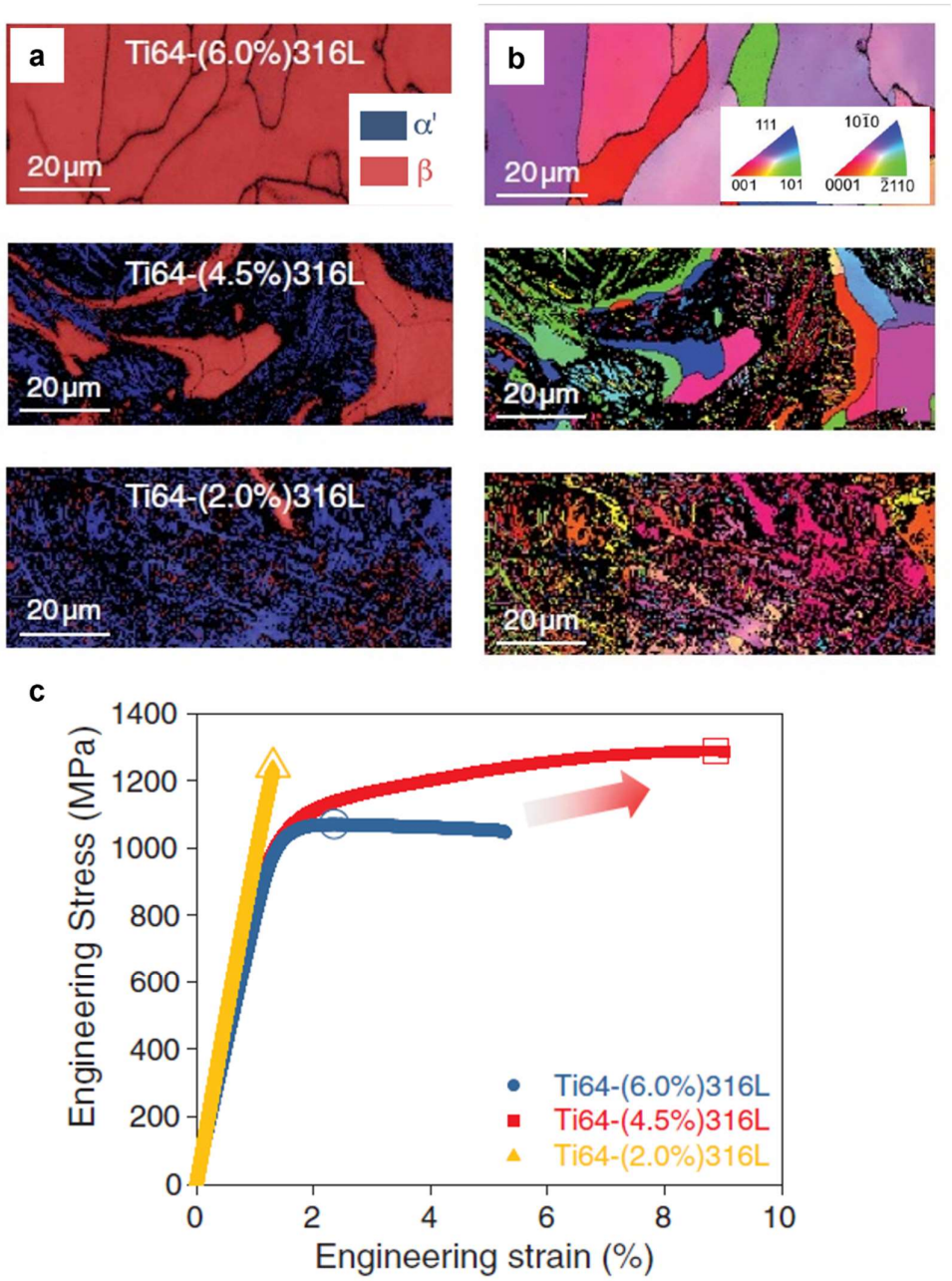

Figure 29. (a) Phase and (b) orientation maps of Ti-6Al-4V+316L alloys. (c) Tensile behaviour of the alloys [338].

When two dissimilar alloys (in terms of their physical properties) are joined together using AM process, a unique 'fish scale' interface phase could occur (depending on the process parameters), which is essentially two materials interpenetrating and forming a staggered/ overlapping (or independent) morphology [339,340]. This phenomenon is the result of collective effects of recoil pressure, Marangoni force, surface tension and melt pool shape, and

is of great significance to understanding the distribution of chemical heterogeneity in the in situ alloyed materials [341].

4.6. Phase transformations during the different stages of fusion-based AM

In many industrial applications, wherein AM is being explored for replacing the CM methods for producing structural components, the desired phase structure in the as-printed alloy is typically an equilibrium phase with similar stability as that in the CM counterparts. For example, a CM 316L component can be replaced with a LPBF 316L one that is topologically optimized, if and only if its microstructure in the as-built condition is fully austenitic that is 'intended' or 'desired'. However, the nature of the solidification during the AM process introduces unavoidable complexities to the nature of phase transformations of the chosen alloy. Hence, the final as-printed microstructure may not always have phase(s) desired, except for pure metals [322]. In the ternary and complex alloy systems, high melting point solute elements are rejected out of the high-velocity solidification front, as discussed in the previous section [342]. In extreme cases of local chemical concentration gradient, the local compositions may be sufficient enough to form non-equilibrium phases [343]. Depending on the cooling rate and alloy composition, the as-printed microstructure could either possess an equilibrium phase (which is realized by sequential evolution due to the slow cooling rate, post fabrication, as observed in EPBF) or retain the metastable phase that results from the high cooling rate (LPBF/LDED process) or a mixture of the two. In this section, we summarize the diverse phase evolution during AM processes such as LPBF, DED and EPBF of some frequently utilized alloy systems. Our purpose is to simplify the rapid reactions that occur during AM into primary and secondary phase transformations. Such categorization is presented to systematically document the variation in the phases observed in the as-printed state, using different processes within the same alloy system. Secondly, the transformation products are categorized as desired and undesired phases, based on the following two criteria: (a) whether the phase is initially intended, as compared to CM counterpart or not, and (b) if the phase improves or deteriorates the mechanical perfoamnce of the alloy.

The schematic displayed in **Figure 30** gives an overview of all the possible phase transformations that could occur during AM. Primary transformation is defined by the formation of the dominant microstructural phase from the liquid melt during solidification. The microstructural phase formed through this reaction governs the properties of the alloy. While the equilibrium phase formed by primary transformation is mostly desirable, any metastable

phase formed may or may not be desirable (depending on a case-to-case basis). Secondary phase transformation is divided into two sub-categories: (i) unavoidable phase formation that accompanies the primary phase formation. Examples for such transformations are oxidation and sublimation, which are predominantly undesired and are covered in the next section. (ii) Transformation of primary phase into secondary phase assisted by the heat built-up that often occurs during the AM process. These transformations are a consequence of reheating, remelting, tempering between individual layer builds or simply cooling, which can be either diffusional or diffusion-less. A complex alloy like the 17-4 PH martensitic stainless steel and Ni based superalloy IN718 may have simultaneous and sequential occurrence of multiple transformations that are mentioned above, based on the type of AM process. In the following section, the primary and secondary phases formed in widely studied alloy systems like stainless steels, IN718, Ti-6Al-4V, and Al alloys are discussed, in terms of desired and undesired phases.

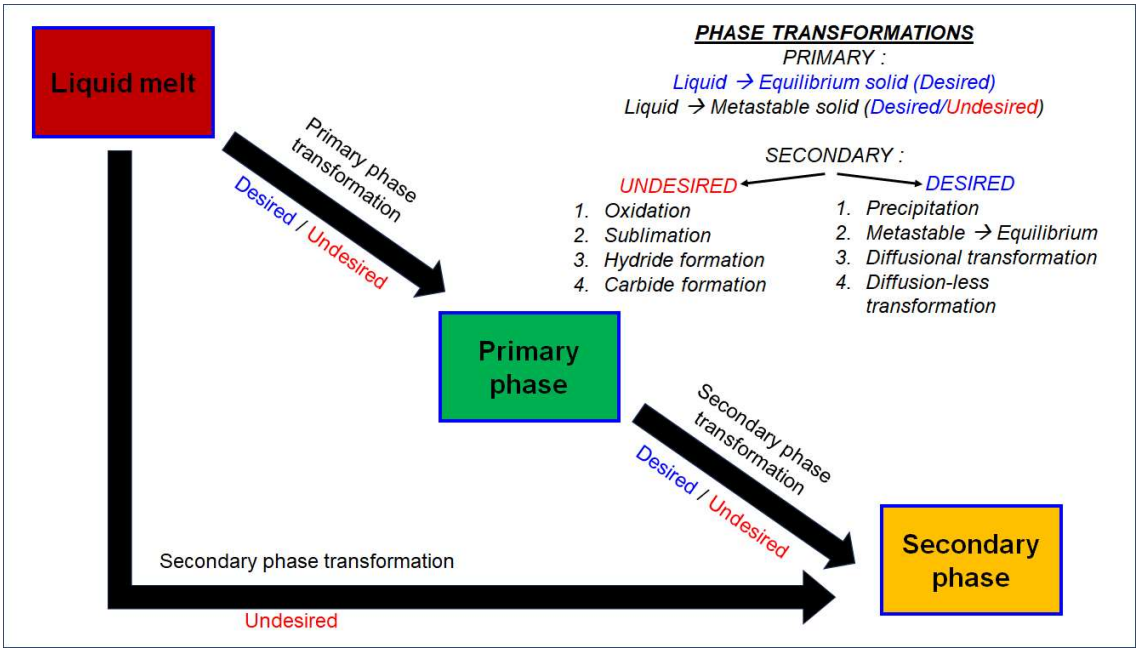

Figure 30. Various phase transformation encountered during additive manufacturing.

4.6.1. 316L austenitic stainless steel

316L is a corrosion-resistant steel with ~17-20 % Cr, 8-12 % Ni additions, and a low carbon content (<0.1%). The higher Ni wt.% (as compared to other SS-like PH grades, low alloy steels, or maraging steels) makes this alloy completely austenitic at room temperature. However, at temperatures above the austenite stability range (500 – 1200 °C), δ-ferrite can nucleate due to the high Cr content in it. Depending on the AM process, the following two microstructural

possibilities can occur in the as-printed format: (i) fully austenitic phase (γ-FCC), which also is the primary phase, and (ii) austenite (γ) + δ-ferrite dual phase alloy. Here, δ-ferrite is the non-equilibrium or metastable phase retained due to high cooling rate. In addition, the alloy may have undesirable secondary phases such as a network of Cr or Mo enriched regions, carbides, and nano-sized oxides.

Most of the published work on LPBF 316L report a single-phase austenitic microstructure [344–347]. Although, the high cooling rate leads to the segregation of Cr and Mo at the sub-grain boundaries, the formation of δ-ferrite appears suppressed in almost all the recent works [44,348,349]. Only a few works report the presence of the secondary ferrite in the as-built specimens [91,344,350]. However, this could be due to other external factors. For instance, the XRD patterns of the raw material powder particle indicate the presence of BCC a ferrite phase in the works by Sun et al. [91] and Choo et al. [350]. Hence, it is possible that the raw material used by them has a higher fraction of Cr, as compared to the rest, reported in the literature. Similarly, a very low fraction of finely sized ferrite was reported by Saedi et al. at cellular boundaries [344]. Representative microstructures with the primary γ and secondary δ phases in the LPBF 316L are shown in **Figure 30**.

In an early LDED work by Yadollahi et al. [351], a δ-ferrite (rich in Cr, Mo, and Si), with a volume fraction of ~ 9%, was reported; it appears to nucleate at the austenite grain boundaries, as shown in **Figure 31** (a1). Solutionizing the alloy at 1150 °C for 2 h removes the δ-ferrite phase and improved the ductility, at a small cost of the strength. On the other hand, Ziętala et al. [352] reported the presence of δ-ferrite stringers at the sub-grain or cellular boundaries of 316L produced using the LDED technique. XRD on the as-built and the feedstock powder confirmed that the ferrite formed during solidification. It is noteworthy that the scan speed and laser power in this work are much higher (approaching the thermal history of LPBF based process), as compared to those used by Yadollahi et al. [351]. This observation indicates a correlation between the thermal history (specifically, the cooling rate), location, size, and fraction of ferrite. In another study, Saboori et al. [353] reported the effect of scan rotation angle between layers on the fraction of δ-ferrite. It was reported that a higher cooling rate (effectively) during the 90° rotation (as opposed to 67°) caused larger undercooling and easier partitioning of Cr, Mn, and Mo elements to form ferrite. However, the location of the ferrite, at the austenitic grain boundaries or cellular boundaries, was not identified. Zheng et al. [354] reported a very low fraction of ferrite (< 1.5%) at the cellular boundaries and triple points in

the LDED 316L with a large laser scan speed. Contrastingly, there are some studies which do not report any δ-ferrite or their influence on the mechanical properties [355]. In an extreme scenario, Li et al. [322] also found no evidence of ferrite when the laser power was varied from 1000 to 1500 W, because Ni (an austenite forming element) was surprisingly segregated along with Cr and Mo, in contrast to the earlier reports. While the mechanism behind this anomalous behaviour is not yet known, it should be noted that the overall laser density and powder feed rate were an order of magnitude higher in the work of Li et al. [322].

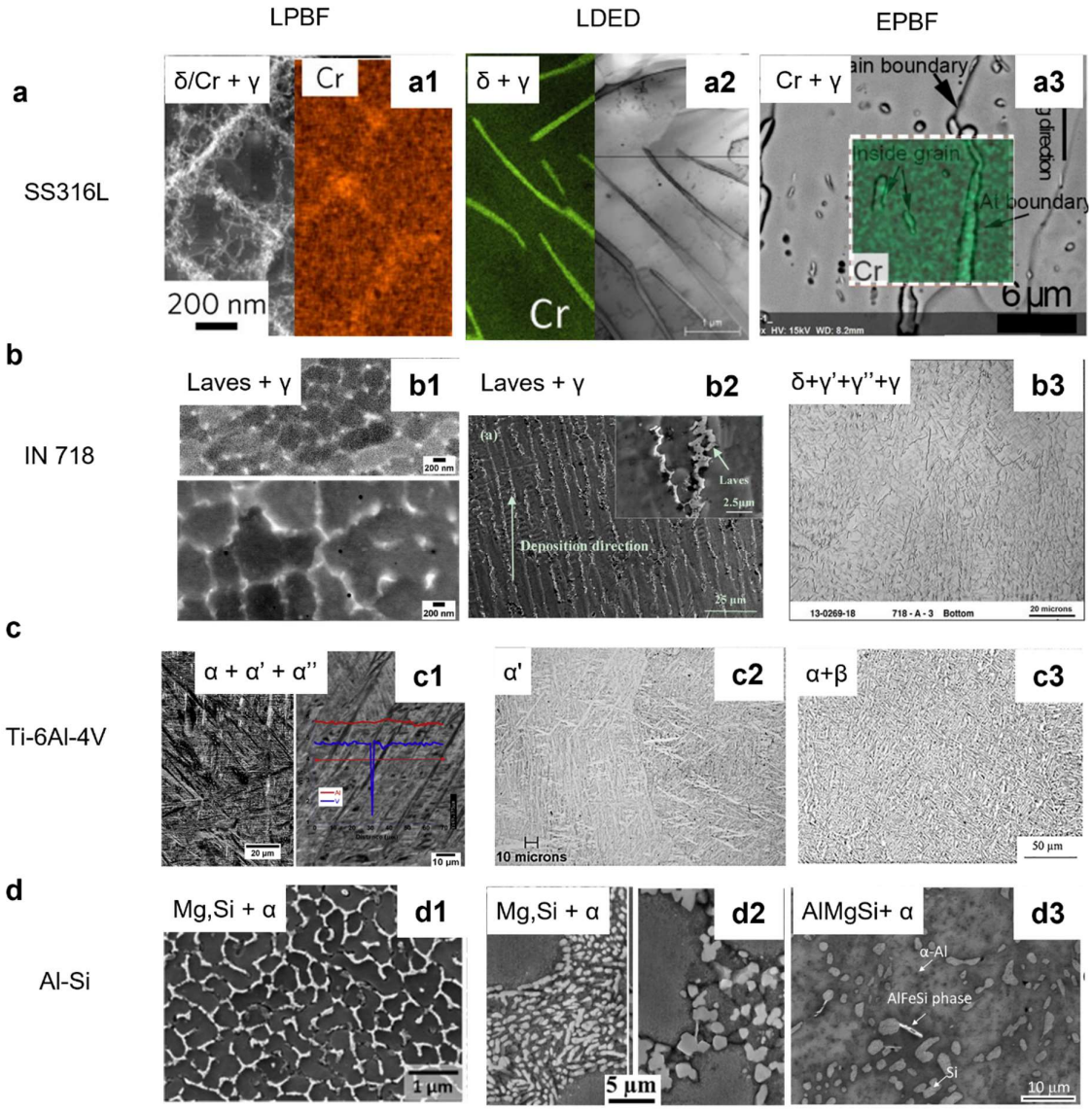

Figure 31. Effect of rapid solidification (cooling rate) on the primary phase formation in as-built alloys. (a) 316L – a1: LPBF [348], a2: LDED [352], a3: EPBF [289] (b) IN718 – b1: LPBF [356], b2: LDED [357], b3: EPBF [358], (c) Ti-6Al-4V – c1: LPBF [359], c2: LDED [360], c3: EPBF [245], and (d) Al-Si – d1: LPBF [361], d2: LDED [362] , d3:EPBF [363].

In the case of 316L manufactured using EPBF, the as-printed microstructure consists of the σ phase that is rich in Cr, and Mo, instead of δ-ferrite, as illustrated in **Figure 31** (a) [289,290,364]. The exposure of alloy to a high substrate temperature (>850 °C) for long periods of > 8-10 h results in the diffusion of Cr and Mo to grain boundaries, followed by transformation to $Cr_{23}C_6$ and subsequently, to the σ phase. However, these phases are classified as secondary phases formed due to the tempering cycles involved during the EPBF process. The variations in the 316L microstructure in different AM processes are illustrated in **Figure 31** (a). When compared to CM 316L, the appearance of δ ferrite in the AM alloys, which may seem like an undesired phase as it reduces the overall volume fraction of γ austenite, can be noted. However, the higher hardness of δ compared to the matrix can lead to higher tensile strength, without compromising ductility. Kumar et al. [10] have shown that in binder jet printed 316L, presence of low fraction of δ phase (~4-5%) at γ grain boundaries hindered the propagation of short fatigue cracks and enhanced high cycle fatigue strength. If such microstructures can be attained using the LPBF or LDED techniques, δ phase may be considered a desired secondary phase from microstructural engineering perspective.

4.6.2. Martensitic stainless steels

The chemical compositions (with high Cr wt.%) in CM steel grades such as 15-5 PH, 17-4 PH, and 18-8 PH lead to fully martensitic (α') microstructures, which results in high strength combined with good corrosion resistance. Following the solutionizing heat treatment and quenching, α' is the desired phase of 17-4 PH steel that forms by diffusion-less transformation from γ, below T_s = 135 °C. This alloy is magnetic and hence, cannot be processed using the EPBF technique, due to the magnetic interference with the source beam. Lastly, this alloy is strengthened by precipitation hardening of Cu nano-clusters, which is enabled by aging heat treatment on a fully α' microstructure in the temperature range of 480 – 670 ºC [12,13]. Fabrication of these steels by LPBF and LDED process leads to heterogenous microstructures i.e., a combination of primary α' phase, along with varying fractions of secondary δ and γ phases. As the contents of the ferrite stabilizing elements, such as Cr, Mo, and Nb, are much higher than in 316L, the volume fraction of metastable δ-ferrite also tends to be much higher in 17-4 PH. In one of the early works, Murr et al. [365] showed the effect of powder precursor phase distribution and fabrication environment on the BCC and FCC phase distributions in the martensitic steels. LPBF 17-4 PH fabricated in an Ar atmosphere resulted in a fully BCC phase microstructure, irrespective of whether the powder was rich in the BCC or FCC phases. On the

other hand, the same powders printed in a N_2 atmosphere resulted in a microstructure with FCC phase being dominant, if the initial powder was dominant in FCC. However, these authors did not ascertain if the BCC phase was α'-martensite or δ-ferrite. Most of the literature concludes that this BCC phase to be α' without sufficient microstructural analysis [365–367], with the hypothesis that the low carbon wt.% inhibits the α' to BCT structure. From the context of the current review, the primary phase observed in these early works was assumed to be the desired α' phase and the secondary phase is γ-FCC.

However, recent work has started to delineate between the two possible BCC phases, through a combination of advanced microscopy and thermodynamics-based calculations. Alnajjar et al. [368] claimed, on the basis of the absence of lath microstructure, that the BCC phase observed was ferrite, and not martensite, in LPBF 17-4 PH. They theorized that the short solidification interval available (due to the high cooling rate) during LPBF causes the alloy to bypass the formation of austenite from ferrite. In the absence of austenite, transformation to martensite is also curtailed at room temperature. This is one of the examples where the primary phase transformation from liquid leads to a fully metastable δ phase, bypassing the formation of desired α' phase. While the δ phase is desired in 316L due to the higher hardness it entails, it is undesirable in 17-4 PH as it restricts the formation of a much stronger α' based microstructure. However, a re-austenitization of 17-4 PH through a heat treatment above the γ-solvus, followed by quenching, leads to the formation of the preferred lath martensitic structure. Thus, contrary to 316L, the primary phase of 17-4 PH is the metastable δ-ferrite phase in both LPBF and LDED processes. Hence, this alloy needs a post-processing heat treatment irrespective of the AM process employed.

Recently, a combination of the α', δ, and γ phases was attained through the modification of Cr_{eq}/Ni_{eq} (which is the empirical value based on all solute atoms in steel that determines the overall phase fraction of austenite and ferrite [369]) by Vunnam et al. [370] during the LPBF of 17-4 PH steel. In another study, Moyle et al. showed that reducing the time between scans of two adjacent hatches can result in a higher fraction of austenite at the grain boundaries in LPBF 17-4 PH [371]. Haines et al. engineered site-specific microstructure by manipulating the cooling rate in regions of interest using a concentric scan strategy from surface to centre [372]. The decrease in cooling rate towards the centre led to the surface regions being δ-rich, while the core is γ-rich. In this context, the primary phases are identified as the undesired δ and desired γ phases in the respective regions. The engineered thermal history is also shown to

induce the precipitation response of Cu nano-clusters and reversed γ-austenite phase in the as-printed alloy, thus making the need for additional aging heat treatment redundant [373]. Such precipitation reactions due to the thermal history of the AM process is an example of the secondary phase transformation. The Cu nano-precipitates and tempered γ films formed on α' lath boundaries are categorized as secondary desired phases.

4.6.3. Inconel 718

Like 17-4 PH, IN718 is heavily alloyed with Cr, Nb, Mo, Ti, and Al, so as to enable precipitation of γ' and γ" precipitates through an aging heat treatment that is typically applied after solutionizing. Despite the large fraction of solute elements in this alloy, which largely remain in solid solution in the as-printed state, the primary solidification phase remains to be γ-FCC structure rich in Ni, Cr, and Fe, irrespective of the cooling rate employed. This is illustrated in **Figure 31** (b) with the primary phase of γ matrix of IN718 fabricated using LPBF (**Figure 31** (b1) [356]), LDED and EPBF. However, there are many possibilities of secondary phases that are rich in solute elements. Trace amounts of the metastable Laves phases rich in Nb and Mo also form, due to the high cooling rate that prevail during solidification [38,313,356,358,374–381] in LPBF and LDED IN718. While the crystal structure of the Laves phase is C14 in both of them, the size, morphology and spacing of the Laves phases can vary, depending on the scan speeds that affect the cooling rates. Since the Laves phase 'consume' Nb, Mo, and Ti solutes, which are required for the strength imparting precipitates, they are undesirable. This non-equilibrium secondary phase can be eliminated by a solutionizing heat treatment, as demonstrated in several research works [343,356,382–387], which is usually followed by long aging treatment in the temperature range 620 to 790 °C for realizing the desired γ' and γ" precipitates. Slow diffusion kinetics of Nb and Mo is the reason for the requirement of a long aging cycle, which is also the reason for them remaining in solution during LPBF and LDED. The slower cooling rate and reheating cycles during EPBF of IN718 leads to the evolution of desired strengthening precipitates γ' and γ" in the as-printed state itself [388]. If the conditions are favorable, it is possible for the concurrent presence of desired (γ', γ") and undesired (δ, TiN, NbC) secondary phases in the as-printed microstructure itself [389]. Kirka et al. [390] showed that EPBF printed 100 mm tall IN718 samples had three distinct regions along the build direction. The topmost region spanning 600 – 750 μm, constituted of the last few layers of the deposit, contains with dendritic sub-grains having γ" precipitates and the interdendritic regions were decorated with Laves phases and carbides. The region below

this, 3.5 mm tall, consisted of cellular subgrains and was devoid of the Laves phases completely. Instead the interdendritic regions were decorated with needle-like δ phases. The remaining build was absent of the sub-grain structures, Laves phases, and had spurious growth of δ phase precipitates. The study confirms that the Laves phases are indeed metastable – a result of greater segregation during EPBF induced solidification process. They get decomposed due to the thermal cycling inherent to the deposition of top layers.

4.6.4. Ti-6Al-4V

The primary phase transformation reaction that occurs during AM of Ti-6Al-4V is liquid to BCC β phase. However, this primary phase is retained only in the EPBF Ti-6Al-4V and the as-built microstructure is dominated by a metastable α' phase that is a consequence of the secondary phase transformation reaction from β below the solvus temperature. **Figure 31** (c) shows a typical acicular α' microstructure, often observed in the LDED and LPBF Ti-6Al-4V. As seen here, the only difference is in the lath morphology – LPBF Ti-6Al-4V has a finer lath size than its LDED counterpart. Even a combination of α' and dual-phase (α+β) microstructure was reported when the process parameters were varied [5,16,17,391–394]. In a very small process window, Xu et al. [394] presented the possibility of obtaining a lamellar ultrafine α+β dual phase microstructure, by realizing in-situ decomposition of α' through an appropriate selection of the layer thickness, laser beam diameter, and energy density combination. This indicates the possibility of two different secondary phase transformations (one each resulting in the formation of either α or α') from the same primary β phase. *Au contraire*, the exposure of the build plates to a temperature above the β solvus (975-995 °C) leads to a dual phase α+β microstructure in EPBF Ti-6Al-4V [395]. In LPBF and LDED, α' can be transformed into a dual-phase equilibrium microstructure through a post-processing heat treatments; such heat treatments can be judiciously utilized to tune the strength, ductility, fracture toughness, and fatigue crack growth resistance combinations [359,396].

Alternatively, remelting or reheating during subsequent laser passes of LPBF/LDED can lead to the decomposition of α' into a α+β microstructure [397,398]. Wang et al. [399] presented the possibility to decompose the metastable phase into equilibrium lamellar phase through remelting in LDED. In a recent work, Hu et al. [400] varied the laser energy density to initiate the simultaneous transformation of β to α, α', and α". Other than the martensitic phases, some work report that the high cooling rate during the LPBF process can also lead to the segregation

of Al along the build height, which leads to the formation undesirable Ti_3Al intermetallic phase [391,401], which can embrittle the alloy.

4.6.5. Al Alloys

The representative segregation behaviour and microstructural variations in LPBF [324,361,402–411], LDED [362,412–416], and EPBF [363] Al-Si based alloys is shown in **Figure 31** (d). For the purpose of this review, only the lean composittion of Al-Si (hypoeutectic composition) is considered. Since the melting point of Si is more than twice that of Al, Si is the first to segregate in liquid. Such eutectic Si rich segregation regions found in Al-Si based alloys fabricated by AM processes are shown in **Figure 31** (d1) [361]. They can be categorized as primary undesired phase, as ideally, Si should be rich in solid solution of Al. This phase transformation is followed by liquid to α-Al solid solution phase, which is also the primary desired phase. For instance, Thijs et al. [417] identified three zones of Si segregated regions based on the Si particle's morphology and size, and correlated them to the heat input. Within each meltpool, both coarse and fine Si particles were observed – coarse at the melt-pool boundary and fine at the melt-pool centre. They are accompanied by coarse and fine cellular grains of the Al matrix. The Si phase within these 2 zones also appear interconnected. The thickness of the segregated region is controlled by heat input received. Also, the thickness of the cellular boundary and the average thickness of the Si-precipates are in the same range. Once solidified, heat input from the subsequent laser scanning creates a HAZ in the solidified Al-Si layer. The fine eutectic Si segregated network break into sub-micron size discrete Si precipitates in the HAZ. Similar microstructure with a size and morphology gradient of segregated Si was later confirmed by Moses et al. [324], which significantly affected the elastic plastic fracture toughness of LPBF AlSi10Mg. Detailed TEM characterization by Wu et al. showed that the individual Si particles within the cellular regions are randomly oriented [418]. While it is ideal for Si to be in solid solution, it is seen that Si nano-dispersion in the Al matrix can improve the mechanical properties of the alloy [330]. Lastly, the secondary transformation during solidification is undesired and unavoidable oxidation reaction as reported by Louvis et al. [419], Kotadia et al. [420], and Thijs et al. [417].

The issue of oxidation can be avoided in the EPBF process. Bian et al. were the first to produce 100% dense Al-Si10Mg alloy using EPBF technique [363]. Sub-micron sized Si particles are observed even in the EBPF Al-Si alloy. Most importantly, the Si particles do not just decorate

the grain or cell boundaries, but rather uniformly distributed in the matrix. Additionally, AlFeSi particles are also observed. The slow cooling kinetics enables the formation of this phase in the EPBF Al-Si system.

4.6.6. High Entropy Alloys

Contrary to the conventional alloy design in which one element constitutes a majority and hence termed as the 'principal element', HEAs or multi-principal element alloys (MPEAs) contain three or more principal elements [421,422]. Often composed of single or multiple solid solution phases and devoid of intermetallics, HEAs exhibit superior properties such as hardness, low- and high-temperature tensile strength and fracture resistance, resistance to wear, corrosion, and oxidation [423]. Due to the obvious advantages HEAs have – one of them being microstructural stability at higher temperatures, their fabrication is being explored through a variety of AM techniques; these have been summarized in a number of reviews [5,424–426]. Unlike the multi-component alloy systems discussed in the earlier sub-sections, the segregation behaviour of the constituent elements in HEAs are far more complex and the efforts to decipher them for annealing conditions are underway – through analytical segregation models [427], combined MC-MD simulations [428,429], and combination of MD with machine learning (ML) [430]. During the conditions of rapid solidification that prevails during AM, however, the segregation behaviour will differ due to the metastable or non-equilibrium state of the phenomena. For instance, Sun et al. [256] reported segregation free grain boundaries and residual-stress induced hot cracking in their FCC-phase LPBF CoCrFeNi HEA despite reports on tendencies of GB segregation of Cr in CoCrFeNi [428] and of Cr and Ni in CoCrFeNiMn [431] HEAs under annealing/ageing conditions. In a later work on LPBF $CoCrFeNiAl_x$ alloy, Sun et al. [261] report interdendritic segregation of Al during solidification and the formation of B2 (NiAl)/BCC (Cr-rich) phases that could absorb the residual strain during solidification. Hence, a reduction in the density of hot cracks was observed with increasing Al content until primarily crack-free samples were obtained for 0.5 molar ratio Al – affiliated to intermittent decoration of GBs with B2/BCC phases. With an increase in the Al content, continuous GB network of B2/BCC phases led to an increase in hot-cracking. In a noteworthy work, Kumar et al. [49] have reported segregation of Ni and Al at the cellular boundaries (or interdendritic regions) during LPBF of $CoCrFeNiAl_{0.5}$ HEA. Here the segregation behaviour could be predicted from their respective equilibrium partition coefficients. They postulated that a supersaturated BCC B2 phase formed during solidification that underwent spinodal

decomposition and resulted in BCC B2 (NiAl) and BCC A2 (Cr-rich) phases. As a result, a honeycomb nano-bridged microstructure is obtained where the B2 phases restrict the dislocation movement and nano twins resulting in superior tensile properties and fracture toughness at ambient and cryogenic temperatures. This illucidates the advantages that rapid solidification driven segregation can have in producing a variety of advanced materials using AM.

4.7. Sublimation/vaporization of the alloying elements and consequences thereof on the solidified microstructure

Vaporization during AM is a secondary phase transformation process and is an unintended consequence of the highly localized energy input from the heat source. The loss of alloying elements, which occurs as a result of it, can alter the composition and consequently, the microstructure of the AM part, markedly. It also could have a direct bearing on the porosity in the printed part. Based on the heat input, processing atmosphere, physical properties of the powders, and the gas circulation system of the AM unit, the detrimental defects could be a relatively high fraction of keyhole and LoF pores, powder denudation, plume, or splatter. However, a major loss could be observed to the material property itself. The vaporization rate of any pure element is determined by the saturated vapour pressure (P_s) of the metal in the melt pool. This, in turn, is influenced by the element's latent heat of vaporisation, boiling point, and the temperature of the melt pool (T_{mp}). Based on the Clapeyron-Clausius equation, Liu and Wen [432] recently estimated the variation of P_s with the melt temperature for different elements that have high vaporization susceptibility, **Figure 32**. It shows that Zn's P_s is ~13 times higher than that of Ti. Consequently, the vaporization of alloying elements is one of the main challenges that needs to be overcome for achieving efficient printability of Zn, Mg, and Al alloys. Next, we discuss in detail, the several challenges and the consequences of vaporization.

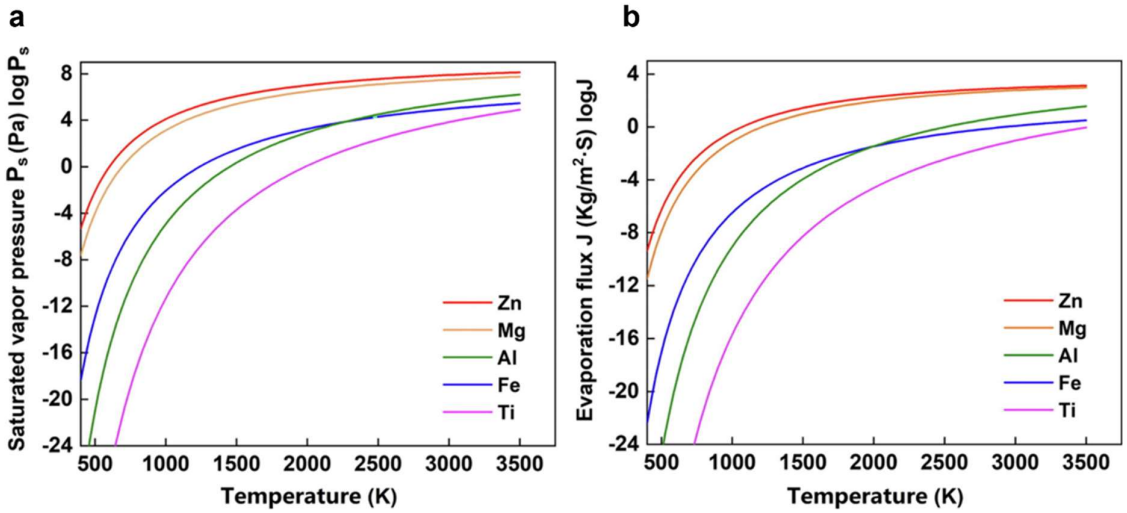

Figure 32. Saturated vapour pressure and vaporization flux of various metals prone to vaporization [432].

Keyhole formation is a key detrimental feature that results from vaporization during AM, which, in turn, leads to several cascading issues in some alloys. During LPBF, keyhole melt pools are known to form when a higher laser power, a lower scan velocity, a smaller laser spot size, or a combination of these three processing parameters are utilized. Due to the localized nature of the input energy, alloying elements with higher P_s are readily vaporized. A cavity is formed when the recoil pressure of the vaporized metal pushes outwards, thus forming a keyhole pore. The inner surface of such keyholes further reflects the incoming laser beam infinitely to cause increased laser absorptivity within the keyhole. This results in a narrow morphology of the pore as shown in **Figure 21**.

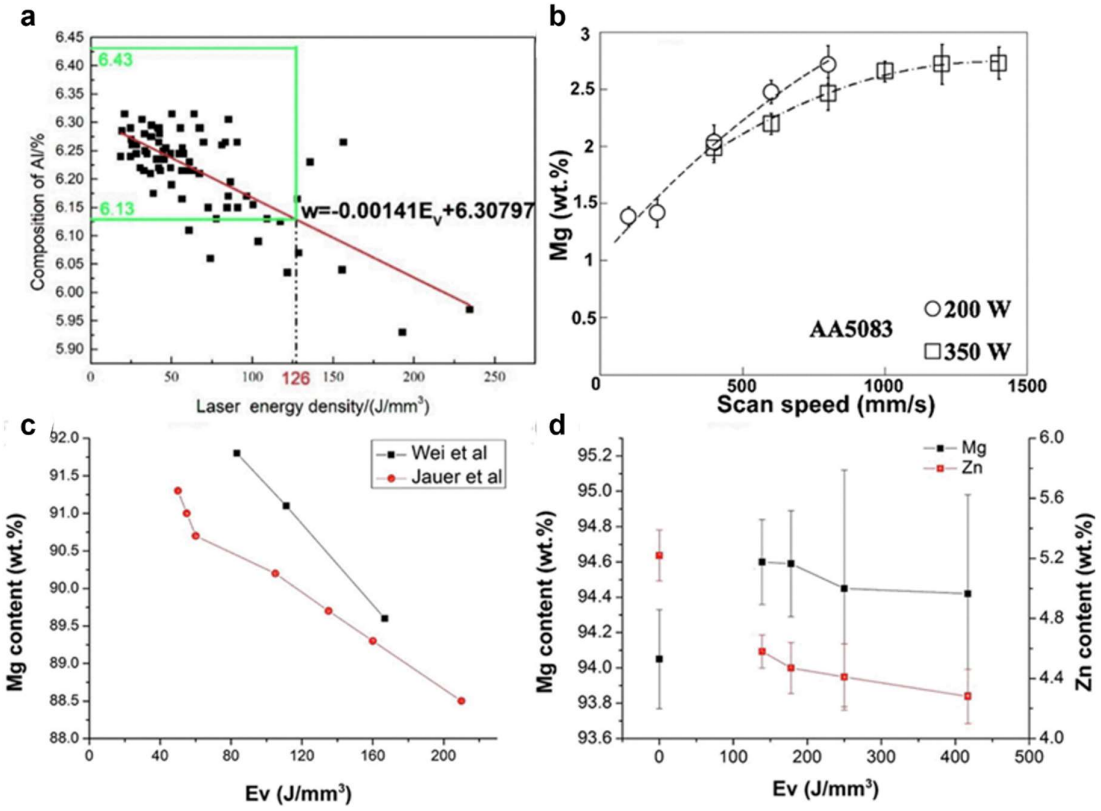

Figure 33. Composition change under different energy inputs during LPBF: (a) Ti6Al4V [433], (b) AA5083 [434], (c) AZ91D [435–438] and (d) ZK60 [435].

Powder denudation is directly affected by vaporization during LPBF. Recent in-situ experimental investigation on 316L and Ti-6Al-4V by Matthews et al. [439] showed that the depletion of powder particles in the vicinity of the melt track arises from a balance between vapour flux and the entrainment of powder particles in a shear flow of gas driven by vapour jet at the melt track. Chen et al. [440] performed simulations of the LPBF process on 316L and observed significant powder escape, when vaporization was assumed, due to the vortex flow around the melt pool. Bidare et al. [441] reported the plume composed of Fe vapour and other metal ions during LPBF 316L. The crucial side effect of the plume is the attenuation of the incoming laser energy, which reduces the overall manufacturing efficiency.

The following five types of spatters are identified by Young et al. [442] with the help of dynamic X-ray imaging:

1. Solid spatter is caused by the ejection of unmelted powder particles that are outside the laser interaction zone by the vapor jet generated from laser-powder interaction.

2. Metallic jet spatter is caused by to the formation of the depression zone (primarily known as a keyhole) where the generation of instense recoil pressure leads to necking of the protruded regions and ejection of metallic spheres.
3. Powder agglomeration spatter is caused by the agglomeration of feedstock powders in the bed with the existing spatter.
4. Entrainment melting spatter is caused by the particles from the bed that get entrained by the flowing ambient gas to the laser beam, get melted, and get ejected due to the vapour jet.
5. Defect induced spatter occurs when the laser interacts with existing defects in the build such as large pores, causing sudden instability that results in spatter.

All the above often lead to compounding defects in a build. In LPBF, where the particle sizes are often in the 15 – 63 μm range ideally suitable for a set combination of laser spot size and layer thickness, coalesced spatters can often exceed this range and generate defects in the powder bed or get entrapped in the melt pool to generate sizeable pores.

The selective vaporization of alloying elements with high P_s can significantly change the chemical composition of the deposited alloy, as compared to that of the feedstock powders. This, in turn, can affect the stability of the resulting microstructural phases and the mechanical performance of the fabricated alloy. Zhang et al. [433] showed significantly lower Al wt.% (vaporization loss of >0.15 wt.%) in LPBF Ti-6Al-4V, when the laser energy input exceeded 126 J/mm^3, (**Figure 33** (a)) Al has a significantly higher vaporization rate than Ti and V. Al being an α-phase stabilizer in the Ti alloys, its loss leads to a higher fraction of β in the final microstructure. In another study focused on the LPBF printability of Ti-48Al-2Nb-2Cr, ~2 at.% reduction in Al was observed resulting in a dramatic decrease in α-hcp and increase in β-bcc phase. Similar changes to the solute content in Al and Mg alloys are shown in **Figure 33** (b), (c), and (d).

Substantial efforts are already made to additively manufacture Al alloys – mainly the Al-Si alloys, particularly AlSi10Mg, in view of their technological importance [420] [443,444]. In the conventional castings of AlSi10Mg, Si and Mg promote strength and ductility through formation of Mg_2Si precipitates post heat-treatment. Moreover, they form the eutectic which has a lower solidification range and is resistant to solidification cracks [443]. However, during the AM processing of this alloy, selective vaporization of Mg occurs due to the large disparity in its evaporation temperature with the other constituent elements [319]. The evaporation of these constituent elements could lead to keyhole porosity, spatters, and impact the alloy

composition. Moreover, as their presence lowers the liquidus and eutectic temperatures [445], their evaporation during AM could also affect the solidification range and make the microstructure prone to cracking. In their recent investigations on the LPBF of three Al-alloys – Zicromal® (Al-Cr-Zr-Mn), Scalmalloy® (Al-Mg-Sc-Mn-Zr) and Scancromal® (Al-Cr-Sc-Zr), Bärtl et al. [446] found out contrasting melt pool solidification behaviour of the first two with Scancromal®. They report that a moderate keyhole-mode of melt pool formed for Zicromal® and Scalmalloy®, as opposed to conduction mode in the LPBF Scancromal®. This can be attributed to the substantial evaporation of Mn (~ 70 %) in the first and Mg (100 %) in the second. They also reported columnar+equiaxed microstructure in the melt pools of the first two alloys and epitaxial grain growth in the Scancromal® samples that let to large columnar grains extending through several layers. However, the authors did not attribute this microstructural evolution to the distinct melt pool modes. Instead, the presence of constituent elements acting as potential heterogeneous nucleation sites was suggested as the main reason. Though it is highly likely, our understanding also suggests that the microstructural evolution can be correlated to the mode of the melt pool (keyhole for columnar+equiaxed and conduction for epitaxially grown columnar grains) which is governed by the extent of evaporation of the constituent elements.

As observed in the preceding subsection, the final chemical composition of an alloy plays an important role in the phase evolution and the as-printed microstructure. Hence, the effects of vaporisation should be closely monitored and eliminated (if possible) to attain desired the microstructure in alloys in which the alloying elements have a highly diverse P_S.

4.8. Part-geometry dependent thermal history and solidification parameter evolution

As already established, the heat flow out of the melt pool drives its solidification. It follows, hence, that the geometry of the part being fabricated can exert a significant effect on the heat transfer, and consequently, will also affect the solidification behavior and the resulting microstructure. This can lead to heterogeneity in the mechanical properties of AM parts with complex geometries and unpredictable responses when in operation. Despite playing such a key role in ensuring (or limiting) the adaptation of AM to industrial applications, the impact of part geometries on the melt pool solidification and its microstructure is still in the nascent stages of exploration, as detailed here.

Pioneering investigations on the impact of part geometry in EPBF Ti-6Al-4V by Antonysamy et al. [285] revealed the strengthening of strong <001> prior-β grain structure with increasing wall-thickness in the bulk of the cross-section. This was attributed to the deterring effect of heterogeneous nucleation from partially melted powder particles present at the periphery, which resulted in fine curved prior-β grains and a weak texture in the thinnest samples. Additionally, they showed that a V-shaped geometry aligned with the build direction can result in the selection and growth of the <001> crystallographic texture. The work on EPBF Ti-6Al-4V by Tan et al. [447] established, through numerical simulations, that higher melt pool temperatures and slower cooling rates existed in thicker samples, resulting in an increase in the β phase spacing (**Figure 34** (a)). A contrasting observation was made by Chakraborty et al. [448] in their recent study on the thin wall samples of LPBF RENÉ 108. They reported smaller primary dendrite arm spacing (PDAS) values for thicker walls – which varied from 0.64 μm in the 0.25 mm thick wall specimen to 0.43 μm in the 5 mm thick wall specimen (**Figure 34** (b)). As the PDAS can be directly correlated to the cooling rate of melt pools, the above observation implies that a faster cooling occurs in the thick wall samples. The reason behind it was the larger cross-sectional area facilitated the conduction heat transfer through the deposited layers and not through the wall/powder interfaces. Additionally, the 5 mm thick-walled samples contain substantial solidification cracks that could be correlated to increased stress triaxiality and cooling rate. Investigations on LPBF Ti-6Al-4V by Zhang et al. [449] highlighted a relative increase in the low-angle grain boundaries (LAGBs) with the wall thickness (all printed using the same process parameters), implying a clear distinction in the solidification parameters. The aforementioned studies, however, miss out on corroborating the differences observed in the microstructural evolution and mechanical response with the melt pool shapes or solidification parameters except for determining cooling rate differences by PDAS [448]. From their investigations on EPBF Ti-6Al-4V, Tan et al. [90] illustrated the effect A, I, and V shapes have on the competitive grain growth and crystallographic texture evolutions by using numerical simulations of a melt pool in 2D and experimental observations (**Figure 34** (c)). They reported that in a V-shaped sample, the <0002> α texture strengthened with build height – signifying the <001> prior β texture, and attributed it to the increase in z-direction thermal gradient with height. They also revealed an inverse behaviour in the A-shaped samples whereas in the I-shaped samples, texture evolution was mostly independent of the build height. In a later work, Chandra et al. [28] varied the prism angle of a custom X-shaped geometry among 60°, 90°, and 120° and found a bell-curve effect on the resulting crystallographic texture and grain width in EPBF 316L (**Figure 34** (d)). With the help of numerical simulations of the electron

beam driven melting/solidification process, they report that for the X-90 samples (90° prism angle) the thermal gradient was more aligned to the build direction, thus resulting in a stronger <001> texture despite having similar cooling conditions to the other shapes. Though observations such as these are new, they are still limited to certain applications – such as the intention to achieve a near-monocrystalline microstructure, and can not be generalized.

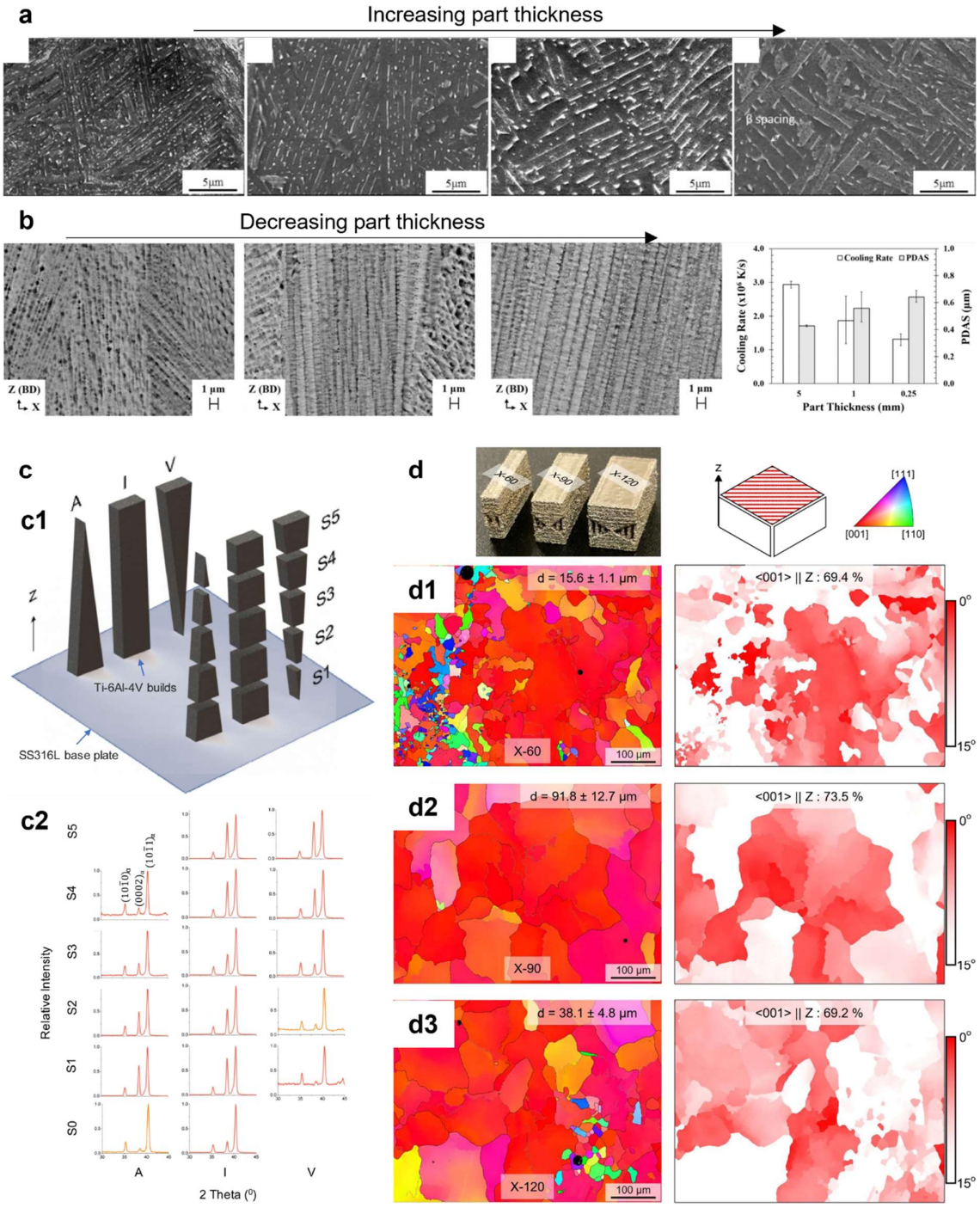

Figure 34 Effect of part-geometry on the as-built microstructure in (a) EPBF Ti-6Al-4V [447] (b) Dendritic substructure in LPBF RENÉ 108 thin walls [448] (c) A, I, and V shapes investigated – c1, and XRD profiles – c2, obtained during EPBF Ti-6Al-4V [90], (d) Impact of X-shaped part geometries on the IPFz maps obtained in X-60 (d1), X-90 (d2), and X-120 (d3) shapes of EPBF 316L samples [28].

Besides variations in the melt solidification parameters with geometry, an inherent issue exists with AM parts where variations in thermal cycling as well as the location of a melt pool along the build direction impact the microstructure [90]. This is due to the accumulation of heat in the fabricated part with an increasing number of reheating/melting cycles with deposition. Hence, in a continuous deposition process, the process parameters need to be adjusted with build height for optimum solidification that would result in the desired microstructure. The impact of these cycles and geometry on the solidification parameters can be ordered as EPBF (least affected) < LPBF < LDED (most affected). Both of the PBF systems have the advantage of surrounding powder bed that ensures heat transfer through a part's side surfaces are often uniform – though minimal, and sustainence of the powder-bed temperature. EPBF has an added benefit of high temperature (500 – 1100 ^{o}C) and high-vacuum build environment. This ensures that the convection heat transfer is minimal as well as the deposited part and surrounding powder-bed are often at a uniform temperature throughout the build. Some EPBF systems also have algorithms in place to ensure flexibility in process parameters such that specified build temperature is maintained during the fabrication process. Recently, Chandra et al. [35] demonstrated this feature in an Arcam A2XX EBM® system and leveraged it to produce parameteric variations by manipulating the powder-bed thermophysical properties for EPBF 316L. Contrary to this, the LDED process is often most affected by geometry and build height variations given the level of exposure a melt pool has to the conduction, convection, and radiative heat transfers. We envision the need to explore analytical framework development to factor in the volume/area of parts in the process parameter development stages. Such as adding a normalization factor to the energy density depending on the part geometry. A first step in this regard can be to develop such frameworks for one system at a time and then improving its general applicability among different PF-AM systems.

4.9. In-situ alloying

In AM, in-situ alloying refers to the use of a mix of more than one type of metal or alloy powders, such that the alloying process is completed during the melting process, typically

through a laser/electron energy source. The powder mixing process can either be ex-situ or in-situ. Ex-situ powder mixing refers to the powder being pre-blended, which requires less engineering effort as the blending system is not restricted by the chamber of the AM system. In the PBF systems, for instance, multi-powder metering systems with optional mixers can be used [334,450–452]. Some systems also include fixtures that allow different powders of different compositions to be deposited in different regions [453,454] or can be modified to for compositional gradation [312,455]. In LDED, powder nozzles that deposit multiple powder types can be used, with the flow rate of each powder type being adjustable to achieve the desired phase and microstructure [35].

The original purpose of in-situ alloying was to improve compositional flexibility and reduce prealloyed powder feedstock procurement lead time and cost [334]. This approach is useful for rapid prototyping of alloy compositions for printing; for instance, Wei et al. printed Fe-Al_x with increasing Al content along the build direction using LPBF [89]. Printing CoCrFeNi with LPBF can result in solidification cracking issues due to the high viscosity of the melt. By blending Al with CoCrFeNi powder to form $Al_{0.5}$CoCrFeNi (molar ratio), interdendritic precipitates form, which induce residual compressive stress in the surrounding material to prevent cracking [261].

Nevertheless, the use of powder mixing in the solidification process leads to consistency issues and can hinder the part certification process. From a fundamental perspective, it also raises questions about what constitutes an optimized process parameter combination. Usually, a process parameter window is identified when the part relative density is greater than 99.5%. With powder mixing, the compositional homogeneity of the part can vary with the process parameters too. The most common guideline is to obtain a highly dense sample without compositional macro-segregation, which can be challenging to achieve. The parameters that result in optimal relative density may not be sufficient for complete homogenization, as additional energy is needed to drive mass transport and maintain a melt pool for a sufficient amount of time to allow for diffusion [456]. While increasing energy density can improve homogenization, high aspect ratio keyholes can often appear causing significant keyhole-induced porosity. In a powder mixture with a large difference in the melting points of the constituents, this phenomenon becomes more pronounced, resulting in a porosity-segregation dilemma [311]. To overcome this, laser remelting can be used [457], but this approach is time-consuming and energy-inefficient. Additionally, remelting near the boundary of a layer can lead to liquid overflow and poor surface finish. High power input combined with a fast scanning

speeds can increase the efficiency of the melting process, but it may also result in the Rayleigh instability [458], thereby inducing lack-of-fusion pores. To prevent this, Huang et al. [311] used a high-power top hat profile with a stripe scanning strategy to stabilize the melt pool. The fast-scanning speed creates multiple single tracks that interact, combine, and form a low aspect ratio melt pool that suppresses pore formation. The differences between such melt pool formations, in contrast to conventional melt pool, are shown in **Figure 35**. Despite the fast-scanning speed, the melt pool remains large and moves slowly, improving both build rate and homogenization.

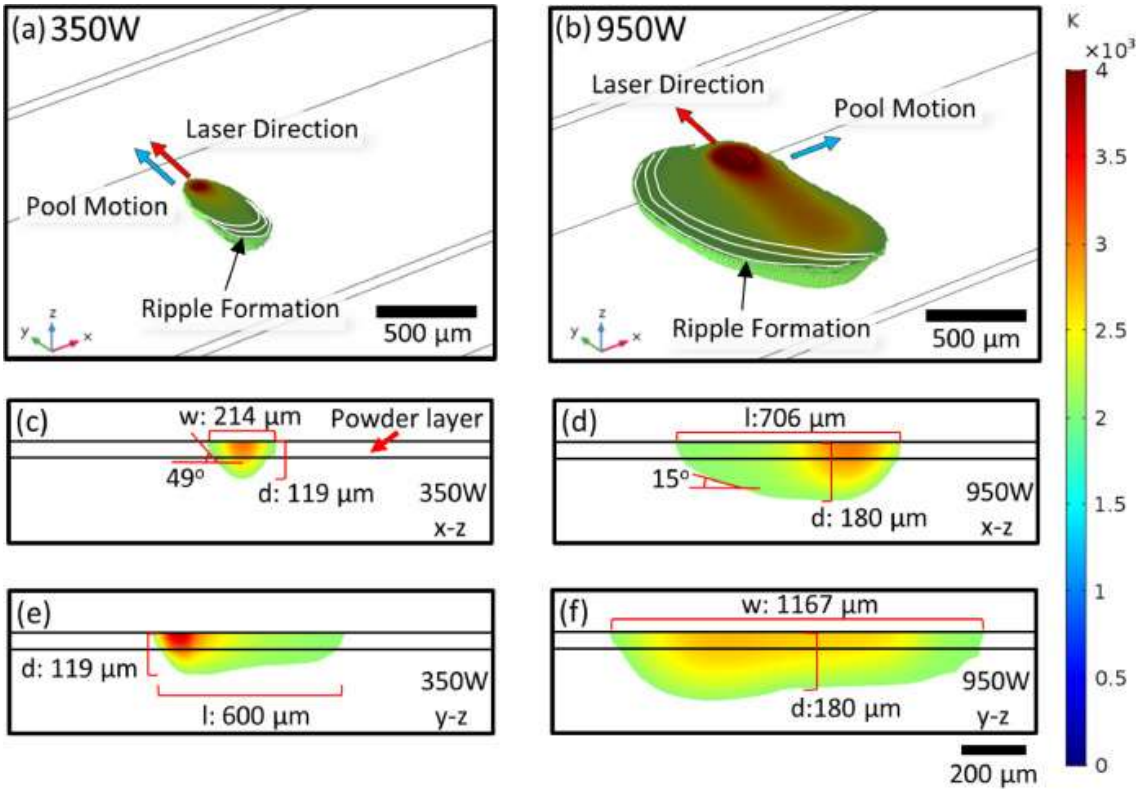

Figure 35 Simulated temperature profile snapshots during laser melting of Ti34Nb, depicting melt pool evolution under different scanning strategies: (a) conventional scanning strategy, (b) high-speed, short-stripe-width scanning strategy with top hat power distribution. Subfigures (c) and (d) illustrate the x-z cross-sections of the simulated profiles perpendicular to the laser scan direction for strategies (a) and (b), respectively. Similarly, subfigures (e) and (f) show cross-sections parallel to the laser scan direction, corresponding to strategies (a) and (b), respectively [311].

Wang et al. conducted a study on the in-situ alloying of Ni-Ti shape memory alloys, which were fabricated using LPBF, EPBF, and LDED [459], to highlighted the performance of each

of them when using blended powder, which undergoes an exothermic reaction during the in sity alloying process. The laser spot diameter of LPBF is in the micron range, around 80 μm, while the laser spot diameter of LDED is in the millimeter range, approximately 2.5 mm. This resulted in a melt pool size in LDED that was 15 times larger than that in LPBF. The limited size of the melt pool in LPBF resulted in fewer powder particles being involved, reducing its ability for homogenization. In comparison, LDED showed the best results for homogenization. On the other hand, EPBF required a high powder bed temperature (450 ^{o}C in this study), leading to powder bed ignition and a highly sintered powder bed. The heat from the exothermic reaction resulted in uneven surface finishes due to a turbulent melt pool. Despite powder bed ignition not happening in LPBF, similarly poor surface finish can be observed.

Due to the complexity of the process, limited simulation studies have focused on the powder of multiple metals/alloys and have been restricted to the LPBF process. Imparting diffusion and determining the intermediate thermomechanical properties of the material is difficult. Liming et al. [460] has demonstrated that the solidification of the multi-alloy melt pool can vary depending on the process parameters . If diffusion is absent, Marangoni convection can drive the mixing of multiple alloys in the stable melt pool, forming a unique fish-scale structure upon solidification. This simulated structure has been observed in many experimental works, but not described in 3D. Furthermore, Tang et al. successfully incorporated diffusion into the simulation of in-situ alloying to provide a more accurate description of the melt pool [461]. Their work showed that melting mixed powder in LPBF can result in localized variations in the melt pool composition across the powder bed.

The utilization of mixed powders provides unique solidification properties and potential applications. One such example is the application of anchorless selective laser melting (ASLM) through eutectic reactions and preheating the powder bed to a high temperature of around 50% of the material's melting point, to relieve residual stress [462,463]. However, pre-alloyed powders can undergo solid-state sintering at this high temperature, leading to powder recoating issues. To address this, the authors used raw powders with a higher melting point than the alloyed product, such as precursor powders of eutectic/hyper/hypo eutectic alloys, to overcome the problem. For instance, the precursor powders of Al12Si [462] and Al339 [463] were able to withstand a preheating temperature of 380°C, resulting in horizontal unsupported overhangs of 10 mm with upward warpage of 1 mm and 0.1 mm for Al12Si and Al339 respectively.

Without the use of mixed powders, the pre-alloyed powder would have agglomerated and caused recoater collision.

Some aluminum alloys (such as those of the 2000, 5000, 6000, and 7000 series) have poor printability due to their larger solidification range, which leads to solidification cracks along columnar grain boundaries [277]. To avoid hot cracking, small equiaxed grains are preferred over the columnar grains produced by LPBF. However, achieving a CET through parameter optimization in LPBF is difficult and sometimes close to impossible when considering part quality. Martin et al. used in-situ alloying to successfully print crack-free Al 7075 and 6061 by inducing heterogeneous nucleation sites to achieve equiaxed fine grains [277]. They used the electrostatic assembly technique of nano-size hydrogen-stabilized zirconium on pre-alloyed Al 7075 and 6061 powders to achieve a homogenous mixture and prevent settling. Zirconium forms the Al_3Zr nucleation phase when melted with aluminum, which acts as nucleation sites. However, producing pre-alloyed wrought aluminum alloys with zirconium through gas atomization is challenging due to the high liquidus temperature of Al_3Zr and its rapid coarsening. This gives a unique proposition to in-situ alloying technique in inducing CET. Al 7075 was also fabricated with the addition of silicon to eliminate hot cracking [464].

A simple model was designed by Li et al. [337] to predict the chemical composition distribution in a LPBF part built with mixed powders. The model uses Poisson's distribution to account for the overlap between melt pools in each layer and from layer to layer. If the melt pool size is highly localized, mesostructuring from compositional heterogeneity can occur even with complete homogenization within a melt pool. The model was verified using experimental data from EDS by using two types of powder mixtures: conventional 22Cr duplex stainless-steel powder + 6 wt.% pure Ni powder, and 22Cr powder + 13 wt.% IN625 alloy powder. The study is significant in that it provides a highly simplified means for compositional mesostructured prediction, without the need to resort to complex computational fluid dynamics modelling.

4.10. Accessory driven in-situ microstructural variation

With the advancement in the understanding of grain growth during AM, several researchers have began to explore in-situ accessories to manipulate the as-built microstructures. Capabilities that have undergone major development in recent years include ultrasonic vibrations (UV) [297,298,465–469], static magnetic fields (SMF) [470–473], in-situ rolling [474–477], laser shock peening [478–480], shot peening [481], and hammer peening [482–

484]. Among the aforementioned techniques, only UV and magnetic fields could affect the solidification behaviour of a melt pool through convection and agitation. The principle involved in the other techniques is to impart plastic deformation to the deposited microstructure, which can alter, potentially, the microstructure of the subsequent layer to an extent. Their effectiveness lays in changing the microstructure of the deformed layer through recrystallization under the impact of thermal cycling. Hence, and keeping in view of the theme (solidification) of this review, we shall only focus in this subsection on the techniques where the microstructure can be manipulated by impacting the solidification behavior during AM.

During the ultrasonic agitation of a melt, melt flow dynamics are improved due to the formation and collapse of cavities from the alternating positive and negative pressures that the ultrasound subjects the molten metal to. In their pioneering work, Cong and Ning [485] employed ultrasonic vibrations during the LDED of 17-4 PH, through a sonotrode attached to the base plate, as illustrated schematically in **Figure 36** (a1). They reported larger melt pool and HAZ dimensions in the UV-assisted samples, with a significant reduction in pores and micro-cracks. The additional UV energy to the melt pool in the form of acoustic power results in an increase in the thermal gradient and imparts instability to the solid-liquid interface, due to cavitation and melt flow, resulting in the fragmentation of dendrite tips. This drives grain nucleation over epitaxial growth and equiaxed grains with average size of 2 μm are obtained in the UV-assisted samples (**Figure 36** (a2)), as opposed to columnar grains (10 μm long) obtained in the benchmark LDED samples (**Figure 36** (a1)). Implementing the same principles, Li et al. [486] obtained highly dense, fine structured AlSi10Mg doped with TiC. They report that a vibration frequency of 969 Hz resulted in a superior microstructure, which surpasses the conventional LDED samples in terms of the mechanical response. While these works demostrated the potential of UV-assited LDED, they were limited to the fabrication of only the thin-walled samples. Todaro et al. [297] first reported UV-induced CET in LDED Ti-6Al-4V blocks. Additionally they showcased implementation of the same setup to produce layered columnar and equiaxed microstructure in LDED IN625 blocks. Interestingly, they obtained much finer equiaxed microstructure for the latter as opposed to the former under the influence of ultrasonic vibrations from the sonotrode operating at a fixed frequency of 20 kHz. In their later work Todaro et al. [298] achieved CET in 316L having an average grain sie of 16 μm. Hence, the UV-induced CET shows dependency on the alloy composition and opens several avenues for the microstructural manipulations for a range of alloy systems using AM. Gorunov [466] implemented variation of UV frequencies (22, 40, 60, 80, and 100 kHz) and the power (30, 65,

and 100 % of 1.5 kW) for every frequency value of the acoustic generators during the UV assisted LDED of Ti-6Al-4V thin walls. Their observations reveal that CET was observed for powers of 65 % and 100 % for all frequency settings. Moreover, by varying the frequency-power combinations, they could control the height of the equiaxed region in the as-built sample, **Figure 36** (b). This shows promise of site-specific UV-driven CET in AM. Aside, Zhang et al. [467] and Gao et al. [468] reported that the use of UV during LDED of the Ni-Ti shape memory alloys suppressed the precipitation of Ti_2Ni [467,468] phase that can otherwise cause embrittlement when in abundance [459]. In a recent advancement in UV-asisted LDED processing, Wang et al. [469] employed a tungsten needle to deliver the vibrations with 20 kHz frequency directly to the melt pool of 1Cr12Ni3MoVN martensitic steel (**Figure 36** (c)). They report CET in their UV-LED samples with a gradual decrease in average grain size with increasing ultrasonic power. Their numerical simulations reveal that the cavitation driven melt agitation results in a marked increase in the melt velocity, solidification rate, and reduction in thermal gradient. If the risk of contamination by the needle in contact with the melt pool can be eliminated or minimized, this technique can be promising in fabricating parts with spatially tailored microstructural variations.

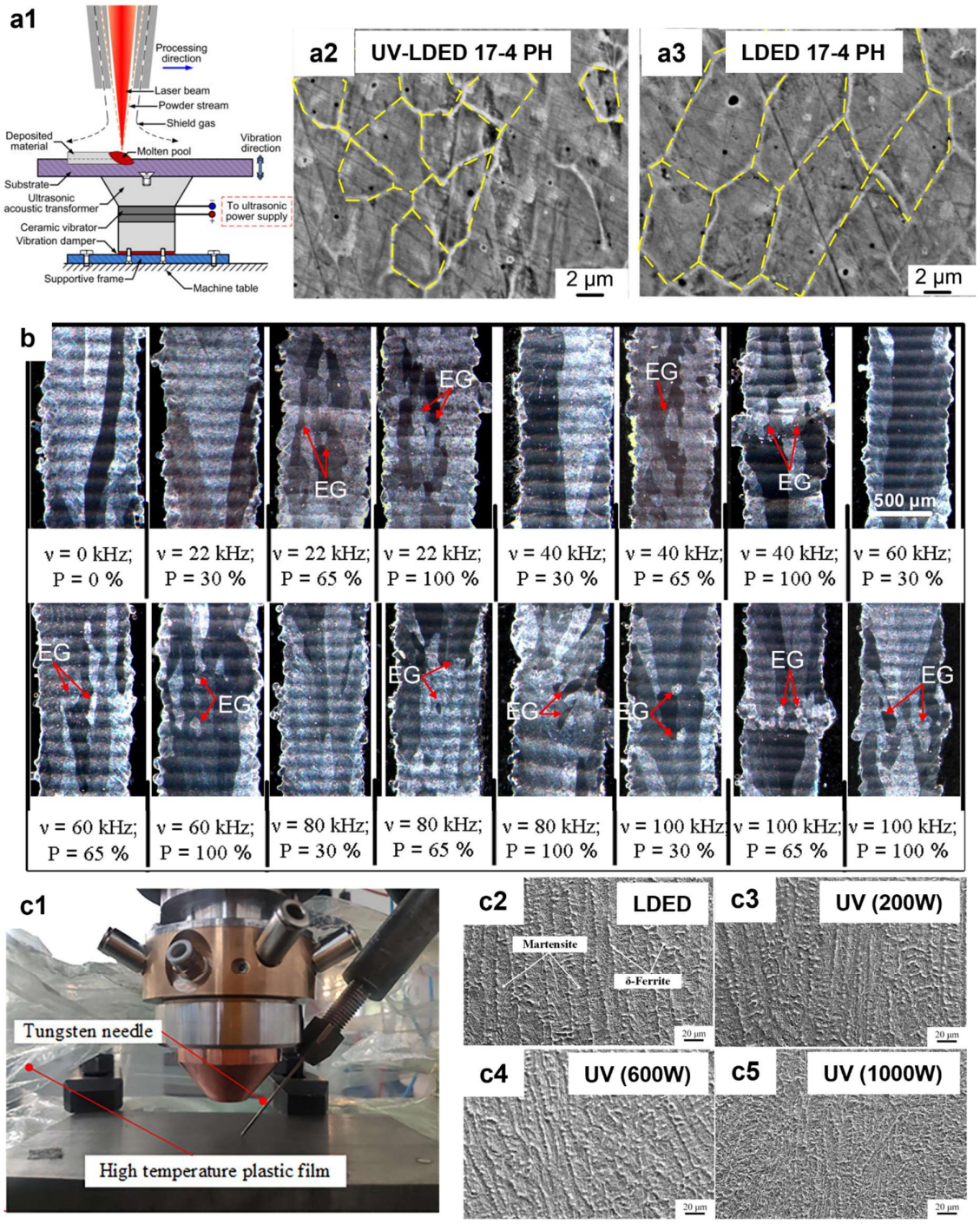

Figure 36 Ultrasonic vibration (UV) assisted AM. (a1) Typical setup compatible with LDED systems. Micrograph of (a1) UV assisted LDED fabricated 17-4 PH steel (a2) LDED fabricated 17-4 PH steel [465]. (b) Effect of UV frequency (ν) and ultrasonic power (P) on the tendency of CET in LDED Ti-6Al-4V samples [466]. (c1) Novel UV setup with a tungsten needle for transferring the vibrations to the melt pool from top. Microstructure of martensitic steel obtain

in (c2) LDED, (c3) LDED+UV (200 W), (c4) LDED+UV (600 W), and (c5) LDED+UV (1000W) [469].

While the applicability of UV is limited to DED, SMF, which is a non-contact technique, was explored in both the LPBF [470,471,473,487] and LDED [472] processes. When a SMF is applied to a melt pool, its effects the flow dynamics in the following two distinct ways.

1. Magneto-hydrodynamic damping (MHD) [471] or electric magnetic damping (EMD) [472] or magnetic damping force (MDF) [473] caused by the movement of the melt pool due to Maragoni convection in the applied external magnetic field.
2. Thermoelectric magnetohydrodynamic (TEMHD) damping [472,487] or thermoelectric magnetic force (TEMF) [473] caused by the thermoelectric currents generated between the solid and liquid regions (mushy zone) due to the difference in phase composition and Seebeck coefficients.

Among the pioneering works on applying SMF to AM, Kang et al. [470] employed permanent magnets at the ends of the build platform resulting in a magnetic flux density (MFD) of 0.2 T during LPBF of commercially pure Ti (CP-Ti). They reported an increase in both UTS and elongation at failure for the SMF-enabled samples and attributed it to a more homogenised microstructure having diffuse crystallographic texture with finer martensitic α'-Ti phase. Similar observations were made by Du et al. [471] during the SMF-enabled LPBF fabrication of AlSi10Mg alloy (**Figure 37** (a) – (c)). With the aid of microstructural observations and numerical simulations at the scale of melt and dendrites, they concluded that both MHD and TEMHD resulted in a reduction in porosity, decrease in inter-dendrite spacing, breaking of the columnar grains that resulted in grain refinement. As a result, they obtained superior tensile properties in the as-built condition in SMF assisted LPBF samples as shown in **Figure 37** (c). Kao et al. [487] developed a multiscale numerical model to investigate the melt pool convection and the resulting microstructural evolution under the non-equilibrium solidification conditions during LPBF of Al10Si alloy under the impact of external magnetic field with varying orientations to the deposition direction. Their results, summarised in **Figure 37** (d1) – (d5), show that in the Case 2, where the MFD vector is towards the -ve y-direction (**Figure 37** (d2)), the TEMHD flow opposes the Marangoni convection. Additionally, they also determined that upon increasing the MFD from 0.1 to 0.5 T, Maragoni convection dominates until 0.4 T, before transitioning smoothly to TEMHD flow at 0.5 T. In case 3, Marangoni convection is

supplemented by the TEMHD flow resulting in wider and shallower melt pools, causing epitaxial grain growth through multiple layers (**Figure 37** (d3)).

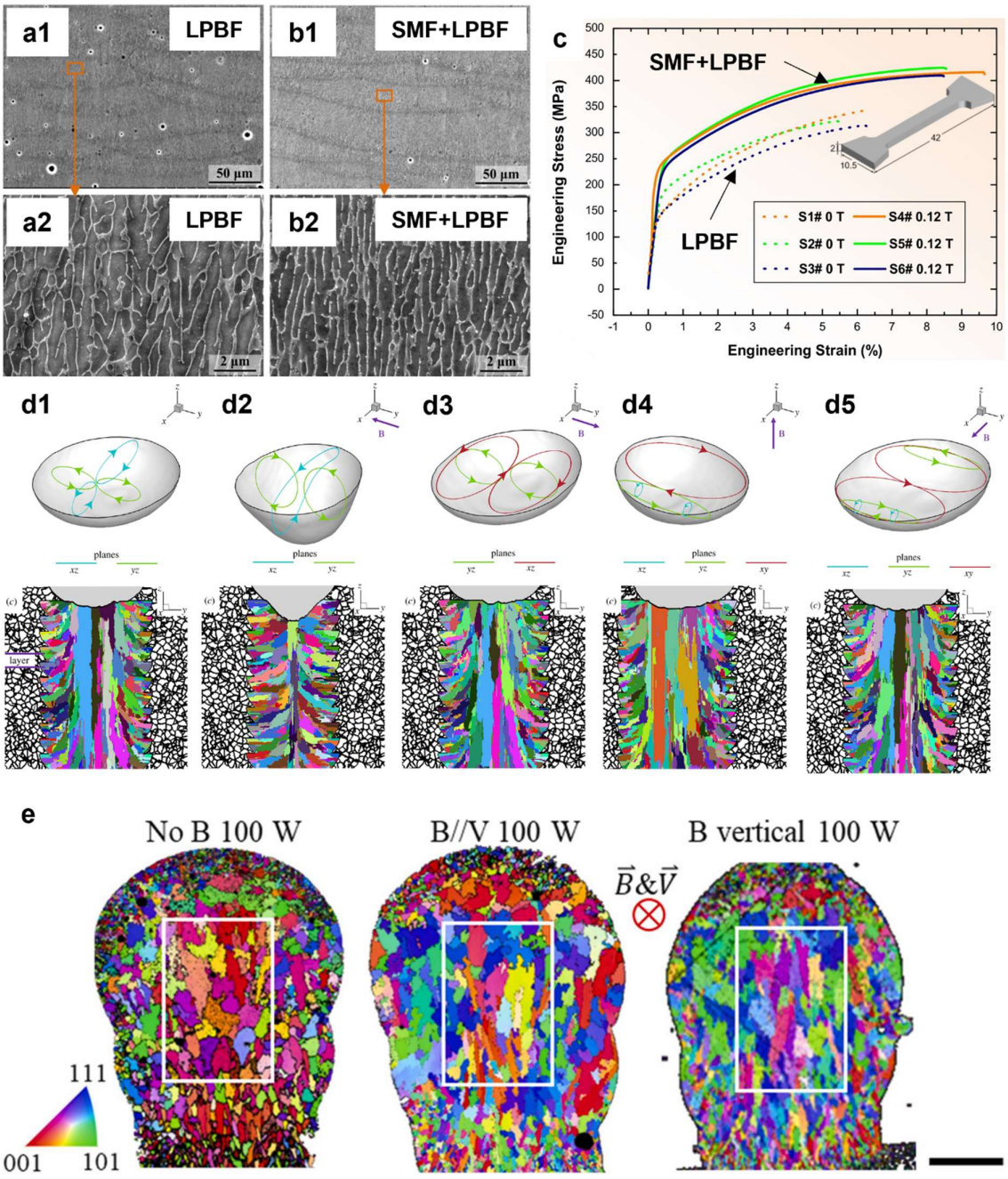

Figure 37: Application of static magnetic field (SMF) to AM. (a) Low and high magnification micrographs of LPBF AlSi10Mg showing pores and coarse dendrites. (b) SMF enabled LPBF microstructure with comparatively less pores and finer dendrites for the same process parameter as (a). (c) Comparative tensile response of LPBF and SMF+LPBF samples of AlSi10Mg [471]. Melt pool flow dynamics and simulated microstrucutral evolution of LPBF

Al10Si alloy – (d1) B = 0 (d2) B || -ve y-direction (d3) B || +ve y-direction (d4) B || +ve z-direction (d5) B || +ve x-direction [487]. (e) Microstructural evolution during LDED of a Ni-based superalloy under the influence of SMF. Scale bar is 250 μm long.

In another investigation of the melt flow dynamics under SMF, Fan et al. [472] performed in-situ synchrotron X-ray imaging of the melt pool during L-DED of Ni-based superalloy single tracks with W-particles as tracers. Their observations reveal the significant role of TEMHD in governing the convection at the bottom and the trailing edge of an LDED melt pool where microstructural evolution occurs. Their observations reveal that the TEMHD flow circulates in the cross-sectional plane when the MFD vector is aligned with the laser scanning direction. As a result, constitutional undercooling at the dendrite tips increases due to the flow of solute from the mush – resulting in increased grain nucleation and growth of the thin columnar grains from the bottom of the melt, as seen in **Figure 37** (e) (Case B//V). When the MFD vector points downward, i.e., opposite to the build direction, TEMHD flow circulates in the horizontal plane. In this case, grain nucleation occurs throughout the height of the trailing melt pool edge from the base. Hence, thinner grains are observed along the height of the deposit, as seen from **Figure 37** (e) (Case B vertical).

Recently, Yu et al. [473] developed a multi-phase numerical model to investigate the melt pool flow dynamics during the LPBF process under the influence of SMF. For their experimental deposition, they placed a permanent magnet below the substrate plate such that the B vector pointed upwards, i.e., along the build direction. In their experiments, the magnitude of MFD was 0.1 T, while the same for numerical simulations varied from 0.1 to 0.5 T. They observed that around the keyhole and the leading edge, Marangoni effect and recoil pressure dominated the flow dynamics. Whereas in the trailing edge, MDF and TEMF were dominant which could cause CET and dendrite deflections.

As evident, research on application of techniques such as UV and SMF to AM, while still nascent, offers considerable promise, especially for tailoring the microstructures of the fabricated alloys. Alhough UV has been applied only to DED thus far, it can be advanced for cladding and repair applications. SMF, on the other hand, requires further exploration for a variety of alloy compositions such that the TEMF primarily responsible for convection near the growth front can be optimised to achieve site-specific microstructural variations. Moreover, further investigations on the impact of SMF in the solid state phase transformations within the

HAZ could be fruitful. Additionally, time-varying electric and magnetic fields are also potential field for research.

5. Opportunities

As summarized in the preceding sections, considerable progress has been made in understanding the solidification process that occurs during AM. Utilization of such an understanding for obtaining the desired microstructures and/or minimize defects was also successfully demonstrated for a number of alloy - AM method combinations. There are opportunities still –both from scientific and technological perspectives—with which the unique solidification pathways in EPBF, LPBF, and LDED AM processes can be further exploited for engineering components with tailored microstructures. These include the ability to achieve metastable microstructures, fine primary dendritic structures, dislocation cells, and columnar growth, which are highlighted in this closing section.

Metastable microstructures: The EPBF, LPBF and LDED AM processes are associated with a fast-cooling rate, which results in alloys that often contain metastable microstructural phases. This characteristic can be utilized, for example, in printing biocompatible low-modulus metastable β titanium to approach the stress shielding problem that is often encountered when a conventional manufacturing route is used. In these alloys, the β BCC phase exhibits a lower Young's modulus compared to the HCP α phase and can be fully retained at room temperature with the addition of sufficient alloying elements [488]. However, these alloying elements are expensive, and excessive amounts will increase the Young's modulus of the β phase, making it imperative to minimize their use while achieving β stabilization. LPBF, due to the rapid cooling intrinisic to it, requires lesser concentrations of the alloying additions, for achieveing the same [311]. This needs to be further explored.

In the context of exploiting the metastable microstructures that occur as a consequence of the rapid solidification, it is worth noting that Li et al. [489] demonstrated that a ductile equiatomic Fe-Co alloy, which exhibits the best soft magnetic properties, in a bulk form can be obtained via LPBF. If the casting route is used for the same alloy, the stable intermetallic phase (with the B2 crystal structure) of Fe-Co, which is highly brittle and hence, renders any post-processing mechanical steps untenable, is obtained. The formation of the B2 phase can be supressed (and a BCC solid solution can be obtained) by adapting rapid quenching methods;

such methods impose a restriction of sub-mm size for the film thickness or powders. In contrast, bulk Fe-Co with BCC structure, which has sufficient ductility can be obtained using LPBF. It can then be machined, as necessary, before being heat treated to a B2 microstructure that is best for the soft-magnetic properties.

Even if metastable microstructural phases are not obtained, alloys with much finer microstructures (as compared the conventionally manufactured ones) can be obtained due to the fast cooling rates associated with AM. For example, in the near-eutectic Al alloys with Si processed using LPBF, a fine microstructure in comparison to the cast counterpart [402,490,491] is obtained as shown in **Figure 38**. Moreover, the solubility limit of Si in Al can be further extended, leading to extensive solid solution strengthening. Coupled with fine microstructure, it led to a substantial enhancement in strength [490]. This signifies an opportunity to explore alloy composition for AM, with supersaturation of the solute element(s) in mind.

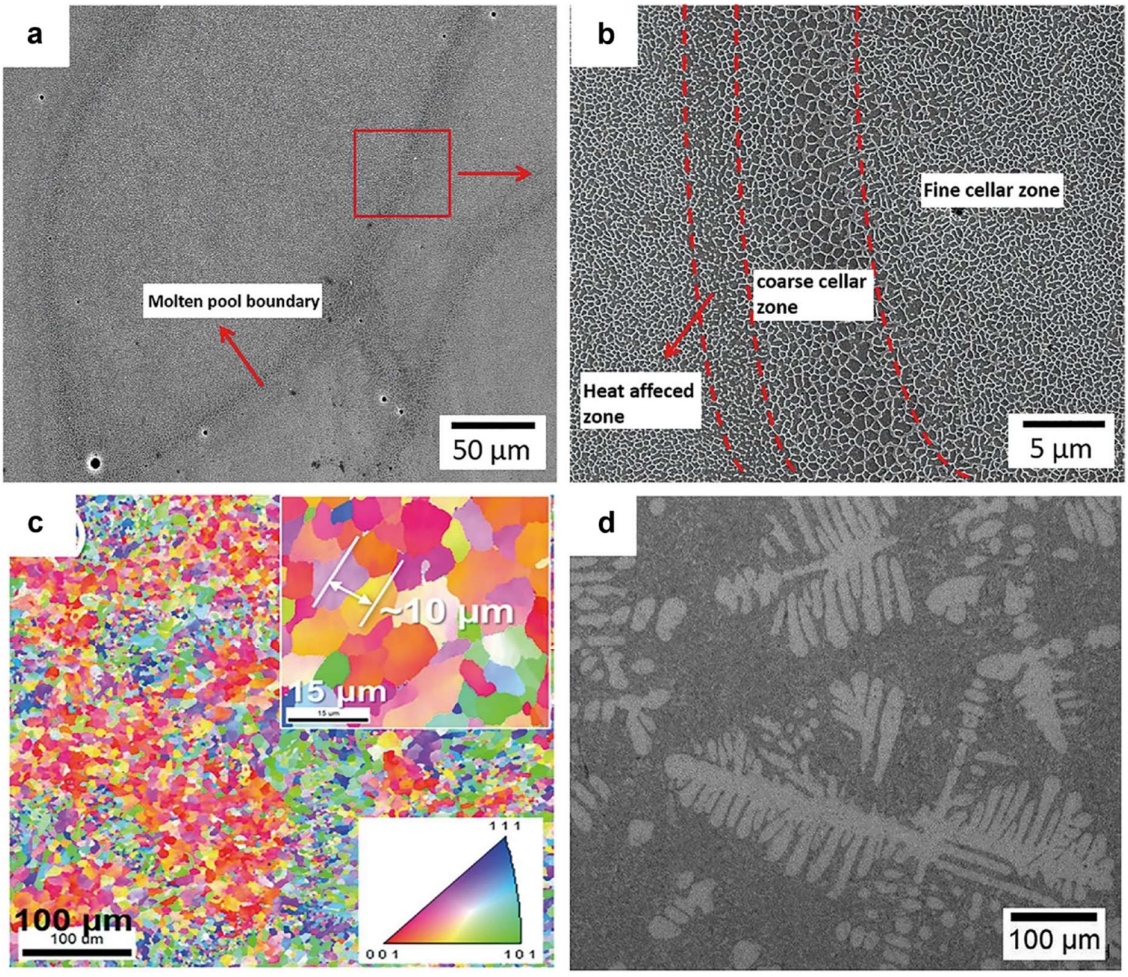

Figure 38. Al-Si alloy microstructure (taken from [490]). (a) Low magnification and (b) High magnification micrographs of fine LPBF as-built microstructure, (c) IPF map [491], and (d) Conventionally cast microstructure [402].

Cellular structures: As already discussed, cellular dendritic structures, with the solute elements segregating to the cell walls, are typical features in many AM alloys. These unique microstructural features, whose size ranges from sub-micron to a maximum of 10 micron scale, span throughout the entire 3D-printed part and provide an unique opportunity in achieving better mechanical properties and functionalities in the AM alloys. For instance, in the LPBF $Al_{0.5}$CrCoFeNi HEA, Kumar et al. [49] obtained a FCC matrix with an interwoven hexagonal net of an ordered B2 phase, as shown in **Figure 39**. The B2's phase formation occurs as a result of Al segregation to the cell boundaries. These phases is 'imperfectly' connected, which results in the formation of nano-bridges of dislocations between them and the matrix phase. This allows for plastic deformation via dislocation motion, and hence, enhances the fracture toughness. Simultaneously, a dense dislocation cell structure that coincides with the cellular dendritic structures provides significant resistance to the dislocation motion, which enhances the strength of the alloy. In Dryepondt et al.'s work, the segregation of solute elements to the solidification cell boundaries was exploited for imparting selective precipitation along them in the as-printed LPBF HK30Nb steel, which was shown to improve the thermal stability of the dislocation cell structure [331]. This is in contrast to that reported by others for LPBF 316L annealed at 800-900 °C [492–494]. Moreover, the high dislocation density in the cell walls led to a significant increase in the HK30Nb steel's strength over the temperature range of 20-900 °C [331]. Dislocation cells are known to provide high strength and high ductility in steels [321,345], and leveraging on precipitates can allow the dislocation structure to be retained after HT procedures. Moreover, the exploitation of cellular structures in LPBF-printed alloys for enhancing corrosion resistance [495–499], hydrogen embrittlement resistance [500], and enhanced condensation heat transfer has also been demonstrated [501].

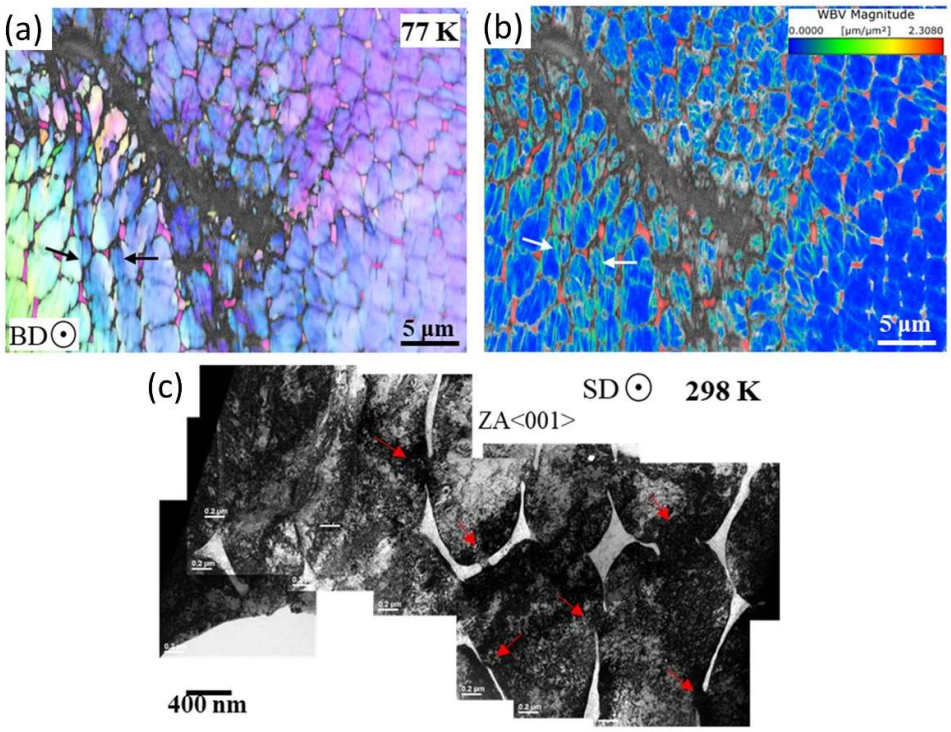

Figure 39 The role of honeycomb cellular structure on the strengthening and toughening of LPBF Al0.5CoCrFeNi [49]. (a) An EBSD IPF map near the crack tip of a compact tension specimen following a fracture toughness test reveals misorientation bands moving through the honeycomb structure (indicated by black arrows), (b) A weighted Burgers vector map from the same region shows that these misorientation bands serve as conduits for dislocation movement, promoting increased plasticity away from the crack tip. (c) TEM analysis in the crack-tip area after the fracture toughness test shows that the B2 phase at cell boundaries restricts dislocation motion, whereas nano-bridges allows the passage of dislocations (indicated by red arrows).

Texturing: AM techniques with directional solidification also provide an opportunity for texturing by leveraging the predominantly epitaxial growth associated with them. For instance, Sun et al. utilized different lasers to achieve either <100> or <110> textures in LPBF 316L to increase twinning-induced plasticity, which provides both high strength and ductility [44]. Huang et al. controlled the strength of <001> crystallographic texture in in-situ alloyed Ti34Nb by controlling the amount of unmelted Nb (unmelted Nb acts as an inoculant) [311]. Meanwhile, Tekumalla et al. managed to produce <100> texture along either the X, Y, or Z axes [502]. Sofinowski et al. achieved three textures with respect to the in-plane direction (perpendicular to the build direction), which can be selected spatially with parameter modulation [503]. This technique is termed “Layer-wise engineering of grain orientation” or

LEGO by the authors, and its spatial texture modulation was demonstrated with a QR code made up of different textures [504] (**Figure 40**).

Texturing is especially useful when the intended application is known. Controlling the texture is beneficial for structural implants made of β titanium alloy, as the <100> direction is the lowest modulus direction desirable for reducing the stress shielding effect [505]. Moreover, since certain crystallographic planes are more corrosion-resistant than others, texturing can be gainfully used for enhancing the corrosion resistance, as a part of surface engineering [506].

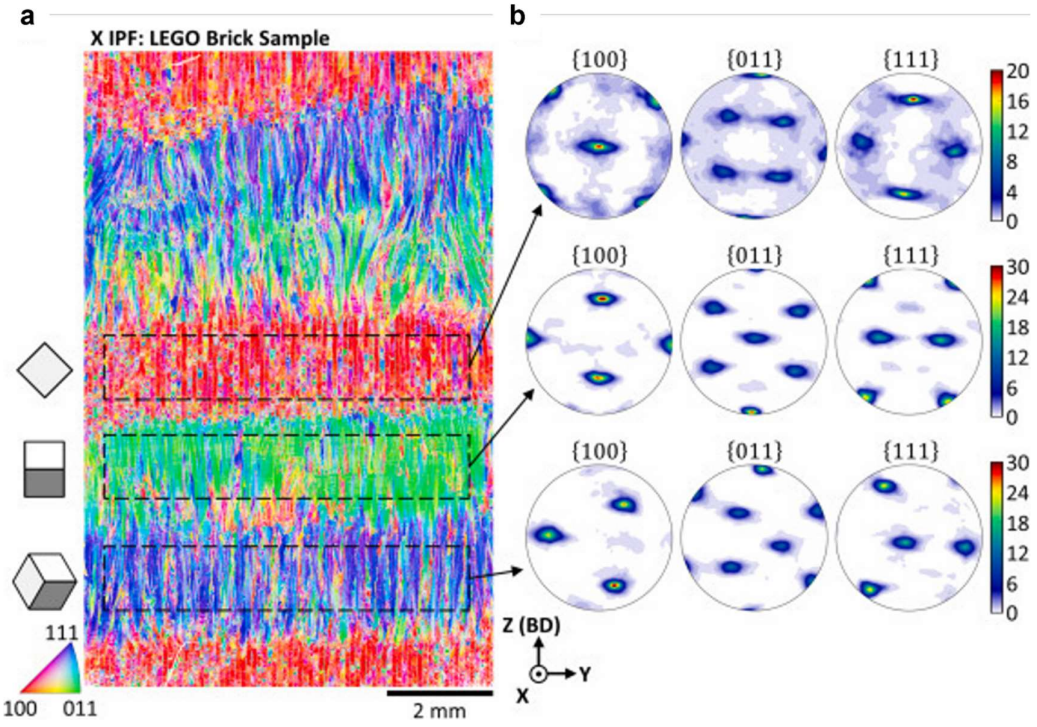

Figure 40. Spatial texture modulation using layer-wise engineering of grain orientation ("LEGO"), with each texture characteristic achieved by using a distinct scan rotation [504].

In closing, we have attempted to summarize the current understanding on the phenomena of rapid solidification that forms the fundamental basis in the three main fusion-based AM technologies: LPBF, LDED, and EPBF, in this review article. A wide variety of micro- and meso-structures can be obtained by selecting appropriate combinations of process parameters and alloy compositions. Those, in turn, can result in unique mechanical performances. For improved spatial resolution and microstructural control, melt pools need to get smaller and, consequently, their solidification more rapid. For a better understanding of the physics involved

in such processes, it is inevitable for the AM research community embrace the non-equilibrium solidification conditions that prevail.

Acknowledgements

The authors acknowledge the financial support from the Agency for Science, Technology and Research (A*STAR) of Singapore via the Structural Metal Alloys Programme (No. A18B1b0061).

References

[1] S. Shao, M.M. Khonsari, S. Guo, W.J. Meng, N. Li, Overview: Additive Manufacturing Enabled Accelerated Design of Ni-based Alloys for Improved Fatigue Life, Addit. Manuf. 29 (2019) 100779. https://doi.org/10.1016/J.ADDMA.2019.100779.

[2] A. Bandyopadhyay, K.D. Traxel, M. Lang, M. Juhasz, N. Eliaz, S. Bose, Alloy design via additive manufacturing: Advantages, challenges, applications and perspectives, Mater. Today. 52 (2022) 207–224. https://doi.org/10.1016/J.MATTOD.2021.11.026.

[3] W.E. Frazier, Metal Additive Manufacturing: A Review, J. Mater. Eng. Perform. 23 (2014) 1917–1928. https://doi.org/10.1007/s11665-014-0958-z.

[4] D. Herzog, V. Seyda, E. Wycisk, C. Emmelmann, Additive manufacturing of metals, Acta Mater. 117 (2016) 371–392. https://doi.org/10.1016/j.actamat.2016.07.019.

[5] S. Gorsse, C. Hutchinson, M. Gouné, R. Banerjee, Additive manufacturing of metals: a brief review of the characteristic microstructures and properties of steels, Ti-6Al-4V and high-entropy alloys, Sci. Technol. Adv. Mater. 18 (2017) 584–610. https://doi.org/10.1080/14686996.2017.1361305.

[6] T. DebRoy, H.L.L. Wei, J.S.S. Zuback, T. Mukherjee, J.W.W. Elmer, J.O.O. Milewski, A.M.M. Beese, A. Wilson-Heid, A. De, W. Zhang, Additive manufacturing of metallic components – Process, structure and properties, Prog. Mater. Sci. 92 (2018) 112–224. https://doi.org/10.1016/j.pmatsci.2017.10.001.

[7] S. Wei, C. Hutchinson, U. Ramamurty, Mesostructure engineering in additive manufacturing of alloys, Scr. Mater. 230 (2023) 115429. https://doi.org/10.1016/J.SCRIPTAMAT.2023.115429.

[8] S.-H. Li, P. Kumar, S. Chandra, U. Ramamurty, Directed energy deposition of metals: processing, microstructures, and mechanical properties, Int. Mater. Rev. 68 (2023) 605–647. https://doi.org/10.1080/09506608.2022.2097411.

[9] M. Ziaee, N.B. Crane, Binder jetting: A review of process, materials, and methods, Addit. Manuf. 28 (2019) 781–801. https://doi.org/10.1016/J.ADDMA.2019.05.031.

[10] P. Kumar, R. Jayaraj, J. Suryawanshi, U.R. Satwik, J. McKinnell, U. Ramamurty, Fatigue strength of additively manufactured 316L austenitic stainless steel, Acta Mater. 199 (2020) 225–239. https://doi.org/10.1016/J.ACTAMAT.2020.08.033.

[11] A. Mostafaei, A.M. Elliott, J.E. Barnes, F. Li, W. Tan, C.L. Cramer, P. Nandwana, M.

Chmielus, Binder jet 3D printing—Process parameters, materials, properties, modeling, and challenges, Prog. Mater. Sci. 119 (2021). https://doi.org/10.1016/j.pmatsci.2020.100707.

[12] J. Radhakrishnan, P. Kumar, S.S. Gan, A. Bryl, J. McKinnell, U. Ramamurty, Microstructure and tensile properties of binder jet printed 17–4 precipitation hardened martensitic stainless steel, Mater. Sci. Eng. A. 860 (2022) 144270. https://doi.org/10.1016/J.MSEA.2022.144270.

[13] J. Radhakrishnan, P. Kumar, S.S. Gan, A. Bryl, J. McKinnell, U. Ramamurty, Fatigue resistance of the binder jet printed 17-4 precipitation hardened martensitic stainless steel, Mater. Sci. Eng. A. 865 (2023) 144451. https://doi.org/10.1016/J.MSEA.2022.144451.

[14] P. Kumar, J. Radhakrishnan, S.S. Gan, A. Bryl, J. McKinnell, U. Ramamurty, Tensile and fatigue properties of the binder jet printed and hot isostatically pressed 316L austenitic stainless steel, Mater. Sci. Eng. A. 868 (2023) 144766. https://doi.org/10.1016/J.MSEA.2023.144766.

[15] E. MacDonald, R. Wicker, Multiprocess 3D printing for increasing component functionality, Science (80-.). 353 (2016). https://doi.org/10.1126/SCIENCE.AAF2093/ASSET/B78C583D-0B9F-44D1-A6AC-B73B34DD79BC/ASSETS/GRAPHIC/353_AAF2093_F7.JPEG.

[16] E. Brandl, F. Palm, V. Michailov, B. Viehweger, C. Leyens, Mechanical properties of additive manufactured titanium (Ti–6Al–4V) blocks deposited by a solid-state laser and wire, Mater. Des. 32 (2011) 4665–4675. https://doi.org/10.1016/J.MATDES.2011.06.062.

[17] B. Baufeld, E. Brandl, O. Van Der Biest, Wire based additive layer manufacturing: Comparison of microstructure and mechanical properties of Ti–6Al–4V components fabricated by laser-beam deposition and shaped metal deposition, J. Mater. Process. Technol. 211 (2011) 1146–1158. https://doi.org/10.1016/J.JMATPROTEC.2011.01.018.

[18] T.M. Butler, C.A. Brice, W.A. Tayon, S.L. Semiatin, A.L. Pilchak, Evolution of Texture from a Single Crystal Ti-6Al-4V Substrate During Electron Beam Directed Energy Deposition, Metall. Mater. Trans. A Phys. Metall. Mater. Sci. 48 (2017) 4441–4446. https://doi.org/10.1007/S11661-017-4219-2/FIGURES/4.

[19] M. Yao, Z. Yao, X. Tao, O. Moliar, Effect of deposition modes on electron beam directed energy deposited inconel 718, Mater. Sci. Technol. (United Kingdom). 36 (2020) 1556–1565. https://doi.org/10.1080/02670836.2020.1802838.

[20] G. Chen, S. Williams, J. Ding, C. Wang, W. Suder, Multi-energy source (MES) configuration for bead shape control in wire-based directed energy deposition (w-DED), J. Mater. Process. Technol. 304 (2022) 117549. https://doi.org/10.1016/J.JMATPROTEC.2022.117549.

[21] M. Yao, Z. Yao, X. Tao, C. Huang, S. Zhang, Alleviating plastic anisotropy of boron modified titanium alloy by constructing layered structure via electron beam directed energy deposition, Addit. Manuf. 50 (2022) 102561. https://doi.org/10.1016/J.ADDMA.2021.102561.

[22] M. Bayat, O. Zinovieva, F. Ferrari, C. Ayas, M. Langelaar, J. Spangenberg, R.

Salajeghe, S. Mohanty, O. Sigmund, J.H. Hattel, Holistic computational design within additive manufacturing through topology optimization combined with multiphysics, multi-scale materials and process modelling, Prog. Mater. Sci. In Press (2023). https://www.sciencedirect.com.remotexs.ntu.edu.sg/science/article/pii/S0079642523000610 (accessed May 1, 2023).

[23] C.L.A. Leung, S. Marussi, R.C. Atwood, M. Towrie, P.J. Withers, P.D. Lee, In situ X-ray imaging of defect and molten pool dynamics in laser additive manufacturing, Nat. Commun. 2018 91. 9 (2018) 1–9. https://doi.org/10.1038/s41467-018-03734-7.

[24] I. Bitharas, N. Parab, C. Zhao, T. Sun, A.D. Rollett, A.J. Moore, The interplay between vapour, liquid, and solid phases in laser powder bed fusion, Nat. Commun. 2022 131. 13 (2022) 1–12. https://doi.org/10.1038/s41467-022-30667-z.

[25] Y. Huang, T.G. Fleming, S.J. Clark, S. Marussi, K. Fezzaa, J. Thiyagalingam, C.L.A. Leung, P.D. Lee, Keyhole fluctuation and pore formation mechanisms during laser powder bed fusion additive manufacturing, Nat. Commun. 2022 131. 13 (2022) 1–11. https://doi.org/10.1038/s41467-022-28694-x.

[26] Z. Wu, G. Tang, S.J. Clark, A. Meshkov, S. Roychowdhury, B. Gould, V. Ostroverkhov, T. Adcock, S.J. Duclos, K. Fezzaa, C. Immer, A.D. Rollett, High frequency beam oscillation keyhole dynamics in laser melting revealed by in-situ x-ray imaging, Commun. Mater. 2023 41. 4 (2023) 1–10. https://doi.org/10.1038/s43246-023-00332-z.

[27] S. Chandra, X. Tan, R.L. Narayan, M. Descoins, D. Mangelinck, S.B. Tor, E. Liu, G. Seet, Nanometer-scale precipitations in a selective electron beam melted nickel-based superalloy, Scr. Mater. 194 (2021) 113661. https://doi.org/10.1016/j.scriptamat.2020.113661.

[28] S. Chandra, X. Tan, P. Kumar, U. Ramamurty, Part geometry-driven crystallographic texture control in a 3D-printed austenitic steel – a strategy for near-monocrystalline microstructure generation, Scr. Mater. 226 (2023) 115255. https://doi.org/10.1016/j.scriptamat.2022.115255.

[29] P. Kontis, E. Chauvet, Z. Peng, J. He, A.K. da Silva, D. Raabe, C. Tassin, J.-J. Blandin, S. Abed, R. Dendievel, B. Gault, G. Martin, Atomic-scale grain boundary engineering to overcome hot-cracking in additively-manufactured superalloys, Acta Mater. 177 (2019) 209–221. https://doi.org/10.1016/j.actamat.2019.07.041.

[30] M. Ramsperger, C. Körner, Selective Electron Beam Melting of the Single Crystalline Nickel-Base Superalloy CMSX-4®: From Columnar Grains to a Single Crystal, in: Superalloys 2016 Proc. 13th Int. Symp. Superalloys, 2016: pp. 981–990.

[31] E. Chauvet, P. Kontis, E.A. Jägle, B. Gault, D. Raabe, C. Tassin, J.-J.J. Blandin, R. Dendievel, B. Vayre, S. Abed, G. Martin, Hot cracking mechanism affecting a non-weldable Ni-based superalloy produced by selective electron beam melting, Acta Mater. 142 (2018) 82–94.

[32] M.R. Gotterbarm, A.M. Rausch, C. Körner, Fabrication of Single Crystals through a μ-Helix Grain Selection Process during Electron Beam Metal Additive Manufacturing, Metals (Basel). 10 (2020) 313. https://doi.org/10.3390/met10030313.

[33] M. Haines, A. Plotkowski, C.L. Frederick, E.J. Schwalbach, S.S. Babu, A sensitivity analysis of the columnar-to-equiaxed transition for Ni-based superalloys in electron

beam additive manufacturing, Comput. Mater. Sci. 155 (2018) 340–349. https://doi.org/10.1016/j.commatsci.2018.08.064.

[34] H.E. Helmer, C. Körner, R.F. Singer, Additive manufacturing of nickel-based superalloy Inconel 718 by selective electron beam melting: Processing window and microstructure, J. Mater. Res. 29 (2014) 1987–1996. https://doi.org/10.1557/JMR.2014.192/FIGURES/13.

[35] S. Chandra, C. Wang, S.B. Tor, U. Ramamurty, X. Tan, Powder-size driven facile microstructure control in powder-fusion metal additive manufacturing processes, Nat. Commun. 2024 151. 15 (2024) 1–14. https://doi.org/10.1038/s41467-024-47257-w.

[36] R.R. Dehoff, M.M. Kirka, W.J. Sames, H. Bilheux, A.S. Tremsin, L.E. Lowe, S.S. Babu, Site specific control of crystallographic grain orientation through electron beam additive manufacturing, Mater. Sci. Technol. 31 (2015) 931–938. https://doi.org/10.1179/1743284714Y.0000000734.

[37] N. Raghavan, R. Dehoff, S. Pannala, S. Simunovic, M. Kirka, J. Turner, N. Carlson, S.S. Babu, Numerical modeling of heat-transfer and the influence of process parameters on tailoring the grain morphology of IN718 in electron beam additive manufacturing, Acta Mater. 112 (2016) 303–314. https://doi.org/10.1016/j.actamat.2016.03.063.

[38] H. Helmer, A. Bauereiß, R.F.F. Singer, C. Körner, Grain structure evolution in Inconel 718 during selective electron beam melting, Mater. Sci. Eng. A. 668 (2016) 180–187. https://doi.org/10.1016/j.msea.2016.05.046.

[39] M.M. Kirka, Y. Lee, D.A. Greeley, A. Okello, M.J. Goin, M.T. Pearce, R.R. Dehoff, Strategy for Texture Management in Metals Additive Manufacturing, JOM. 69 (2017) 523–531. https://doi.org/10.1007/s11837-017-2264-3.

[40] J. Günther, F. Brenne, M. Droste, M. Wendler, O. Volkova, H. Biermann, T. Niendorf, Design of novel materials for additive manufacturing - Isotropic microstructure and high defect tolerance, Sci. Rep. 8 (2018) 1298. https://doi.org/10.1038/s41598-018-19376-0.

[41] T. Lee, H. Bian, K. Aoyagi, H. Ohnishi, T. Hino, Y. Nakatani, A. Chiba, Fabricating 9–12 Cr ferritic/martensitic steels using selective electron beam melting, Mater. Lett. 271 (2020) 127747. https://doi.org/10.1016/j.matlet.2020.127747.

[42] A. Plotkowski, J. Ferguson, B. Stump, W. Halsey, V. Paquit, C. Joslin, S.S.S. Babu, A. Marquez Rossy, M.M.M. Kirka, R.R.R. Dehoff, A stochastic scan strategy for grain structure control in complex geometries using electron beam powder bed fusion, Addit. Manuf. 46 (2021) 102092. https://doi.org/10.1016/j.addma.2021.102092.

[43] M.S. Kenevisi, F. Lin, Selective electron beam melting of high strength Al2024 alloy; microstructural characterization and mechanical properties, J. Alloys Compd. 843 (2020) 155866. https://doi.org/10.1016/j.jallcom.2020.155866.

[44] Z. Sun, X. Tan, S.B. Tor, C.K. Chua, Simultaneously enhanced strength and ductility for 3D-printed stainless steel 316L by selective laser melting, NPG Asia Mater. 10 (2018) 127–136. https://doi.org/10.1038/s41427-018-0018-5.

[45] H. Zhang, H. Zhu, X. Nie, J. Yin, Z. Hu, X. Zeng, Effect of Zirconium addition on crack, microstructure and mechanical behavior of selective laser melted Al-Cu-Mg

alloy, Scr. Mater. 134 (2017) 6–10. https://doi.org/10.1016/J.SCRIPTAMAT.2017.02.036.

[46] Y. He, M. Zhong, N. Jones, J. Beuth, B. Webler, The Columnar-to-Equiaxed Transition in Melt Pools During Laser Powder Bed Fusion of M2 Steel, Metall. Mater. Trans. A. 52 (2021) 4206–4221. https://doi.org/10.1007/s11661-021-06380-9.

[47] H. Ding, Y. Xiao, Z. Bian, Y. Wu, H. Yang, Y. Li, Z. Chen, H. Wang, H. Wang, Effect of in-situ TiB2 particles on microstructure and mechanical properties of Al–Fe–Ni manufactured by selective laser melting, Mater. Sci. Eng. A. 845 (2022) 143065. https://doi.org/10.1016/j.msea.2022.143065.

[48] S. Gao, Z. Li, S. Van Petegem, J. Ge, S. Goel, J.V. Vas, V. Luzin, Z. Hu, H.L. Seet, D.F. Sanchez, H. Van Swygenhoven, H. Gao, M. Seita, Additive manufacturing of alloys with programmable microstructure and properties, Nat. Commun. 2023 141. 14 (2023) 1–11. https://doi.org/10.1038/s41467-023-42326-y.

[49] P. Kumar, S. Huang, D.H. Cook, K. Chen, U. Ramamurty, X. Tan, R.O. Ritchie, A strong fracture-resistant high-entropy alloy with nano-bridged honeycomb microstructure intrinsically toughened by 3D-printing, Nat. Commun. 2024 151. 15 (2024) 1–9. https://doi.org/10.1038/s41467-024-45178-2.

[50] G. Wang, L. Huang, Z. Qin, W. He, L. Tan, F. Liu, Microstructure evolution and columnar to equiaxed transition of oxide dispersion strengthened nickel-based superalloy fabricated by laser metal deposition: From single/multi-track process optimization to bulk sample, J. Alloys Compd. 926 (2022) 166699. https://doi.org/10.1016/j.jallcom.2022.166699.

[51] H. Lv, X. Li, Z. Li, W. Wang, K. Yang, F. Li, H. Xie, Investigation on the columnar-to-equiaxed transition during laser cladding of IN718 alloy, J. Manuf. Process. 67 (2021) 63–76. https://doi.org/10.1016/j.jmapro.2021.04.016.

[52] H. Li, Y. Huang, S. Jiang, Y. Lu, X. Gao, X. Lu, Z. Ning, J. Sun, Columnar to equiaxed transition in additively manufactured CoCrFeMnNi high entropy alloy, Mater. Des. 197 (2021) 109262. https://doi.org/10.1016/J.MATDES.2020.109262.

[53] S. Guan, K. Solberg, D. Wan, F. Berto, T. Welo, T.M. Yue, K.C. Chan, Formation of fully equiaxed grain microstructure in additively manufactured AlCoCrFeNiTi0.5 high entropy alloy, Mater. Des. 184 (2019) 108202. https://doi.org/10.1016/j.matdes.2019.108202.

[54] M.C. Deng, S. Sui, B. Yao, L. Ma, X. Lin, J. Chen, Microstructure and room-temperature tensile property of Ti-5.7Al-4.0Sn-3.5Zr-0.4Mo-0.4Si-0.4Nb-1.0Ta-0.05C with near equiaxed β grain fabricated by laser directed energy deposition technique, J. Mater. Sci. Technol. 101 (2022) 308–320. https://doi.org/10.1016/j.jmst.2021.03.012.

[55] Q.Z. Wang, N. Kang, X. Lin, M. EL Mansori, W.D. Huang, High strength Al-Cu-Mg based alloy with synchronous improved tensile properties and hot-cracking resistance suitable for laser powder bed fusion, J. Mater. Sci. Technol. 141 (2023) 155–170. https://doi.org/10.1016/J.JMST.2022.09.027.

[56] W. Kurz, D.J. Fisher, M. Rappaz, Fundamentals of Solidification 5th Edition, Trans Tech Publications Ltd, 2023. https://doi.org/10.4028/B-V7B35Q.

[57] M.S.. Hashmi, ed., Comprehensive Materials Processing, `, 2014.

[58] P. Zhang, W. Han, Z. Huang, al -, W. Yang, X. Wang, H. Zhou, D. Yang, Y. Yin, X. Kan, Y. Zhao, Z. Zhao, J. Sun, The mechanism of substructure formation and grain growth 316L stainless steel by selective laser melting, Mater. Res. Express. 8 (2021) 096510. https://doi.org/10.1088/2053-1591/AC21EA.

[59] D.H. StJohn, A. Prasad, M.A. Easton, M. Qian, The Contribution of Constitutional Supercooling to Nucleation and Grain Formation, Metall. Mater. Trans. A Phys. Metall. Mater. Sci. 46 (2015) 4868–4885. https://doi.org/10.1007/S11661-015-2960-Y/TABLES/2.

[60] X.Y. Bu, X. Xu, H.F. Lu, J. Cai, W.W. Deng, F. Xing, K.Y. Luo, J.Z. Lu, Extreme high-speed-rate laser directed energy deposition of high strength low carbon stainless steel coating with layered heterogeneous structure, Mater. Sci. Eng. A. 859 (2022) 144203. https://doi.org/10.1016/J.MSEA.2022.144203.

[61] A. Prasad, L. Yuan, P. Lee, M. Patel, D. Qiu, M. Easton, D. StJohn, Towards understanding grain nucleation under Additive Manufacturing solidification conditions, Acta Mater. 195 (2020) 392–403. https://doi.org/10.1016/j.actamat.2020.05.012.

[62] H. Dong, H. Dai, Single-Crystal Casting/Directional Solidification, Compr. Mater. Process. Thirteen Vol. Set. 5 (2014) 89–108. https://doi.org/10.1016/B978-0-08-096532-1.00508-2.

[63] R. Hashimoto, Y. Shibuta, T. Suzuki, Estimation of Solid-liquid Interfacial Energy from Gibbs-Thomson Effect: A Molecular Dynamics Study, ISIJ Int. 51 (2011) 1664–1667. https://doi.org/10.2355/ISIJINTERNATIONAL.51.1664.

[64] W. Kurz, D.J. Fisher, Dendrite growth at the limit of stability: tip radius and spacing, Acta Metall. 29 (1981) 11–20. https://doi.org/10.1016/0001-6160(81)90082-1.

[65] W.W. MULLINS, R.F. SEKERKA, Stability of a Planar Interface During Solidification of a Dilute Binary Alloy, Dyn. Curved Front. (1964) 345–352. https://doi.org/10.1016/B978-0-08-092523-3.50037-X.

[66] Y. Liu, Z. Long, H. Wang, Y. Du, B. Huang, A predictive equation for solute diffusivity in liquid metals, Scr. Mater. 55 (2006) 367–370. https://doi.org/10.1016/J.SCRIPTAMAT.2006.04.019.

[67] H.H. König, N.H. Pettersson, A. Durga, S. Van Petegem, D. Grolimund, A.C. Chuang, Q. Guo, L. Chen, C. Oikonomou, F. Zhang, G. Lindwall, Solidification modes during additive manufacturing of steel revealed by high-speed X-ray diffraction, Acta Mater. 246 (2023) 118713. https://doi.org/10.1016/J.ACTAMAT.2023.118713.

[68] R. Trivedi, W. Kurz, Dendritic growth, Int. Mater. Rev. 39 (1994) 49–74. https://doi.org/10.1179/IMR.1994.39.2.49.

[69] X. Liang, C. Bos, M. Hermans, I. Richardson, An Improved Cellular Automata Solidification Model Considering Kinetic Undercooling, Metall. Mater. Trans. B Process Metall. Mater. Process. Sci. 54 (2023) 1088–1098. https://doi.org/10.1007/S11663-023-02742-3/FIGURES/10.

[70] S. Kou, Welding Metallurgy, John Wiley & Sons, Inc., 2002.

[71] K.S. Kim, Y.K. Kim, K.A. Lee, Effect of repeated laser scanning on the microstructure evolution of carbon-bearing martensitic steel manufactured by laser powder bed

fusion: Quenching-partitioning drives carbon-stabilized austenite formation, Addit. Manuf. 60 (2022) 103262. https://doi.org/10.1016/J.ADDMA.2022.103262.

[72] P. Mohammadpour, H. Yuan, A.B. Phillion, Microstructure evolution of Inconel 625 alloy during single-track Laser Powder Bed Fusion, Addit. Manuf. 55 (2022) 102824. https://doi.org/10.1016/J.ADDMA.2022.102824.

[73] D. Lin, X. Xi, R. Ma, Z. Shi, H. Wei, X. Song, S. Hu, C. Tan, Fabrication of a strong and ductile FeCoCrNiMo0.3 high-entropy alloy with a micro-nano precipitate framework via laser powder bed fusion, Compos. Part B Eng. 266 (2023) 111006. https://doi.org/10.1016/J.COMPOSITESB.2023.111006.

[74] Z. Zhang, Q. Han, Z. Liu, L. Wang, H. Zhang, P. Zhao, G. Zhu, C. Huang, R. Setchi, Cracking behaviour and its suppression mechanisms with TiB2 additions in the laser additive manufacturing of solid-solution-strengthened Ni-based alloys, Compos. Part B Eng. 266 (2023) 111023. https://doi.org/10.1016/J.COMPOSITESB.2023.111023.

[75] J. Wang, S. Wang, W. Li, Y. Yao, X. Wang, Z. Yang, H. Chen, Ultrastrong and ductile additively-manufactured medium-carbon steel via modulating austenite stability, Scr. Mater. 239 (2024) 115780. https://doi.org/10.1016/J.SCRIPTAMAT.2023.115780.

[76] J. Lamb, K.M. Pusch, A.T. Polonsky, C.J. Torbet, S.A.J. Forsik, N. Zhou, R. Geurts, M.P. Echlin, T.M. Pollock, Origins of the High Cracking Resistance of a Co Ni Superalloy During Laser Additive Manufacturing, Submitt. to Scr. Mater. 239 (2023) 1–9. https://doi.org/10.1016/j.scriptamat.2023.115770.

[77] Y. Lei, K. Aoyagi, K. Aota, K. Kuwabara, A. Chiba, Critical factor triggering grain boundary cracking in non-weldable superalloy Alloy713ELC fabricated with selective electron beam melting, Acta Mater. 208 (2021) 116695. https://doi.org/10.1016/J.ACTAMAT.2021.116695.

[78] Y. Lei, K. Aoyagi, A. Chiba, A method to manipulate non-steady-state columnar-to-equiaxed transition in powder bed fusion additive manufacturing using an electron beam, Acta Mater. 227 (2022) 117717. https://doi.org/10.1016/J.ACTAMAT.2022.117717.

[79] Y. Chen, S.J. Clark, D.M. Collins, S. Marussi, S.A. Hunt, D.M. Fenech, T. Connolley, R.C. Atwood, O. V. Magdysyuk, G.J. Baxter, M.A. Jones, C.L.A. Leung, P.D. Lee, Correlative Synchrotron X-ray Imaging and Diffraction of Directed Energy Deposition Additive Manufacturing, Acta Mater. 209 (2021) 116777. https://doi.org/10.1016/J.ACTAMAT.2021.116777.

[80] B. Xiao, R. Chen, J. Zhang, J. Zhang, Y. Zhou, J. Ju, Y. Zhao, L. Xu, T. Yang, Additively manufactured heterogeneous precipitation-strengthened high-entropy alloys with high strength and ductility, Addit. Manuf. 77 (2023) 103795. https://doi.org/10.1016/J.ADDMA.2023.103795.

[81] M. Akmal, W. Jeong, H.J. Ryu, Ti-Zr-Nb based BCC alloy containing Mo prepared by laser directed energy deposition—ω phase and cellular structure, J. Alloys Compd. 969 (2023) 172306. https://doi.org/10.1016/J.JALLCOM.2023.172306.

[82] J.W. Rutter, B. Chalmers, A Prismatic Substructure Formed During Solidification of Metals, Can. J. Phys. 31 (1953) 15–39.

[83] W.A. Tiller, K.A. Jackson, J.W. Rutter, B. Chalmers, The redistribution of solute

atoms during the solidification of metals, Acta Metall. 1 (1953) 428–437. https://doi.org/10.1016/0001-6160(53)90126-6.

[84] W.J. Boettinger, S.R. Coriell, MICROSTRUCTURE FORMATION IN RAPIDLY SOLIDIFIED ALLOYS., NATO ASI Ser. Ser. E Appl. Sci. (1986) 81–108. https://doi.org/10.1007/978-94-009-4456-5_5/COVER.

[85] W. Kurz, D.J. Fisher, Fundamentals of solidification, Third, Trans Tech Publications, 1998.

[86] C. Hagenlocher, F. Fetzer, D. Weller, R. Weber, T. Graf, Explicit analytical expressions for the influence of welding parameters on the grain structure of laser beam welds in aluminium alloys, Mater. Des. 174 (2019) 107791. https://doi.org/10.1016/j.matdes.2019.107791.

[87] D. Zhang, D. Qiu, M.A. Gibson, Y. Zheng, H.L. Fraser, D.H. StJohn, M.A. Easton, Additive manufacturing of ultrafine-grained high-strength titanium alloys, Nat. 2019 5767785. 576 (2019) 91–95. https://doi.org/10.1038/s41586-019-1783-1.

[88] M.H. Mosallanejad, B. Niroumand, C. Ghibaudo, S. Biamino, A. Salmi, P. Fino, A. Saboori, In-situ alloying of a fine grained fully equiaxed Ti-based alloy via electron beam powder bed fusion additive manufacturing process, Addit. Manuf. 56 (2022) 102878. https://doi.org/10.1016/J.ADDMA.2022.102878.

[89] S. Wei, K.B. Lau, J.J. Lee, F. Wei, W.H. Teh, B. Zhang, C.C. Tan, P. Wang, U. Ramamurty, Selective laser melting of Fe–Al alloys with simultaneous gradients in composition and microstructure, Mater. Sci. Eng. A. 821 (2021) 141608. https://doi.org/10.1016/J.MSEA.2021.141608.

[90] X.P. Tan, S. Chandra, Y. Kok, S.B. Tor, G. Seet, N.H. Loh, E. Liu, Revealing competitive columnar grain growth behavior and periodic microstructural banding in additively manufactured Ti-6Al-4 V parts by selective electron beam melting, Materialia. 7 (2019) 100365. https://doi.org/10.1016/j.mtla.2019.100365.

[91] Z. Sun, X. Tan, S.B. Tor, W.Y. Yeong, Selective laser melting of stainless steel 316L with low porosity and high build rates, Mater. Des. 104 (2016) 197–204. https://doi.org/10.1016/j.matdes.2016.05.035.

[92] M.R. Rolchigo, R. LeSar, Application of alloy solidification theory to cellular automata modeling of near-rapid constrained solidification, Comput. Mater. Sci. 163 (2019) 148–161. https://doi.org/10.1016/j.commatsci.2019.03.012.

[93] S.L. Sobolev, Effects of local non-equilibrium solute diffusion on rapid solidification of alloys, Phys. Status Solidi. 156 (1996) 293–303. https://doi.org/10.1002/pssa.2211560208.

[94] K. Karayagiz, L. Johnson, R. Seede, V. Attari, B. Zhang, X. Huang, S. Ghosh, T. Duong, I. Karaman, A. Elwany, R. Arróyave, Finite interface dissipation phase field modeling of Ni–Nb under additive manufacturing conditions, Acta Mater. 185 (2020) 320–339. https://doi.org/10.1016/j.actamat.2019.11.057.

[95] Y. Shibuta, S. Sakane, E. Miyoshi, S. Okita, T. Takaki, M. Ohno, Heterogeneity in homogeneous nucleation from billion-atom molecular dynamics simulation of solidification of pure metal, Nature.Com.Remotexs.Ntu.Edu.Sgmunications 2017 81. 8 (2017) 1–9. https://doi.org/10.1038/s41467-017-00017-5.

[96] J. Lu, J.A. Szpunar, Molecular-dynamics simulation of rapid solidification of aluminum, Acta Metall. Mater. 41 (1993) 2291–2295. https://doi.org/10.1016/0956-7151(93)90311-F.

[97] Q.X. Pei, C. Lu, M.W. Fu, The rapid solidification of Ti3Al : a molecular dynamics study, J. Phys. Condens. Matter. 16 (2004) 4203. https://doi.org/10.1088/0953-8984/16/24/002.

[98] Z.A. Tian, R.S. Liu, H.R. Liu, C.X. Zheng, Z.Y. Hou, P. Peng, Molecular dynamics simulation for cooling rate dependence of solidification microstructures of silver, J. Non. Cryst. Solids. 354 (2008) 3705–3712. https://doi.org/10.1016/J.JNONCRYSOL.2008.04.006.

[99] L. Qi, H.F. Zhang, Z.Q. Hu, Molecular dynamic simulation of glass formation in binary liquid metal: Cu–Ag using EAM, Intermetallics. 12 (2004) 1191–1195. https://doi.org/10.1016/J.INTERMET.2004.04.003.

[100] L. Qi, H.F. Zhang, Z.Q. Hu, P.K. Liaw, Molecular dynamic simulation studies of glass formation and atomic-level structures in Pd–Ni alloy, Phys. Lett. A. 327 (2004) 506–511. https://doi.org/10.1016/J.PHYSLETA.2004.05.043.

[101] G. Zhou, Q. Gao, Molecular dynamics simulation of the solidification of liquid gold nanowires, Solid State Commun. 136 (2005) 32–35. https://doi.org/10.1016/J.SSC.2005.06.020.

[102] S. Ozgen, E. Duruk, Molecular dynamics simulation of solidification kinetics of aluminium using Sutton–Chen version of EAM, Mater. Lett. 58 (2004) 1071–1075. https://doi.org/10.1016/J.MATLET.2003.08.019.

[103] Z.C. Xie, T.H. Gao, X.T. Guo, Q. Xie, Molecular dynamics simulation of nanocrystal formation and deformation behavior of Ti3Al alloy, Comput. Mater. Sci. 98 (2015) 245–251. https://doi.org/10.1016/j.commatsci.2014.10.012.

[104] S. Özdemir Kart, M. Tomak, M. UludoĞan, T. ÇaĞin, Structural, thermodynamical, and transport properties of undercooled binary Pd–Ni alloys, Mater. Sci. Eng. A. 435–436 (2006) 736–744. https://doi.org/10.1016/J.MSEA.2006.07.120.

[105] J. Liu, J.Z. Zhao, Z.Q. Hu, The development of microstructure in a rapidly solidified Cu, Mater. Sci. Eng. A. 452–453 (2007) 103–109. https://doi.org/10.1016/J.MSEA.2006.10.117.

[106] T. Zhang, A. ling Wu, T. kun Gu, H. Liu, Relaxation dynamics in liquid and amorphous copper, Comput. Mater. Sci. 42 (2008) 130–138. https://doi.org/10.1016/J.COMMATSCI.2007.07.010.

[107] T. Zhang, Y.H. Qi, T.K. Gu, X.R. Zhang, Structure and relaxation about the compound Cu3Au during rapid cooling process, J. Alloys Compd. 455 (2008) 398–406. https://doi.org/10.1016/J.JALLCOM.2007.01.120.

[108] F. Li, X.J. Liu, H.Y. Hou, G. Chen, G.L. Chen, Atomistic structural evolution with cooling rates during the solidification of liquid nickel, Intermetallics. 19 (2011) 630–635. https://doi.org/10.1016/J.INTERMET.2010.12.016.

[109] F.A. Celik, Cooling rate dependence of the icosahedral order of amorphous CuNi alloy: A molecular dynamics simulation, Vacuum. 97 (2013) 30–35. https://doi.org/10.1016/J.VACUUM.2013.04.004.

[110] Y.D. Li, Q.L. Cao, C.C. Wang, C.S. Liu, Molecular dynamics study of structural evolution of aluminum during rapid quenching under different pressures, Phys. B Condens. Matter. 406 (2011) 3745–3751. https://doi.org/10.1016/J.PHYSB.2011.06.083.

[111] S. Kazanc, Molecular dynamics study of pressure effect on glass formation and the crystallization in liquid CuNi alloy, Comput. Mater. Sci. 38 (2006) 405–409. https://doi.org/10.1016/J.COMMATSCI.2006.03.008.

[112] J. Liu, J.Z. Zhao, Z.Q. Hu, Pressure effect on the formation and the thermal stability of glassy Cu, Comput. Mater. Sci. 37 (2006) 234–238. https://doi.org/10.1016/J.COMMATSCI.2005.06.011.

[113] S. Kazanc, F.A. Celik, A.K. Yildiz, S. Ozgen, Pressure effect on intermediate structures during transition from amorphous to crystalline states of copper, Comput. Mater. Sci. 40 (2007) 179–185. https://doi.org/10.1016/J.COMMATSCI.2006.11.011.

[114] Y.D. Li, Q.L. Lu, C.C. Wang, S.G. Huang, C.S. Liu, Local order evolution of liquid Cu during glass transition under different pressures: A molecular dynamics study, Phys. B Condens. Matter. 408 (2013) 6–11. https://doi.org/10.1016/J.PHYSB.2012.10.003.

[115] S.W. Kao, J.W. Yeh, T.S. Chin, Rapidly solidified structure of alloys with up to eight equal-molar elements - A simulation by molecular dynamics, J. Phys. Condens. Matter. 20 (2008) 145214. https://doi.org/10.1088/0953-8984/20/14/145214.

[116] H. Chen, Q. Fang, K. Zhou, Y. Liu, J. Li, Unraveling atomic-scale crystallization and microstructural evolution of a selective laser melted FeCrNi medium-entropy alloy, CrystEngComm. 22 (2020) 4136–4146. https://doi.org/10.1039/D0CE00358A.

[117] G. Singh, A.M. Waas, V. Sundararaghavan, Understanding defect structures in nanoscale metal additive manufacturing via molecular dynamics, Comput. Mater. Sci. 200 (2021) 110807. https://doi.org/10.1016/J.COMMATSCI.2021.110807.

[118] S. Kurian, R. Mirzaeifar, Selective laser melting of aluminum nano-powder particles, a molecular dynamics study, Addit. Manuf. 35 (2020) 101272. https://doi.org/10.1016/J.ADDMA.2020.101272.

[119] I.R. Jamil, A.M. Mustaquim, M. Islam, M.N. Hasan, Molecular dynamics perspective of the effects of laser thermal configurations on the dislocation and mechanical characteristics of FeNiCrCoCu HEA through powder bed fusion process, Mater. Today Commun. 33 (2022) 104998. https://doi.org/10.1016/J.MTCOMM.2022.104998.

[120] M. Bahramyan, R.T. Mousavian, J.G. Carton, D. Brabazon, Nano-scale simulation of directional solidification in TWIP stainless steels: A focus on plastic deformation mechanisms, Mater. Sci. Eng. A. 812 (2021) 140999. https://doi.org/10.1016/J.MSEA.2021.140999.

[121] Q. Bizot, O. Politano, V. Turlo, F. Baras, Molecular dynamics simulations of nanoscale solidification in the context of Ni additive manufacturing, Materialia. 27 (2023) 101639. https://doi.org/10.1016/j.mtla.2022.101639.

[122] C.A. Gandin, M. Rappaz, A 3D cellular automaton algorithm for the prediction of dendritic grain growth, Acta Mater. 45 (1997) 2187–2195. https://doi.org/10.1016/S1359-6454(96)00303-5.

[123] Y. Lian, Z. Gan, C. Yu, D. Kats, W.K. Liu, G.J. Wagner, A cellular automaton finite volume method for microstructure evolution during additive manufacturing, Mater. Des. 169 (2019) 107672. https://doi.org/10.1016/j.matdes.2019.107672.

[124] Z. Zhang, Z.J. Tan, X.X. Yao, C.P. Hu, P. Ge, Z.Y. Wan, J.Y. Li, Q. Wu, Numerical methods for microstructural evolutions in laser additive manufacturing, Comput. Math. with Appl. 78 (2019) 2296–2307. https://doi.org/10.1016/J.CAMWA.2018.07.011.

[125] A. Aggarwal, A. Chouhan, S. Patel, D.K.K. Yadav, A. Kumar, A.R.R. Vinod, K.G.G. Prashanth, N.P.P. Gurao, Role of impinging powder particles on melt pool hydrodynamics, thermal behaviour and microstructure in laser-assisted DED process: A particle-scale DEM – CFD – CA approach, Int. J. Heat Mass Transf. 158 (2020) 119989. https://doi.org/10.1016/j.ijheatmasstransfer.2020.119989.

[126] D.R. Liu, S. Wang, W. Yan, Grain structure evolution in transition-mode melting in direct energy deposition, Mater. Des. 194 (2020) 108919. https://doi.org/10.1016/j.matdes.2020.108919.

[127] S. Liu, Y.C. Shin, Prediction of 3D microstructure and phase distributions of Ti6Al4V built by the directed energy deposition process via combined multi-physics models, Addit. Manuf. 34 (2020) 101234. https://doi.org/10.1016/J.ADDMA.2020.101234.

[128] K. Jin, Z. Yang, P. Chen, G. Huang, X. Qiao, Dynamic solidification process during laser cladding of IN718: Multi-physics model, solute suppressed nucleation and microstructure evolution, Int. J. Heat Mass Transf. 192 (2022) 122907. https://doi.org/10.1016/j.ijheatmasstransfer.2022.122907.

[129] Z. Chen, C. Wang, C. Tang, Y.Z. Lek, S.Y. Kandukuri, H. Du, H. Gao, K. Zhou, Microstructure and mechanical properties of a Monel K-500 alloy fabricated by directed energy deposition, Mater. Sci. Eng. A. 857 (2022) 144113. https://doi.org/10.1016/j.msea.2022.144113.

[130] L. Wang, D. Zhang, C. Chen, H. Fu, X. Sun, Multi-physics field coupling and microstructure numerical simulation of laser cladding for engine crankshaft based on CA-FE method and experimental study, Surf. Coatings Technol. 438 (2022) 128396. https://doi.org/10.1016/j.surfcoat.2022.128396.

[131] G. Meng, Y. Gong, J. Zhang, L. Zhu, H. Xie, J. Zhao, Multi-scale simulation of microstructure evolution during direct laser deposition of Inconel718, Int. J. Heat Mass Transf. 191 (2022) 122798. https://doi.org/10.1016/j.ijheatmasstransfer.2022.122798.

[132] K. Jin, Z. Yang, P. Chen, P. Feng, X. Qiao, Modeling of solidification process during multi-track laser cladding with 3D cellular automata coupling gas-liquid interface tracking and solute suppression nucleation, J. Mater. Process. Technol. 315 (2023) 117927. https://doi.org/10.1016/j.jmatprotec.2023.117927.

[133] M. Grujicic, G. Cao, R.S. Figliola, Computer simulations of the evolution of solidification microstructure in the LENS^{TM} rapid fabrication process, Appl. Surf. Sci. 183 (2001) 43–57. https://doi.org/10.1016/S0169-4332(01)00553-0.

[134] L. Shi, J. Wang, S. Xu, J. Li, C. Chen, T. Hu, H. Sundar, Z. Ren, Modeling of epitaxial growth of single crystal superalloys fabricated by directed energy deposition, Mater. Today Commun. 35 (2023) 105899. https://doi.org/10.1016/j.mtcomm.2023.105899.

[135] P. Nie, O.A. Ojo, Z. Li, Numerical modeling of microstructure evolution during laser

additive manufacturing of a nickel-based superalloy, Acta Mater. 77 (2014) 85–95. https://doi.org/10.1016/J.ACTAMAT.2014.05.039.

[136] J. Zhang, F. Liou, W. Seufzer, K. Taminger, A coupled finite element cellular automaton model to predict thermal history and grain morphology of Ti-6Al-4V during direct metal deposition (DMD), Addit. Manuf. 11 (2016) 32–39. https://doi.org/10.1016/j.addma.2016.04.004.

[137] M.R. Rolchigo, M.Y. Mendoza, P. Samimi, D.A. Brice, B. Martin, P.C. Collins, R. LeSar, Modeling of Ti-W Solidification Microstructures Under Additive Manufacturing Conditions, Metall. Mater. Trans. A Phys. Metall. Mater. Sci. 48 (2017) 3606–3622. https://doi.org/10.1007/S11661-017-4120-Z/FIGURES/11.

[138] J. Zhang, W. Li, L. Yan, F. Liou, A two-dimensional simulation of grain structure growth within the substrate and the fusion zone during direct metal deposition, Comptes Rendus - Mec. 346 (2018) 1072–1086. https://doi.org/10.1016/j.crme.2018.08.003.

[139] J. Akram, P. Chalavadi, D. Pal, B. Stucker, Understanding grain evolution in additive manufacturing through modeling, Addit. Manuf. 21 (2018) 255–268. https://doi.org/10.1016/j.addma.2018.03.021.

[140] X. Li, W. Tan, Numerical investigation of effects of nucleation mechanisms on grain structure in metal additive manufacturing, Comput. Mater. Sci. 153 (2018) 159–169. https://doi.org/10.1016/J.COMMATSCI.2018.06.019.

[141] M.R. Rolchigo, R. LeSar, Modeling of binary alloy solidification under conditions representative of Additive Manufacturing, Comput. Mater. Sci. 150 (2018) 535–545. https://doi.org/10.1016/j.commatsci.2018.04.004.

[142] A. Zinoviev, O. Zinovieva, V. Ploshikhin, V. Romanova, R. Balokhonov, Evolution of grain structure during laser additive manufacturing. Simulation by a cellular automata method, Mater. Des. 106 (2016) 321–329. https://doi.org/10.1016/j.matdes.2016.05.125.

[143] X. Ao, H. Xia, J. Liu, Q. He, Simulations of microstructure coupling with moving molten pool by selective laser melting using a cellular automaton, Mater. Des. 185 (2020) 108230. https://doi.org/10.1016/j.matdes.2019.108230.

[144] O. Zinovieva, A. Zinoviev, V. Romanova, R. Balokhonov, Three-dimensional analysis of grain structure and texture of additively manufactured 316L austenitic stainless steel, Addit. Manuf. 36 (2020) 101521. https://doi.org/10.1016/j.addma.2020.101521.

[145] M. Gerstgrasser, R. Jakob, K.S. Pandya, J. Stirnimann, K. Wegener, CA single track microstructure simulation of nickel base alloy CM247LC and stainless steel S316L, including experimental validation of S316L, Mater. Des. 199 (2021) 109395. https://doi.org/10.1016/j.matdes.2020.109395.

[146] X. Ao, H. Xia, J. Liu, Q. He, S. Lin, A numerical study of irregular eutectic in Al-Si alloys under a large undercooling, Comput. Mater. Sci. 186 (2021) 110049. https://doi.org/10.1016/j.commatsci.2020.110049.

[147] A. Baumard, D. Ayrault, O. Fandeur, C. Bordreuil, F. Deschaux-Beaume, Numerical prediction of grain structure formation during laser powder bed fusion of 316 L stainless steel, Mater. Des. 199 (2021) 109434.

https://doi.org/10.1016/j.matdes.2020.109434.

[148] K. Teferra, D.J. Rowenhorst, Optimizing the cellular automata finite element model for additive manufacturing to simulate large microstructures, Acta Mater. 213 (2021) 116930. https://doi.org/10.1016/j.actamat.2021.116930.

[149] V. Romanova, M.S. Mohebbi, E. Dymnich, R. Balokhonov, V. Ploshikhin, A physically-based computational approach for processing-microstructure-property linkage of materials additively manufactured by laser powder bed fusion, Int. J. Mech. Sci. 219 (2022) 107103. https://doi.org/10.1016/j.ijmecsci.2022.107103.

[150] O. Zinovieva, V. Romanova, R. Balokhonov, Effects of scanning pattern on the grain structure and elastic properties of additively manufactured 316L austenitic stainless steel, Mater. Sci. Eng. A. 832 (2022) 142447. https://doi.org/10.1016/j.msea.2021.142447.

[151] W.L. Wang, W.Q. Liu, X. Yang, R.R. Xu, Q.Y. Dai, Multi-scale simulation of columnar-to-equiaxed transition during laser selective melting of rare earth magnesium alloy, J. Mater. Sci. Technol. 119 (2022) 11–24. https://doi.org/10.1016/j.jmst.2021.12.029.

[152] S. Pramod, D. Kesavan, Melting modes of laser powder bed fusion (L-PBF) processed IN718 alloy: Prediction and experimental analysis, Adv. Ind. Manuf. Eng. 6 (2023) 100106. https://doi.org/10.1016/j.aime.2022.100106.

[153] O. Lopez-Botello, U. Martinez-Hernandez, J. Ramírez, C. Pinna, K. Mumtaz, Two-dimensional simulation of grain structure growth within selective laser melted AA-2024, Mater. Des. 113 (2017) 369–376. https://doi.org/10.1016/j.matdes.2016.10.031.

[154] T. Camus, D. Maisonnette, O. Baulin, O. Senninger, G. Guillemot, C.-A. Gandin, Three-dimensional modeling of solidification grain structures generated by laser powder bed fusion, Materialia. 30 (2023) 101804. https://doi.org/10.1016/j.mtla.2023.101804.

[155] C. Panwisawas, C. Qiu, M.J. Anderson, Y. Sovani, R.P. Turner, M.M. Attallah, J.W. Brooks, H.C. Basoalto, Mesoscale modelling of selective laser melting: Thermal fluid dynamics and microstructural evolution, Comput. Mater. Sci. 126 (2017) 479–490. https://doi.org/10.1016/J.COMMATSCI.2016.10.011.

[156] A.R.A. Dezfoli, W.S. Hwang, W.C. Huang, T.W. Tsai, Determination and controlling of grain structure of metals after laser incidence: Theoretical approach, Sci. Reports 2017 71. 7 (2017) 1–11. https://doi.org/10.1038/srep41527.

[157] J. Yang, H. Yu, H. Yang, F. Li, Z. Wang, X. Zeng, Prediction of microstructure in selective laser melted Ti6Al4V alloy by cellular automaton, J. Alloys Compd. 748 (2018) 281–290. https://doi.org/10.1016/J.JALLCOM.2018.03.116.

[158] O. Zinovieva, A. Zinoviev, V. Ploshikhin, Three-dimensional modeling of the microstructure evolution during metal additive manufacturing, Comput. Mater. Sci. 141 (2018) 207–220. https://doi.org/10.1016/j.commatsci.2017.09.018.

[159] Y. Zhang, J. Zhang, Modeling of solidification microstructure evolution in laser powder bed fusion fabricated 316L stainless steel using combined computational fluid dynamics and cellular automata, Addit. Manuf. 28 (2019) 750–765. https://doi.org/10.1016/J.ADDMA.2019.06.024.

[160] M.S. Mohebbi, V. Ploshikhin, Implementation of nucleation in cellular automaton simulation of microstructural evolution during additive manufacturing of Al alloys, Addit. Manuf. 36 (2020) 101726. https://doi.org/10.1016/j.addma.2020.101726.

[161] R. Shi, S.A. Khairallah, T.T. Roehling, T.W. Heo, J.T. McKeown, M.J. Matthews, Microstructural control in metal laser powder bed fusion additive manufacturing using laser beam shaping strategy, Acta Mater. 184 (2020) 284–305. https://doi.org/10.1016/j.actamat.2019.11.053.

[162] A. Rai, M. Markl, C. Körner, A coupled Cellular Automaton–Lattice Boltzmann model for grain structure simulation during additive manufacturing, Comput. Mater. Sci. 124 (2016) 37–48. https://doi.org/10.1016/j.commatsci.2016.07.005.

[163] A. Rai, H. Helmer, C. Körner, Simulation of grain structure evolution during powder bed based additive manufacturing, Addit. Manuf. 13 (2017) 124–134. https://doi.org/10.1016/j.addma.2016.10.007.

[164] J.A. Koepf, M.R. Gotterbarm, M. Markl, C. Körner, 3D multi-layer grain structure simulation of powder bed fusion additive manufacturing, Acta Mater. 152 (2018) 119–126. https://doi.org/10.1016/j.actamat.2018.04.030.

[165] J.A. Koepf, D. Soldner, M. Ramsperger, J. Mergheim, M. Markl, C. Körner, Numerical microstructure prediction by a coupled finite element cellular automaton model for selective electron beam melting, Comput. Mater. Sci. 162 (2019) 148–155. https://doi.org/10.1016/j.commatsci.2019.03.004.

[166] S. Chandra, X. Tan, R.L. Narayan, C. Wang, S.B. Tor, G. Seet, A generalised hot cracking criterion for nickel-based superalloys additively manufactured by electron beam melting, Addit. Manuf. 37 (2021) 101633. https://doi.org/10.1016/j.addma.2020.101633.

[167] F. Xiong, C. Huang, O.L. Kafka, Y. Lian, W. Yan, M. Chen, D. Fang, Grain growth prediction in selective electron beam melting of Ti-6Al-4V with a cellular automaton method, Mater. Des. 199 (2021) 109410. https://doi.org/10.1016/j.matdes.2020.109410.

[168] Y. Yu, Y. Li, F. Lin, W. Yan, A multi-grid Cellular Automaton model for simulating dendrite growth and its application in additive manufacturing, Addit. Manuf. 47 (2021) 102284. https://doi.org/10.1016/J.ADDMA.2021.102284.

[169] W. Yan, Y. Lian, C. Yu, O.L. Kafka, Z. Liu, W.K. Liu, G.J. Wagner, An integrated process–structure–property modeling framework for additive manufacturing, Comput. Methods Appl. Mech. Eng. 339 (2018) 184–204. https://doi.org/10.1016/J.CMA.2018.05.004.

[170] M. Rolchigo, A. Plotkowski, J. Belak, Sensitivity of cellular automata grain structure predictions for high solidification rates, Comput. Mater. Sci. 196 (2021) 110498. https://doi.org/10.1016/j.commatsci.2021.110498.

[171] B. Chen, Q. Zhang, D. Sun, Z. Wang, Effects of shear flows on columnar dendritic microstructure during rapid solidification of IN718 alloy: A cellular automaton-lattice Boltzmann modeling study, J. Cryst. Growth. 585 (2022) 126583. https://doi.org/10.1016/j.jcrysgro.2022.126583.

[172] M. Rolchigo, S.T. Reeve, B. Stump, G.L. Knapp, J. Coleman, A. Plotkowski, J. Belak,

ExaCA: A performance portable exascale cellular automata application for alloy solidification modeling, Comput. Mater. Sci. 214 (2022) 111692. https://doi.org/10.1016/j.commatsci.2022.111692.

[173] Z. Yang, H. Fang, K. Jin, J. He, W. Ge, W. Yan, Physics-driven modeling of electron beam welding of Al-Cu alloys from molten pool flow, microstructure to mechanical properties, J. Mater. Process. Technol. 308 (2022) 117703. https://doi.org/10.1016/j.jmatprotec.2022.117703.

[174] E. Dorari, K. Ji, G. Guillemot, C.A. Gandin, A. Karma, Growth competition between columnar dendritic grains – The role of microstructural length scales, Acta Mater. 223 (2022) 117395. https://doi.org/10.1016/j.actamat.2021.117395.

[175] C. Gu, M.P. Moodispaw, A.A. Luo, Cellular automaton simulation and experimental validation of eutectic transformation during solidification of Al-Si alloys, Npj Comput. Mater. 8 (2022) 1–9. https://doi.org/10.1038/s41524-022-00824-5.

[176] S.M. Elahi, R. Tavakoli, I. Romero, D. Tourret, Grain growth competition during melt pool solidification — Comparing phase-field and cellular automaton models, Comput. Mater. Sci. 216 (2023) 111882. https://doi.org/10.1016/j.commatsci.2022.111882.

[177] S. Liu, Y.C. Shin, Integrated 2D cellular automata-phase field modeling of solidification and microstructure evolution during additive manufacturing of Ti6Al4V, Comput. Mater. Sci. 183 (2020) 109889. https://doi.org/10.1016/j.commatsci.2020.109889.

[178] S. Liu, K. min Hong, Y.C. Shin, A novel 3D cellular automata-phase field model for computationally efficient dendrite evolution during bulk solidification, Comput. Mater. Sci. 192 (2021) 110405. https://doi.org/10.1016/j.commatsci.2021.110405.

[179] Y. Lian, Z. Gan, C. Yu, D. Kats, W.K. Liu, G.J. Wagner, A cellular automaton finite volume method for microstructure evolution during additive manufacturing, Mater. Des. 169 (2019) 107672. https://doi.org/10.1016/J.MATDES.2019.107672.

[180] O. Andreau, I. Koutiri, P. Peyre, J.D. Penot, N. Saintier, E. Pessard, T. De Terris, C. Dupuy, T. Baudin, Texture control of 316L parts by modulation of the melt pool morphology in selective laser melting, J. Mater. Process. Technol. 264 (2019) 21–31. https://doi.org/10.1016/J.JMATPROTEC.2018.08.049.

[181] N. Ren, J. Li, R. Zhang, C. Panwisawas, M. Xia, H. Dong, J. Li, Solute trapping and non-equilibrium microstructure during rapid solidification of additive manufacturing, Nat. Commun. 2023 141. 14 (2023) 1–13. https://doi.org/10.1038/s41467-023-43563-x.

[182] J.A. Koepf, D. Soldner, M. Ramsperger, J. Mergheim, M. Markl, C. Körner, Numerical microstructure prediction by a coupled finite element cellular automaton model for selective electron beam melting, Comput. Mater. Sci. 162 (2019) 148–155. https://doi.org/10.1016/J.COMMATSCI.2019.03.004.

[183] S. Raghavan, G. Singh, S. Sondhi, S. Srikanth, Construction of a pseudo-binary phase diagram for multi-component Ni-base superalloys, Calphad. 38 (2012) 85–91.

[184] J.A. Koepf, M.R. Gotterbarm, M. Markl, C. Körner, 3D multi-layer grain structure simulation of powder bed fusion additive manufacturing, Acta Mater. 152 (2018) 119–126. https://doi.org/10.1016/J.ACTAMAT.2018.04.030.

[185] J. Lipton, M.E. Glicksman, W. Kurz, Dendritic growth into undercooled alloy metals, Mater. Sci. Eng. 65 (1984) 57–63. https://doi.org/10.1016/0025-5416(84)90199-X.

[186] M. Rappaz, S.A. David, J.M. Vitek, L.A. Boatner, Analysis of solidification microstructures in Fe-Ni-Cr single-crystal welds, Metall. Trans. A. 21 (1990) 1767–1782. https://doi.org/10.1007/BF02672593/METRICS.

[187] J. Bragard, A. Karma, Y.H. Lee, M. Plapp, Linking phase-field and atomistic simulations to model dendritic solidification in highly undercooled melts, Interface Sci. 10 (2002) 121–136. https://doi.org/10.1023/A:1015815928191/METRICS.

[188] T.M. Rodgers, J.D. Madison, V. Tikare, Simulation of metal additive manufacturing microstructures using kinetic Monte Carlo, Comput. Mater. Sci. 135 (2017) 78–89. https://doi.org/10.1016/j.commatsci.2017.03.053.

[189] W. Li, M. Soshi, Modeling analysis of grain morphologies in Directed energy deposition (DED) coating with different laser scanning patterns, Mater. Lett. 251 (2019) 8–12. https://doi.org/10.1016/J.MATLET.2019.05.027.

[190] K.L. Johnson, T.M. Rodgers, O.D. Underwood, J.D. Madison, K.R. Ford, S.R. Whetten, D.J. Dagel, J.E. Bishop, Simulation and experimental comparison of the thermo-mechanical history and 3D microstructure evolution of 304L stainless steel tubes manufactured using LENS, Comput. Mech. 61 (2018) 559–574. https://doi.org/10.1007/S00466-017-1516-Y/FIGURES/14.

[191] T.M. Rodgers, J.E. Bishop, J.D. Madison, Direct numerical simulation of mechanical response in synthetic additively manufactured microstructures, Model. Simul. Mater. Sci. Eng. 26 (2018) 055010. https://doi.org/10.1088/1361-651X/aac616.

[192] S. Sunny, H. Yu, R. Mathews, A. Malik, W. Li, Improved grain structure prediction in metal additive manufacturing using a Dynamic Kinetic Monte Carlo framework, Addit. Manuf. 37 (2021) 101649. https://doi.org/10.1016/j.addma.2020.101649.

[193] T.M. Rodgers, D. Moser, F. Abdeljawad, O.D.U. Jackson, J.D. Carroll, B.H. Jared, D.S. Bolintineanu, J.A. Mitchell, J.D. Madison, Simulation of powder bed metal additive manufacturing microstructures with coupled finite difference-Monte Carlo method, Addit. Manuf. 41 (2021) 101953. https://doi.org/10.1016/J.ADDMA.2021.101953.

[194] J.D. Hunt, Steady state columnar and equiaxed growth of dendrites and eutectic, Mater. Sci. Eng. 65 (1984) 75–83. https://doi.org/10.1016/0025-5416(84)90201-5.

[195] M. Uddagiri, O. Shchyglo, I. Steinbach, B. Wahlmann, C. Koerner, Phase-Field Study of the History-Effect of Remelted Microstructures on Nucleation During Additive Manufacturing of Ni-Based Superalloys, Metall. Mater. Trans. A Phys. Metall. Mater. Sci. 54 (2023) 1825–1842. https://doi.org/10.1007/S11661-023-07004-0/FIGURES/15.

[196] W.J. Boettinger, J.A. Warren, C. Beckermann, A. Karma, Phase-Field Simulation of Solidification, Https://Doi.Org.Remotexs.Ntu.Edu.Sg/10.1146/Annurev.Matsci.32.101901.155803. 32 (2003) 163–194. https://doi.org/10.1146/ANNUREV.MATSCI.32.101901.155803.

[197] W. Xiao, S. Li, C. Wang, Y. Shi, J. Mazumder, H. Xing, L. Song, Multi-scale simulation of dendrite growth for direct energy deposition of nickel-based superalloys, Mater. Des. 164 (2019) 107553. https://doi.org/10.1016/j.matdes.2018.107553.

[198] A. Jammal, G. Wang, Z. JiaXin, H. Yang, S. Yang, Y. Zhong, Y. Rong, Multi-scale modelling of solidification and microstructure evolution in laser-deposition of T15 high speed steel, J. Manuf. Process. 50 (2020) 24–33. https://doi.org/10.1016/j.jmapro.2019.12.024.

[199] X.X. Yao, X. Gao, Z. Zhang, Three-dimensional microstructure evolution of Ti–6Al–4V during multi-layer printing: a phase-field simulation, J. Mater. Res. Technol. 20 (2022) 934–949. https://doi.org/10.1016/j.jmrt.2022.07.101.

[200] L.-X. Lu, N. Sridhar, Y.-W. Zhang, Phase field simulation of powder bed-based additive manufacturing, Acta Mater. 144 (2018) 801–809. https://doi.org/10.1016/j.actamat.2017.11.033.

[201] T. Xue, Z. Gan, S. Liao, J. Cao, Physics-embedded graph network for accelerating phase-field simulation of microstructure evolution in additive manufacturing, Npj Comput. Mater. 8 (2022) 201. https://doi.org/10.1038/s41524-022-00890-9.

[202] M. Wei, W.J. Ding, G. Vastola, Y.W. Zhang, Quantitative study on the dynamics of melt pool and keyhole and their controlling factors in metal laser melting, Addit. Manuf. 54 (2022) 102779. https://doi.org/10.1016/J.ADDMA.2022.102779.

[203] J. Shinjo, A. Kutsukake, A. Arote, Y.T. Tang, D.G. McCartney, R.C. Reed, C. Panwisawas, Physics-based thermal-chemical-fluid-microstructure modelling of in-situ alloying using additive manufacturing: Composition-microstructure control, Addit. Manuf. 64 (2023) 103428. https://doi.org/10.1016/j.addma.2023.103428.

[204] P. Liu, Z. Wang, Y. Xiao, M.F. Horstemeyer, X. Cui, L. Chen, Insight into the mechanisms of columnar to equiaxed grain transition during metallic additive manufacturing, Addit. Manuf. 26 (2019) 22–29. https://doi.org/10.1016/J.ADDMA.2018.12.019.

[205] D. Liu, Y. Wang, Mesoscale multi-physics simulation of rapid solidification of Ti-6Al-4V alloy, Addit. Manuf. 25 (2019) 551–562. https://doi.org/10.1016/J.ADDMA.2018.12.005.

[206] J. Berry, A. Perron, J.L. Fattebert, J.D. Roehling, B. Vrancken, T.T. Roehling, D.L. Rosas, J.A. Turner, S.A. Khairallah, J.T. McKeown, M.J. Matthews, Toward multiscale simulations of tailored microstructure formation in metal additive manufacturing, Mater. Today. 51 (2021) 65–86. https://doi.org/10.1016/j.mattod.2021.09.024.

[207] A.F. Chadwick, P.W. Voorhees, The development of grain structure during additive manufacturing, Acta Mater. 211 (2021) 116862. https://doi.org/10.1016/j.actamat.2021.116862.

[208] M. Yang, L. Wang, W. Yan, Phase-field modeling of grain evolution in additive manufacturing with addition of reinforcing particles, Addit. Manuf. 47 (2021) 102286. https://doi.org/10.1016/j.addma.2021.102286.

[209] M. Yang, L. Wang, W. Yan, Phase-field modeling of grain evolutions in additive manufacturing from nucleation, growth, to coarsening, Npj Comput. Mater. 7 (2021) 56. https://doi.org/10.1038/s41524-021-00524-6.

[210] S.M. Elahi, R. Tavakoli, A.K. Boukellal, T. Isensee, I. Romero, D. Tourret, Multiscale simulation of powder-bed fusion processing of metallic alloys, Comput. Mater. Sci.

209 (2022) 111383. https://doi.org/10.1016/j.commatsci.2022.111383.

[211] M. Okugawa, Y. Ohigashi, Y. Furishiro, Y. Koizumi, T. Nakano, Equiaxed grain formation by intrinsic heterogeneous nucleation via rapid heating and cooling in additive manufacturing of aluminum-silicon hypoeutectic alloy, J. Alloys Compd. 919 (2022) 165812. https://doi.org/10.1016/j.jallcom.2022.165812.

[212] R. Laskowski, R. Ahluwalia, G.T.W. Hock, C.S. Ying, C.N. Sun, P. Wang, D.T.C. Cheh, N.M.L. Sharon, G. Vastola, Y.W. Zhang, Concurrent modeling of porosity and microstructure in multilayer three-dimensional simulations of powder-bed fusion additive manufacturing of INCONEL 718, Addit. Manuf. 60 (2022) 103266. https://doi.org/10.1016/j.addma.2022.103266.

[213] S. Sahoo, K. Chou, Phase-field simulation of microstructure evolution of Ti–6Al–4V in electron beam additive manufacturing process, Addit. Manuf. 9 (2016) 14–24. https://doi.org/10.1016/J.ADDMA.2015.12.005.

[214] P.W. Liu, Z. Wang, Y.H. Xiao, R.A. Lebensohn, Y.C. Liu, M.F. Horstemeyer, X.Y. Cui, L. Chen, Integration of phase-field model and crystal plasticity for the prediction of process-structure-property relation of additively manufactured metallic materials, Int. J. Plast. 128 (2020) 102670. https://doi.org/10.1016/j.ijplas.2020.102670.

[215] M.H. Burden, J.D. Hunt, Cellular and dendritic growth. I, J. Cryst. Growth. 22 (1974) 99–108. https://doi.org/10.1016/0022-0248(74)90126-2.

[216] S.H. Cho, T. Okane, T. Umeda, The contribution of the nucleation process to grain formation in calculating solidification microstructure by CA-DFD, Sci. Technol. Adv. Mater. 2 (2001) 241–245. https://doi.org/10.1016/S1468-6996(01)00059-6/XML.

[217] H. Yin, S.D. Felicelli, Dendrite growth simulation during solidification in the LENS process, Acta Mater. 58 (2010) 1455–1465. https://doi.org/10.1016/J.ACTAMAT.2009.10.053.

[218] L. Zhang, I. Steinbach, Phase-field model with finite interface dissipation: Extension to multi-component multi-phase alloys, Acta Mater. 60 (2012) 2702–2710. https://doi.org/10.1016/J.ACTAMAT.2012.02.032.

[219] D. Rosenthal, The theory of moving sources of heat and its application to metal treatments, Trans. Am. Soc. Mech. Eng. 68 (1946) 849–866.

[220] S. Safdar, A.J. Pinkerton, L. Li, M.A. Sheikh, P.J. Withers, An anisotropic enhanced thermal conductivity approach for modelling laser melt pools for Ni-base super alloys, Appl. Math. Model. 37 (2013) 1187–1195. https://doi.org/10.1016/j.apm.2012.03.028.

[221] P. Michaleris, Modeling metal deposition in heat transfer analyses of additive manufacturing processes, Finite Elem. Anal. Des. 86 (2014) 51–60. https://doi.org/10.1016/j.finel.2014.04.003.

[222] D. Riedlbauer, T. Scharowsky, R.F. Singer, P. Steinmann, C. Körner, J. Mergheim, Macroscopic simulation and experimental measurement of melt pool characteristics in selective electron beam melting of Ti-6Al-4V, Int. J. Adv. Manuf. Technol. (2016) 1–9.

[223] S. Chandra, G. Phanikumar, G.L. Seet, S.B. Tor, C.K. Chua, Multi-scale modeling of additive manufacturing process, in: Proc. Int. Conf. Prog. Addit. Manuf., 2016.

[224] E. Toyserkani, A. Khajepour, S. Corbin, 3-D finite element modeling of laser cladding by powder injection: effects of laser pulse shaping on the process, Opt. Lasers Eng. 41 (2004) 849–867. https://doi.org/10.1016/S0143-8166(03)00063-0.

[225] R. Ye, J.E. Smugeresky, B. Zheng, Y. Zhou, E.J. Lavernia, Numerical modeling of the thermal behavior during the LENS® process, Mater. Sci. Eng. A. 428 (2006) 47–53. https://doi.org/10.1016/j.msea.2006.04.079.

[226] P. Carlone, G.S. Palazzo, R. Pasquino, Inverse analysis of the laser forming process by computational modelling and methods, Comput. Math. with Appl. 55 (2008) 2018–2032. https://doi.org/10.1016/j.camwa.2007.09.003.

[227] G.N. Labeas, Development of a local three-dimensional numerical simulation model for the laser forming process of aluminium components, J. Mater. Process. Technol. 207 (2008) 248–257. https://doi.org/10.1016/j.jmatprotec.2007.12.098.

[228] Y. Xiong, W.H. Hofmeister, Z. Cheng, J.E. Smugeresky, E.J. Lavernia, J.M. Schoenung, In situ thermal imaging and three-dimensional finite element modeling of tungsten carbide–cobalt during laser deposition, Acta Mater. 57 (2009) 5419–5429. https://doi.org/10.1016/j.actamat.2009.07.038.

[229] I. Pitz, A. Otto, M. Schmidt, Simulation of the laser beam forming process with Moving Meshes for large aluminium plates, Phys. Procedia. 5 (2010) 363–369. https://doi.org/10.1016/j.phpro.2010.08.063.

[230] A.M. Kamara, W. Wang, S. Marimuthu, L. Li, Modelling of the melt pool geometry in the laser deposition of nickel alloys using the anisotropic enhanced thermal conductivity approach, Proc. Inst. Mech. Eng. Part B J. Eng. Manuf. 225 (2011) 87–99.

[231] L. Han, K.M. Phatak, F.W. Liou, Modeling of laser cladding with powder injection, Metall. Mater. Trans. B. 35 (2004) 1139–1150. https://doi.org/10.1007/s11663-004-0070-0.

[232] H. Qi, J. Mazumder, H. Ki, Numerical simulation of heat transfer and fluid flow in coaxial laser cladding process for direct metal deposition, J. Appl. Phys. 100 (2006) 024903. https://doi.org/10.1063/1.2209807.

[233] X. He, J. Mazumder, Transport phenomena during direct metal deposition, J. Appl. Phys. 101 (2007) 053113. https://doi.org/10.1063/1.2710780.

[234] O.B. Kovalev, A. V. Zaitsev, D. Novichenko, I. Smurov, Theoretical and Experimental Investigation of Gas Flows, Powder Transport and Heating in Coaxial Laser Direct Metal Deposition (DMD) Process, J. Therm. Spray Technol. 20 (2011) 465–478. https://doi.org/10.1007/s11666-010-9539-3.

[235] S. Chandra, B.C. Rao, A study of process parameters on workpiece anisotropy in the laser engineered net shaping (LENS TM) process, J. Phys. D. Appl. Phys. 50 (2017) 225303. https://doi.org/10.1088/1361-6463/aa6d3b.

[236] E. Attar, C. Körner, Lattice Boltzmann method for dynamic wetting problems, J. Colloid Interface Sci. 335 (2009) 84–93. https://doi.org/10.1016/j.jcis.2009.02.055.

[237] E. Attar, C. Körner, Lattice Boltzmann model for thermal free surface flows with liquid–solid phase transition, Int. J. Heat Fluid Flow. 32 (2011) 156–163. https://doi.org/10.1016/j.ijheatfluidflow.2010.09.006.

[238] R. Ammer, M. Markl, U. Ljungblad, C. Körner, U. Rüde, Simulating fast electron beam melting with a parallel thermal free surface lattice Boltzmann method, Comput. Math. with Appl. 67 (2014) 318–330. https://doi.org/10.1016/j.camwa.2013.10.001.

[239] C. Körner, E. Attar, P. Heinl, Mesoscopic simulation of selective beam melting processes, J. Mater. Process. Technol. 211 (2011) 978–987. https://doi.org/10.1016/j.jmatprotec.2010.12.016.

[240] M. Bayat, W. Dong, J. Thorborg, A.C. To, J.H. Hattel, A review of multi-scale and multi-physics simulations of metal additive manufacturing processes with focus on modeling strategies, Addit. Manuf. 47 (2021) 102278. https://doi.org/10.1016/J.ADDMA.2021.102278.

[241] M. Bayat, O. Zinovieva, F. Ferrari, C. Ayas, M. Langelaar, J. Spangenberg, R. Salajeghe, K. Poulios, S. Mohanty, O. Sigmund, J. Hattel, Holistic computational design within additive manufacturing through topology optimization combined with multiphysics multi-scale materials and process modelling, Prog. Mater. Sci. 138 (2023) 101129. https://doi.org/10.1016/J.PMATSCI.2023.101129.

[242] M. Gäumann, C. Bezençon, P. Canalis, W. Kurz, Single-Crystal Laser Deposition of Superalloys: Processing-Microstructure Maps, Acta Mater. 49 (2001) 1051–1062. https://doi.org/10.1016/S1359-6454(00)00367-0.

[243] J.M. Vitek, The effect of welding conditions on stray grain formation in single crystal welds – theoretical analysis, Acta Mater. 53 (2005) 53–67. https://doi.org/10.1016/j.actamat.2004.08.039.

[244] S. Bontha, N.W. Klingbeil, P.A. Kobryn, H.L. Fraser, Thermal process maps for predicting solidification microstructure in laser fabrication of thin-wall structures, J. Mater. Process. Technol. 178 (2006) 135–142. https://doi.org/10.1016/j.jmatprotec.2006.03.155.

[245] S.S. Al-Bermani, M.L. Blackmore, W. Zhang, I. Todd, The origin of microstructural diversity, texture, and mechanical properties in electron beam melted Ti-6Al-4V, Metall. Mater. Trans. A. 41 (2010) 3422–3434. https://doi.org/10.1007/s11661-010-0397-x.

[246] D. Ma, P.R. Sahm, Primary spacing in directional solidification, Metall. Mater. Trans. A. 29 (1998) 1113–1119. https://doi.org/10.1007/s11661-998-0303-y.

[247] J.D. Hunt, Cellular and primary dendrite spacings, in: Solidif. Cast. Met., Sheffield, England, 1979: pp. 3–9.

[248] L. Wang, Y. Wei, X. Zhan, F. Yu, X. Cao, C. Gu, W. Ou, Simulation of dendrite growth in the laser welding pool of aluminum alloy 2024 under transient conditions, J. Mater. Process. Technol. 246 (2017) 22–29. https://doi.org/10.1016/J.JMATPROTEC.2017.03.005.

[249] R. Trivedi, INTERDENDRITIC SPACING: PART II. A COMPARISON OF THEORY AND EXPERIMENT., Metall. Trans. A, Phys. Metall. Mater. Sci. 15 A (1984) 977–982. https://doi.org/10.1007/BF02644689/METRICS.

[250] N. Wang, S. Mokadem, M. Rappaz, W. Kurz, Solidification cracking of superalloy single- and bi-crystals, Acta Mater. (2004). https://doi.org/10.1016/j.actamat.2004.03.047.

[251] G. Agarwal, M. Amirthalingam, S.C. Moon, R.J. Dippenaar, I.M. Richardson, M.J.M. Hermans, Experimental evidence of liquid feeding during solidification of a steel, Scr. Mater. 146 (2018) 105–109.

[252] E.-J. Chun, S.-J. Lee, J. Suh, J.-S. Lee, N. Kang, K. Saida, Influence of metallic sodium on repair weldability for type 316FR stainless steel, J. Weld. Join. 35 (2017) 79–88.

[253] C. Fink, M. Zinke, D. Keil, Evaluation of hot cracking susceptibility of nickel-based alloys by the PVR test, Weld. World. 56 (2012) 37–43.

[254] W. Ren, F. Lu, R. Yang, X. Liu, Z. Li, Liquation cracking in fiber laser welded joints of inconel 617, J. Mater. Process. Technol. 226 (2015) 214–220.

[255] Y. Chen, F. Lu, K. Zhang, P. Nie, S.R. Elmi Hosseini, K. Feng, Z. Li, Dendritic microstructure and hot cracking of laser additive manufactured Inconel 718 under improved base cooling, J. Alloys Compd. 670 (2016) 312–321.

[256] Z. Sun, X.P. Tan, M. Descoins, D. Mangelinck, S.B. Tor, C.S. Lim, Revealing hot tearing mechanism for an additively manufactured high-entropy alloy via selective laser melting, Scr. Mater. 168 (2019) 129–133.

[257] L.N. Carter, M.M. Attallah, R.C. Reed, Laser powder bed fabrication of nickel-base superalloys: influence of parameters; characterisation, quantification and mitigation of cracking, Superalloys 2012. (2012) 577–586.

[258] L.N. Carter, C. Martin, P.J. Withers, M.M. Attallah, The influence of the laser scan strategy on grain structure and cracking behaviour in SLM powder-bed fabricated nickel superalloy, J. Alloys Compd. 615 (2014) 338–347.

[259] B. Ruttert, M. Ramsperger, L. Mujica Roncery, I. Lopez-Galilea, C. Körner, W. Theisen, Impact of hot isostatic pressing on microstructures of CMSX-4 Ni-base superalloy fabricated by selective electron beam melting, Mater. Des. 110 (2016) 720–727. https://doi.org/10.1016/j.matdes.2016.08.041.

[260] M. Rappaz, J.-M. Drezet, M. Gremaud, A new hot-tearing criterion, Metall. Mater. Trans. A. 30 (1999) 449–455.

[261] Z. Sun, X. Tan, C. Wang, M. Descoins, D. Mangelinck, S.B. Tor, E.A. Jägle, S. Zaefferer, D. Raabe, Reducing hot tearing by grain boundary segregation engineering in additive manufacturing: example of an AlxCoCrFeNi high-entropy alloy, Acta Mater. 204 (2021) 116505. https://doi.org/10.1016/J.ACTAMAT.2020.116505.

[262] Z. Liu, Z. Tan, D. He, Z. Zhou, X. Guo, W. Shao, H. Yao, Y. Xue, L. Cui, Simultaneously improved the strength and ductility of laser powder bed fused Al-Cr-Fe-Ni-V high-entropy alloy by hot isostatic pressing: Microcrack closure and precipitation strengthening, J. Mater. Sci. Technol. 180 (2024) 55–68. https://doi.org/10.1016/J.JMST.2023.04.052.

[263] Y. Wang, X. Lin, N. Kang, Z. Wang, Q. Wang, Y. Liu, W. Huang, Laser powder bed fusion of Zr-modified Al–Cu–Mg alloy: Crack-inhibiting, grain refinement, and mechanical properties, Mater. Sci. Eng. A. 838 (2022) 142618. https://doi.org/10.1016/J.MSEA.2022.142618.

[264] Y. Qi, Z. Hu, H. Zhang, X. Nie, C. Zhang, H. Zhu, High strength Al–Li alloy development for laser powder bed fusion, Addit. Manuf. 47 (2021) 102249.

https://doi.org/10.1016/J.ADDMA.2021.102249.

[265] A. Fardan, A. Fazi, R.L. Peng, T. Mishurova, M. Thuvander, G. Bruno, H. Brodin, E. Hryha, Fine-Tuning Melt Pools and Microstructures: Taming Cracks in Powder Bed Fusion—Laser Beam of a non-weldable Ni-base Superalloy, Materialia. 34 (2024) 102059. https://doi.org/10.1016/J.MTLA.2024.102059.

[266] L. Liu, D. Wang, G. Deng, Z. Liu, C. Tan, X. Zhou, C. Han, R. Jiang, Y. Yang, Crack inhibition to enhance strength-ductility of CM247LC alloy fabricated by laser powder bed fusion, Mater. Sci. Eng. A. 875 (2023) 145114. https://doi.org/10.1016/J.MSEA.2023.145114.

[267] A. Sonawane, G. Roux, J.J. Blandin, A. Despres, G. Martin, Cracking mechanism and its sensitivity to processing conditions during laser powder bed fusion of a structural aluminum alloy, Materialia. 15 (2021) 100976. https://doi.org/10.1016/J.MTLA.2020.100976.

[268] J. Choe, K.T. Kim, J.H. Yu, J.M. Park, D.Y. Yang, S. ho Jung, S. Jo, H. Joo, M. Kang, S.Y. Ahn, S.G. Jeong, E.S. Kim, H. Lee, H.S. Kim, A novel route for predicting the cracking of inoculant-added AA7075 processed via laser powder bed fusion, Addit. Manuf. 62 (2023) 103370. https://doi.org/10.1016/J.ADDMA.2022.103370.

[269] J. Du, Y. Yang, Y. Ren, H. Wu, Q. Shan, X. Wu, Y. Lu, I. Baker, A crack-free Ti-modified Al-Cu alloy processed by in-situ alloying laser powder bed fusion: Tribological behaviors and mechanical properties, J. Alloys Compd. 960 (2023) 170549. https://doi.org/10.1016/J.JALLCOM.2023.170549.

[270] M. Kusano, Y. Takata, A. Yumoto, M. Watanabe, Effects of time per layer and part geometry on thermal history and microcracking in the fabrication of nickel superalloy samples by laser powder bed fusion, Addit. Manuf. 80 (2024) 103987. https://doi.org/10.1016/J.ADDMA.2024.103987.

[271] M. Hafezi, A. Kermanpur, A. Rezaeian, S. Saeidirad, V. Nikneshan, H. Rabieifar, E. Kamouri Yousefabad, Investigating crack formation in IN738LC Ni-based superalloy fabricated by laser powder-bed fusion process, J. Mater. Res. Technol. 29 (2024) 1983–2002. https://doi.org/10.1016/J.JMRT.2024.01.264.

[272] Y. Wang, X. Lin, Y. Zhao, T. Zhang, J. Fu, N. Zheng, Z. Wang, W. Huang, Cracking mechanism and its susceptibility to scanning speed during laser power bed fusion processed high-strength 2024Al alloy, Mater. Charact. 194 (2022) 112344. https://doi.org/10.1016/J.MATCHAR.2022.112344.

[273] A.L. Kitt, L. Mohr, L. Kerwin, A. Bhaduri, H. Seyyedhosseinzadeh, A. Dhakad, D. Kmiotek, C. Shen, S. Huang, A. Kiedrowski, L. Yuan, Physics-based crack formation model for René 80 in laser blown directed energy deposition: Theory and experiment, Addit. Manuf. 73 (2023) 103675. https://doi.org/10.1016/J.ADDMA.2023.103675.

[274] S. Kou, A criterion for cracking during solidification, Acta Mater. 88 (2015) 366–374.

[275] X. Zhang, Y. Mu, N. Lu, Q. Li, S. Chen, Y. Zhou, X. Sun, J. Liang, J. Li, Effect of solid solution elements on cracking susceptibility of Ni-based superalloys during additive manufacturing, J. Mater. Sci. Technol. 190 (2024) 218–228. https://doi.org/10.1016/J.JMST.2023.11.073.

[276] J. Fu, H. Li, X. Song, M.W. Fu, Multi-scale defects in powder-based additively

manufactured metals and alloys, J. Mater. Sci. Technol. 122 (2022) 165–199. https://doi.org/10.1016/J.JMST.2022.02.015.

[277] J.H. Martin, B.D. Yahata, J.M. Hundley, J.A. Mayer, T.A. Schaedler, T.M. Pollock, 3D printing of high-strength aluminium alloys, Nature. 549 (2017) 365–369. https://doi.org/10.1038/nature23894.

[278] Y.L. Hu, X. Lin, X.B. Yu, J.J. Xu, M. Lei, W.D. Huang, Effect of Ti addition on cracking and microhardness of Inconel 625 during the laser solid forming processing, J. Alloys Compd. 711 (2017) 267–277. https://doi.org/10.1016/j.jallcom.2017.03.355.

[279] S.Y. Zhou, Y. Su, H. Wang, J. Enz, T. Ebel, M. Yan, Selective laser melting additive manufacturing of 7xxx series Al-Zn-Mg-Cu alloy: Cracking elimination by co-incorporation of Si and TiB2, Addit. Manuf. 36 (2020) 101458. https://doi.org/10.1016/j.addma.2020.101458.

[280] W. Zhou, G. Zhu, R. Wang, C. Yang, Y. Tian, L. Zhang, A. Dong, D. Wang, D. Shu, B. Sun, Inhibition of cracking by grain boundary modification in a non-weldable nickel-based superalloy processed by laser powder bed fusion, Mater. Sci. Eng. A. (2020). https://doi.org/10.1016/j.msea.2020.139745.

[281] X. Dang, Y. Li, K. Chen, U. Ramamurty, S. Luo, X. Liang, W. He, Avoiding cracks in additively manufactured non-weldable directionally solidified Ni-based superalloys, Addit. Manuf. 59 (2022) 103095. https://doi.org/10.1016/J.ADDMA.2022.103095.

[282] Y. Zhao, Z. Ma, L. Yu, Y. Liu, New alloy design approach to inhibiting hot cracking in laser additive manufactured nickel-based superalloys, Acta Mater. 247 (2023) 118736. https://doi.org/10.1016/J.ACTAMAT.2023.118736.

[283] E. Chauvet, C. Tassin, J.-J. Blandin, R. Dendievel, G. Martin, Producing Ni-base superalloys single crystal by selective electron beam melting, Scr. Mater. 152 (2018) 15–19. https://doi.org/10.1016/j.scriptamat.2018.03.041.

[284] Y. Liu, Y. Wang, R. Savinov, J. Shi, Epitaxial growth of a single-crystal nickel-based superalloy during laser melting with high-power flat-top laser, Opt. Laser Technol. 144 (2021) 107444. https://doi.org/10.1016/J.OPTLASTEC.2021.107444.

[285] A.A. Antonysamy, J. Meyer, P.B. Prangnell, Effect of build geometry on the β-grain structure and texture in additive manufacture of Ti6Al4V by selective electron beam melting, Mater. Charact. 84 (2013) 153–168. https://doi.org/10.1016/j.matchar.2013.07.012.

[286] M. Ramsperger, R.F. Singer, C. Körner, Microstructure of the nickel-base superalloy CMSX-4 fabricated by selective electron beam melting, Metall. Mater. Trans. A Phys. Metall. Mater. Sci. 47 (2016) 1469–1480.

[287] M.R. Gotterbarm, M. Seifi, D. Melzer, J. Džugan, A.A. Salem, Z.H. Liu, C. Körner, Small scale testing of IN718 single crystals manufactured by EB-PBF, Addit. Manuf. 36 (2020) 101449. https://doi.org/10.1016/j.addma.2020.101449.

[288] P. Fernandez-Zelaia, M.M. Kirka, A.M. Rossy, Y. Lee, S.N. Dryepondt, Nickel-based superalloy single crystals fabricated via electron beam melting, Acta Mater. 216 (2021) 117133. https://doi.org/10.1016/J.ACTAMAT.2021.117133.

[289] Y. Zhong, L.E. Rännar, L. Liu, A. Koptyug, S. Wikman, J. Olsen, D. Cui, Z. Shen, Additive manufacturing of 316L stainless steel by electron beam melting for nuclear

fusion applications, J. Nucl. Mater. 486 (2017) 234–245. https://doi.org/10.1016/j.jnucmat.2016.12.042.

[290] C. Wang, X. Tan, E. Liu, S.B. Tor, Process parameter optimization and mechanical properties for additively manufactured stainless steel 316L parts by selective electron beam melting, Mater. Des. 147 (2018) 157–166. https://doi.org/10.1016/j.matdes.2018.03.035.

[291] C. Burkhardt, M. Wendler, R. Lehnert, M. Hauser, P. Clausnitzer, O. Volkova, H. Biermann, A. Weidner, Fine-grained microstructure without texture obtained by electron beam powder bed fusion for AISI 304 L-based stainless steel, Addit. Manuf. 69 (2023) 103539. https://doi.org/10.1016/J.ADDMA.2023.103539.

[292] J.H. Martin, B. Yahata, J. Mayer, R. Mone, E. Stonkevitch, J. Miller, M.R. O'Masta, T. Schaedler, J. Hundley, P. Callahan, T. Pollock, Grain refinement mechanisms in additively manufactured nano-functionalized aluminum, Acta Mater. 200 (2020) 1022–1037. https://doi.org/10.1016/j.actamat.2020.09.043.

[293] F. Yan, W. Xiong, E. Faierson, Grain structure control of additively manufactured metallic materials, Materials (Basel). 10 (2017) 1260. https://doi.org/10.3390/ma10111260.

[294] Q. Tan, J. Zhang, Q. Sun, Z. Fan, G. Li, Y. Yin, Y. Liu, M.X. Zhang, Inoculation treatment of an additively manufactured 2024 aluminium alloy with titanium nanoparticles, Acta Mater. (2020). https://doi.org/10.1016/j.actamat.2020.06.026.

[295] Z. Sun, B. Sun, V. Soh, C. Lee, D. Lau, F. Wei, A.K. da Silva, M. Lin, C.C. Tan, P. Wang, U. Ramamurty, Laser powder bed fusion of crack-susceptible stainless maraging steel undergoing solid-state phase transformations, Acta Mater. 263 (2024) 119534. https://doi.org/10.1016/J.ACTAMAT.2023.119534.

[296] M.L. Montero-Sistiaga, S. Pourbabak, J. Van Humbeeck, D. Schryvers, K. Vanmeensel, Microstructure and mechanical properties of Hastelloy X produced by HP-SLM (high power selective laser melting), Mater. Des. 165 (2019) 107598. https://doi.org/10.1016/j.matdes.2019.107598.

[297] C.J. Todaro, M.A. Easton, D. Qiu, D. Zhang, M.J. Bermingham, E.W. Lui, M. Brandt, D.H. StJohn, M. Qian, Grain structure control during metal 3D printing by high-intensity ultrasound, Nat. Commun. 11 (2020) 142. https://doi.org/10.1038/s41467-019-13874-z.

[298] C.J. Todaro, M.A. Easton, D. Qiu, M. Brandt, D.H. StJohn, M. Qian, Grain refinement of stainless steel in ultrasound-assisted additive manufacturing, Addit. Manuf. 37 (2021) 101632. https://doi.org/10.1016/j.addma.2020.101632.

[299] Z. Zou, M. Simonelli, J. Katrib, G. Dimitrakis, R. Hague, Refinement of the grain structure of additive manufactured titanium alloys via epitaxial recrystallization enabled by rapid heat treatment, Scr. Mater. 180 (2020) 66–70. https://doi.org/10.1016/j.scriptamat.2020.01.027.

[300] X. Yu, X. Lin, F. Liu, L. Wang, Y. Tang, J. Li, S. Zhang, W. Huang, Influence of post-heat-treatment on the microstructure and fracture toughness properties of Inconel 718 fabricated with laser directed energy deposition additive manufacturing, Mater. Sci. Eng. A. 798 (2020) 140092. https://doi.org/10.1016/j.msea.2020.140092.

[301] W. Kurz, B. Giovanola, R. Trivedi, Theory of microstructural development during rapid solidification, Acta Metall. 34 (1986) 823–830. https://doi.org/10.1016/0001-6160(86)90056-8.

[302] Z. Wang, J. Wang, X. Lin, N. Kang, T. Zhang, Y. Wang, L. Wang, C. Dang, W. Huang, Solidification microstructure evolution and its correlations with mechanical properties and damping capacities of Mg-Al-based alloy fabricated using wire and arc additive manufacturing, J. Mater. Sci. Technol. 144 (2023) 28–44. https://doi.org/10.1016/J.JMST.2022.10.019.

[303] X. Lin, Y. Li, M. Wang, L. Feng, J. Chen, W. Huang, Columnar to equiaxed transition during alloy solidification, Sci. China, Ser. E Technol. Sci. 46 (2003) 475–489. https://doi.org/10.1360/02YE0337/METRICS.

[304] M. Ansari, A. Martinez-Marchese, M. Khamooshi, A. Keshavarzkermani, R. Esmaeilizadeh, E. Toyserkani, Analytical modeling of multi-track powder-fed laser directed energy deposition: On the relationships among process, deposition dimensions, and solidification microstructure in additively manufactured near-β titanium alloy, J. Mater. Process. Technol. 306 (2022) 117643. https://doi.org/10.1016/J.JMATPROTEC.2022.117643.

[305] H.R. Abedi, O.A. Ojo, Numerical Modeling of Gas Tungsten Arc Welding of a Newly Developed Cobalt-Based Superalloy, Metall. Mater. Trans. A Phys. Metall. Mater. Sci. 52 (2021) 5043–5054. https://doi.org/10.1007/S11661-021-06451-X/FIGURES/19.

[306] A.K. Singh, Y. Mundada, P. Bajaj, M.B. Wilms, J.P. Patil, S.K. Mishra, A. Arora, Microstructure engineering during directed energy deposition of Al-0.5Sc-0.5Si using heated build platform, Int. J. Heat Mass Transf. 202 (2023) 123679. https://doi.org/10.1016/J.IJHEATMASSTRANSFER.2022.123679.

[307] Y. Wang, X. Lin, Y. Zhao, Z. Wang, X. Yu, X. Gao, W. Huang, Laser powder bed fusion of Zr-modified Al-Cu-Mg alloy: Processability and elevated-temperature mechanical properties, J. Mater. Sci. Technol. 136 (2023) 223–235. https://doi.org/10.1016/J.JMST.2022.07.027.

[308] Z. Wang, X. Lin, L. Wang, Y. Cao, Y. Zhou, W. Huang, Microstructure evolution and mechanical properties of the wire + arc additive manufacturing Al-Cu alloy, Addit. Manuf. 47 (2021) 102298. https://doi.org/10.1016/J.ADDMA.2021.102298.

[309] W.E. King, H.D. Barth, V.M. Castillo, G.F. Gallegos, J.W. Gibbs, D.E. Hahn, C. Kamath, A.M. Rubenchik, Observation of keyhole-mode laser melting in laser powder-bed fusion additive manufacturing, J. Mater. Process. Technol. 214 (2014) 2915–2925. https://doi.org/https://doi.org/10.1016/j.jmatprotec.2014.06.005.

[310] F. Wei, S. Wei, K.B. Lau, W.H. Teh, J.J. Lee, H.L. Seng, C.C. Tan, P. Wang, U. Ramamurty, Compositionally graded AlxCoCrFeNi high-entropy alloy manufactured by laser powder bed fusion, Materialia. 21 (2022). https://doi.org/10.1016/j.mtla.2021.101308.

[311] S. Huang, R.L. Narayan, J.H.K. Tan, S.L. Sing, W.Y. Yeong, Resolving the porosity-unmelted inclusion dilemma during in-situ alloying of Ti34Nb via laser powder bed fusion, Acta Mater. 204 (2021). https://doi.org/10.1016/j.actamat.2020.116522.

[312] S. Wei, Y. Zhao, S.H. Li, S. Chen, K.B. Lau, V. Soh, J.J. Lee, B. Zhang, C.C. Tan, P. Wang, U. Ramamurty, Laser powder bed fusion of a Cu-Ni-Al alloy using the

compositional grading approach, Scr. Mater. 231 (2023) 115441. https://doi.org/10.1016/J.SCRIPTAMAT.2023.115441.

[313] J. Radhakrishnan, P. Kumar, S. Li, Y. Zhao, U. Ramamurty, Unnotched fatigue of Inconel 718 produced by laser beam-powder bed fusion at 25 and 600°C, Acta Mater. 225 (2022) 117565.

[314] M. Grasso, B.M. Colosimo, Process defects and in situ monitoring methods in metal powder bed fusion: a review, Meas. Sci. Technol. 28 (2017) 44005.

[315] M. Grasso, B.M. Colosimo, Process defects and in situ monitoring methods in metal powder bed fusion: a review, Meas. Sci. Technol. 28 (2017) 044005. https://doi.org/10.1088/1361-6501/AA5C4F.

[316] A. Sola, A. Nouri, Microstructural porosity in additive manufacturing: The formation and detection of pores in metal parts fabricated by powder bed fusion, J. Adv. Manuf. Process. 1 (2019). https://doi.org/10.1002/AMP2.10021.

[317] R. Cunningham, A. Nicolas, J. Madsen, E. Fodran, E. Anagnostou, M.D. Sangid, A.D. Rollett, Analyzing the effects of powder and post-processing on porosity and properties of electron beam melted Ti-6Al-4V, Mater. Res. Lett. 5 (2017) 516–525. https://doi.org/10.1080/21663831.2017.1340911.

[318] C.L.A. Leung, S. Marussi, M. Towrie, R.C. Atwood, P.J. Withers, P.D. Lee, The effect of powder oxidation on defect formation in laser additive manufacturing, Acta Mater. 166 (2019) 294–305. https://doi.org/10.1016/J.ACTAMAT.2018.12.027.

[319] N.T. Aboulkhair, N.M. Everitt, I. Ashcroft, C. Tuck, Reducing porosity in AlSi10Mg parts processed by selective laser melting, Addit. Manuf. 1–4 (2014) 77–86. https://doi.org/10.1016/J.ADDMA.2014.08.001.

[320] J. Ren, Y. Zhang, D. Zhao, Y. Chen, S. Guan, Y. Liu, L. Liu, S. Peng, F. Kong, J.D. Poplawsky, G. Gao, T. Voisin, K. An, Y.M. Wang, K.Y. Xie, T. Zhu, W. Chen, Strong yet ductile nanolamellar high-entropy alloys by additive manufacturing, Nature. 608 (2022) 62–68. https://doi.org/10.1038/s41586-022-04914-8.

[321] L. Liu, Q. Ding, Y. Zhong, J. Zou, J. Wu, Y.-L. Chiu, J. Li, Z. Zhang, Q. Yu, Z. Shen, Dislocation network in additive manufactured steel breaks strength–ductility trade-off, Mater. Today. 21 (2018) 354–361.

[322] S.H. Li, Y. Zhao, P. Kumar, U. Ramamurty, Effect of initial dislocation density on the plastic deformation response of 316L stainless steel manufactured by directed energy deposition, Mater. Sci. Eng. A. 851 (2022) 143591. https://doi.org/10.1016/J.MSEA.2022.143591.

[323] S.-H.H. Li, Y. Zhao, J. Radhakrishnan, U. Ramamurty, A micropillar compression investigation into the plastic flow properties of additively manufactured alloys, Acta Mater. 240 (2022) 118290.

[324] M.J. Paul, Q. Liu, J.P. Best, X. Li, J.J. Kruzic, U. Ramamurty, B. Gludovatz, Fracture resistance of AlSi10Mg fabricated by laser powder bed fusion, Acta Mater. 211 (2021). https://doi.org/10.1016/j.actamat.2021.116869.

[325] K.M. Bertsch, G. Meric de Bellefon, B. Kuehl, D.J. Thoma, Origin of dislocation structures in an additively manufactured austenitic stainless steel 316L, Acta Mater. 199 (2020) 19–33. https://doi.org/https://doi.org/10.1016/j.actamat.2020.07.063.

[326] D. Kong, C. Dong, S. Wei, X. Ni, L. Zhang, R. Li, L. Wang, C. Man, X. Li, About metastable cellular structure in additively manufactured austenitic stainless steels, Addit. Manuf. 38 (2021) 101804. https://doi.org/https://doi.org/10.1016/j.addma.2020.101804.

[327] H.L. Wei, J.W. Elmer, T. DebRoy, Three-dimensional modeling of grain structure evolution during welding of an aluminum alloy, Acta Mater. 126 (2017) 413–425. https://doi.org/10.1016/j.actamat.2016.12.073.

[328] M.S. Pham, B. Dovgyy, P.A. Hooper, C.M. Gourlay, A. Piglione, The role of side-branching in microstructure development in laser powder-bed fusion, Nat. Commun. 2020 111. 11 (2020) 1–12. https://doi.org/10.1038/s41467-020-14453-3.

[329] Q. Ding, Y. Zhang, X. Chen, X. Fu, D. Chen, S. Chen, L. Gu, F. Wei, H. Bei, Y. Gao, M. Wen, J. Li, Z. Zhang, T. Zhu, R.O. Ritchie, Q. Yu, Tuning element distribution, structure and properties by composition in high-entropy alloys, Nature. 574 (2019) 223–227. https://doi.org/10.1038/s41586-019-1617-1.

[330] S.H. Li, Y. Zhao, U. Ramamurty, Role of the solidification cells on the yield strength of the Al-Si-Mg alloy manufactured using laser powder bed fusion: A micropillar compression study, Scr. Mater. 234 (2023) 115566. https://doi.org/10.1016/J.SCRIPTAMAT.2023.115566.

[331] S. Dryepondt, P. Nandwana, K.A. Unocic, R. Kannan, P. Fernandez Zelaia, F.A. List, High temperature high strength austenitic steel fabricated by laser powder-bed fusion, Acta Mater. 231 (2022) 117876. https://doi.org/https://doi.org/10.1016/j.actamat.2022.117876.

[332] T.H. Becker, P. Kumar, U. Ramamurty, Fracture and fatigue in additively manufactured metals, Acta Mater. 219 (2021) 117240. https://doi.org/10.1016/J.ACTAMAT.2021.117240.

[333] Z.G. Zhu, X.H. An, W.J. Lu, Z.M. Li, F.L. Ng, X.Z. Liao, U. Ramamurty, S.M.L. Nai, J. Wei, Selective laser melting enabling the hierarchically heterogeneous microstructure and excellent mechanical properties in an interstitial solute strengthened high entropy alloy, Mater. Res. Lett. 7 (2019) 453–459. https://doi.org/10.1080/21663831.2019.1650131/SUPPL_FILE/TMRL_A_1650131_SM4652.DOCX.

[334] S.L. Sing, S. Huang, G.D. Goh, G.L. Goh, C.F. Tey, J.H.K. Tan, W.Y. Yeong, Emerging metallic systems for additive manufacturing: In-situ alloying and multi-metal processing in laser powder bed fusion, Prog. Mater. Sci. 119 (2021) 100795. https://doi.org/10.1016/J.PMATSCI.2021.100795.

[335] M. Simonelli, N.T. Aboulkhair, P. Cohen, J.W. Murray, A.T. Clare, C. Tuck, R.J.M. Hague, A comparison of Ti-6Al-4V in-situ alloying in Selective Laser Melting using simply-mixed and satellited powder blend feedstocks, Mater. Charact. 143 (2018) 118–126. https://doi.org/10.1016/J.MATCHAR.2018.05.039.

[336] S. Huang, P. Kumar, W.Y. Yeong, R.L. Narayan, U. Ramamurty, Fracture behavior of laser powder bed fusion fabricated Ti41Nb via in-situ alloying, Acta Mater. 225 (2022) 117593. https://doi.org/10.1016/J.ACTAMAT.2021.117593.

[337] H. Li, S. Thomas, C. Hutchinson, Delivering microstructural complexity to additively manufactured metals through controlled mesoscale chemical heterogeneity, Acta

Mater. 226 (2022) 117637. https://doi.org/10.1016/J.ACTAMAT.2022.117637.

[338] T. Zhang, Z. Huang, T. Yang, H. Kong, J. Luan, A. Wang, D. Wang, W. Kuo, Y. Wang, C.T. Liu, In situ design of advanced titanium alloy with concentration modulations by additive manufacturing, Science (80-.). 374 (2021) 478–482. https://doi.org/10.1126/SCIENCE.ABJ3770/SUPPL_FILE/SCIENCE.ABJ3770_SM.PDF.

[339] L. Yao, S. Huang, U. Ramamurty, Z. Xiao, On the formation of “Fish-scale” morphology with curved grain interfacial microstructures during selective laser melting of dissimilar alloys, Acta Mater. 220 (2021) 117331. https://doi.org/10.1016/J.ACTAMAT.2021.117331.

[340] C. Wei, L. Liu, Y. Gu, Y. Huang, Q. Chen, Z. Li, L. Li, Multi-material additive-manufacturing of tungsten - copper alloy bimetallic structure with a stainless-steel interlayer and associated bonding mechanisms, Addit. Manuf. 50 (2022) 102574. https://doi.org/10.1016/J.ADDMA.2021.102574.

[341] S. Wei, Y. Zhao, B. Zhang, P. Wang, U. Ramamurty, Mesoscopic chemical heterogeneities in laser powder bed fused CoCrMo and Ni mixed powders and their effect on the mechanical properties, Mater. Sci. Eng. A. 888 (2023) 145795. https://doi.org/10.1016/J.MSEA.2023.145795.

[342] K.G. Prashanth, J. Eckert, Formation of metastable cellular microstructures in selective laser melted alloys, J. Alloys Compd. 707 (2017) 27–34. https://doi.org/10.1016/j.jallcom.2016.12.209.

[343] S. Sui, H. Tan, J. Chen, C. Zhong, Z. Li, W. Fan, A. Gasser, W. Huang, The influence of Laves phases on the room temperature tensile properties of Inconel 718 fabricated by powder feeding laser additive manufacturing, Acta Mater. 164 (2019) 413–427. https://doi.org/10.1016/J.ACTAMAT.2018.10.032.

[344] K. Saeidi, X. Gao, Y. Zhong, Z.J. Shen, Hardened austenite steel with columnar sub-grain structure formed by laser melting, Mater. Sci. Eng. A. 625 (2015) 221–229. https://doi.org/10.1016/j.msea.2014.12.018.

[345] Y. Zhong, L. Liu, S. Wikman, D. Cui, Z. Shen, Intragranular cellular segregation network structure strengthening 316L stainless steel prepared by selective laser melting, J. Nucl. Mater. 470 (2016) 170–178. https://doi.org/10.1016/J.JNUCMAT.2015.12.034.

[346] X. Lou, P.L. Andresen, R.B. Rebak, Oxide inclusions in laser additive manufactured stainless steel and their effects on impact toughness and stress corrosion cracking behavior, J. Nucl. Mater. 499 (2018) 182–190. https://doi.org/10.1016/J.JNUCMAT.2017.11.036.

[347] E. Liverani, S. Toschi, L. Ceschini, A. Fortunato, Effect of selective laser melting (SLM) process parameters on microstructure and mechanical properties of 316L austenitic stainless steel, J. Mater. Process. Technol. 249 (2017) 255–263. https://doi.org/10.1016/j.jmatprotec.2017.05.042.

[348] Y.M. Wang, T. Voisin, J.T. McKeown, J. Ye, N.P. Calta, Z. Li, Z. Zeng, Y. Zhang, W. Chen, T.T. Roehling, R.T. Ott, M.K. Santala, P.J. Depond, M.J. Matthews, A. V. Hamza, T. Zhu, Additively manufactured hierarchical stainless steels with high strength and ductility, Nat. Mater. (2018). https://doi.org/10.1038/NMAT5021.

[349] T. Voisin, J.B. Forien, A. Perron, S. Aubry, N. Bertin, A. Samanta, A. Baker, Y.M. Wang, New insights on cellular structures strengthening mechanisms and thermal stability of an austenitic stainless steel fabricated by laser powder-bed-fusion, Acta Mater. 203 (2021) 116476. https://doi.org/10.1016/j.actamat.2020.11.018.

[350] H. Choo, K.L. Sham, J. Bohling, A. Ngo, X. Xiao, Y. Ren, P.J. Depond, M.J. Matthews, E. Garlea, Effect of laser power on defect, texture, and microstructure of a laser powder bed fusion processed 316L stainless steel, Mater. Des. 164 (2019) 107534. https://doi.org/10.1016/j.matdes.2018.12.006.

[351] A. Yadollahi, N. Shamsaei, S.M. Thompson, D.W. Seely, Effects of process time interval and heat treatment on the mechanical and microstructural properties of direct laser deposited 316L stainless steel, Mater. Sci. Eng. A. 644 (2015) 171–183. https://doi.org/10.1016/J.MSEA.2015.07.056.

[352] M. Ziętala, T. Durejko, M. Polański, I. Kunce, T. Płociński, W. Zieliński, M. Łazińska, W. Stępniowski, T. Czujko, K.J. Kurzydłowski, Z. Bojar, The microstructure, mechanical properties and corrosion resistance of 316L stainless steel fabricated using laser engineered net shaping, Mater. Sci. Eng. A. 677 (2016) 1–10. https://doi.org/10.1016/j.msea.2016.09.028.

[353] A. Saboori, G. Piscopo, M. Lai, A. Salmi, S. Biamino, An investigation on the effect of deposition pattern on the microstructure, mechanical properties and residual stress of 316L produced by Directed Energy Deposition, Mater. Sci. Eng. A. 780 (2020) 139179. https://doi.org/10.1016/J.MSEA.2020.139179.

[354] B. Zheng, J.C. Haley, N. Yang, J. Yee, K.W. Terrassa, Y. Zhou, E.J. Lavernia, J.M. Schoenung, On the evolution of microstructure and defect control in 316L SS components fabricated via directed energy deposition, Mater. Sci. Eng. A. 764 (2019) 138243. https://doi.org/10.1016/J.MSEA.2019.138243.

[355] M. Ma, Z. Wang, X. Zeng, Effect of energy input on microstructural evolution of direct laser fabricated IN718 alloy, Mater. Charact. 106 (2015) 420–427. https://doi.org/10.1016/j.matchar.2015.06.027.

[356] R. Jayaraj Radhakrishnan, P. Kumar, H.L. Seet, S.M.L. Nai, P. Wang, U. Ramamurty, Cascading of the as-built microstructure through heat treatment and its role on the tensile properties of laser powder bed fused Inconel 718, Materialia. 21 (2022) 101272. https://doi.org/10.1016/j.mtla.2021.101272.

[357] F. Liu, F. Lyu, F. Liu, X. Lin, C. Huang, Laves phase control of inconel 718 superalloy fabricated by laser direct energy deposition via δ aging and solution treatment, J. Mater. Res. Technol. 9 (2020) 9753–9765. https://doi.org/10.1016/J.JMRT.2020.06.061.

[358] L.M. Sochalski-Kolbus, E.A. Payzant, P.A. Cornwell, T.R. Watkins, S.S. Babu, R.R. Dehoff, M. Lorenz, O. Ovchinnikova, C. Duty, Comparison of Residual Stresses in Inconel 718 Simple Parts Made by Electron Beam Melting and Direct Laser Metal Sintering, Metall. Mater. Trans. A Phys. Metall. Mater. Sci. 46 (2015) 1419–1432. https://doi.org/10.1007/s11661-014-2722-2.

[359] P. Kumar, O. Prakash, U. Ramamurty, Micro-and meso-structures and their influence on mechanical properties of selectively laser melted Ti-6Al-4V, Acta Mater. 154 (2018) 246–260. https://doi.org/10.1016/J.ACTAMAT.2018.05.044.

[360] S. Liu, Y.C. Shin, Additive manufacturing of Ti6Al4V alloy: A review, Mater. Des. (2019). https://doi.org/10.1016/j.matdes.2018.107552.

[361] R.I. Revilla, I. De Graeve, Influence of Si Content on the Microstructure and Corrosion Behavior of Additive Manufactured Al-Si Alloys, J. Electrochem. Soc. 165 (2018) C926–C932. https://doi.org/10.1149/2.0101814JES/XML.

[362] M.J. Paul, T. Klein, C. Simson, J. Niedermayer, J.J. Kruzic, B. Gludovatz, Strength and fracture resistance of in-situ alloyed compositionally-graded Al-Si processed by dual-wire arc directed energy deposition, Addit. Manuf. 60 (2022) 103291. https://doi.org/10.1016/J.ADDMA.2022.103291.

[363] H. Bian, K. Aoyagi, Y. Zhao, C. Maeda, T. Mouri, A. Chiba, Microstructure refinement for superior ductility of Al–Si alloy by electron beam melting, Addit. Manuf. 32 (2020) 100982. https://doi.org/10.1016/J.ADDMA.2019.100982.

[364] L.E. Rännar, A. Koptyug, J. Olsén, K. Saeidi, Z. Shen, Hierarchical structures of stainless steel 316L manufactured by Electron Beam Melting, Addit. Manuf. 17 (2017) 106–112. https://doi.org/10.1016/J.ADDMA.2017.07.003.

[365] L.E. Murr, E. Martinez, J. Hernandez, S. Collins, K.N. Amato, S.M. Gaytan, P.W. Shindo, Microstructures and Properties of 17-4 PH Stainless Steel Fabricated by Selective Laser Melting, J. Mater. Res. Technol. 1 (2012) 167–177. https://doi.org/10.1016/S2238-7854(12)70029-7.

[366] A. Yadollahi, N. Shamsaei, S.M. Thompson, A. Elwany, L. Bian, Effects of building orientation and heat treatment on fatigue behavior of selective laser melted 17-4 PH stainless steel, Int. J. Fatigue. 94 (2017) 218–235. https://doi.org/10.1016/j.ijfatigue.2016.03.014.

[367] H.K. Rafi, D. Pal, N. Patil, T.L. Starr, B.E. Stucker, Microstructure and Mechanical Behavior of 17-4 Precipitation Hardenable Steel Processed by Selective Laser Melting, J. Mater. Eng. Perform. 23 (2014) 4421–4428. https://doi.org/10.1007/S11665-014-1226-Y/FIGURES/8.

[368] M. Alnajjar, F. Christien, K. Wolski, C. Bosch, Evidence of austenite by-passing in a stainless steel obtained from laser melting additive manufacturing, Addit. Manuf. 25 (2019) 187–195. https://doi.org/10.1016/J.ADDMA.2018.11.004.

[369] H. Berns, V. Gavriljuk, B. Shanina, Intensive Interstitial Strengthening of Stainless Steels, Adv. Eng. Mater. 10 (2008) 1083–1093. https://doi.org/10.1002/ADEM.200800214.

[370] S. Vunnam, A. Saboo, C. Sudbrack, T.L. Starr, Effect of powder chemical composition on the as-built microstructure of 17-4 PH stainless steel processed by selective laser melting, Addit. Manuf. 30 (2019) 100876. https://doi.org/10.1016/J.ADDMA.2019.100876.

[371] M.S. Moyle, N. Haghdadi, X.Z. Liao, S.P. Ringer, S. Primig, On the microstructure and texture evolution in 17-4 PH stainless steel during laser powder bed fusion: Towards textural design, J. Mater. Sci. Technol. 117 (2022) 183–195. https://doi.org/10.1016/J.JMST.2021.12.015.

[372] M.P. Haines, M.S. Moyle, V. V. Rielli, V. Luzin, N. Haghdadi, S. Primig, Experimental and computational analysis of site-specific formation of phases in laser

powder bed fusion 17–4 precipitate hardened stainless steel, Addit. Manuf. 73 (2023) 103686. https://doi.org/10.1016/J.ADDMA.2023.103686.

[373] M.P. Haines, M.S. Moyle, V. V. Rielli, N. Haghdadi, S. Primig, Site-specific Cu clustering and precipitation in laser powder-bed fusion 17–4 PH stainless steel, Scr. Mater. 241 (2024) 115891. https://doi.org/10.1016/J.SCRIPTAMAT.2023.115891.

[374] A. Hilaire, E. Andrieu, X. Wu, High-temperature mechanical properties of alloy 718 produced by laser powder bed fusion with different processing parameters, Addit. Manuf. 26 (2019) 147–160. https://doi.org/10.1016/j.addma.2019.01.012.

[375] S. Ghorbanpour, M.E. Alam, N.C. Ferreri, A. Kumar, B.A. McWilliams, S.C. Vogel, J. Bicknell, I.J. Beyerlein, M. Knezevic, Experimental characterization and crystal plasticity modeling of anisotropy, tension-compression asymmetry, and texture evolution of additively manufactured Inconel 718 at room and elevated temperatures, Int. J. Plast. 125 (2020) 63–79. https://doi.org/10.1016/j.ijplas.2019.09.002.

[376] Q. Jia, D. Gu, Selective laser melting additive manufacturing of Inconel 718 superalloy parts: Densification, microstructure and properties, J. Alloys Compd. 585 (2014) 713–721. https://doi.org/10.1016/j.jallcom.2013.09.171.

[377] Y.N. Zhang, X. Cao, P. Wanjara, M. Medraj, Oxide films in laser additive manufactured Inconel 718, Acta Mater. 61 (2013) 6562–6576. https://doi.org/10.1016/j.actamat.2013.07.039.

[378] S.Y. Liu, H.Q. Li, C.X. Qin, R. Zong, X.Y. Fang, The effect of energy density on texture and mechanical anisotropy in selective laser melted Inconel 718, Mater. Des. 191 (2020) 108642. https://doi.org/10.1016/J.MATDES.2020.108642.

[379] M. Ni, C. Chen, X. Wang, P. Wang, R. Li, X. Zhang, K. Zhou, Anisotropic tensile behavior of in situ precipitation strengthened Inconel 718 fabricated by additive manufacturing, Mater. Sci. Eng. A. 701 (2017) 344–351. https://doi.org/10.1016/j.msea.2017.06.098.

[380] O. Gokcekaya, T. Ishimoto, S. Hibino, J. Yasutomi, T. Narushima, T. Nakano, Unique crystallographic texture formation in Inconel 718 by laser powder bed fusion and its effect on mechanical anisotropy, Acta Mater. 212 (2021) 116876. https://doi.org/10.1016/J.ACTAMAT.2021.116876.

[381] P.D. Nezhadfar, A.S. Johnson, N. Shamsaei, Fatigue behavior and microstructural evolution of additively manufactured Inconel 718 under cyclic loading at elevated temperature, Int. J. Fatigue. 136 (2020) 105598. https://doi.org/10.1016/J.IJFATIGUE.2020.105598.

[382] Z. Wang, K. Guan, M. Gao, X. Li, X. Chen, X. Zeng, The microstructure and mechanical properties of deposited-IN718 by selective laser melting, J. Alloys Compd. 513 (2012) 518–523. https://doi.org/10.1016/j.jallcom.2011.10.107.

[383] E. Chlebus, K. Gruber, B. Kuźnicka, J. Kurzac, T. Kurzynowski, Effect of heat treatment on the microstructure and mechanical properties of Inconel 718 processed by selective laser melting, Mater. Sci. Eng. A. 639 (2015) 647–655. https://doi.org/10.1016/J.MSEA.2015.05.035.

[384] D. Zhang, W. Niu, X. Cao, Z. Liu, Effect of standard heat treatment on the microstructure and mechanical properties of selective laser melting manufactured

Inconel 718 superalloy, Mater. Sci. Eng. A. 644 (2015) 32–40. https://doi.org/10.1016/J.MSEA.2015.06.021.

[385] M.E. Aydinöz, F. Brenne, M. Schaper, C. Schaak, W. Tillmann, J. Nellesen, T. Niendorf, On the microstructural and mechanical properties of post-treated additively manufactured Inconel 718 superalloy under quasi-static and cyclic loading, Mater. Sci. Eng. A. 669 (2016) 246–258. https://doi.org/10.1016/J.MSEA.2016.05.089.

[386] W. Huang, J. Yang, H. Yang, G. Jing, Z. Wang, X. Zeng, Heat treatment of Inconel 718 produced by selective laser melting: Microstructure and mechanical properties, Mater. Sci. Eng. A. 750 (2019) 98–107. https://doi.org/10.1016/J.MSEA.2019.02.046.

[387] J.R. Zhao, F.Y. Hung, T.S. Lui, Microstructure and tensile fracture behavior of three-stage heat treated inconel 718 alloy produced via laser powder bed fusion process, J. Mater. Res. Technol. 9 (2020) 3357–3367. https://doi.org/10.1016/J.JMRT.2020.01.030.

[388] S.H. Sun, Y. Koizumi, T. Saito, K. Yamanaka, Y.P. Li, Y. Cui, A. Chiba, Electron beam additive manufacturing of Inconel 718 alloy rods: Impact of build direction on microstructure and high-temperature tensile properties, Addit. Manuf. 23 (2018) 457–470. https://doi.org/10.1016/J.ADDMA.2018.08.017.

[389] D. Deng, J. Moverare, R.L. Peng, H. Söderberg, Microstructure and anisotropic mechanical properties of EBM manufactured Inconel 718 and effects of post heat treatments, Mater. Sci. Eng. A. 693 (2017) 151–163. https://doi.org/10.1016/J.MSEA.2017.03.085.

[390] M.M. Kirka, K.A. Unocic, N. Raghavan, F. Medina, R.R. Dehoff, S.S. Babu, Microstructure Development in Electron Beam-Melted Inconel 718 and Associated Tensile Properties, JOM. 68 (2016) 1012–1020. https://doi.org/10.1007/S11837-016-1812-6/METRICS.

[391] L. Thijs, F. Verhaeghe, T. Craeghs, J. Van Humbeeck, J.P. Kruth, A study of the microstructural evolution during selective laser melting of Ti-6Al-4V, Acta Mater. 58 (2010) 3303–3312. https://doi.org/10.1016/j.actamat.2010.02.004.

[392] J.C. Heigel, P. Michaleris, E.W. Reutzel, Thermo-mechanical model development and validation of directed energy deposition additive manufacturing of Ti–6Al–4V, Addit. Manuf. 5 (2015) 9–19. https://doi.org/10.1016/J.ADDMA.2014.10.003.

[393] Y. Zhai, D.A. Lados, E.J. Brown, G.N. Vigilante, Understanding the microstructure and mechanical properties of Ti-6Al-4V and Inconel 718 alloys manufactured by Laser Engineered Net Shaping, Addit. Manuf. 27 (2019) 334–344. https://doi.org/10.1016/j.addma.2019.02.017.

[394] W. Xu, M. Brandt, S. Sun, J. Elambasseril, Q. Liu, K. Latham, K. Xia, M. Qian, Additive manufacturing of strong and ductile Ti-6Al-4V by selective laser melting via in situ martensite decomposition, Acta Mater. 85 (2015) 74–84. https://doi.org/10.1016/j.actamat.2014.11.028.

[395] X. Tan, Y. Kok, W.Q. Toh, Y.J. Tan, M. Descoins, D. Mangelinck, S.B. Tor, K.F. Leong, C.K. Chua, Revealing martensitic transformation and α/β interface evolution in electron beam melting three-dimensional-printed Ti-6Al-4V, Sci. Rep. (2016). https://doi.org/10.1038/srep26039.

[396] P. Kumar, U. Ramamurty, Microstructural optimization through heat treatment for enhancing the fracture toughness and fatigue crack growth resistance of selective laser melted Ti6Al4V alloy, Acta Mater. 169 (2019) 45–59. https://doi.org/10.1016/J.ACTAMAT.2019.03.003.

[397] A. Grabowski, T. Florian, J. Wieczorek, M. Adamiak, Structuring of the Ti6Al4V alloy surface by pulsed laser remelting, Appl. Surf. Sci. 535 (2021) 147618. https://doi.org/10.1016/J.APSUSC.2020.147618.

[398] Y. Cai, Z. Peng, J. Chen, H. Chen, J. Xiong, Grain refinement and anisotropy improvement of arc-directed energy deposited Ti–6Al–4V with oscillating laser, Mater. Sci. Eng. A. 893 (2024) 146144. https://doi.org/10.1016/J.MSEA.2024.146144.

[399] Y. Wang, G. Yang, S. Zhou, C. Sun, B. Li, D. An, S. Zhang, S. Xiu, Effect of laser remelting on microstructure and mechanical properties of Ti–6Al–4V alloy prepared by inside-beam powder feeding, Mater. Sci. Eng. A. 861 (2022) 144266. https://doi.org/10.1016/J.MSEA.2022.144266.

[400] K. Hu, W. Gao, S. Wang, X. Jiang, H. Yu, D. Sun, The relationship between an input energy density and the microstructure evolution of the Ti-6Al-4V alloy via laser remelting, Mater. Charact. 209 (2024) 113703. https://doi.org/10.1016/J.MATCHAR.2024.113703.

[401] M. Yan, M.S. Dargusch, T. Ebel, M. Qian, A transmission electron microscopy and three-dimensional atom probe study of the oxygen-induced fine microstructural features in as-sintered Ti–6Al–4V and their impacts on ductility, Acta Mater. 68 (2014) 196–206. https://doi.org/10.1016/J.ACTAMAT.2014.01.015.

[402] J. Suryawanshi, K.G. Prashanth, S. Scudino, J. Eckert, O. Prakash, U. Ramamurty, Simultaneous enhancements of strength and toughness in an Al-12Si alloy synthesized using selective laser melting, Acta Mater. 115 (2016) 285–294. https://doi.org/10.1016/j.actamat.2016.06.009.

[403] L.P. Lam, D.Q. Zhang, Z.H. Liu, C.K. Chua, Phase analysis and microstructure characterisation of AlSi10Mg parts produced by Selective Laser Melting, Https://Doi.Org.Remotexs.Ntu.Edu.Sg/10.1080/17452759.2015.1110868. 10 (2015) 207–215. https://doi.org/10.1080/17452759.2015.1110868.

[404] Q. Yan, B. Song, Y. Shi, Comparative study of performance comparison of AlSi10Mg alloy prepared by selective laser melting and casting, J. Mater. Sci. Technol. 41 (2020) 199–208. https://doi.org/10.1016/J.JMST.2019.08.049.

[405] T. Hanemann, L.N. Carter, M. Habschied, N.J.E. Adkins, M.M. Attallah, M. Heilmaier, In-situ alloying of AlSi10Mg+Si using Selective Laser Melting to control the coefficient of thermal expansion, J. Alloys Compd. 795 (2019) 8–18. https://doi.org/10.1016/j.jallcom.2019.04.260.

[406] W.H. Kan, Y. Nadot, M. Foley, L. Ridosz, G. Proust, J.M. Cairney, Factors that affect the properties of additively-manufactured AlSi10Mg: Porosity versus microstructure, Addit. Manuf. 29 (2019) 100805. https://doi.org/10.1016/J.ADDMA.2019.100805.

[407] J.H. Rao, Y. Zhang, K. Zhang, A. Huang, C.H.J. Davies, X. Wu, Multiple precipitation pathways in an Al-7Si-0.6Mg alloy fabricated by selective laser melting, Scr. Mater. 160 (2019) 66–69. https://doi.org/10.1016/J.SCRIPTAMAT.2018.09.045.

[408] M. Cabrini, F. Calignano, P. Fino, S. Lorenzi, M. Lorusso, D. Manfredi, C. Testa, T. Pastore, Corrosion Behavior of Heat-Treated AlSi10Mg Manufactured by Laser Powder Bed Fusion, Mater. 2018, Vol. 11, Page 1051. 11 (2018) 1051. https://doi.org/10.3390/MA11071051.

[409] S. Marola, D. Manfredi, G. Fiore, M.G. Poletti, M. Lombardi, P. Fino, L. Battezzati, A comparison of Selective Laser Melting with bulk rapid solidification of AlSi10Mg alloy, J. Alloys Compd. 742 (2018) 271–279. https://doi.org/10.1016/J.JALLCOM.2018.01.309.

[410] D.M. Xu, G.Q. Li, X.L. Wan, R.L. Xiong, G. Xu, K.M. Wu, M.C. Somani, R.D.K. Misra, Deformation behavior of high yield strength – High ductility ultrafine-grained 316LN austenitic stainless steel, Mater. Sci. Eng. A. 688 (2017) 407–415. https://doi.org/10.1016/j.msea.2017.02.009.

[411] X.P. Li, G. Ji, Z. Chen, A. Addad, Y. Wu, H.W. Wang, J. Vleugels, J. Van Humbeeck, J.P. Kruth, Selective laser melting of nano-TiB2 decorated AlSi10Mg alloy with high fracture strength and ductility, Acta Mater. 129 (2017) 183–193. https://doi.org/10.1016/J.ACTAMAT.2017.02.062.

[412] G. Langelandsvik, A. Horgar, T. Furu, H.J. Roven, O.M. Akselsen, Comparative study of eutectic Al-Si alloys manufactured by WAAM and casting, Int. J. Adv. Manuf. Technol. 110 (2020) 935–947. https://doi.org/10.1007/S00170-020-05735-7/FIGURES/17.

[413] Q. Miao, D. Wu, D. Chai, Y. Zhan, G. Bi, F. Niu, G. Ma, Comparative study of microstructure evaluation and mechanical properties of 4043 aluminum alloy fabricated by wire-based additive manufacturing, Mater. Des. 186 (2020) 108205. https://doi.org/10.1016/J.MATDES.2019.108205.

[414] R.A. Michi, A. Plotkowski, A. Shyam, R.R. Dehoff, S.S. Babu, Towards high-temperature applications of aluminium alloys enabled by additive manufacturing, Int. Mater. Rev. 67 (2022) 298–345. https://doi.org/10.1080/09506608.2021.1951580.

[415] C. Su, X. Chen, S. Konovalov, R. Arvind Singh, S. Jayalakshmi, L. Huang, Effect of Deposition Strategies on the Microstructure and Tensile Properties of Wire Arc Additive Manufactured Al-5Si Alloys, J. Mater. Eng. Perform. 30 (2021) 2136–2146. https://doi.org/10.1007/S11665-021-05528-3/FIGURES/12.

[416] M. Javidani, J. Arreguin-Zavala, J. Danovitch, Y. Tian, M. Brochu, Additive Manufacturing of AlSi10Mg Alloy Using Direct Energy Deposition: Microstructure and Hardness Characterization, J. Therm. Spray Technol. 26 (2017) 587–597. https://doi.org/10.1007/S11666-016-0495-4/FIGURES/11.

[417] L. Thijs, K. Kempen, J.P. Kruth, J. Van Humbeeck, Fine-structured aluminium products with controllable texture by selective laser melting of pre-alloyed AlSi10Mg powder, Acta Mater. 61 (2013) 1809–1819. https://doi.org/10.1016/J.ACTAMAT.2012.11.052.

[418] J. Wu, X.Q. Wang, W. Wang, M.M. Attallah, M.H. Loretto, Microstructure and strength of selectively laser melted AlSi10Mg, Acta Mater. 117 (2016) 311–320. https://doi.org/10.1016/J.ACTAMAT.2016.07.012.

[419] E. Louvis, P. Fox, C.J. Sutcliffe, Selective laser melting of aluminium components, J. Mater. Process. Technol. 211 (2011) 275–284.

https://doi.org/10.1016/J.JMATPROTEC.2010.09.019.

[420] H.R. Kotadia, G. Gibbons, A. Das, P.D. Howes, A review of Laser Powder Bed Fusion Additive Manufacturing of aluminium alloys: Microstructure and properties, Addit. Manuf. 46 (2021) 102155. https://doi.org/10.1016/J.ADDMA.2021.102155.

[421] J.W. Yeh, S.K. Chen, S.J. Lin, J.Y. Gan, T.S. Chin, T.T. Shun, C.H. Tsau, S.Y. Chang, Nanostructured High-Entropy Alloys with Multiple Principal Elements: Novel Alloy Design Concepts and Outcomes, Adv. Eng. Mater. 6 (2004) 299–303. https://doi.org/10.1002/ADEM.200300567.

[422] B. Cantor, I.T.H. Chang, P. Knight, A.J.B. Vincent, Microstructural development in equiatomic multicomponent alloys, Mater. Sci. Eng. A. 375–377 (2004) 213–218. https://doi.org/10.1016/J.MSEA.2003.10.257.

[423] Y. Zhang, T.T. Zuo, Z. Tang, M.C. Gao, K.A. Dahmen, P.K. Liaw, Z.P. Lu, Microstructures and properties of high-entropy alloys, Prog. Mater. Sci. 61 (2014) 1–93. https://doi.org/10.1016/J.PMATSCI.2013.10.001.

[424] S. Chen, Y. Tong, P.K. Liaw, Additive Manufacturing of High-Entropy Alloys: A Review, Entropy 2018, Vol. 20, Page 937. 20 (2018) 937. https://doi.org/10.3390/E20120937.

[425] A. Ostovari Moghaddam, N.A. Shaburova, M.N. Samodurova, A. Abdollahzadeh, E.A. Trofimov, Additive manufacturing of high entropy alloys: A practical review, J. Mater. Sci. Technol. 77 (2021) 131–162. https://doi.org/10.1016/J.JMST.2020.11.029.

[426] S. Guan, J. Ren, S. Mooraj, Y. Liu, S. Feng, S. Zhang, J. Liu, X. Fan, P.K. Liaw, W. Chen, Additive Manufacturing of High-Entropy Alloys: Microstructural Metastability and Mechanical Behavior, J. Phase Equilibria Diffus. 2021 425. 42 (2021) 748–771. https://doi.org/10.1007/S11669-021-00913-W.

[427] J. Luo, N. Zhou, High-entropy grain boundaries, Commun. Mater. 2023 41. 4 (2023) 1–8. https://doi.org/10.1038/s43246-023-00335-w.

[428] R. Babicheva, A. Jarlöv, H. Zheng, S. Dmitriev, E. Korznikova, M. Ling Sharon Nai, U. Ramamurty, K. Zhou, Effect of short-range ordering and grain boundary segregation on shear deformation of CoCrFeNi high-entropy alloys with Al addition, Comput. Mater. Sci. 215 (2022) 111762. https://doi.org/10.1016/J.COMMATSCI.2022.111762.

[429] T. He, Y. Qi, Y. Ji, M. Feng, Grain boundary segregation-induced strengthening-weakening transition and its ideal maximum strength in nanopolycrystalline FeNiCrCoCu high-entropy alloys, Int. J. Mech. Sci. 238 (2023) 107828. https://doi.org/10.1016/J.IJMECSCI.2022.107828.

[430] C. Hu, J. Luo, Data-driven prediction of grain boundary segregation and disordering in high-entropy alloys in a 5D space, Mater. Horizons. 9 (2022) 1023–1035. https://doi.org/10.1039/D1MH01204E.

[431] K. Ming, L. Li, Z. Li, X. Bi, J. Wang, Grain boundary decohesion by nanoclustering Ni and Cr separately in CrMnFeCoNi high-entropy alloys, Sci. Adv. 5 (2019). https://doi.org/10.1126/SCIADV.AAY0639/SUPPL_FILE/AAY0639_SM.PDF.

[432] J. Liu, P. Wen, Metal vaporization and its influence during laser powder bed fusion process, Mater. Des. 215 (2022) 110505.

https://doi.org/10.1016/J.MATDES.2022.110505.

[433] G. Zhang, J. Chen, M. Zheng, Z. Yan, X. Lu, X. Lin, W. Huang, Element Vaporization of Ti-6Al-4V Alloy during Selective Laser Melting, Met. 2020, Vol. 10, Page 435. 10 (2020) 435. https://doi.org/10.3390/MET10040435.

[434] L. Zhou, H. Hyer, S. Park, H. Pan, Y. Bai, K.P. Rice, Y. Sohn, Microstructure and mechanical properties of Zr-modified aluminum alloy 5083 manufactured by laser powder bed fusion, Addit. Manuf. 28 (2019) 485–496. https://doi.org/10.1016/J.ADDMA.2019.05.027.

[435] K. Wei, Z. Wang, X. Zeng, Influence of element vaporization on formability, composition, microstructure, and mechanical performance of the selective laser melted Mg–Zn–Zr components, Mater. Lett. 156 (2015) 187–190. https://doi.org/10.1016/J.MATLET.2015.05.074.

[436] K. Wei, M. Gao, Z. Wang, X. Zeng, Effect of energy input on formability, microstructure and mechanical properties of selective laser melted AZ91D magnesium alloy, Mater. Sci. Eng. A. 611 (2014) 212–222. https://doi.org/10.1016/J.MSEA.2014.05.092.

[437] Saprykin, Y.P. Sharkeev, N. Saprykina, E.A. Ibragimov, Selective Laser Melting of Magnesium, Key Eng. Mater. 839 (2020) 144–149. https://doi.org/10.4028/WWW.SCIENTIFIC.NET/KEM.839.144.

[438] N.A. Zumdick, L. Jauer, L.C. Kersting, T.N. Kutz, J.H. Schleifenbaum, D. Zander, Additive manufactured WE43 magnesium: A comparative study of the microstructure and mechanical properties with those of powder extruded and as-cast WE43, Mater. Charact. 147 (2019) 384–397. https://doi.org/10.1016/J.MATCHAR.2018.11.011.

[439] M.J. Matthews, G. Guss, S.A. Khairallah, A.M. Rubenchik, P.J. Depond, W.E. King, Denudation of metal powder layers in laser powder bed fusion processes, Acta Mater. 114 (2016) 33–42. https://doi.org/10.1016/J.ACTAMAT.2016.05.017.

[440] H. Chen, W. Yan, Spattering and denudation in laser powder bed fusion process: Multiphase flow modelling, Acta Mater. 196 (2020) 154–167. https://doi.org/10.1016/J.ACTAMAT.2020.06.033.

[441] P. Bidare, I. Bitharas, R.M. Ward, M.M. Attallah, A.J. Moore, Fluid and particle dynamics in laser powder bed fusion, Acta Mater. 142 (2018) 107–120. https://doi.org/10.1016/J.ACTAMAT.2017.09.051.

[442] Z.A. Young, Q. Guo, N.D. Parab, C. Zhao, M. Qu, L.I. Escano, K. Fezzaa, W. Everhart, T. Sun, L. Chen, Types of spatter and their features and formation mechanisms in laser powder bed fusion additive manufacturing process, Addit. Manuf. 36 (2020) 101438. https://doi.org/10.1016/J.ADDMA.2020.101438.

[443] A. Aversa, G. Marchese, A. Saboori, E. Bassini, D. Manfredi, S. Biamino, D. Ugues, P. Fino, M. Lombardi, New Aluminum Alloys Specifically Designed for Laser Powder Bed Fusion: A Review, Mater. 2019, Vol. 12, Page 1007. 12 (2019) 1007. https://doi.org/10.3390/MA12071007.

[444] F. Alghamdi, M. Haghshenas, Microstructural and small-scale characterization of additive manufactured AlSi10Mg alloy, SN Appl. Sci. 1 (2019) 1–10. https://doi.org/10.1007/S42452-019-0270-5/FIGURES/12.

[445] X. Zhu, H. Yang, X. Dong, S. Ji, The effects of varying Mg and Si levels on the microstructural inhomogeneity and eutectic Mg2Si morphology in die-cast Al–Mg–Si alloys, J. Mater. Sci. 54 (2019) 5773–5787. https://doi.org/10.1007/S10853-018-03198-6/TABLES/3.

[446] M. Bärtl, X. Xiao, J. Brillo, F. Palm, Influence of Surface Tension and Evaporation on Melt Dynamics of Aluminum Alloys for Laser Powder Bed Fusion, J. Mater. Eng. Perform. 31 (2022) 6221–6233. https://doi.org/10.1007/S11665-022-06592-Z/TABLES/5.

[447] X. Tan, Y. Kok, Y.J. Tan, G. Vastola, Q.X. Pei, G. Zhang, Y.-W.W. Zhang, S.B. Tor, K.F. Leong, C.K. Chua, An experimental and simulation study on build thickness dependent microstructure for electron beam melted Ti-6Al-4V, J. Alloys Compd. 646 (2015) 303–309. https://doi.org/10.1016/j.jallcom.2015.05.178.

[448] A. Chakraborty, R. Tangestani, W. Muhammad, T. Sabiston, J.P. Masse, R. Batmaz, A. Wessman, É. Martin, Micro-cracking mechanism of RENÉ 108 thin-wall components built by laser powder bed fusion additive manufacturing, Mater. Today Commun. 30 (2022) 103139. https://doi.org/10.1016/J.MTCOMM.2022.103139.

[449] Z. Zhang, X. Yang, F. Song, X. Yao, T. Zhang, S. Liu, H. Tang, Assessment of microstructural evolution and associated tensile behavior in thin-walled Ti6Al4V parts manufactured via selective laser melting, Mater. Charact. 194 (2022) 112481. https://doi.org/10.1016/J.MATCHAR.2022.112481.

[450] X. Zhang, Y. hui Chueh, C. Wei, Z. Sun, J. Yan, L. Li, Additive manufacturing of three-dimensional metal-glass functionally gradient material components by laser powder bed fusion with in situ powder mixing, Addit. Manuf. 33 (2020) 101113. https://doi.org/10.1016/J.ADDMA.2020.101113.

[451] A.G. Demir, B. Previtali, Multi-material selective laser melting of Fe/Al-12Si components, Manuf. Lett. 11 (2017) 8–11. https://doi.org/10.1016/J.MFGLET.2017.01.002.

[452] J. Chen, Y. Yang, C. Song, D. Wang, S. Wu, M. Zhang, Influence mechanism of process parameters on the interfacial characterization of selective laser melting 316L/CuSn10, Mater. Sci. Eng. A. 792 (2020) 139316. https://doi.org/10.1016/J.MSEA.2020.139316.

[453] S. ZHONGJI, S. LEONG, C. KAI, L. ALEXANDER, Hopper for Powder Bed Fusion Additive Manufacturing, 2017. https://worldwide.espacenet.com/publicationDetails/biblio?CC=WO&NR=2017018935A1&KC=A1&FT=D&ND=4&date=20170202&DB=&locale=en_EP# (accessed May 9, 2024).

[454] Y. Wen, B. Zhang, R.L. Narayan, P. Wang, X. Song, H. Zhao, U. Ramamurty, X. Qu, Laser powder bed fusion of compositionally graded CoCrMo-Inconel 718, Addit. Manuf. 40 (2021) 101926. https://doi.org/10.1016/J.ADDMA.2021.101926.

[455] S. Wei, Y. Zhao, B. Zhang, P. Wang, U. Ramamurty, On the banded microstructures in CoCrMo-Ni in-situ alloyed through laser powder bed fusion, Mater. Lett. 361 (2024) 136077. https://doi.org/10.1016/J.MATLET.2024.136077.

[456] M. Fischer, D. Joguet, G. Robin, L. Peltier, P. Laheurte, In situ elaboration of a binary Ti–26Nb alloy by selective laser melting of elemental titanium and niobium mixed

powders, Mater. Sci. Eng. C. 62 (2016) 852–859. https://doi.org/10.1016/J.MSEC.2016.02.033.

[457] E.G. Brodie, A.E. Medvedev, J.E. Frith, M.S. Dargusch, H.L. Fraser, A. Molotnikov, Remelt processing and microstructure of selective laser melted Ti25Ta, J. Alloys Compd. 820 (2020) 153082. https://doi.org/10.1016/J.JALLCOM.2019.153082.

[458] C. Tang, K.Q. Le, C.H. Wong, Physics of humping formation in laser powder bed fusion, Int. J. Heat Mass Transf. 149 (2020) 119172. https://doi.org/10.1016/J.IJHEATMASSTRANSFER.2019.119172.

[459] C. Wang, X.P. Tan, Z. Du, S. Chandra, Z. Sun, C.W.J. Lim, S.B. Tor, C.S. Lim, C.H. Wong, Additive manufacturing of NiTi shape memory alloys using pre-mixed powders, J. Mater. Process. Technol. 271 (2019) 152–161. https://doi.org/10.1016/j.jmatprotec.2019.03.025.

[460] L. Yao, Z. Xiao, S. Huang, U. Ramamurty, The formation mechanism of metal-ceramic interlayer interface during laser powder bed fusion, Virtual Phys. Prototyp. 18 (2023). https://doi.org/10.1080/17452759.2023.2235324.

[461] C. Tang, L. Yao, H. Du, Computational framework for the simulation of multi material laser powder bed fusion, Int. J. Heat Mass Transf. 191 (2022) 122855. https://doi.org/10.1016/J.IJHEATMASSTRANSFER.2022.122855.

[462] P. Vora, K. Mumtaz, I. Todd, N. Hopkinson, AlSi12 in-situ alloy formation and residual stress reduction using anchorless selective laser melting, Addit. Manuf. 7 (2015) 12–19. https://doi.org/10.1016/J.ADDMA.2015.06.003.

[463] P. Vora, R. Martinez, N. Hopkinson, I. Todd, K. Mumtaz, Customised Alloy Blends for In-Situ Al339 Alloy Formation Using Anchorless Selective Laser Melting, Technol. 2017, Vol. 5, Page 24. 5 (2017) 24. https://doi.org/10.3390/TECHNOLOGIES5020024.

[464] M.L. Montero Sistiaga, R. Mertens, B. Vrancken, X. Wang, B. Van Hooreweder, J.P. Kruth, J. Van Humbeeck, Changing the alloy composition of Al7075 for better processability by selective laser melting, J. Mater. Process. Technol. 238 (2016) 437–445. https://doi.org/10.1016/J.JMATPROTEC.2016.08.003.

[465] W. Cong, F. Ning, A fundamental investigation on ultrasonic vibration-assisted laser engineered net shaping of stainless steel, Int. J. Mach. Tools Manuf. 121 (2017) 61–69. https://doi.org/10.1016/J.IJMACHTOOLS.2017.04.008.

[466] A.I. Gorunov, Additive manufacturing of Ti6Al4V parts using ultrasonic assisted direct energy deposition, J. Manuf. Process. 59 (2020) 545–556. https://doi.org/10.1016/J.JMAPRO.2020.10.024.

[467] D. Zhang, Y. Li, H. Wang, W. Cong, Ultrasonic vibration-assisted laser directed energy deposition in-situ synthesis of NiTi alloys: Effects on microstructure and mechanical properties, J. Manuf. Process. 60 (2020) 328–339. https://doi.org/10.1016/J.JMAPRO.2020.10.058.

[468] S. Gao, O.P. Bodunde, M. Qin, W.H. Liao, P. Guo, Effects of ultrasonic vibration on microstructures and thermal properties of nickel-titanium shape memory alloy fabricated by directed energy deposition, Manuf. Lett. 34 (2022) 16–19. https://doi.org/10.1016/J.MFGLET.2022.08.010.

[469] Z. Wang, F. Jiang, C. Guo, X. Xing, Z. Yang, H. Li, C. Liu, D. Xu, G. Jiang, S. Konovalov, Effects of ultrasonic vibration on microstructure and mechanical properties of 1Cr12Ni3MoVN alloy fabricated by directed energy deposition, Ultrasonics. 132 (2023) 106989. https://doi.org/10.1016/J.ULTRAS.2023.106989.

[470] N. Kang, H. Yuan, P. Coddet, Z. Ren, C. Bernage, H. Liao, C. Coddet, On the texture, phase and tensile properties of commercially pure Ti produced via selective laser melting assisted by static magnetic field, Mater. Sci. Eng. C. 70 (2017) 405–407. https://doi.org/10.1016/J.MSEC.2016.09.011.

[471] D. Du, J.C. Haley, A. Dong, Y. Fautrelle, D. Shu, G. Zhu, X. Li, B. Sun, E.J. Lavernia, Influence of static magnetic field on microstructure and mechanical behavior of selective laser melted AlSi10Mg alloy, Mater. Des. 181 (2019) 107923. https://doi.org/10.1016/J.MATDES.2019.107923.

[472] X. Fan, T.G. Fleming, D.T. Rees, Y. Huang, S. Marussi, C.L.A. Leung, R.C. Atwood, A. Kao, P.D. Lee, Thermoelectric magnetohydrodynamic control of melt pool flow during laser directed energy deposition additive manufacturing, Addit. Manuf. 71 (2023) 103587. https://doi.org/10.1016/J.ADDMA.2023.103587.

[473] S. Yu, C. Chen, S. Xu, T. Hu, S. Shuai, J. Wang, J. Zhao, Z. Ren, Effect of static magnetic field on the molten pool dynamics during laser powder bed fusion of Inconel 718 superalloy, Int. J. Therm. Sci. 197 (2024) 108851. https://doi.org/10.1016/J.IJTHERMALSCI.2023.108851.

[474] X. Tian, Y. Zhu, C.V.S. Lim, J. Williams, R. Boyer, X. Wu, K. Zhang, A. Huang, Isotropic and improved tensile properties of Ti-6Al-4V achieved by in-situ rolling in direct energy deposition, Addit. Manuf. 46 (2021) 102151. https://doi.org/10.1016/J.ADDMA.2021.102151.

[475] C. Li, Y. Tian, Y. Chen, P. Hodgson, X. Wu, Y. Zhu, A. Huang, Hierarchical layered and refined grain structure of Inconel 718 superalloy produced by rolling-assisted directed energy deposition, Addit. Manuf. Lett. 1 (2021) 100009. https://doi.org/10.1016/J.ADDLET.2021.100009.

[476] W.H. Kan, D. Jiang, M. Humbert, X. Gao, V.K. Bhatia, G. Proust, Y. Zhu, P. Hodgson, A. Huang, Effect of in-situ layer-by-layer rolling on the microstructure, mechanical properties, and corrosion resistance of a directed energy deposited 316L stainless steel, Addit. Manuf. 55 (2022) 102863. https://doi.org/10.1016/J.ADDMA.2022.102863.

[477] C. Li, P. Hodgson, M. Preuss, Y. Chen, X. Wu, Y. Zhu, Y. Tian, A. Huang, Rolling-assisted direct energy deposited Inconel 718: Microstructural evolution and mechanical properties after optimized heat treatment, J. Mater. Sci. Technol. 144 (2023) 118–127. https://doi.org/10.1016/J.JMST.2022.10.021.

[478] J. Chi, Z. Cai, H. Zhang, H. Zhang, W. Guo, Z. Wan, G. Han, P. Peng, Z. Zeng, Combining manufacturing of titanium alloy through direct energy deposition and laser shock peening processes, Mater. Des. 203 (2021) 109626. https://doi.org/10.1016/J.MATDES.2021.109626.

[479] H. Lu, L. Wu, H. Wei, J. Cai, K. Luo, X. Xu, J. Lu, Microstructural evolution and tensile property enhancement of remanufactured Ti6Al4V using hybrid manufacturing of laser directed energy deposition with laser shock peening, Addit. Manuf. 55 (2022)

102877. https://doi.org/10.1016/J.ADDMA.2022.102877.

[480] S.N. Singh, A.B. Deoghare, Enhanced fatigue performance of laser directed energy deposition fabricated Ti6Al4V alloy using laser shock peening, Procedia Struct. Integr. 56 (2024) 11–18. https://doi.org/10.1016/J.PROSTR.2024.02.031.

[481] X. Zhang, S. Huang, D. Li, J. Geng, F. Yang, Q. Li, An approach to improve the microstructure and mechanical properties: A hybrid manufacturing of laser directed energy deposition and shot peening, Addit. Manuf. 55 (2022) 102686. https://doi.org/10.1016/J.ADDMA.2022.102686.

[482] D. Wu, C. Yu, Q. Wang, F. Niu, G. Ma, H. Wang, C. Zhou, B. Zhang, Synchronous-hammer-forging-assisted laser directed energy deposition additive manufacturing of high-performance 316L samples, J. Mater. Process. Technol. 307 (2022) 117695. https://doi.org/10.1016/J.JMATPROTEC.2022.117695.

[483] S. Zhou, Z. Liu, G. Yang, X. Li, J. Wang, X. Guo, X. Wang, Heterostructure microstructure and laves phase evolution mechanisms during inter-layer hammering hybrid directed energy deposition (DED) process, Mater. Sci. Eng. A. 886 (2023) 145668. https://doi.org/10.1016/J.MSEA.2023.145668.

[484] A. Mithal, N. Maharjan, S. Idapalapati, Microstructural evolution in laser-based directed energy deposition of 316 L stainless steel with interlayer deformation, Mater. Charact. 209 (2024) 113779. https://doi.org/10.1016/J.MATCHAR.2024.113779.

[485] F. Ning, W. Cong, Microstructures and mechanical properties of Fe-Cr stainless steel parts fabricated by ultrasonic vibration-assisted laser engineered net shaping process, Mater. Lett. 179 (2016) 61–64. https://doi.org/10.1016/J.MATLET.2016.05.055.

[486] C. Li, S. Sun, C. Liu, Q. Lu, P. Ma, Y. Wang, Microstructure and mechanical properties of TiC/AlSi10Mg alloy fabricated by laser additive manufacturing under high-frequency micro-vibration, J. Alloys Compd. 794 (2019) 236–246. https://doi.org/10.1016/J.JALLCOM.2019.04.287.

[487] A. Kao, T. Gan, C. Tonry, I. Krastins, K. Pericleous, Thermoelectric magnetohydrodynamic control of melt pool dynamics and microstructure evolution in additive manufacturing, Philos. Trans. R. Soc. A. 378 (2020). https://doi.org/10.1098/RSTA.2019.0249.

[488] M. Friák, W.A. Counts, D. Ma, B. Sander, D. Holec, D. Raabe, J. Neugebauer, Theory-guided materials design of multi-phase Ti-Nb alloys with bone-matching elastic properties, Materials (Basel). 5 (2012) 1853–1872.

[489] S. Li, K.B. Lau, D. Wuu, F. Wei, M. Lin, A. Cheong, P. Wang, C.C. Tan, U. Ramamurty, 3D printing of ductile equiatomic Fe-Co alloy for soft magnetic applications, Addit. Manuf. 47 (2021) 102291. https://doi.org/10.1016/J.ADDMA.2021.102291.

[490] J. Zhang, B. Song, Q. Wei, D. Bourell, Y. Shi, A review of selective laser melting of aluminum alloys: Processing, microstructure, property and developing trends, J. Mater. Sci. Technol. 35 (2019) 270–284. https://doi.org/https://doi.org/10.1016/j.jmst.2018.09.004.

[491] B. Chen, S.K. Moon, X. Yao, G. Bi, J. Shen, J. Umeda, K. Kondoh, Strength and strain hardening of a selective laser melted AlSi10Mg alloy, Scr. Mater. 141 (2017) 45–49.

https://doi.org/https://doi.org/10.1016/j.scriptamat.2017.07.025.

[492] K. Saeidi, X. Gao, F. Lofaj, L. Kvetková, Z.J. Shen, Transformation of austenite to duplex austenite-ferrite assembly in annealed stainless steel 316L consolidated by laser melting, J. Alloys Compd. 633 (2015) 463–469. https://doi.org/10.1016/j.jallcom.2015.01.249.

[493] S. Dryepondt, P. Nandwana, P. Fernandez-Zelaia, F. List, Microstructure and high temperature tensile properties of 316L fabricated by laser powder-bed fusion, Addit. Manuf. 37 (2021) 101723. https://doi.org/10.1016/j.addma.2020.101723.

[494] E. Tascioglu, Y. Karabulut, Y. Kaynak, Influence of heat treatment temperature on the microstructural, mechanical, and wear behavior of 316L stainless steel fabricated by laser powder bed additive manufacturing, Int. J. Adv. Manuf. Technol. 107 (2020) 1947–1956.

[495] C. Man, C. Dong, T. Liu, D. Kong, D. Wang, X. Li, The enhancement of microstructure on the passive and pitting behaviors of selective laser melting 316L SS in simulated body fluid, Appl. Surf. Sci. 467 (2019) 193–205.

[496] J. Suryawanshi, T. Baskaran, O. Prakash, S.B. Arya, U. Ramamurty, On the corrosion resistance of some selective laser melted alloys, Materialia. 3 (2018) 153–161.

[497] Q. Chao, V. Cruz, S. Thomas, N. Birbilis, P. Collins, A. Taylor, P.D. Hodgson, D. Fabijanic, On the enhanced corrosion resistance of a selective laser melted austenitic stainless steel, Scr. Mater. 141 (2017) 94–98.

[498] D. Kong, C. Dong, X. Ni, L. Zhang, H. Luo, R. Li, L. Wang, C. Man, X. Li, The passivity of selective laser melted 316L stainless steel, Appl. Surf. Sci. 504 (2020) 144495.

[499] M.J.K. Lodhi, K.M. Deen, M.C. Greenlee-Wacker, W. Haider, Additively manufactured 316L stainless steel with improved corrosion resistance and biological response for biomedical applications, Addit. Manuf. 27 (2019) 8–19.

[500] J.M. Park, Y. Zhao, T. Voisin, D.H. Lee, S. ichi Komazaki, Y. Ko, D.I. Kim, J.Y. Suh, H.N. Han, Y.M. Wang, U. Ramamurty, J. il Jang, Hydrogen uptake and its influence in selective laser melted austenitic stainless steel: A nanoindentation study, Scr. Mater. 194 (2021) 113718. https://doi.org/10.1016/J.SCRIPTAMAT.2020.113718.

[501] J.Y. Ho, K.F. Rabbi, S. Khodakarami, S. Sett, T.N. Wong, K.C. Leong, W.P. King, N. Miljkovic, Ultrascalable Surface Structuring Strategy of Metal Additively Manufactured Materials for Enhanced Condensation, Adv. Sci. 9 (2022) 2104454. https://doi.org/https://doi.org/10.1002/advs.202104454.

[502] S. Tekumalla, J.E. Chew, S.W. Tan, M. Krishnan, M. Seita, Towards 3-D texture control in a β titanium alloy via laser powder bed fusion and its implications on mechanical properties, Addit. Manuf. 59 (2022) 103111. https://doi.org/https://doi.org/10.1016/j.addma.2022.103111.

[503] K.A. Sofinowski, S. Raman, X. Wang, B. Gaskey, M. Seita, Layer-wise engineering of grain orientation (LEGO) in laser powder bed fusion of stainless steel 316L, Addit. Manuf. 38 (2021) 101809. https://doi.org/https://doi.org/10.1016/j.addma.2020.101809.

[504] K. Sofinowski, M. Wittwer, M. Seita, Encoding data into metal alloys using laser

powder bed fusion, Addit. Manuf. 52 (2022) 102683. https://doi.org/https://doi.org/10.1016/j.addma.2022.102683.

[505] R. Hermann, H. Hermann, M. Calin, B. Büchner, J. Eckert, Elastic constants of single crystalline β-Ti70Nb30, Scr. Mater. 66 (2012) 198–201.

[506] U.F. Kocks, C.N. Tomé, H.-R. Wenk, Texture and anisotropy: preferred orientations in polycrystals and their effect on materials properties, Cambridge university press, 2000.